

PAUL SCHERRER INSTITUT



# Annual Report 2010

Electrochemistry Laboratory

<http://ecl.web.psi.ch>

**COVER PHOTO:**

In the search for better battery materials hundreds of laboratory test batteries are electrochemically cycled at the same time under controlled conditions. The photograph shows such test batteries.

© Paul Scherrer Institut

PAUL SCHERRER INSTITUT



## Electrochemistry Laboratory

# Annual Report 2010

Hardcopies of this report are available from:

Isabella Kalt (isabella.kalt@psi.ch)

Paul Scherrer Institut

5232 Villigen PSI

Switzerland

A full version of this report is also available on the web:

<http://ecl.web.psi.ch>

Paul Scherrer Institut  
Electrochemistry Laboratory  
5232 Villigen PSI  
Switzerland

Secretary

Phone +41 (0)56 310 29 19

Fax +41 (0)56 310 44 15

**Publisher**  
Electrochemistry Laboratory  
Paul Scherrer Institut  
5232 Villigen PSI

**Editorial Team**  
Isabella Kalt  
Rüdiger Kötz  
Günther G. Scherer

**Printing**  
Paul Scherrer Institut

ISSN 1661-5379  
PSI Electrochemistry Laboratory – Annual Report 2010

© Paul Scherrer Institut

# CONTENTS

- 1 EDITORIAL**  
G.G. Scherer
- 3 SCIENTIFIC CONTRIBUTIONS 2010**
- FUEL CELLS - MATERIALS**
- 5** Effect of styrene/methacrylonitrile composition on the performance of radiation grafted ETFE based membranes for PEFCs
- 7** Styrene-co-(meth)acrylonitrile radiation grafted ETFE based membranes: Influence of the  $\alpha$ -methyl and nitrile group on membrane properties
- 9** Does methacrylonitrile (MAN) affect the conductivity and crystallinity of styrene based membranes for fuel cells?
- 11** A simulation study on the radical ( $\text{HO}^\bullet$ ,  $\text{H}^\bullet$ , and  $\text{HOO}^\bullet$ ) formation and membrane degradation in PEFC
- 13** The DEMMEA project: Understanding the degradation mechanisms of membrane-electrode assembly and optimization of individual components
- 15 FUEL CELLS - DIAGNOSTICS**
- 17** Transient Helox operation as a tool for the study of PEFC mass transport limitations
- 19** Neutron imaging of isothermal sub-zero degree Celsius cold-start of a PEFC
- 21** A two-dimensional impedance model on the channel/rib scale of PEFCs
- 23** Investigating the low frequency inductive behavior in subsaturated PEFCs
- 24** PEFC membrane parameter determination using *in situ* laser absorption spectroscopy and 1+1 dimensional modeling
- 26** Locally resolved EIS in channel and land areas of PEFCs
- 28** Investigation of mass transport phenomena in channel and land areas during start-up and shutdown of PEFCs
- 30** Mitigation strategies for start-stop induced degradation in channel and land areas of a PEFC
- 32** Correlation of local water content and current density transients in channel and land areas of a PEFC
- 33** TEM sectioning as a method to determine Pt losses in PEFCs
- 34** 3D imaging of catalyst support corrosion in polymer electrolyte fuel cells
- 36** A novel approach for a 1D-model for PEFC
- 37** Development of *in situ* X-ray tomographic microscopy for PEFC
- 39** A new fuel cell / battery hybrid concept for automotive applications
- 41** Degradation of the gas separation in PEFCs characterized by local gas permeation analysis
- 43 BATTERIES & SUPERCAPACITORS - MATERIALS**
- 45** Rate capability of graphite anodes in lithium-ion batteries
- 46** Oxygen evolution from  $\text{Li}_2\text{MnO}_3$ -stabilized  $\text{Li}(\text{Ni}_x\text{Mn}_y\text{Co}_z)\text{O}_2$  electrode materials
- 48** Continuous flame synthesis of carbon-coated nano- $\text{LiFePO}_4$  for Li-ion batteries
- 50** Microwave-assisted preparation of sulphur-carbon composite materials for lithium-sulphur batteries
- 52** Synthesis of an artificial SEI on carbon by grafting and other chemical methods to decrease the irreversible charge loss
- 54** Conductive carbon networks in positive electrodes for Li-ion batteries
- 56** Investigation of the electrochemical activation of partially reduced graphite oxide
- 58** Characterization of full cell electrochemical hybrid energy storage systems
- 61 BATTERIES & SUPERCAPACITORS - DIAGNOSTICS**
- 63** Neutron imaging of a complete lithium-ion cell with  $\text{Li}_2\text{MnO}_3$ -stabilized  $\text{Li}(\text{Ni}_x\text{Mn}_y\text{Co}_z)\text{O}_2$  cathode material vs. graphite

- 65 Structural investigations of  $\text{Li}_2\text{MnO}_3\text{-Li}(\text{Mn}_x\text{Ni}_y\text{Co}_z)\text{O}_2$  – neutron diffraction, *in situ* X-ray diffraction and *in situ* Raman spectroscopy
- 67 Combined *in situ* FTIR and Raman microscopy of electrode materials
- 68 Study of overcharge behavior of  $\text{Li}_{1+x}(\text{Ni}_{1/3}\text{Mn}_{1/3}\text{Co}_{1/3})_{1-x}\text{O}_2$  using *in situ* synchrotron diffraction
- 70 Effect of water on capacitance fading for supercapacitors using propylene carbonate as solvent
- 72 Investigation of kinetics of ion transport on supercapacitors using nanoporous starburst carbon spheres as a model electrode
- 75 **CATALYSIS & INTERFACES**
- 77 Longevity test of sputtered anodes in PEFCs – Different recovery effects after CO-poisoning?
- 78 Platinum based cathodes for PEFCs prepared by magnetron sputtering
- 79 Platinum dissolution at the anode and cathode of PEFCs caused by start/stop and load cycling
- 80 Investigations on the corrosion of the microporous and gas diffusion layer in PEFCs
- 82 The effect of low relative reactant gas humidity on carbon corrosion in PEFCs
- 84 The effect of lower voltage limit on the assessment of catalyst layer durability in PEFCs by potential cycling
- 85 Acid leaching of  $\text{PtCo}_x/\text{C}$  catalysts for oxygen reduction
- 87 STM study of Pt/C model electrodes prepared via e-beam lithography
- 89 Ionic liquids in vacuo: Concept and design of a newly developed *in situ* XPS cell
- 91 The potential window of imidazolium based ionic liquids - A comparative XPS, DFT and electrochemical study
- 93 **THE ELECTROCHEMISTRY LABORATORY**
- 95 Impressions
- 97 Structure
- 99 ECL-personnel
- 100 These PhD students from ECL graduated in 2010
- 101 Exchange students, diploma theses
- 102 Seminar, invited speakers
- 103 Awards
- 104 Conferences – Symposia
- 105 Review activities of the laboratory
- 106 Industrial partners
- 107 Documentation

Fundamental electrochemical research and the knowledge created thereby is the prerequisite to bring novel concepts and ideas forward to possible applications and transfer it to technology. This is particularly of interest in the area of electrochemical energy technologies. For many years, our Laboratory has dedicated its efforts to various aspects of electrochemical energy conversion in fuel cells and electrochemical energy storage in batteries and double layer capacitors, by bridging this gap between fundamental research and engineering aspects.

This approach has allowed us to transfer our genuine know-how to industry at an early stage. In this respect, the past year 2010 was a very successful one. On one side, we could announce first results of our collaboration with Belenos AG, Biel, namely the development and demonstration of a 25 kW H<sub>2</sub>/O<sub>2</sub> fuel cell stack fulfilling the demanding specifications for its integration into an all-electric power train. Future oriented, we could announce the participation as an academic founding partner of the BASF international research network *Electrochemistry and Batteries*. In addition to these two highlights, we continued to work on many other technology transfer projects. In accordance to our philosophy, aspects of fundamental electrochemistry pursued to be in focus of our work.

With the 44 contributions to this report, we deliver an overview on activities and results achieved during the course of the year 2010. Materials research for the electrochemical devices of interest, diagnostic methods and results of their *ex situ* and *in situ* applications, and systems issues are the topics.

In addition to our daily scientific work, dissemination of results and education of our co-workers and the scientific community are of prime importance.

“Electrochemistry in Switzerland” was the topic of our 26<sup>th</sup> One-Day-Symposium on Electro-chemistry, which took place on May 5, 2010. Close to 100 participants from several countries expressed their interest in electrochemical research and industrial activities. The topic was introduced by Patrik Schmuki, University of Erlangen, providing an overview on past and today's Electrochemistry in Switzerland from the outside. Hubert Girault, Ecole Polytechnique Fédéral de Lausanne, presented his view on *Interfacial Electrochemistry: A Special Focus on Soft Interfaces*. An overview on *Electrochemical Energy Research in Switzerland* was given by A. Wokaun, Paul Scherrer Institut and O. Bucheli, HTceramix-SOFCpower, Yverdon-les-Bains,

referring to different operating temperature regimes of the respective devices. J.C. Puipe, Steiger SA, Châtel-St-Denis, L. Philippe, Empa Thun, and T. Suter, Empa, Dübendorf, addressed issues of *Electrochemical Surface Treatments and Corrosion*, and Caspar Demuth, ZHAW, Wädenswil, reported on *Electrochemical Sensors: Trends and Challenges in Academic and Industrial R&D*. Finally, L. Schlapbach, former director of Empa, gave an outlook on *Future*

*Electrochemical R&D Activities in Switzerland* and the possibilities for their funding.

Today, we are already looking forward to our 27th One-Day-Symposium, taking place on May 11, 2011, where we address the important topic of *Electromobility*. Lecturers from academia and industry will deliver their views on the future of the various technologies comprising the overall topic electromobility.

We will be delighted to welcome many of you on this occasion, which also offers you a possibility to start or continue discussion with us on possible joint interests.

Please enjoy reading our Electrochemistry Laboratory Annual Report 2010.

Günther G. Scherer



# SCIENTIFIC CONTRIBUTIONS 2010

FUEL CELLS

MATERIALS



# Effect of styrene/methacrylonitrile composition on the performance of radiation grafted ETFE based membranes for PEFCs

H. Ben youcef, K. Jetsrisuparb, L. Gubler, A. Wokaun, G.G. Scherer

phone: +41 56 310 4188, e-mail: hicham.ben-youcef@psi.ch

The development of radiation grafted membranes for fuel cell application is directed towards the improvement of the cost effectiveness, chemical/oxidative stability, and reliability. During fuel cell operation, the membrane is subjected to chemical, thermal, and mechanical stress. Evidently, the selection of the base film and grafted polymer is a key to control and improve the membrane properties. The grafting of the  $\alpha$ -methylstyrene/methacrylonitrile (AMS/MAN) copolymer into fluorinated base films resulted in a membrane with an improved chemical stability under fuel cell operation (80°C) in comparison to a styrene grafted membrane [1]. In the first approach, the MAN was used as co-monomer to promote the grafting of the  $\alpha$ -methylstyrene (AMS), due to its poor radical polymerization kinetics and low ceiling temperature (60°C) [1]. Thus, the MAN was thought to be a "dead mass" in the system, i.e., it was thought not to contribute to the proton conductivity and performance of the grafted membrane. Recently, we showed that the observed stability is not only the result of the  $\alpha$ -position protection in AMS compared to styrene, but also the incorporation of the MAN monomer itself [2]. We have adopted an approach using styrene-co-MAN co-grafted into poly(ethylene-*alt*-tetrafluoroethylene) (ETFE) base film to evaluate the influence of the MAN content on the performance of grafted membranes at fixed ion exchange capacity (IEC).

## Experimental

Based on a detailed kinetics study [3], a set of membranes based on ETFE (25  $\mu\text{m}$ , Dupont) with fixed ion exchange capacity (IEC) of  $\sim 1.5 \text{ mmol}\cdot\text{g}^{-1}$  and with different molar fractions of styrene/MAN were prepared. The membranes were prepared with different styrene/MAN molar fractions (0.2, 0.4, 0.6, 0.8 and 1) in the initial grafting solution, as described previously [3-4]. The styrene/MAN composition in the grafted ETFE films was determined by FTIR analysis (Table 1).

#	Membrane	GL	Styrene molar fraction in the film	Ion exchange capacity
		%	-	$\text{mmol}\cdot\text{g}^{-1}$
1	S-co-MAN	61	$0.39 \pm 0.02$	$1.59 \pm 0.03$
2	S-co-MAN	38	$0.56 \pm 0.02$	$1.43 \pm 0.05$
3	S-co-MAN	34	$0.64 \pm 0.04$	$1.55 \pm 0.01$
4	S-co-MAN	29	$0.77 \pm 0.04$	$1.61 \pm 0.05$
5	S-co-MAN	23	$1.00 \pm 0.00$	$1.54 \pm 0.02$
6	Nafion 212	-	-	$1.10 \pm 0.02$

**Table 1.** Graft level (GL), molar fraction and ion exchange capacity (mass base) of the styrene/MAN grafted ETFE based membranes. Data for Nafion 212 is presented for comparison.

The grafted membranes were impregnated with 0.5 % Nafion solution, dried and hotpressed (110 °C / 40 kN / 180 s) together with poly(ethylene naphthalate) (PEN) sub-gaskets of 25  $\mu\text{m}$  thickness and gas diffusion electrodes (type JM EL162, Johnson Matthey Fuel Cells) with a platinum loading of  $0.4 \text{ mg cm}^{-2}$ . The MEA

was assembled into a single fuel cell with an active area of  $16 \text{ cm}^2$  and operated at a temperature of 80 °C and at a constant current density of  $500 \text{ mA}\cdot\text{cm}^{-2}$ . The electrochemical characterization techniques, namely, high frequency resistance (HFR), polarization curves, electrochemical impedance spectroscopy (EIS) (impedance at HF intercept and polarization resistance), and  $\text{H}_2$  crossover, were measured. Experimental details of the used procedures are available elsewhere [4].

## Results

The styrene-co-MAN grafted membranes were characterized for their *ex situ* fuel cell relevant properties (IEC, water uptake and through plane conductivity) (Table 2).

#	Water uptake	Ion exchange capacity	Thickness	Conductivity
	%	$\text{mmol}\cdot\text{cm}^{-3}$	$\mu\text{m}$	$\text{mS}\cdot\text{cm}^{-1}$
1	$61 \pm 2$	$1.26 \pm 0.04$	$45 \pm 2$	$84 \pm 11$
2	$47 \pm 3$	$1.34 \pm 0.03$	$41 \pm 1$	$93 \pm 9$
3	$49 \pm 1$	$1.39 \pm 0.03$	$40 \pm 2$	$100 \pm 9$
4	$38 \pm 2$	$1.61 \pm 0.04$	$39 \pm 1$	$85 \pm 3$
5	$35 \pm 2$	$1.52 \pm 0.19$	$37 \pm 1$	$86 \pm 6$
6	$39 \pm 1$	$1.28 \pm 0.03$	$65 \pm 1$	$78 \pm 4$

**Table 2.** *Ex situ* properties of the styrene/MAN grafted ETFE based membranes and Nafion 212. Conductivity measurement were performed at fully swollen state at RT.

The volume based IEC shows clearly the effect of the increase of MAN content (GL increases) on the dimensional change of the grafted membrane (Table 2). In fact, the volume based IEC decreases with the decrease of styrene molar fraction in the grafted membrane, whereas the water uptake and the thickness showed an opposite trend. Interestingly, the membrane conductivity was not improved either with the increase of water uptake nor with the increase of the volume based IEC. This finding is quite different from what has been observed previously for the styrene based membranes and the linearly increasing trend of conductivity with graft level i.e., improving proton mobility with an increase of water uptake [4]. Therefore, the hydrophilicity of the nitrile group and its ability to form hydrogen bonds with water do not improve the proton mobility. The question to address in near future is related to the nano-scale morphology of the co-grafted membranes at lower molar styrene fraction and its effect on proton transport.

To ensure good lamination between the grafted membrane and the electrodes, the ETFE based membranes were impregnated with Nafion/ethanol solution 5 % (v/v), while Nafion 212 showed good lamination when hot-pressed with the electrode without need of impregnation. The assembled MEAs were tested under steady conditions and the single fuel cell performance was evaluated *in situ* by recording polarization curves after 24 h operation (Figure 1). No

significant change of the recorded HF resistance values were measured with the decrease of the styrene molar fraction. A slight difference in the cell voltage between the different MEAs was determined at high current densities. The MEA based on a styrene molar fraction of 0.56 showed comparable performance in comparison to that of Nafion 212.

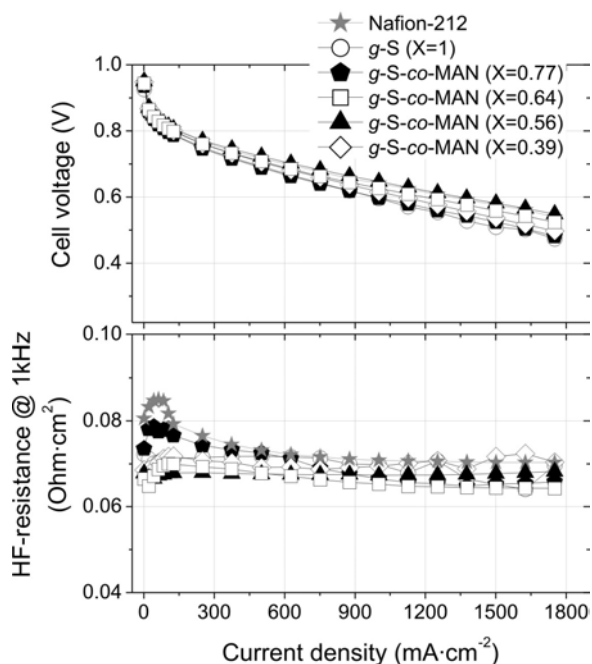


**Figure 1.** Polarization curves of MEAs based on grafted ETFE-g-styrene-co-MAN based membranes and Nafion 212 at a cell temperature of 80 °C;  $H_2/O_2$  at a stoichiometry of 1.5/2, atmospheric gas pressure, full humidification at 80 °C.

To determine the origin of the differences in the MEA's performance, electrochemical impedance spectra were recorded (Figure 2). No significant change in the impedance values extracted at the intercept at high frequency was measured, which correlates quite well to the *ex situ* conductivity values (Table 1). However, the polarization resistance, which is a measure of the quality of the interfacial properties of the MEAs, showed a clear trend. The membranes with high styrene molar fraction (0.77 and 1) in the grafted membrane showed similar polarization resistance values and were by ~50 % higher than those of the other membranes, including the MEA based on Nafion 212.

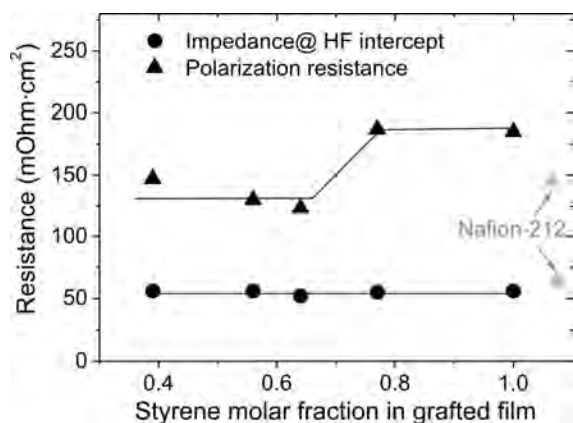


**Figure 2.** Ohmic resistance and polarization resistance of MEAs based on ETFE-g-styrene-co-MAN membranes and Nafion 212, based on ac impedance spectra recorded at a dc current density of 500  $mA\cdot cm^{-2}$  (frequency range: 0.1 Hz – 50 kHz).

Evidently, the combination of Nafion solution impregnation procedure and improved surface properties introduced by the polarity of the nitrile group of MAN to some extent induce better adhesion properties between the electrode and the grafted membrane.

To evaluate *in situ* the mechanical integrity of the grafted membranes and the influence of styrene/MAN composition, the  $H_2$  crossover was measured electrochemically in  $H_2 / N_2$  mode at 80 °C (Figure 3). The  $H_2$  crossover gradually decreases with a decrease of the styrene molar fraction and all grafted samples show lower permeability values than the Nafion<sup>®</sup>212 sample. We note here that Nafion 212 is thicker than all styrene-co-MAN grafted membranes (Table 2). It is expected that an increase of membrane thickness with an increase of MAN molar fraction will lead to a reduced permeability. Likewise, an increase of GL and water uptake is assumed to lead to an increase in membrane permeability. In addition, the nitrile group was pointed out to be the functional group of choice to be incorporated into polymer materials in order to improve their gas barrier properties [5].

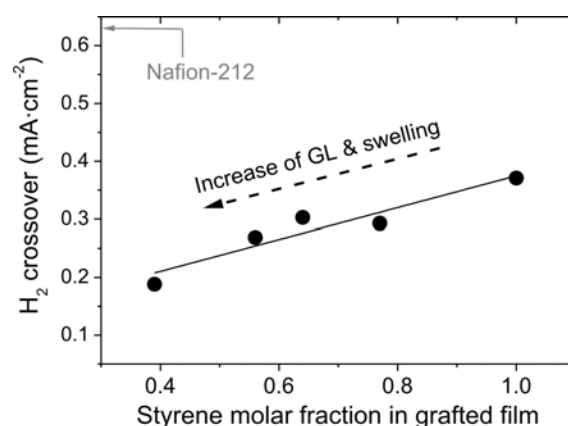


**Figure 3.** Hydrogen crossover of ETFE-g-styrene-co-MAN based membranes and Nafion 212 measured electrochemically in  $H_2 / N_2$  mode at 80 °C.

It is clear that the improvement of performance of styrene-co-MAN grafted membrane is governed by the combination of good interfacial properties, optimized monomer composition, and reduced gas permeability. The styrene-co-MAN grafted membranes exhibit comparable interfacial properties and performance at high MAN content, when assembled with JM electrodes. Furthermore, grafted membranes exhibit lower gas crossover and higher dimensional stability than the Nafion 212 membrane.

## References

- [1] L. Gubler, M. Slaski, F. Wallasch, A. Wokaun, G.G. Scherer, *J. Membr. Sci.* **339**, 68-77 (2009).
- [2] H. Ben youcef, L. Gubler, S. Alkan-Gürsel, D. Henkensmeier, A. Wokaun, G.G. Scherer, *Electrochem. Commun.* **11**, 941-444 (2009).
- [3] K. Jetsrisuparb, H. Ben youcef, G.G. Scherer, A. Wokaun, L. Gubler, *PSI Electrochemistry - Annual Report 2009*, 9-10, ISSN 1661-5379 (2010).
- [4] H. Ben youcef, Ph.D. Thesis, ETH No. 18215, Swiss Federal Institut of Technology Zürich (2009).
- [5] A.E. Barnabeo, W.S. Creasy, L.M. Robeson, *J. Polym. Sci.: Polym. Chem. Ed.* **13**, 1975-1986 (1979).

# Styrene-co-(meth)acrylonitrile radiation grafted ETFE based membranes: Influence of the $\alpha$ -methyl and nitrile group on membrane properties

H. Ben youcef, K. Jetsrisuparb, A. Waibel<sup>1</sup>, L. Gubler, G.G. Scherer, A. Wokaun

phone: +41 56 310 4188, e-mail: hicham.ben-youcef@psi.ch

The second generation proton exchange membrane for fuel cells prepared by radiation induced grafting of  $\alpha$ -methylstyrene / methacrylonitrile (AMS / MAN) copolymer into fluorinated base films showed improved chemical stability under fuel cell operation (80°C) [1]. In the first approach, MAN was used as co-monomer to promote the grafting of the AMS, due to its poor radical polymerization kinetics and low ceiling temperature (60°C) [1]. Thus, the MAN was thought to be a "dead mass" in the system, i.e. not contributing to the proton conductivity and performance of the grafted membrane. Recently, it was shown that the observed stability is not only the result of the  $\alpha$ -position protection in AMS as compared to styrene, but also the incorporation of the MAN monomer itself [2]. However, the role of MAN for the stability of these membranes is not yet understood. In this contribution, we have adopted an approach using styrene-co-MAN and styrene-co-acrylonitrile (AN) co-grafted into poly(ethylene-*alt*-tetrafluoroethylene) (ETFE) base film to evaluate the influence of these two factors mentioned before on the *ex situ* fuel cell relevant membrane properties.

## Experimental

Based on a detailed kinetics study, a set of styrene-co-AN and styrene-co-MAN grafted films based on ETFE (25  $\mu\text{m}$ , Dupont) with fixed graft level (GL) of ~ 40 % and with different styrene molar fractions (molar fraction of styrene is  $X(\text{styrene}) = 0.2, 0.4, 0.6, 0.8, 1$  in the initial grafting solution) were prepared. The styrene-co-MAN and styrene-co-AN grafted ETFE base films were characterized by FTIR analysis. Membranes obtained by sulfonation of grafted films were characterized *ex situ* to determine their fuel cell relevant properties, namely, ion exchange capacity (IEC), swelling, conductivity and dimensional stability (wet $\rightarrow$ dry) [3]. Membrane electrode assemblies (MEA) were prepared by hotpressing selected grafted membranes onto gas diffusion electrodes (type JM EL162 / Johnson Matthey Fuel Cells, platinum loading 0.4 mg Pt cm<sup>-2</sup>) and then characterized *in situ* in a single fuel cell

## Results

Detailed kinetics studies using both monomer combinations were performed and the film compositions were determined using FTIR spectroscopy. The understanding of the radiation induced co-grafting of two monomers was important to ensure an optimal control of the grafted films' resulting composition. Thus, reactivity ratios for the different monomer combinations of  $r(\text{styrene}) = 0.53 \pm 0.07$ ,  $r(\text{AN}) = 0.22 \pm 0.05$  and  $r(\text{styrene}) = 0.50 \pm 0.06$ ,  $r(\text{MAN}) = 0.13 \pm 0.03$  were determined for styrene-co-AN and styrene-co-MAN grafted films, respectively. Both monomers show similarities when co-grafted with styrene. However, it is important to point out that AN can not be grafted well into ETFE alone, as it is the case with MAN. This is most likely due to the difference in solubility and polarity factors between the two nitrile monomers [4]. Due to its stronger polarity, AN is more soluble in water than MAN and the polyacrylonitrile (PAN) is known to be insoluble

in its monomer. Band shifts at 2234 cm<sup>-1</sup> wavenumber value (band of the C $\equiv$ N group) were observed in both systems with an increase of AN / MAN content in grafted films. Thus, the generated intramolecular/intermolecular interactions showed clearly the influence of the polarity of the nitrile group on ETFE grafted films [2-4]. Grafted films with fixed GL (40%) and with different molar fractions were prepared and subsequently sulfonated to obtain proton exchange membranes.

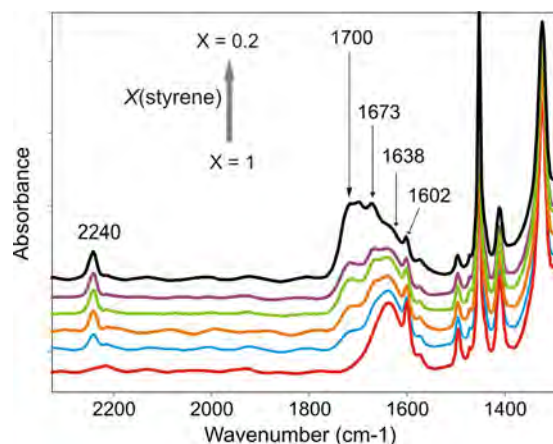


Figure 1. FTIR spectra of styrene-co-AN grafted membranes at different styrene molar fraction and at fix graft level (GL ~ 40 %).

Based on the FTIR spectra of membranes, the shift observed in the C $\equiv$ N wavenumber value disappeared after sulfonation in both monomer combination systems (Figure 1-2). The spectra of the styrene-co-AN based membranes revealed that the nitrile groups were partially hydrolysed into amide and carboxylic acid (Figure 1), whereas the styrene-co-MAN based membranes were not subjected to significant change (Figure 2). Only the highly MAN grafted film subjected to the sulfonation procedure showed slight hydrolysis (Figure 2).

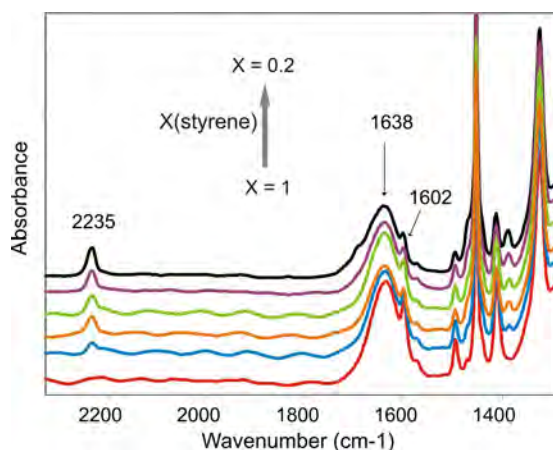
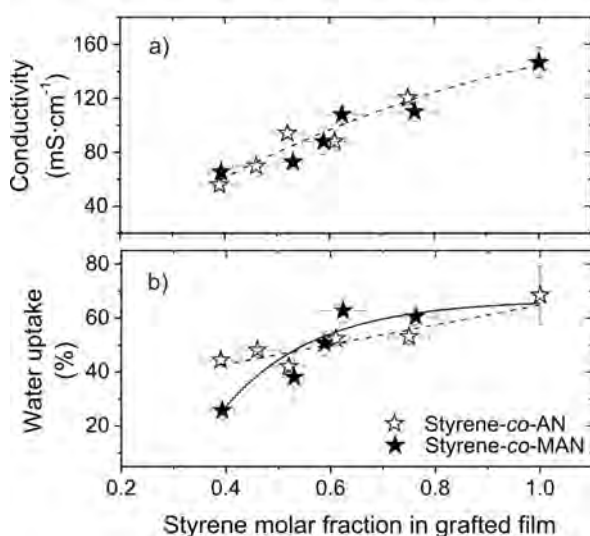


Figure 2. FTIR spectra of styrene-co-MAN grafted membranes at different styrene molar fraction and at fix graft level (GL ~40 %).

<sup>1</sup> Internship student from ETH Zürich

Indeed, new peaks appearing at wavenumber values of  $1673\text{ cm}^{-1}$  and  $1700\text{ cm}^{-1}$  assigned to C=O stretch vibration of the amide and carboxylic acid group, respectively, were observed. Furthermore, the extent of hydrolysis increases with an increase of AN content in the grafted membrane (Figure 1). The observed response to the sulfonation procedure of both systems was not expected. It is obvious that the hydrolysis of the nitrile group is hindered in case of MAN containing films. On the one hand, the difference in polarity between the nitrile group in MAN and AN may explain the sensitivity of AN to be readily hydrolysed during the sulfonation procedure [4]. On the other hand, the difference in the intramolecular/intermolecular interactions between the styrene-co-AN and styrene-co-MAN chains may play a non-negligible role. Furthermore, steric hindrance due to the presence of the  $\alpha\text{-CH}_3$  group in the MAN is assumed to create different conformation of polymer chains and different tacticity with respect to AN [5].



**Figure 3.** Ex situ fuel cell relevant properties of styrene-co-AN and styrene-co-MAN grafted ETFE based membranes.

A detailed comparison of ex situ fuel cell relevant properties was carried out based on styrene-co-AN and styrene-co-MAN grafted ETFE based membranes with IEC values ranging from 1.2 to 2.4 mmol·g<sup>-1</sup>. The experimental IEC values correlate reasonably well with the theoretical values calculated based on the GL and molar fraction of monomers in the grafted films determined by FTIR (data not shown). The derived degree of sulfonation is around 95%. The IEC and conductivity are enhanced with an increase of the molar fraction of styrene in the grafted membrane and no significant difference was observed between the styrene-co-AN and styrene-co-MAN grafted membranes (Figure 3a). This result is not in agreement with the evolution of water uptake (Figure 3b). Higher swelling values were observed for the styrene-co-AN at lower styrene content than for the styrene-co-MAN membranes. The hydrolysis of part of the nitrile group into carboxylic acid group may explain the observed improvement in the swelling of the styrene-co-AN membranes. The data comparison between both systems revealed that the additional water uptake at low styrene content in the styrene-co-AN grafted membranes is not contributing to the proton mobility.

Two selected membranes based on styrene-co-AN and styrene-co-MAN grafted ETFE with a styrene molar fraction of 0.6 were tested *in situ* in the single fuel cell (Figure 4). The styrene-co-MAN based MEA showed

comparable performance to that of the Nafion 212 based MEA. However, lower cell voltage and higher frequency resistance (HFR) values were measured for the styrene-co-AN based MEA in comparison to other MEAs with increasing current density after only 24 h operation.

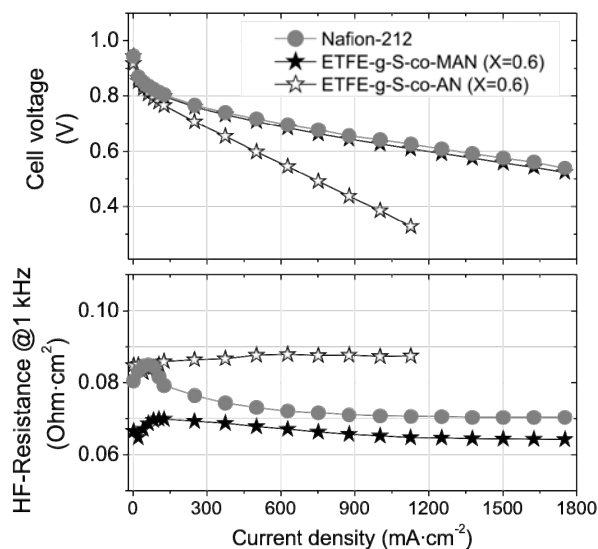


**Figure 4.** Polarization curves of MEAs at a cell temperature of 80°C; H<sub>2</sub>/O<sub>2</sub> at a stoichiometry of 1.5/2, atmospheric gas pressure, full humidification at 80°C.

In fact, the HFR value of the styrene-co-AN based MEA started to gradually increase after only 6 h of fuel cell operation (80 °C), whereas the styrene-co-MAN MEA showed a stable HFR value over the testing time (< 50 h). Furthermore, the interfacial resistance and H<sub>2</sub> crossover of the styrene-co-AN were higher than that of the styrene-co-MAN based MEA (Table 1).

#	Membrane	H <sub>2</sub> crossover mA·cm <sup>-2</sup>	Interfacial resistance mOhm·cm <sup>2</sup>
1	S-co-AN	0.452	516
2	S-co-MAN	0.139	254
3	Nafion 212	0.638	143

**Table 1.** H<sub>2</sub> crossover and interfacial resistance of styrene-co-MAN, styrene-co-AN based membranes and Nafion 212.

The sensitivity of the nitrile group in AN to be readily hydrolysed to a carbonyl group, combined with its unprotected  $\alpha$ -position in comparison to MAN, may explain the observed poorer *in situ* fuel cell relevant properties and lower stability of the styrene-co-AN based MEA.

## References

- [1] L. Gubler, M. Slaski, F. Wallasch, A. Wokaun, G.G. Scherer, J. Membr. Sci. **339**, 68-77 (2009).
- [2] H. Ben youcef, L. Gubler, S.A. Gürsel, D. Henkensmeier, A. Wokaun, G.G. Scherer, Electrochem. Commun. **11**, 941-944 (2009).
- [3] K. Jetsrisuparb, H. Ben youcef, G.G. Scherer, A. Wokaun, L. Gubler, PSI Electrochemistry - Annual Report 2009, 9-11, ISSN 1661-5379 (2010).
- [4] D.J. T. Hill, L. Dong, J., H.O'Donnell, J. Polym. Sci.: Part A: Polym. Chem. **31**, 2951-2957 (1993).
- [5] J.S. Roman, B. Vazquez, M. Valero, G.M. Guzman, Macromolecules **24**, 6089-6094 (1991).

## Does methacrylonitrile (MAN) affect the conductivity and crystallinity of styrene based membranes for fuel cells?

K. Jetsrisuparb, H. Ben youcef, G.G. Scherer, A. Wokaun, L. Gubler

phone: +41 56 310 2162, e-mail: kaewta.jetsrisuparb@psi.ch

Our group has developed partially fluorinated proton exchange membranes synthesized by pre-irradiation grafting of styrene onto 25  $\mu\text{m}$  base films (e.g. ETFE) and subsequent sulfonation. The grafted polymer chains are formed in the amorphous region of the polymer substrate, hosting the functional groups and proton conducting sites. In addition to the amorphous phase, the crystalline phase of the ETFE contributes to the mechanical strength of the membrane.

The polystyrene sulfonic acid (PSSA) domains enable proton conduction. However, PSSA is prone to degradation in the fuel cell environment caused by radicals ( $\text{HO}^\bullet$ ,  $\text{HOO}^\bullet$ ), which are formed as a result of  $\text{H}_2$  and  $\text{O}_2$  permeation through the membrane. Incorporation of methacrylonitrile (MAN) as a comonomer to styrene effectively reduces gas permeation through the membrane and thereby enhances the durability of the fuel cell membrane [1]. Membrane properties, particularly conductivity and structural characteristics, are strongly correlated to the overall performance of the fuel cell. In this study, we investigated the effect of co-grafted MAN on membrane conductivity and its thermal properties.

### Experimental

The ETFE-*g*-styrene / MAN membranes with a fixed ion exchange capacity (IEC) of around 1.5 mmol/g were prepared from 25  $\mu\text{m}$  thick ETFE films by pre-irradiation with electron beam, grafting, and sulfonation [2]. The IEC and conductivity were measured using the procedure reported previously [2]. In addition, thermal analysis of the membrane was carried out in triplicate with differential scanning calorimetry (DSC) under  $\text{N}_2$  atmosphere. The membranes were converted to salt form ( $\text{K}^+$ ) and dried at 80  $^\circ\text{C}$  for at least 6 hours. Single heating curves were recorded with a heating rate of 20  $^\circ\text{C}/\text{min}$  from 30-320  $^\circ\text{C}$ . The melting temperature was determined based on the temperature at the maximum heat flow of the melting endotherms.

The intrinsic crystallinity  $C_i$  of the membranes has been determined to exclude the dilution effect caused by the grafted component as follows:

$$C_i = \frac{\Delta H_f}{\Delta H_0} \cdot \left(1 + GL + \frac{GL_{\text{styrene}} \cdot M_{\text{SO}_3^-}}{M_{\text{styrene}}}\right)$$

where  $\Delta H_f$  is the heat of fusion of the membrane and  $\Delta H_0$  is the heat of fusion of 100% crystalline ETFE (113.4 kJ/g).  $M$  is the molar mass, where the subscripts indicate the species.  $GL$  symbolizes the graft level and  $GL_{\text{styrene}}$  is defined as the relative graft level of styrene.

$$GL_{\text{styrene}} = \frac{m_{\text{styrene}}}{m_{\text{ETFE}}} \cdot 100\%$$

where  $m$  refers to the mass and the subscripts define the species. The hydration number  $\lambda$  represents the number of water molecules per sulfonic acid group in the swollen membrane:

$$\lambda = \frac{n(\text{H}_2\text{O})}{n(\text{H}^+)}$$

### Results and Discussion

The relative mass of the grafted styrene with respect to the total mass of the dry membrane is kept constant while the MAN content is varied. The synthesized membranes have an IEC of  $1.53 \pm 0.07$  mmol/g with different molar fractions of styrene ( $X_{\text{styrene}}$ ). The graft level of membranes with  $X_{\text{styrene}}=1$  and 0.4 differs by a factor of 3 (Figure 1). The water uptake of the membrane is significantly higher in membranes with lower styrene molar fraction. The incorporation of MAN enhances the hydrophilicity of the membranes, hence the water content increases.

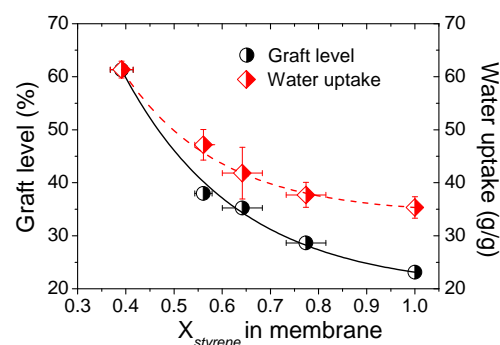


**Figure 1.** Effect of styrene molar fraction on graft level (circle) and water uptake (square) for ETFE-*g*-styrene / MAN membranes with an IEC of  $1.53 \pm 0.07$  mmol/g.  $X_{\text{styrene}}$  is the molar fraction of styrene with respect to the total monomer content in the membrane.

Typically, the conductivity of the membranes is strongly dependent on the hydration state of the membrane and the water present in the membrane governs proton mobility [3]. The water uptake and IEC of styrene containing membranes, i.e. purely styrene grafted membranes, are closely related. By increasing the IEC, the water uptake increases considerably as a consequence and with that the conductivity (Figure 2). Surprisingly, an increase in the water uptake of ETFE-*g*-styrene / MAN membranes with fixed IEC does not lead to higher proton mobility. No differences in conductivity were observed for the various co-grafted membranes. Thus, there are water molecules which do not promote the mobility of the charge carriers. The conductivity of Nafion<sup>®</sup> 212 is included for comparison.

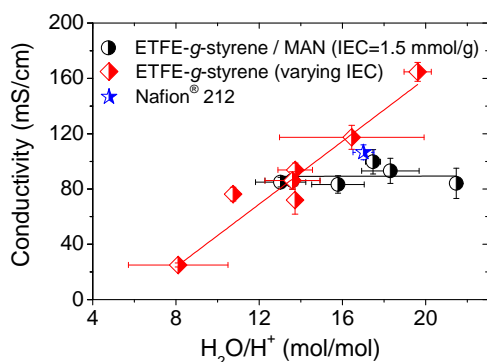


**Figure 2.** Membrane conductivity as a function of hydration number.

The structural changes of ETFE can be influenced by the graft level, the water uptake, and the number of sulfonated groups, which can lead to a disruption of the crystallites. The melting of the crystalline phase leads to broad endotherms in DSC experiments as typically observed for semicrystalline polymers. A similar shape of endotherms of the styrene / MAN co-grafted membranes (in salt form) and the ungrafted ETFE was obtained (Figure 3).

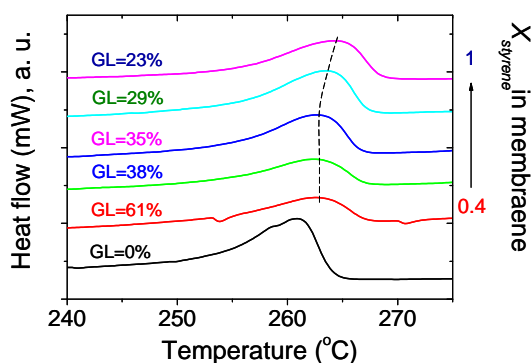


**Figure 3.** Melting endotherms of an ungrafted ETFE film (GL=0%) and styrene / MAN co-grafted membranes in  $K^+$  form with similar IEC, yet different graft levels.

The melting temperatures of all membranes in salt form are higher than that of the ungrafted ETFE film. By incorporating MAN as co-monomer, the co-grafted membranes with fixed IEC exhibit higher melting temperature with decreasing graft level (increasing  $X_{\text{styrene}}$ ). The temperature shift indicates that the grafts in the amorphous phase induced changes in the crystalline domain. In addition, the recrystallization thermograms showed that crystal formation was affected by the graft components (results not shown).

By introducing MAN into the grafted chain, the physical interactions (e.g. ionic crosslinking) between the sulfonic acid groups in the amorphous region may be reduced and as a result the melting temperature decreases. A detailed study is under investigation.

Due to the sulfonation of the grafted film, a decrease in intrinsic crystallinity of ETFE was found for membranes compared to that of the ungrafted ETFE film (Figure 4). Independent of the composition of the graft component, the intrinsic crystallinity of membranes with fixed IEC (in salt form) remains almost identical over the entire range of graft levels from 23% to 61%. The lower intrinsic crystallinity compared to the base film may be attributed to the grafted branches carrying potassium styrene sulfonate, which disrupt crystalline regions of the ETFE.

Similar results were also report on FEP based membranes by Gupta *et al* [4].

Disruption of crystalline domains was not found in the grafted (un sulfonated) state [5]. We have confirmed that membranes containing only MAN are not conducting since sulfonation of MAN does not take place. Therefore, by incorporation of MAN through changing the graft level, the intrinsic crystallinity of the membranes with fixed IEC is not affected. The destruction of crystallites is only caused by sulfonated groups of grafted styrene.

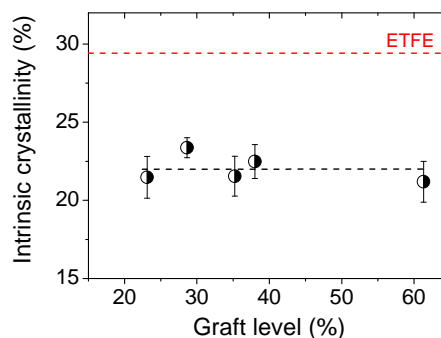


**Figure 4.** The intrinsic crystallinity of styrene / MAN co-grafted membranes (in salt form) with similar IEC compared to that of ungrafted ETFE film.

## Conclusions

In the fully hydrated ETFE-*g*-styrene / MAN membranes, the conductivity is governed by the mass based IEC. An increase in hydrophilicity by introducing MAN to the polymer matrix increases the water sorption of the co-grafted membrane, yet does not lead to an improved proton conductivity of ETFE-*g*-styrene / MAN membranes for a given IEC. It is suggested that some of the water molecules associated with MAN do not contribute to proton conduction.

The observation based on DSC indicates that the graft components have an impact on the crystalline domain. The melting temperature decreases with the graft level. The grafted styrene carrying potassium sulfonate groups disrupts the crystal structure and decreases the intrinsic crystallinity of ETFE accordingly. The incorporation of MAN into the polymer matrix however does not lead to a change in the intrinsic crystallinity of ETFE.

The thermal properties of ETFE-*g*-styrene / MAN (non-sulfonated) films will be studied to exclude the effect of the interactions induced by sulfonic acid groups. Besides, mechanical testing of the co-grafted membranes will be carried out.

## References

- [1] H. Ben youcef, L. Gubler, S. Alkan Gürsel, D. Henkensmeier, A. Wokaun, G.G. Scherer, *Electrochem. Commun.* **11**, 941-944 (2009).
- [2] K. Jetsrisuparb, H. Ben youcef, G.G. Scherer, A. Wokaun, L. Gubler, *PSI Electrochemistry Laboratory - Annual Report 2009*, 9-11, ISSN 1661-5379 (2010).
- [3] T.A. Zawodzinski, J. Davey, J. Valerio, S. Gottesfeld, *Electrochim. Acta* **40**, 297-302 (1995).
- [4] B. Gupta, O. Haas, G.G. Scherer, *J. Appl. Polym. Sci.* **51**, 469-476 (1994).
- [5] B. Gupta, G.G. Scherer, *Angew. Makromol. Chem.* **210**, 151-164 (1993).

# A simulation study on the radical (HO•, H•, and HOO•) formation and membrane degradation in PEFC

L. Gubler, S.M. Dockheer<sup>1</sup>, G.G. Scherer, W.H. Koppenol<sup>1</sup>

phone: +41 56 310 2673, e-mail: lorenz.gubler@psi.ch

In the polymer electrolyte fuel cell (PEFC), hydrogen and oxygen are made to react electrochemically to produce electricity at high efficiency, water and heat. A noble metal catalyst such as platinum located at the membrane-electrode interface on the anode and cathode side, promotes the oxidation of hydrogen and the reduction of oxygen. The current PEFC technology suffers from insufficient durability for the fuel cell to be used in electric cars or stationary power units. The membrane degradation of the PEFC is a major concern and needs to be understood to make effective countermeasures possible. The diffusion of O<sub>2</sub> through the membrane to the anode side and its reaction with adsorbates on the anode Pt catalyst leads to the formation of radicals, which attack the membrane and cause ionomer degradation. According to a similar mechanism, H<sub>2</sub> crossover causes radical formation on the cathode side.

## Reactive Intermediates

The formation of hydrogen peroxide has been confirmed by its detection in product water and by the use of an *in situ* probe technique [1]. In addition, the radicals HO•, H• and HOO• have been detected in an operating fuel cell via spin trapping or a fluorescent probe technique [2]. Whereas H<sub>2</sub>O<sub>2</sub> is kinetically a rather weak oxidant, the generated radicals cause considerable oxidative stress and can attack weak ionomer constituents. The mechanism of radical formation has been discussed with some controversy during the past decades. Radicals may be created directly at the electrodes and then attack the membrane at the surface. Since the lifetime of the radicals is very short, diffusion into the membrane is unlikely [3]. The indirect pathway involves first the formation of the much longer-lived H<sub>2</sub>O<sub>2</sub> on the anode and, or, cathode, which may diffuse into the membrane. The decomposition of H<sub>2</sub>O<sub>2</sub> to yield HO• radicals, catalyzed by impurities such as Fe-ions, is well known (Fenton reaction). According to this mechanism, radicals can be created inside the membrane.

#	Reaction	Rate constant
1	HO• + R <sub>i</sub> CF <sub>2</sub> COOH → products	<10 <sup>6</sup> M <sup>-1</sup> s <sup>-1</sup>
2	HO• + PSSA → products	4·10 <sup>8</sup> M <sup>-1</sup> s <sup>-1</sup>
3	H <sub>2</sub> O <sub>2</sub> → 2 HO•	1.2·10 <sup>-7</sup> s <sup>-1</sup>
4	HO• + H <sub>2</sub> O <sub>2</sub> → HOO• + H <sub>2</sub> O	2.7·10 <sup>7</sup> M <sup>-1</sup> s <sup>-1</sup>
5	HOO• + H <sub>2</sub> O <sub>2</sub> → HO• + H <sub>2</sub> O + O <sub>2</sub>	1 M <sup>-1</sup> s <sup>-1</sup>
6	HO• + H <sub>2</sub> → H• + H <sub>2</sub> O	4.3·10 <sup>7</sup> M <sup>-1</sup> s <sup>-1</sup>
7	H• + O <sub>2</sub> → HOO•	1.2·10 <sup>10</sup> M <sup>-1</sup> s <sup>-1</sup>
8	2 HOO• → H <sub>2</sub> O <sub>2</sub> + O <sub>2</sub>	8.6·10 <sup>5</sup> M <sup>-1</sup> s <sup>-1</sup>
9	Fe <sup>2+</sup> + H <sub>2</sub> O <sub>2</sub> + H <sup>+</sup> → Fe <sup>3+</sup> + HO• + H <sub>2</sub> O	63 M <sup>-1</sup> s <sup>-1</sup>
10	Fe <sup>2+</sup> + HO• + H <sup>+</sup> → Fe <sup>3+</sup> + H <sub>2</sub> O	2.3·10 <sup>8</sup> M <sup>-1</sup> s <sup>-1</sup>
11	Fe <sup>2+</sup> + HOO• + H <sup>+</sup> → Fe <sup>3+</sup> + H <sub>2</sub> O <sub>2</sub>	1.2·10 <sup>6</sup> M <sup>-1</sup> s <sup>-1</sup>
12	Fe <sup>3+</sup> + HOO• → Fe <sup>2+</sup> + O <sub>2</sub> + H <sup>+</sup>	2·10 <sup>4</sup> M <sup>-1</sup> s <sup>-1</sup>
13	Fe <sup>3+</sup> + H <sub>2</sub> O <sub>2</sub> → Fe <sup>2+</sup> + HOO• + H <sup>+</sup>	4·10 <sup>-5</sup> M <sup>-1</sup> s <sup>-1</sup>

**Table 1.** Reactions involving H<sub>2</sub>O<sub>2</sub>, the fuel cell reactants (H<sub>2</sub>, O<sub>2</sub>), Fe-ion impurity and radical intermediates (HO•, H•, HOO•) and PFSA ionomer with reactive end-groups (R<sub>i</sub>CF<sub>2</sub>COOH) considered in this simulation study.

## Kinetic Scheme

To simulate these reactions, we assume that H<sub>2</sub>O<sub>2</sub> is the “parent” molecule and investigate the type and concentration of radicals formed inside the membrane. We assume a constant concentration of H<sub>2</sub>O<sub>2</sub> of 0.5 mM, which is comparable to the values experimentally determined. A number of relevant reactions are considered (Table 1), which include the attack of HO• on weak carboxylic end-groups found in perfluorosulfonic acid (PFSA) membranes, such as Nafion® (reaction 1). The concentrations of radicals are calculated as a function of the Fe-ion content, under the assumption of a constant concentration of H<sub>2</sub> and O<sub>2</sub>, which diffused into the membrane from the anode and cathode compartment, of 10 and 7.5 mM, respectively (Figure 1). We find that the concentration of HO•, the most aggressive of the three radicals with E°(HO•/H<sub>2</sub>O) = 2.7 V, is in the range of 10<sup>-15</sup> M. Primary pathways for HO• creation are the homolytic decomposition of H<sub>2</sub>O<sub>2</sub> (reaction 3) and the Fenton reaction (reaction 9). The presence of H<sub>2</sub> and O<sub>2</sub> in the membrane is crucial, because hydrogen radicals, E°(H•/H<sub>2</sub>) = 2.3 V, can be created via reaction 6, followed by the creation of hydrogen dioxide radicals, E°(HOO•/H<sub>2</sub>O<sub>2</sub>) = 1.5 V, via

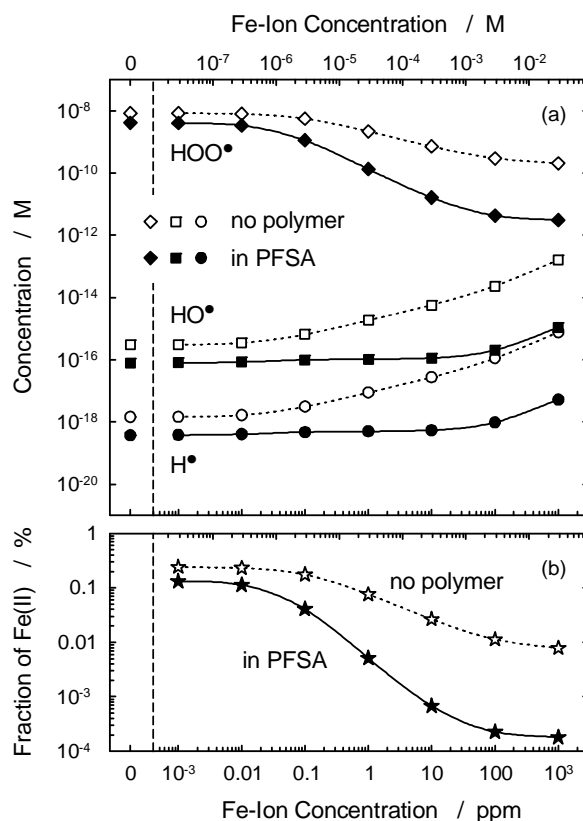


**Figure 1.** (a) Concentration of radicals, (b) fraction of Fe<sup>2+</sup> with respect to the total Fe-ion content.

<sup>1</sup> ETH Zürich

reaction 7. The concentration of  $\text{H}^\bullet$  is even lower than that of  $\text{HO}^\bullet$ , but  $\text{HOO}^\bullet$  is predicted to be present at a level of  $10^{-9}$  M. Figure 1 shows the radical concentrations in the absence of ionomer attack, and when a fraction of the  $\text{HO}^\bullet$  reacts with the  $-\text{COOH}$  end groups, whose concentration is estimated at an upper limit of 1.17 M, which corresponds to 5 % of the total  $-\text{CF}_2-$  count in the PFSA main chain.

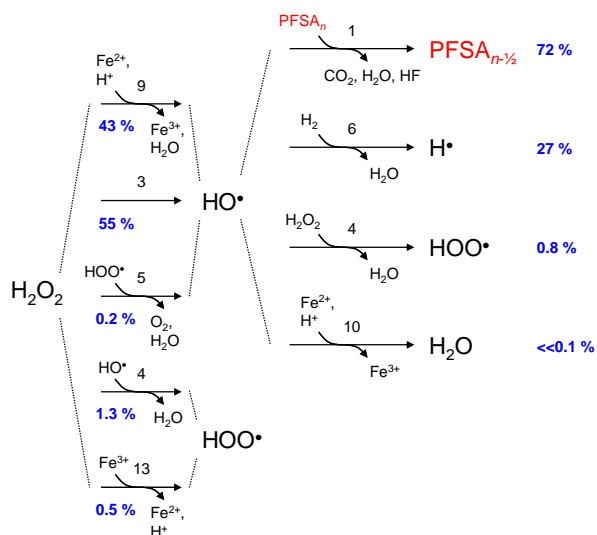


**Figure 2.** Reaction sequence with contributions of each reaction (in blue) at an Fe-ion concentration of 1 ppm and a  $-\text{COOH}$  end-group concentration in the PFSA ionomer of 1.17 M.

A scheme of the reaction sequence starting from  $\text{H}_2\text{O}_2$  is shown in Figure 2. At low Fe-ion content ( $<1$  ppm),  $\text{HO}^\bullet$  formation proceeds mainly via the homolysis of  $\text{H}_2\text{O}_2$  (reaction 3). With increasing Fe-ion level, the Fenton reaction (reaction 9) becomes more and more dominant. The contribution by reaction 5 (Haber-Weiss reaction) to  $\text{HO}^\bullet$  generation is negligible under the prevailing conditions. Due to its high electrode potential, the hydroxyl radical can attack the ionomer via the weak end-groups which results in unzipping of the chain. The removal of one  $-\text{CF}_2-$  unit requires two  $\text{HO}^\bullet$  molecules. The reaction of  $\text{HO}^\bullet$  with  $\text{H}_2$  (reaction 6) also represents an important pathway; hence molecular hydrogen can be regarded as a  $\text{HO}^\bullet$  scavenger. Although the Fenton reaction contributes significantly to the creation of  $\text{HO}^\bullet$ , the rate of the reaction is limited by the low ratio of  $\text{Fe}^{2+}/\text{Fe}^{3+}$ . Since the reactions for the reduction of  $\text{Fe}^{3+}$  back to  $\text{Fe}^{2+}$  are rather slow (reactions 12 and 13), over 99.9 % of the Fe-ions are in the +III oxidation state and therefore not available for the Fenton reaction.

For the development of partially fluorinated membranes, such as the PSI Membrane prepared by radiation induced graft copolymerization, different radical attack mechanisms have to be considered [4]. An implication of using poly(styrenesulfonic acid) (PSSA) based membranes is that  $\text{HO}^\bullet$  reacts rapidly with the aromatic ring (reaction 2). Follow-up reactions can lead to chain scission or the formation of stable reaction products. In general, however, partially fluorinated membranes face greater challenges regarding chemical stability compared to perfluorinated membranes.

## Discussion

The reaction mechanisms of the radical intermediates with a PFSA ionomer such as Nafion® are still controversially discussed. Based on this simulation including weak end-group attack by  $\text{HO}^\bullet$ , which has been widely accepted, we can estimate the rate of membrane degradation by calculating the fluoride emission rate (FER) based on reaction 1 for a membrane of  $50\ \mu\text{m}$  thickness. Furthermore, we can extrapolate to a temperature of  $90^\circ\text{C}$ , using an activation energy of  $70\ \text{kJ/mol}$ , to compare with experimental data. It is found that the calculated rate is one to two orders of magnitude lower than the experimental data reported in the literature. Following arguments may be put forward in this context:

- Many of the fuel cell accelerated tests are carried out under sub-saturated humidity conditions, leading to an effectively higher  $\text{H}_2\text{O}_2$  concentration due to "lack of dilution" with water.
- As highlighted at the beginning, radicals may be formed directly at the electrodes and attack the membrane from the surface.
- In the fuel cell, there is also Pt dissolution from the cathode and redeposition of Pt-particles in the membrane, which act as  $\text{H}_2\text{O}_2$  decomposition catalyst, thereby increasing the rate of  $\text{HO}^\bullet$  formation.
- There are additional ionomer attack mechanisms (e.g., direct side-chain attack), which are less well understood today and not quantified.

It has been argued that attack of the PFSA side-chain could play a significant role. In addition, from a thermochemical point of view, fluorine abstraction by  $\text{H}^\bullet$  from PFSA is conceivable. Last but not least, there is little known at the moment about the reactions that  $\text{HOO}^\bullet$  can undergo. This could be relevant in view of the much higher concentration of  $\text{HOO}^\bullet$  over  $\text{HO}^\bullet$  (and  $\text{H}^\bullet$ ).

## Conclusions

The kinetic simulation study reported here yields radical concentrations and ionomer attack rates at conditions relevant of those in an operating fuel cell.  $\text{HO}^\bullet$  is the most aggressive radical, leading to polymer degradation. The complex kinetic framework highlights the probability of various reaction pathways. Yet still, not all the mechanisms are sufficiently well understood and need further experimental studies, e.g., via pulse radiolysis of representative model compounds.

## References

- W. Liu, D. Zuckerbrod, J. Electrochem. Soc. **152**, A1165-A1170 (2005).
- M. Danilczuk, F.D. Coms, S. Schlick, J. Phys. Chem. B **113**, 8031-8042 (2009).
- L. Gubler, S.M. Dockheer, M.M. Menampambath, A. Wokaun, G.G. Scherer, PSI Electrochemistry Laboratory – Annual Report 2009, 5-6, ISSN 1661-5379 (2010).
- S.M. Dockheer, L. Gubler, P.L. Bounds, A.S. Domazou, G.G. Scherer, A. Wokaun, W.H. Koppenol, Phys. Chem. Chem. Phys. **12**, 11609-11616 (2010).

# The DEMMEA project: Understanding the degradation mechanisms of membrane-electrode assembly and optimization of individual components

G. Neophytides, I.A. Schneider

phone: +41 56 310 2165, e-mail: [george.neophytides@psi.ch](mailto:george.neophytides@psi.ch)

## Description of the project

The objective of the project is to understand the functional operation and degradation mechanisms of high temperature  $\text{H}_3\text{PO}_4$  imbibed PEM and its electrochemical interface. During the course of the project, the degradation mechanisms will be thoroughly studied and novel catalysts will be developed. Low loading Pt or nanostructured alloyed Pt electrocatalysts and catalytic layers, which will be supported on finely dispersed or structurally organized, modified carbon supports (e.g. nanotubes, pyrolytic carbon) so that a stable electrocatalytic layer with full metal electrocatalyst utilization can be achieved. Another challenging area of the project is the optimization of this technology through the development of stable, long lasting, polymer structures with high ionic conductivity. The development of both, novel catalysts and polymers, is aiming to more active and stable electrochemical interfaces with minimal Pt loads. Due to the low abundance and high intrinsic cost of Pt, the future fuel cell technology and its cost effective implementation must reduce dependence on cost drivers, such as platinum.

The high temperature PEM membrane-electrode assembly (MEA) will be based on a) PBI and variants as control group and b) the advanced state of the art MEAs based on aromatic polyethers bearing pyridine units, which can act as basic polar groups and interact through an acid base reaction with  $\text{H}_3\text{PO}_4$ . These MEAs have been developed and optimized successfully and were tested at temperatures up to  $200^\circ\text{C}$ , where they exhibit stable and efficient operation. In the present project, these advanced materials in the form of membrane-electrode assemblies will be studied and tested in single fuel cells with regards to their operating conditions and long term stability, aiming to the development of a series of diagnostic tests that will lead in the design and development of an accelerated test and prediction tool for the MEA's performance. If the fundamentals of the failure mechanisms can be really understood, then the use of that information will guide the development of new materials or system approaches to mitigate these failures.

## The role of PSI

The Paul Scherrer Institut is a partner and a workpackage leader. More specifically, the Electrochemistry Laboratory will contribute to the project through the diagnostic techniques developed. The purpose is to investigate the local degradation phenomena and the mechanisms of the catalytic layer: Pt dissolution and redeposition, known as the Ostwald ripening process, Pt migration, Pt agglomeration, and carbon support corrosion. All the above have as a result the loss of active surface area of the expensive Pt catalyst. Mitigating these processes will help reducing the amounts of catalysts used and essentially reduce the production costs of the MEA.

In the Electrochemistry Laboratory of PSI locally resolved applications of the well known electrochemical techniques have been developed [4]. As a first approach local I-E measurements will be acquired followed by electrochemical impedance spectra and cyclic voltammetry measurements. This can help us investigate thoroughly the effect of water in carbon corrosion. Li and Lane have showed that water is the only source of oxygen in the carbon corrosion mechanisms [2, 3]. Also Schneider et al. has shown through neutron radiography that in low temperature systems, water accumulates in the outlet region of the electrode [1]. This should also apply to the water vapor partial pressure at higher temperatures.

Furthermore, combining the results of the electrochemical techniques with results of X-ray tomography, Focused Ion Beam SEM, and XRD measurements could provide insights on the effects that medium and long term degradation has on the catalyst layer and on the membrane.

## References

- [1] I.A. Schneider, D. Kramer, A. Wokaun, G.G. Scherer, *Electrochem. Comm.* **7**, 1393-1397 (2005).
- [2] Wei Li, Alan M. Lane, *Electrochem. Comm.* **11**, 1187-1190 (2009).
- [3] Wei Li, Alan M. Lane, *Electrochim. Acta*, **55**, 6926-6931 (2010).
- [4] I.A. Schneider, D. Kramer, A. Wokaun, G.G. Scherer, *J. Electrochem. Soc.* **154**, B770-B782 (2007).



FUEL CELLS

DIAGNOSTICS



## Transient Helox operation as a tool for the study of PEFC mass transport limitations

P. Boillat, P. Oberholzer, R. Siegrist, G.G. Scherer, A. Wokaun, A. Kästner, E.H. Lehmann

phone: +41 56 310 2743, e-mail: pierre.boillat@psi.ch

In order to quantify the losses related to different limiting phenomena occurring in Polymer Electrolyte Fuel Cells (PEFC), advanced diagnostics tools are required. In this context, a method for the evaluation of molecular diffusion losses, based on the comparison of the performance of a cell operated on air and on Helox mixture (21% O<sub>2</sub> + 79% He) was developed. The use of Helox as a diagnostic gas mixture was occasionally reported in the literature (e.g. [1]), where two polarization curves (one recorded with air and one with Helox) are compared. In the presently reported method, instead of repeating each experiment twice, the cell was operated normally with air, and the cathode gas was changed to Helox for short periods of time. This transient technique allows to compare air and Helox operation at almost the same time, avoiding measurement errors induced by long term changes in the cell state, as for example variations of voltage related to the oxide coverage of the catalyst. Moreover, the use of short pulses permits to reduce as much as possible drying effects related to the increased diffusivity of water vapour in Helium [2]. Simultaneous to the diffusion losses measurement using this technique, the distribution of liquid water in the cell was measured, using high resolution neutron imaging, in order to establish correlations between the accumulation of water and diffusion losses.

### Experimental

The experiments presented here were realized on a small scale differential cell with an active area of 0.5 cm<sup>2</sup>, with graphite flow fields having a rib and channel width of 1 mm. The membrane electrode assembly (MEA) was composed of a catalyst coated membrane (CCM) of type Primea 5710 (Gore, USA) with carbon paper gas diffusion layers (GDL) of type Sigracet GDL24BC (SGL Carbon Group, Germany). The cell was operated at 2 bar<sub>a</sub> and 70°C. During all experiments, the gases fed to the cell were H<sub>2</sub> on the anode and air on the cathode, with short periods (2 s) of operation with Helox on the cathode, repeated each 30 s.

The result of two different experiments will be presented here, both realized at a constant current density of 1.5 A/cm<sup>2</sup>. In the steady state experiment, the cell was initially operated at low relative humidity (anode 20%, cathode 0%) and increased in 20% steps, first on the anode, then on the cathode, until full humidification. Each combination of relative humidity values was kept for 10 minutes, and the results presented correspond to the average of the 2 last minutes of operation for each step. During 2 minutes (starting 6 minutes after the change of humidity), 2 s pulses with pure O<sub>2</sub> were applied instead of the usual Helox pulses. In the transient experiment, the relative humidity was changed instantly from a high humidity condition (100% RH on both sides) to a low humidity condition (40% RH on anode and dry cathode).

During all experiments, *in plane* neutron imaging was performed in order to measure the water content in the cell, in particular in the gas diffusion layers. The setup

used for neutron imaging [3] has a spatial resolution of ~20 μm. Exposure times of 10 s were used, corresponding to an acquisition rate of one image each 15 s approximately, when taking into account the read out delay.

### Results

Examples of the time evolution of voltage and resistivity during Helox pulses are presented in Figure 1. A delay of approximately 1 second is observed between the switch to Helox and the corresponding change of voltage. The time lag corresponds to the transport of gas from the gas switching valve to the cell. For the high and middle humidity conditions, the voltage reaches a stable value during the gas pulse and no increase of resistivity is observed. For the dry condition, the resistivity increases and the cell voltage decreases. In order to minimize the errors due to drying, the point for the voltage measurement under Helox was chosen at 1.2 s after the valve switch – just after the voltage has stabilized.

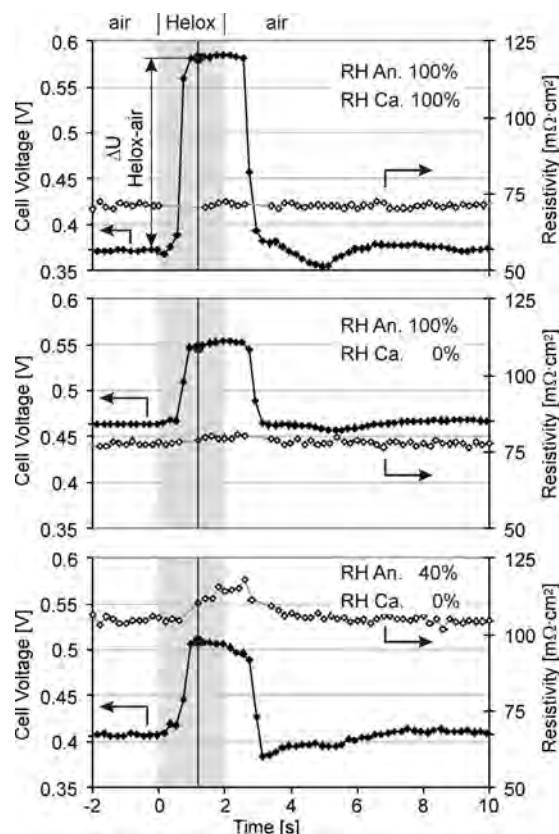


**Figure 1.** Evolution of cell voltage and resistivity during 2s Helox steps, for 3 different combinations of anode and cathode relative humidity. The vertical line represents the time of measurement for the “Helox” voltage ( $t = 1.2$ s). Current density is 1.5 A/cm<sup>2</sup>.

The voltages measured in operation with air, Helox and O<sub>2</sub> are presented in Figure 2 for the different values of relative humidity of the steady state experiment. The values displayed as “air” correspond to the values measured just before the gas switch, while the values

displayed as “Helox” and “O<sub>2</sub>” are measured 1.2 s after the switch to the respective gas, as explained above. The voltage difference between Helox and air operation ( $\Delta U_{\text{Helox-air}}$ ) clearly increases for the highest values of humidity. A point needing clarification is whether the value of  $\Delta U_{\text{Helox-air}}$  can be considered to represent the total of voltage loss induced by molecular diffusion limitations. Such an assumption implies that the voltage loss, due to diffusive transport in Helox operation is negligible, which is not necessarily true. By comparing Helox and O<sub>2</sub> operation, we can support this assumption: the voltage difference between these two gases remains unchanged by the accumulation of water, which was responsible for a significant drop of voltage for operation with air. Thus, we can consider the method presented here as a reasonable evaluation of the losses related to molecular diffusion.

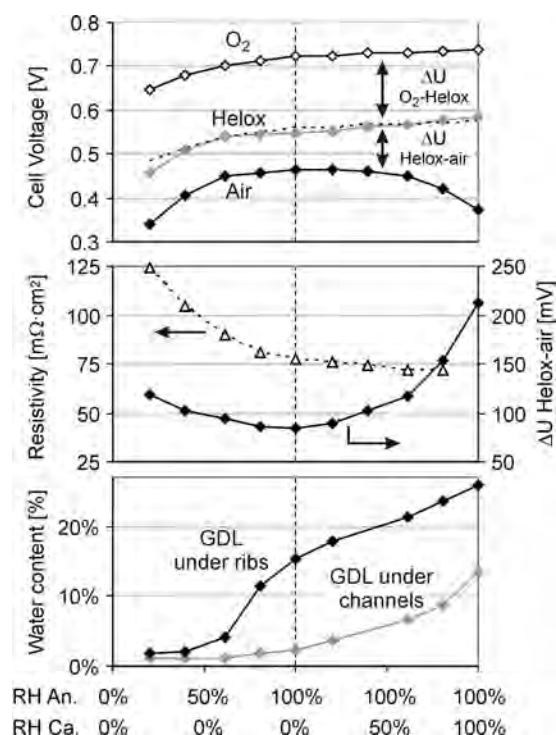


**Figure 2.** Measured electrochemical parameters and water content as a function of the gas flows relative humidity. Current density is 1.5 A/cm<sup>2</sup>.

In the low humidity range, higher diffusion losses are measured than in the middle humidity range, which may not appear intuitive, as the amount of water in the GDLs is reduced to nearly zero. To understand this result, the differences between rib and channel areas must be considered. When the membrane is well humidified, a higher current density can be expected for the channel region than for the rib region. As the membrane resistance increases and plays a more important role, the current density will decrease in the channel region and increase in the rib region, which will result in an increase of the diffusion losses. In summary, the diffusion loss corresponding to the GDL structure only (in absence of liquid water) is not an intrinsic property of the cell construction, but depends on a particular current density distribution. It is, however, possible to define a minimal diffusion loss, corresponding to the optimal case where the membrane is perfectly humidified but there is no water in the GDL. In the steady state experiment, the lowest measured diffusion loss for the current density of 1.5 A/cm<sup>2</sup> is approximately 80 mV, for the case of a fully humidified

anode and a dry cathode. In this condition, there is still a significant amount of water under the ribs, but it can be considered to have a low effect on diffusion losses. To support this assumption, we can firstly observe that in the operation points around this optimal point, there is a significant variation of the water content in the rib region, with no or very little change of the diffusion losses. The observation of the transient experiment results (Figure 3) gives further insight: we can observe that the change of water content in the channel region is well correlated to the dramatic reduction of diffusion losses (during 1.5 min after the change) while the variation in the ribs region is slower (drying time is approximately 5 min).

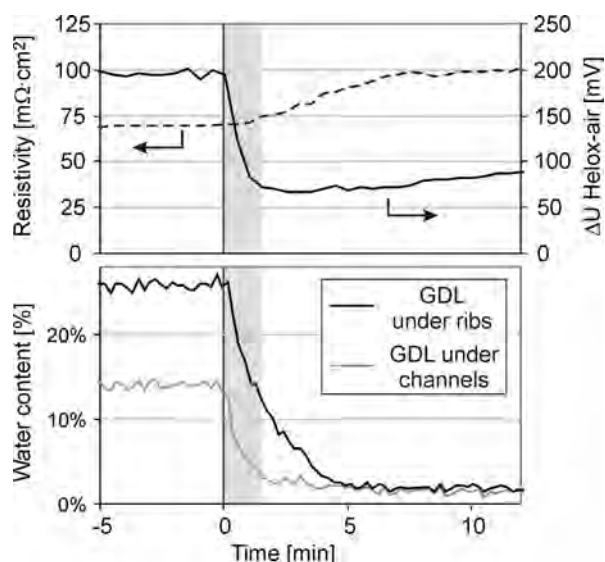


**Figure 3.** Evolution of  $\Delta U_{\text{Helox-air}}$ , cell resistivity and water content following a step change in a relative humidity at  $t=0$ . Initial RH is 100% on both sides. Final RH is 40% on anode side and 0% on cathode side. Current density is 1.5 A/cm<sup>2</sup>.

## Conclusion

The use of transient Helox operation was established as an efficient method for evaluating the voltage loss related to molecular diffusion in differential PEFCs. Using this method, the relation between water accumulation in porous media and diffusion losses was studied. For the particular cell design studied here, the diffusion limitations were evaluated to represent a loss of 70-80 mV in absence of liquid water in the porous media, and of 200 mV approximately for the conditions of highest humidity. Using a transient experiment and by comparing the temporal evolution of water content in the different regions of the GDL with the temporal evolution of diffusion losses, the region under the channels was identified as the most critical region for water accumulation.

## References

- [1] T.R. Ralph, M.T. Hogarth, *Platinum Metals Review* **46**, 3 (2002).
- [2] P. Boillat, P. Oberholzer, R. Perego, E.H. Lehmann, A. Kästner, G.G. Scherer, A. Wokaun, *PSI Electrochemistry Laboratory - Annual Report 2009*, 21, ISSN 1661-5379 (2010).
- [3] P. Boillat, G. Frei, E.H. Lehmann, G.G. Scherer, A. Wokaun, *Electrochem. Solid-State Lett.* **13**, B25-B27 (2010).

# Neutron imaging of isothermal sub-zero degree Celsius cold-start of a PEFC

P. Oberholzer, P. Boillat, R. Siegrist, G.G. Scherer, A. Wokaun

phone: +41 56 310 5637, e-mail: pierre.oberholzer@psi.ch

As candidate for the main power supply device in automotive systems, the PEFC must be able to be operated at sub-zero temperatures for cold-start. The polymer electrolyte, typically a Nafion™ membrane, offers sufficient proton conductivity at sub-zero temperatures. The major issue occurring during cold-start is the poor removal of the generated water that can lead to complete blocking of the electrode pores so that access of O<sub>2</sub> to active sites is hindered and, as a consequence, the cell voltage finally drops. As any auxiliary heating device is not desirable, a common strategy is to keep sufficient amount of heat produced inside the system to increase the temperature sufficiently in this lapse of time to avoid high level of water accumulation and make the cold-start successful. This requires both, an appropriate thermal management as well as suitable operating conditions to reach a sufficient operating time.

Taking benefit of the high resolution neutron imaging set-up available at PSI, we imaged isothermal sub-zero cold-starts of differential PEFCs positioned in *in plane* configuration. Keeping the temperature constant during the experiment allows being independent of the thermal management of the real technical design so as to understand basics of transport limitations. Different operating parameters are investigated in the present study, e.g., the temperature and the constant current density applied.

## Experimental

A specific set-up was designed to provide enough cooling power to the cell. An issue specifically emerging of neutron imaging is to prevent any condensation or freezing of water in the spaces located outside the cell and inside the field of view. Heated housing, thermally insulated of the cell is used for that purpose. On its external sides, its temperature is high enough to avoid condensing water from ambient air. Internally, dry N<sub>2</sub> is circulated avoiding freezing of the water in this volume.

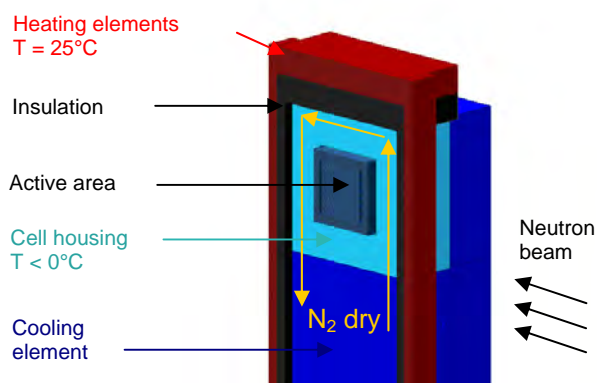


**Figure 4.** Sectional view showing the chamber where dry N<sub>2</sub> is circulated.

Three different current densities were applied in galvanostatic mode: 0.05, 0.1 and 0.2 A/cm<sup>2</sup> at three

different temperatures: -10, -15 and -20°C. The following procedure was applied for all experiments:

- 1) Drying the cell at 25°C.
- 2) Conditioning at 25°C with N<sub>2</sub> at 50% relative humidity.
- 3) Quick drying of the pipes and the cell channels at 25°C to avoid ice formation during cooling.
- 4) Cooling down the cell to the required temperature.
- 5) Operating the cell until the voltage drops by applying the required current and using dry gases (H<sub>2</sub> and air, both at 100 nml/min).
- 6) Automatically stopping the current and the gas flows when the voltage drops.
- 7) Drying the cell at low temperature.
- 8) Heating up the cell to ambient temperature.

## Results

The voltage drop occurs after very different lapses of time, according to the operating conditions (Figure 4). The total amount of water produced during this time, which depends on the current, is not constant. Both, an increased current at a given temperature and a decreased temperature at a given current are detrimental to the working time. The observation of ice/liquid water distribution and evolution can give clues to understand the different transport limitations taking place in the cell.

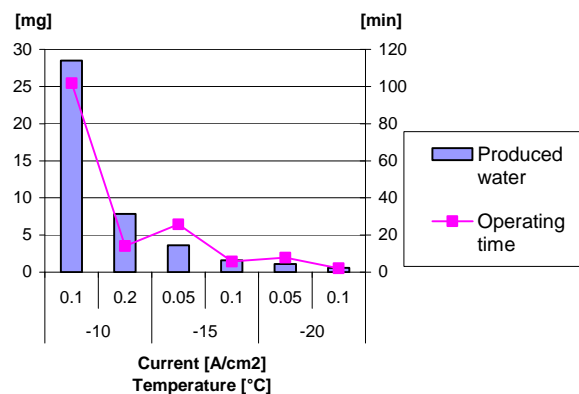


**Figure 5.** Comparison of operating time and total amount of water produced.

Let us consider the cold-start in three experiments conducted at the same current density ( $i = 0.1 \text{ A/cm}^2$ ) but at different temperatures (Figure 2). The voltage is plotted, as well as the water content in the MEA area, as this region presents clear trends, according to the experiments. But the images of the whole cell are showed at the times of the voltage drop.

The following results can be observed. At -20°C, the operating time is limited to two minutes only. No condensed phase is visible outside the MEA. The accumulation rate of water within the MEA seems to stay constant until the voltage drops, at which moment it shows a slight increase.

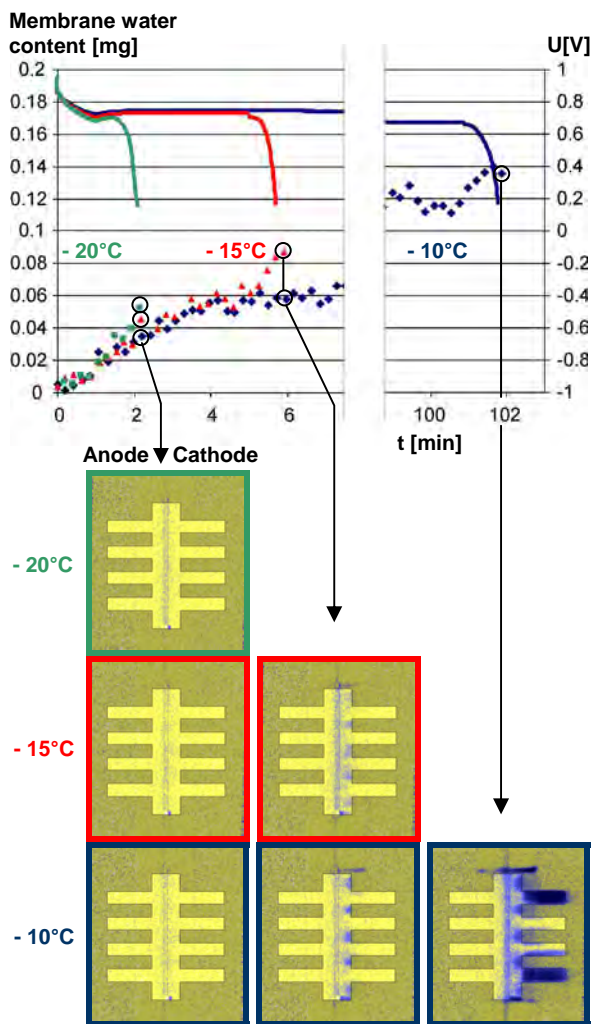


**Figure 6.** Effect of temperature at low current density ( $0.1 \text{ A/cm}^2$ ) on the voltage and the liquid/ice water evolution during sub-zero isothermal start-up.

For experiments at higher temperatures, less water accumulates in this area and it continues increasing until  $t = 4$  min. At this time, both experiments present a reduction of the accumulation rate. At  $t = 6$  min, the water accumulation rate suddenly increases again at  $-15^\circ\text{C}$  and the voltage drops. The corresponding image reveals that the porous media (GDL) shows a significant content of water, especially under the ribs. At the same moment, the image taken at  $-10^\circ\text{C}$  shows a similar distribution. In this case, accumulation of water slowly pursues until the final voltage drop, 102 min after the start.

Let us now try to interpret what has been observed. When starting the cell with dry porous media, two limitations can be basically expected: the first being a diffusive limitation of the water vapour transport in the porous media, the second being a limited quantity of water vapour uptake by the gas. As it is reasonable to consider that both limitations will be critical at these temperatures, due to the low saturation pressure of the gas, it could be expected that different accumulation rates would be induced by the dependence of the saturation pressure on the temperature, which is not clearly the case here. If water will be produced or rapidly converted to ice, then diffusion should be getting progressively more and more limiting as the pores of the different media are getting filled, which is not

observed either, as the accumulation is reduced at  $t = 4$  min. The sudden increase of water accumulation at the very last operating moments of these two experiments is also hard to explain by solely a diffusive transport that should not present such a discontinuity of trend. At last, concerning the experiment carried out at  $-10^\circ\text{C}$ , the shape of the condensed water emerging from the porous media and filling progressively the channels is hard to defend if only an ice phase is considered.

It is then reasonable to assume that a capillary flow must help removing the water during these cold-start experiments. To argue the presence of liquid water at sub-zero temperatures, two hypotheses can be made. Firstly, as heat is produced by the reaction in the centre of the cell, while its housing is kept cooled, a temperature gradient exists through the different layers. According to a simple calculation, this difference, however, is less than  $1^\circ\text{C}$ , so that the whole system can be considered to be maintained well under  $0^\circ\text{C}$ . Secondly, as the water electrochemically produced is assumed to be pure by essence, the presence of a meta-stable state of water, called super-cooled water, can be proposed here. This assumption has already been reported in other studies [1].

It would justify the presence of capillary flow in these experiments and thus the efficient removal of water observed. Moreover, as super-cooled water is meta-stable, it can rapidly be converted into ice, if a nucleus of ice appears somewhere in its bulk. This would explain the sudden change of the accumulation rate. For the voltage drop at  $-15^\circ\text{C}$ , it can be imagined that rapid freezing of water present under the ribs and partially under channels, makes the water evacuation strongly dependant on the diffusive flow. As it is not sufficient for the evacuation, the water produced gets confined in the MEA area. The membrane gets saturated and the water produced blocks the access to the active areas inside the catalyst layer, finally causing the voltage drop.

## Conclusion

Isothermal sub-zero cold-starts of fuel cells were performed using *in plane* neutron imaging as visualization tool of the liquid/ice water distribution. Different temperatures and current densities were investigated. Very different operating times were observed with no constant integral amount of water produced.

First, results tend to indicate that super-cooled water is present in the system so that capillary flow is taking place in the removal of the water produced. The sudden voltage drop is well correlated with a rapid accumulation of water in the MEA. Such a discontinuity of trend in water accumulation could be explained by the very fast freezing of the super-cooled water, as it is one of its properties.

Further experiments will be conducted on the same procedure, but with a wider variation of parameters, e.g., the relative humidity used for the conditioning. As a goal, sufficient statistics should be acquired to allow a judgement on the reproducibility of the operating time.

## References

- [1] Y. Ishikawa, H. Hamada, M. Uehara, M. Shiozawa, J. Power Sources **179**, 547-552 (2008).

## A two-dimensional impedance model on the channel/rib scale of PEFCs

M.H. Bayer, S. von Dahlen, I.A. Schneider

phone: +41 56 310 5304, e-mail: michael.bayer@psi.ch

In the previous report, we have given experimental proof that in air fed PEFCs consumption of oxygen, while it diffuses under the ribs, leads to significant mass transport losses and to characteristic features in the locally resolved impedance spectra on channel/rib scale, especially negative values for the polarization resistance at high loads [1, 2]. In this work, we model the impedance, using a two-dimensional, purely diffusive model. This model accounts, for the first time, for lateral effects in PEFC impedance measurements.

### Model formulation

The model considers mass transport in the GDL by binary diffusion of oxygen in nitrogen, according to Fick's law (1). For the sake of simplicity an isotropic effective diffusion coefficient of  $D_{\text{eff}} = 0.05 \text{ cm}^2/\text{s}$  [3] is used. The calculated element is a single repetitive unit of the air cathode consisting of one channel and rib (1.2 mm wide each) with periodic boundary conditions in lateral direction (*in plane* direction,  $y$ -direction). In the *across the MEA* direction (*through plane* direction,  $z$ -direction), the model considers the GDL ( $t_{\text{GDL}} = 200 \text{ }\mu\text{m}$ ,  $\varepsilon = 0.6$ ) and the catalyst layer, which is just treated here as an additional  $10 \text{ }\mu\text{m}$  thick GDL element. The electrochemical reaction, which causes a mass flux of oxygen, due to the Faradaic current (1), is assumed to take place in the center of the catalyst layer. The vector  $\hat{\mathbf{z}}$  is the normal vector in  $z$ -direction, pointing from the channel to the membrane. The oxygen concentration in the gas channels is assumed to be constant ( $c_{\text{ch}} = 5.17 \text{ mol/m}^3$ ) and uniform, due to the very high air flow rate.

$$\begin{aligned} \mathbf{I}_D(y, z, t) &= -D_{\text{eff}} \cdot \nabla c(y, z, t) \\ \mathbf{I}_F(y, t) &= \frac{j_F(y, t)}{4F} \hat{\mathbf{z}} \end{aligned} \quad (1)$$

The electrochemical reaction is described by the Tafel equation (Tafel slope  $b = 69 \text{ mV/dec}$ ,  $j_0 = 1 \text{ mA/cm}^2$ ,  $c_{\text{atm}} = 35.52 \text{ mol/m}^3$ ). Here, a reaction order of 0.79 is used [4], which already considers the effect of the oxygen concentration on the Nernst potential. The current is calculated by equation system (2). The underlying local electrode model is a Randles cell equivalent circuit, which accounts for an ohmic series resistance  $R = 0.1 \text{ }\Omega\text{cm}^2$  and for the capacitance of the electrochemical double layer  $C_{\text{dl}} = 150 \text{ mF/cm}^2$  [5]. In equation (2),  $\eta_{\text{el}}$  is the local voltage drop across the double layer and  $c_{\text{el}}$  is the local oxygen concentration in the catalyst layer.

$$\begin{aligned} j_F(y, t) &= j_0 \cdot \left( \frac{c_{\text{el}}(y, t)}{c_{\text{atm}}} \right)^{0.79} \cdot \exp\left( \frac{\eta_{\text{el}}(y, t)}{b} \right) \\ \frac{\partial}{\partial t} \eta_{\text{el}}(y, t) &= \frac{1}{C_{\text{dl}}} (j(y, t) - j_F(y, t)) \\ j(y, t) &= \frac{\eta(t) - \eta_{\text{el}}(y, t)}{R} \end{aligned} \quad (2)$$

The set of equations is discretized on a rectangular grid and solved using a low order finite volume method.

Conservation of species is the only conservation law considered, as given by equation (3).

$$\begin{aligned} \varepsilon \cdot \frac{\partial}{\partial t} c(y, z, t) &= -\text{div } \mathbf{I}(y, z, t) \\ \mathbf{I}(y, z, t) &= \mathbf{I}_D(y, z, t) + \mathbf{I}_F(y, z, t) \end{aligned} \quad (3)$$

For the steady state calculations the time derivatives in equations (2, 3) are set to zero. The resulting algebraic equations are solved in Mathematica. The steady state solution of (2) can be expressed in terms of the Lambert W function  $W\{x\}$  (equation (4)).

$$\begin{aligned} j^{(\text{ss})}(y) &= j_F^{(\text{ss})}(y) = \\ &= \frac{b}{R} W \left\{ \frac{R \cdot j_0 \cdot \left( c_{\text{el}}^{(\text{ss})}(y) / c_{\text{atm}} \right)^{0.79} \cdot \exp(\eta^{(\text{ss})} / b)}{b} \right\} \end{aligned} \quad (4)$$

For the calculation of the locally resolved impedance spectra, the local current response to a 1 mV step in the overpotential  $\eta$  is calculated at two different steady state cell currents  $j_1 = 0.6 \text{ A/cm}^2$  and  $j_2 = 1.3 \text{ A/cm}^2$  within four characteristic sections of channel and land: channel center (CC), channel edge (CE), land center (LC), and land edge (LE). The results are transformed from time domain into frequency domain via discrete Fourier transform [6].

### Results and discussion

The results of two-dimensional steady state and transient calculations for a PEFC air cathode are presented in Figure 1. The calculated two-dimensional, steady state, oxygen concentration profile in a single repetitive unit of the air cathode is shown for two loads  $j_1 = 0.6 \text{ A/cm}^2$  and  $j_2 = 1.3 \text{ A/cm}^2$  in Figure 1a. The shape of the oxygen concentration profile at the air electrode governs the characteristics of the respective lateral current distribution at steady state, as expressed by equation (4). The calculated oxygen concentration profile (Figure 1a) is consistent with the experimental observation of a local current maximum in the channel region at higher cell current, as seen in the previous article. In the channel area, the oxygen concentration  $c_{\text{ss}}$  is kept at a high level in *through plane* direction across the whole GDL thickness. The oxygen concentration  $c_{\text{ss}}$  decreases, however, severely underneath the ribs in *in plane* direction. In particular, at higher current density, the local oxygen concentration  $c_{\text{ss}}$  approaches values near zero in the rib center (Figure 1a). At a low steady state oxygen concentration  $c_{\text{ss}}$ , the local cell current in the rib center is highly sensitive to changes in the oxygen concentration  $\Delta c$ , since the associated change of the oxygen concentration polarization depends on the ratio  $\Delta c / c_{\text{ss}}$  [7, 8]. This effect becomes important in the discussion of the local transient response of the cell.

Calculated local current transients to a 1 mV step perturbation are shown in Figure 1b, 1c for two steady state cell currents  $j_1 = 0.6 \text{ A/cm}^2$  and  $j_2 = 1.3 \text{ A/cm}^2$ . After the voltage step, the observed change in current

density is limited initially by the ohmic series resistance ( $R = 0.1 \Omega\text{cm}^2$ ) to a maximum value of  $10 \text{ mA/cm}^2$  throughout the entire electrode area. The local current transients exhibit a capacitive behavior (Figure 1b, 1c).

The characteristic decay is governed by double layer charging and a changing oxygen concentration in *through plane* and *in plane* direction. The time to reach steady state is, therefore, virtually equal, and at a minimum in the channel area (CC, CE). Underneath the ribs (LC, LE), however, this time increases gradually in lateral direction with increasing diffusion path length for molecular oxygen as a consequence of increasing distance from the channel (Figure 1b, 1c).

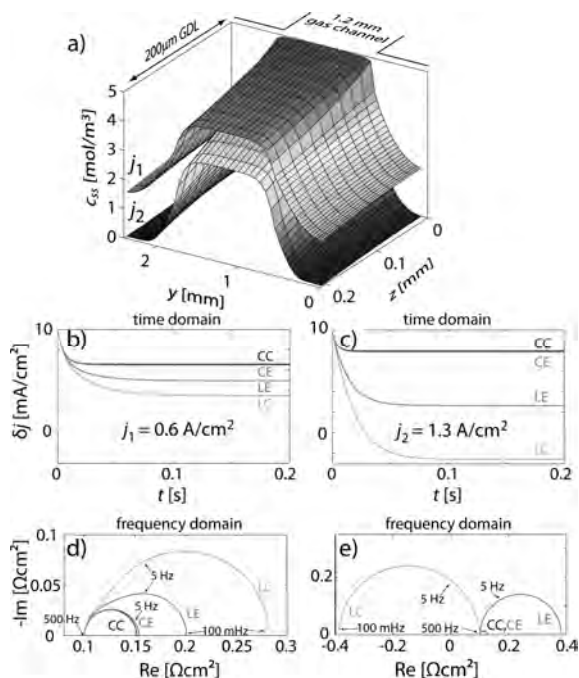


**Figure 1.** a) Calculated two-dimensional steady state oxygen concentration profile at a total cell current of  $j_1 = 0.6 \text{ A/cm}^2$  and  $j_2 = 1.3 \text{ A/cm}^2$  for the repetitive unit of a  $1.2 \text{ mm}$  channel cathode flow field (channel:land ratio 1:1), b, c) calculated local current transients ( $1 \text{ mV}$  step perturbation) at a cell current of  $j_1 = 0.6 \text{ A/cm}^2$  (b) and  $j_2 = 1.3 \text{ A/cm}^2$  (c) in four characteristic areas of the flow field: channel center (CC), channel edge (CE), land edge (LE) and land center (LC), and d, e) locally resolved impedance spectra as obtained via discrete Fourier transform of the time domain data at  $j_1$  (d) and  $j_2$  (e).

The opposite trend is observed for the total increase of the local steady state current density (Figure 1b, 1c) after the step. Here, a decreasing value is observed toward the rib center (LC) as a result of increasing oxygen concentration polarization losses in lateral direction, as oxygen is consumed while it diffuses *in plane* underneath the ribs. At lower cell current ( $j_1 = 0.6 \text{ A/cm}^2$ ) the obtained local change in current density is still positive in all four characteristic areas of the flow field (Figure 1b). At higher cell current ( $j_2 = 1.3 \text{ A/cm}^2$ ) and low oxygen concentration  $c_{ss}$  underneath the ribs (Figure 1a), the increase in oxygen concentration polarization in the rib center (LC) overcompensates the total perturbation voltage amplitude upon reaching steady state after the step [4]. As a result, the local steady state current density actually decreases, despite

an overall increasing cell polarization (Figure 1c (LC)). Consequently, after Fourier transform of the time domain data, a negative low frequency intercept is obtained in the local spectrum [6] of the rib center (Figure 1e) at high load current ( $j_2 = 1.3 \text{ A/cm}^2$ ), while the local spectra still exhibit positive low frequency resistance values at a lower load current ( $j_1 = 0.6 \text{ A/cm}^2$ ) in all characteristic areas of the cathode flow field (Figure 1d).

With the set of parameters used here, the three captured processes of i) double layer charging, ii) *through plane* diffusion, and iii) *in plane* diffusion and consumption of oxygen cannot be separated and only one loop is distinguishable. The purely diffusive model is notwithstanding able to capture the key experimental finding, namely the negative low frequency intercept in the local spectrum underneath the ribs at high load.

## Conclusion

The effect of reactant depletion along the channel, as observed in our previous work [6] has its analogue in the reactant depletion as gases diffuse underneath the ribs. While the *down the channel* inhomogeneities are a consequence of finite gas flow rates and can be safely ignored in differential cells, the inhomogeneities on channel/rib scale are a direct consequence of the chosen cell design and always have to be taken into account.

Other than in the *along the channel* direction, where typical length scales are in the order of several centimeters, the inhomogeneities in the *perpendicular to the channel* direction are on the submillimeter scale. Hence, a true two-dimensional model has to be used here, rather than the 1+1-dimensional formulation, which can be used for the *along the channel* model [6, 8].

## References

- [1] I. A. Schneider, M. H. Bayer, S. von Dahlen, in Polymer Electrolyte Membrane and Direct Methanol Fuel Cell Technology, C. Roth and C. Hartnig, Editors, Woodhead Publishing, Cambridge, UK, ISBN Nummer: 978-1845697747 (2010).
- [2] I.A. Schneider, M.H. Bayer, S. von Dahlen, "Locally Resolved Electrochemical Impedance Spectroscopy in Channel and Land Areas of a Differential Polymer Electrolyte Fuel Cell", J. Electrochem. Soc. **158** (3) B343-B348 (2011).
- [3] R. Flückiger, S.A. Freunberger, D. Kramer, A. Wokaun, G.G. Scherer, F.N. Büchi, Electrochim. Acta **54**, 551 (2008).
- [4] K.C. Neyerlin, W. Gu, J. Jorne, H.A. Gasteiger, J. Electrochem. Soc. **153** (10), A1955 (2006).
- [5] S.K. Roy, M.E. Orazem, J. Electrochem. Soc. **156**, B203 (2009).
- [6] I.A. Schneider, M.H. Bayer, A. Wokaun, G.G. Scherer, ECS Trans. **25** (1) 937 (2009).
- [7] I. A. Schneider, S. Freunberger, D. Kramer, A. Wokaun, G.G. Scherer, J. Electrochem. Soc. **154**, B383 (2007).
- [8] D. Kramer, I.A. Schneider, A. Wokaun, G.G. Scherer, ECS Trans. **3** (1) 1249 (2006).

# Investigating the low frequency inductive behavior in subsaturated PEFCs

M.H. Bayer, I.A. Schneider

phone: +41 56 310 5304, e-mail: michael.bayer@psi.ch

In our recent work, we have studied intensively the low frequency inductive loop in subsaturated PEFC [1]. We have shown that the major part of this loop has its origin in a changing membrane resistance with ac current, due to the slow hydration and dehydration of the polymer electrolyte with ac current. In Figure 1 the integral impedance response of the cell is plotted down to a modulation frequency of 0.5 mHz. We used pure gases (hydrogen with 40% rh on the anode, dry oxygen on the cathode) at 330 ml<sub>r</sub>/min. The inductive loop at low frequencies is typical for PEFCs at low humidity [1]. Of special interest is the quasi linear branch, which becomes apparent at frequencies below 10 mHz.

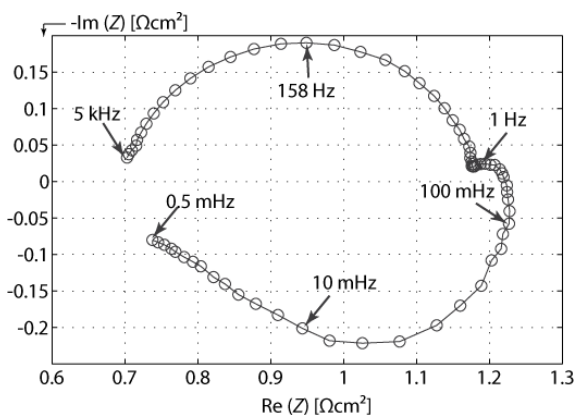


**Figure 1.** Integral spectrum recorded at 10 A cell current down to 0.5 mHz. At low frequencies ( $f < 10$  mHz) the spectrum shows an apparent linear behavior.

The reason for this unexpected behavior has not been discussed yet. Our previous work has shown, however, that it is not connected to the membrane resistance, as the impedance of the membrane shows a semicircle like behavior at low frequencies [1]. Also, the pure local spectrum does show a linear low frequency branch, as becomes apparent in our data [2].

A possible explanation can be given, if we take into account the porous structure of the electrode. If the Damjanovic mechanism is considered, low frequency inductive loops could be measured and explained by Antoine et al [3]. Such an inductive step in the elementary kinetics can, under some circumstance, lead to a low frequency behavior like it is observed in our cell. Porous electrodes can be described in a first approach by the transmission line model [4]. For this consideration, we exchange the model for the faradaic impedance in the standard model [4] by an element that accounts for adsorption relaxation [5]. The resulting electrical circuit is shown in Figure 2a. For the sake of simplicity no mass transport limitation is included here. The resulting low frequency response for a given set of parameters is shown in Figure 2b, for four different values of  $R_0$ . At very low values for  $R_0$ , a linear low frequency branch becomes visible. This is the equivalent to the linear behavior at high frequencies, which originates from the electrochemical double layer [4]. However, only if the serial resistance to the coil  $R_0$  is very small compared to the catalyst layer protonic

resistance, the low frequency linear branch becomes prominent (Figure 2b). Such low values are probably not realistic for the ORR. In addition, the inductive behavior, originating from effects other than membrane hydration, has to be small, as we have already shown that the major part of the low frequency inductive loop stems from the membrane [1]. However, still it is worth considering this effect when impedance spectroscopy is used to investigate the elementary kinetics, as a change in the elementary reactions, might change the impedance in a more complicated way, due to the porous electrode structure.

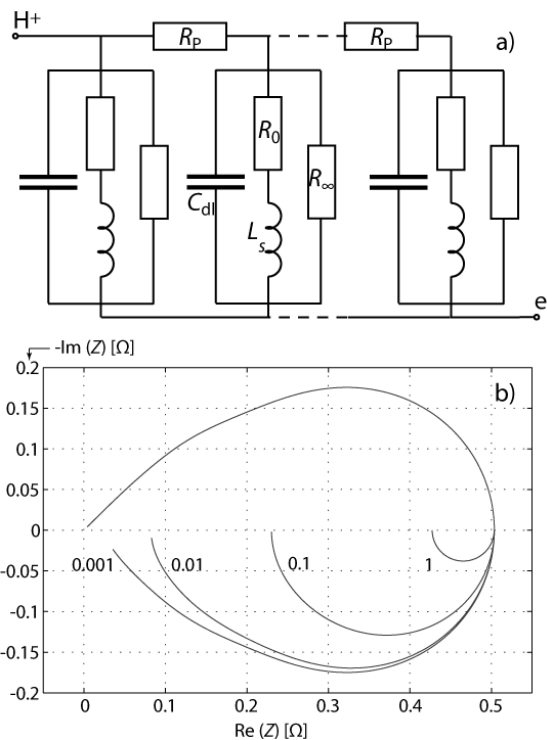


**Figure 1.** (a) Schematic of the transmission line [4], in which a Faradaic impedance element is used, which can account for surface adsorption relaxation [5]. (b) Calculated impedance spectra obtained (b) for four different values of  $R_0$  noted in the graph (in  $\Omega$ ). The other values are constant ( $R_p = 0.7 \Omega$ ,  $R_\infty = 0.3 \Omega$ ,  $L_s = 2.4 H$ ,  $C_{dl} = 0.002 F$ ).

## References

- [1] I.A. Schneider, M.H. Bayer, A. Wokaun, G.G. Scherer, *J. Electrochem. Soc.* **155**, B783 (2008).
- [2] I.A. Schneider, M.H. Bayer, P. Boillat, A. Wokaun, G.G. Scherer, *ECS Transactions* **11**, 461 (2007).
- [3] O. Antoine, Y. Bultel, R. Durand, *J. Electroanal. Chem.* **499**, 85-94 (2001).
- [4] R. de Levie in P. Delahay (ed.), "Advances in Electrochemistry and Electrochemical Engineering", vol. VI, Interscience, New York, 329 (1967).
- [5] D.A. Harrington, B.E. Conway, *Electrochim. Acta* **32** (12), 1703-1712 (1987).

# PEFC membrane parameter determination using *in situ* laser absorption spectroscopy and 1+1 dimensional modeling

M.H. Bayer, S. von Dahlen, I.A. Schneider

phone: +41 56 310 5304, e-mail: michael.bayer@psi.ch

In this work, we used our setup for the dynamic measurement of the water partial pressure along the gas channels during electrochemical impedance spectroscopy (EIS) [1], together with our 1+1 dimensional model [1] in order to determine important membrane parameters *in situ*. Therefore, we performed a series of experiments, which allowed the sequential determination of different parameters [2]. First, we determined the effective water diffusion coefficient across the membrane, then the electroosmotic drag EOD coefficient, third the ionic conductivity, and last the water sorption isotherm. All experiments were performed with the same MEA in our 63 cm<sup>2</sup> linear cell [3].

## Results

The effective water diffusion coefficient in the membrane can be determined from the net water flux over the MEA at zero external cell current. Without an applied cell current, no water is produced or transported by EOD. Hence, the only two processes involved in the water management are transport based on activation gradients across the MEA and advection in the flow channels. Humidity profiles along the channel for different anode inlet humidity and dry oxygen at the cathode inlet are shown in Figure 1. The flow rate was set to 660 ml<sub>n</sub>/min on both sides of the cell. Assuming a fast water sorption at the interfaces, the diffusion of water across the membrane is the limiting process. This allows a functional fitting of the effective water diffusion coefficient in the membrane, using the mean square error as the merit function.

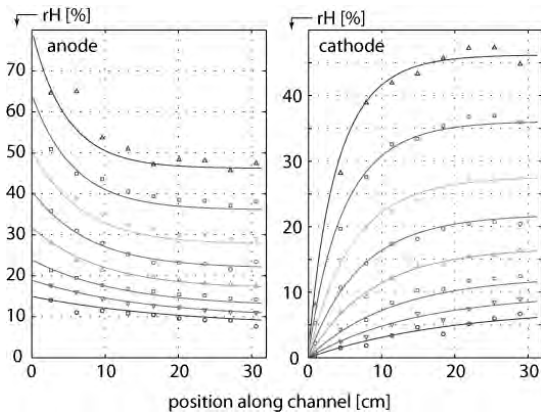


**Figure 1.** Humidity profiles along the channel at zero load. In this and the other graphs, symbols represent measured results, while lines represent the calculated results with the best set of parameters, as shown in Figure 4.

After the activity driven water transport has been quantified, the EOD coefficient  $n_d$  can be determined by measuring the water profiles along the flow field for different cell currents. To get a stronger dependence of the water concentration on the current, the flow rates

were reduced to 330 ml<sub>n</sub>/min with 40% rh at the anode and a dry cathode. The results are shown in Figure 2. For this step, the measured current density distribution

(Figure 2c) was used in the model. The humidity along the cathode channel is gradually increasing (Figure 2b), due to water production and EOD, while the humidity at the anode first decreases, before it gets rehydrated by back-diffusion of water from the cathode (Figure 2a). The EOD coefficient determines the shape of the profile, as the diffusion coefficient is known from an independent measurement. A water independent drag coefficient was assumed. With that assumption, the best fit was obtained using  $n_d = 1.073$ , consistent to literature data [4].

With the known humidity profiles and the determined diffusion and drag coefficient, the water profiles across the membrane can be calculated for all positions along the channel. The HFR at 5 kHz was taken as a measure for the membrane resistance and serial resistances. The resistance decreases along the channel (Figure 2d), as the membrane gets better hydrated. In the model the membrane resistance is calculated from the water profiles across the membrane, which are available through the previous experiments.

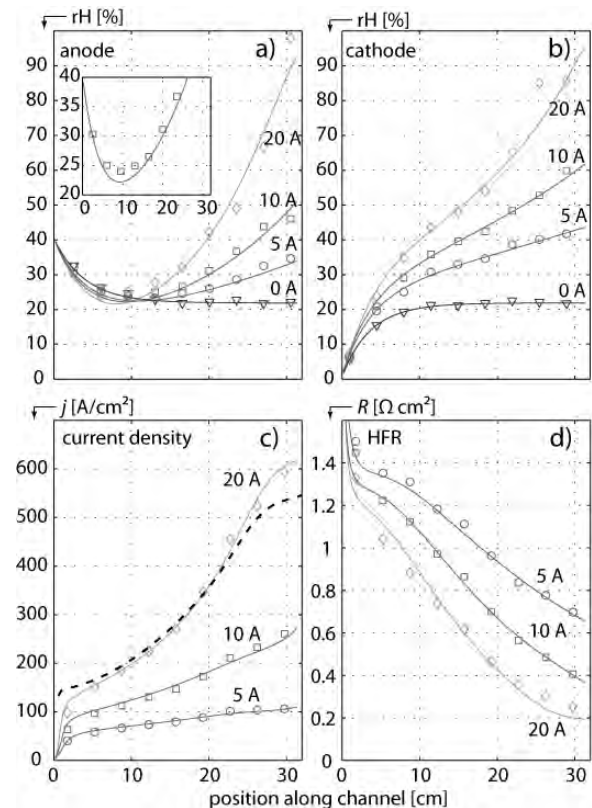


**Figure 2.** Humidity profiles along the channel (a,b) at different loads, corresponding current density (c) and resistance distribution (d).

To close the parameter determination process, the current density distribution has to result from the resistance and reactant distribution. If the catalyst layer sheet resistance of the cathode is not taken into account, the current distribution cannot be described by

the model (dashed line in Figure 2c). If we assume that one third of the catalyst layer sheet resistance contributes to the ohmic losses [5], the fit is significantly better (Figure 2c).

For the determination of the water sorption isotherm, transient techniques are needed. The water sorption isotherm states how many water molecules are needed to change the hydration state of the membrane and, hence, it sets the timescale for processes, involving changes in membrane hydration. We have shown that during ac impedance spectroscopy in PEFCs operated on subsaturated gases, a resistance oscillation builds up, due to the slow hydration and dehydration of the polymer electrolyte with ac current [6]. The hydration of the membrane is the slowest process in subsaturated PEFCs. Consequently, it defines the characteristic frequency of the water concentration oscillation, which builds up along the gas channels [1,7]. Amplitude and phase of the frequency response of the relative humidity on the ac cell current  $Z_c(f)$  [1] is plotted in Figure 3 for three positions along the anode and cathode flow field, respectively. Important for this work are characteristic kinks in the phase of the signal at the cathode and the monotonically changing phase at the anode. These characteristics allow a fitting of the derivative of the water sorption isotherm with respect to water activity.

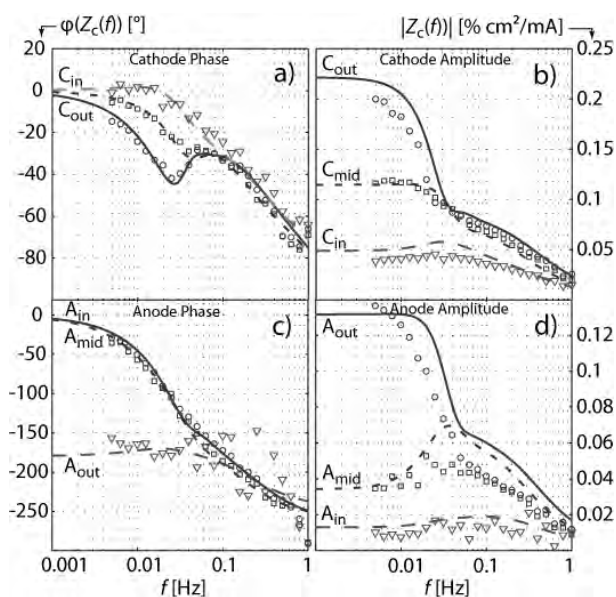


**Figure 3.** Phase and amplitude of  $Z_c(f)$  for three positions along the anode and cathode gas channels.

The results obtained from our approach are compared to correlations from three different literature references (Figure 4) [8-10]. In our experiments, we got all data *in situ* from one membrane, while the literature data originate from different batches of Nafion 117 membranes. Our data are comparable to the literature curves, but do not resemble exactly one of the correlations, except the determined derivative of the water sorption, which is identical to one literature curve [8]. Consequently, we use this correlation for our cell. The *in situ* determination of the membrane parameters is necessary to get a self consistent interpretation of the impedance response in subsaturated PEFCs. The dynamic measurement of the water partial pressure in the channel is, thereby, a valuable tool to understand and quantify the limiting processes.

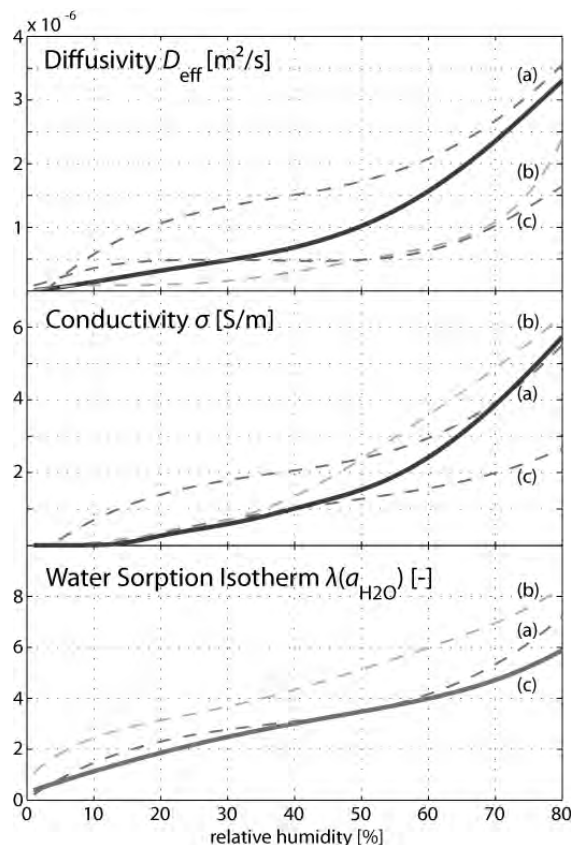


**Figure 4.** Effective Diffusivity, ionic conductivity and water sorption isotherm as a function of relative humidity from fits to our data (bold lines). For comparison literature correlations are included as dashed curves ((a) [8], (b) [9], (c) [10]).

## References

- [1] M.H. Bayer, A. Wokaun, G.G. Scherer, I.A. Schneider, ECS Transactions **25** (1), 949-960 (2009).
- [2] M.H. Bayer, A. Wokaun, G.G. Scherer, I.A. Schneider, FuelCell2010-33041 in "Proceedings of the ASME 2010 Eighth International Fuel Cell Science, Engineering and Technology Conference", June 14-16, 2010, Brooklyn, New York, USA (2010).
- [3] I.A. Schneider, D. Kramer, A. Wokaun, G.G. Scherer, J. Electrochem. Soc. **154**, B770 (2007).
- [4] T.A. Zawodzinski, J. Davey, J. Valerio, S. Gottesfeld, 1995, Electrochim. Acta **40**, 297-302 (1995).
- [5] R. Makharia, M.F. Mathias, D.R. Baker, J. Electrochem. Soc. **152** (5), A970-A977 (2005).
- [6] I.A. Schneider, M.H. Bayer, A. Wokaun, G.G. Scherer, J. Electrochem. Soc. **155**, B783 (2008).
- [7] I.A. Schneider, M.H. Bayer, P. Boillat, A. Wokaun, G.G. Scherer, ECS Transactions **11**, 461 (2007).
- [8] T.A. Zawodzinski, M. Neeman, L.O. Sillerud, S. Gottesfeld, J. Phys. Chem. **95**, 6040-6044 (1991).
- [9] S. Ochi, O. Kamishima, J. Mizusaki, J. Kawamura., Solid State Ionics **180**, 580-584. (2009).
- [10] A.A. Kulikovskiy, J. Electrochem. Soc. **150**, A1432 (2003).

## Locally resolved EIS in channel and land areas of PEFCs

I.A. Schneider, M.H. Bayer, S. von Dahlen

phone: +41 56 310 2795, e-mail: ingo.schneider@psi.ch

Transient techniques like electrochemical impedance spectroscopy (EIS) or cyclic voltammetry (CV) are important tools in PEFC diagnostics [1]. Employment of these techniques focuses primarily on a characterization of the most elemental part of a PEFC, namely the membrane electrode assembly (MEA), and therefore the effect of the flow fields and associated *in plane* inhomogeneities on transient response [1-3] are often excluded from the discussion.

However, transient techniques are generally used *in situ* in technical cells and consequently, the contribution of *in plane* processes like reactant depletion along the flow channels or underneath the ribs of PEFC flow field structures must seriously be taken into account.

This has been demonstrated, in particular, for PEFC air cathodes. Our earlier work focused on the effect of *down the channel* inhomogeneities on PEFC impedance response [1, 4, 5]. In our experiments, a low frequency capacitive loop appeared in both integral and local spectra only at lower air stoichiometry. Our results have proven that the appearance of this loop is primarily indicative of a limitation of cell performance, due to depletion of oxygen in the *down the channel* direction at finite air flow rates [1, 4, 5]. The use of a one-dimensional *through the MEA* PEFC impedance model for the interpretation of the results would therefore undoubtedly take into account the wrong phenomena. A key feature of the local spectra, namely the appearance of negative low frequency resistance values in the spectra of the outlet region at low air stoichiometry, is a direct consequence of high oxygen depletion in flow direction [4, 5]. As an important consequence, this feature is only captured by models which take into account the *down the channel* dimension, e.g., 1D + 1D impedance models [4].

Following up our results, we continue our discussion with an assessment of the importance of lateral inhomogeneities on the millimeter scale of channel and lands in the direction *perpendicular to the flow channels* for PEFC impedance response. The assessment is crucial, since it is often assumed in EIS measurements that small cells, which are operated at high gas flow rates (differential cells) [2, 3] provide quasi homogeneous reaction conditions all over the active area. Therefore, locally resolved EIS [1, 5] was employed for the first time in channel and land areas of a differential cell with sub-millimeter resolution [6].

### Results and Discussion

The results of steady state and ac impedance measurements are presented in Figure 1. Integral data and results of locally resolved measurements in channel and land areas of the cathode flow field are shown. The integral *iU* curve of the cell is displayed in Figure 1a (black curve). This curve appears to approach limiting current density at higher cell polarization.

The higher slope of the *iU* curve at high current densities above  $1 \text{ A/cm}^2$  (Figure 1a, black curve) is consistent with the observed strong increase of the integral impedance spectrum toward lower cell voltage (Figure 1b, black curve). An approach based on one-

dimensional PEFC models would probably take into account here an increasing mass transport limitation in the *through the MEA* direction (e.g. across the GDL) to account for these phenomena at lower cell voltage.

However, this conclusion is clearly put into question by the results of spatially resolved current density and impedance measurements in channel and land areas (Figure 1). The *iU* characteristics of channel and land regions are shown in Figure 1a (grey curves). The current production increases, virtually unhindered, with increasing cell polarization in the channel area; yet, in the land area, the current production stops to increase already at cell voltages below  $U = 0.4 \text{ V}$ . This result demonstrates that the apparent onset of limiting current conditions in the integral *iU* curve (Figure 1a, black curve) at higher cell polarization is actually more a change of the slope of this curve, as the current production stops to increase underneath the ribs and continues to rise only in half of the electrode area within the channel region.

An interesting phenomenon becomes apparent in the *iU* characteristics of the rib center (Figure 1c). At higher total cell polarization ( $U \leq 0.3 \text{ V}$ ), the local current production actually decreases despite the increasing total cell polarization. Note that this phenomenon occurred already at cell voltages of  $U \leq 0.6 \text{ V}$  for higher performance CCMs. A similar effect was observed and analyzed earlier in the *down the channel* direction of  $\text{H}_2/\text{air}$  PEFCs [1, 4, 5]. The negative slope of the local polarization (*iη*) curve in the rib center is a result of oxygen concentration polarization losses due to oxygen depletion in lateral direction. Oxygen is consumed in the oxygen reduction reaction, while it diffuses under the rib. As a result of the 'ever' increasing oxygen consumption with increasing total cell polarization in the rib edge and channel area, the total increase in cell polarization is finally overcompensated in the rib center by increasing oxygen concentration polarization losses [1, 3, 4, 6], and thereby the local current decreases despite an increasing total cell polarization. This phenomenon was also observed at a lower GDL compression and with GDL materials, which employ a microporous layer (MPL). It has an important impact on the locally resolved impedance spectra in channel and land areas. Locally resolved impedance spectra as obtained at a cell voltage of  $U = 0.5 \text{ V}$  and  $U = 0.2 \text{ V}$  are presented in Figure 1d and Figure 1e. Already at a cell voltage of  $U = 0.5 \text{ V}$ , a second low frequency loop develops in the local spectra underneath the ribs. This loop becomes more strongly pronounced, with increasing distance from the channel and an increasing *in plane* diffusion path length for molecular oxygen (Figure 1d). This indicates that the appearance of the low frequency loop must be associated with the depletion of oxygen in the land area. The conclusion is supported by the appearance of a negative low frequency intercept [1, 3-6] in the local spectrum of the rib center at higher total cell polarization ( $U = 0.2 \text{ V}$ ) (Figure 1e), where the slope of the respective local polarization (*iη*) curve exhibits a negative value (Figure 1c).

These unique features, which appear in the rib center at low cell voltage and high oxygen consumption, are key indicators for a limitation of cell performance, due to depletion of oxygen underneath the ribs.

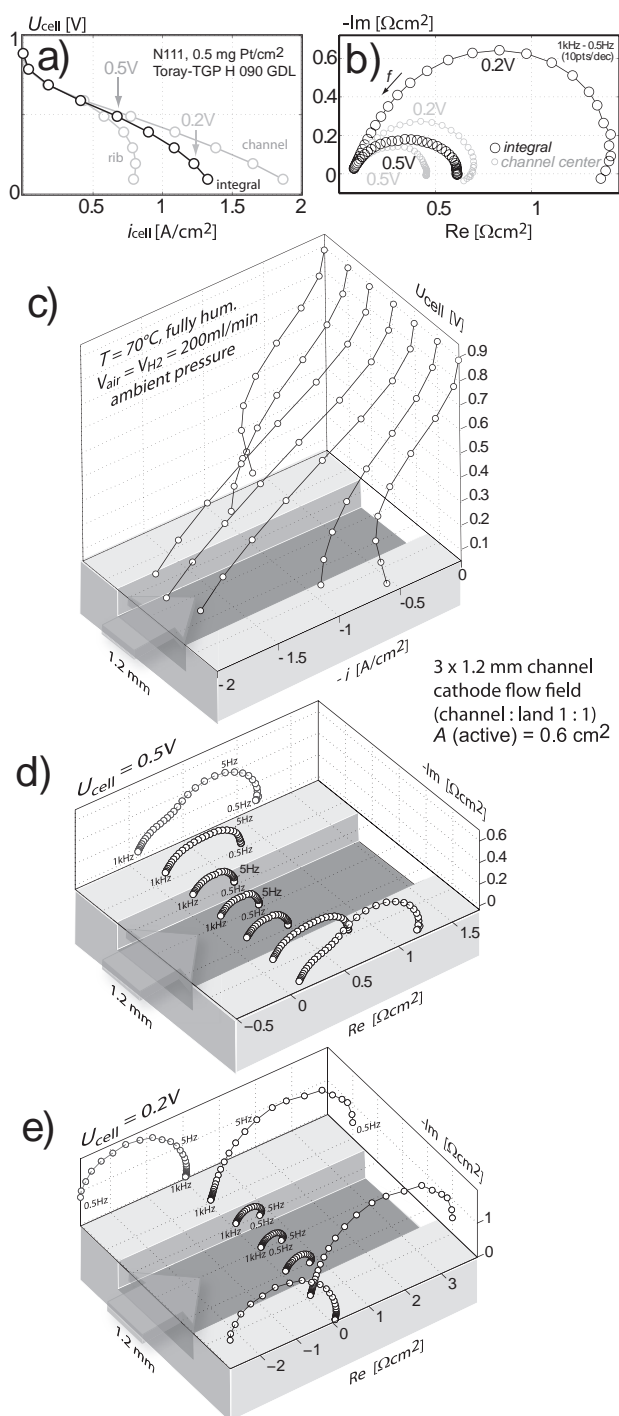


**Figure 1.** Integral and locally resolved measurements in a differential  $H_2/air$  PEFC: a) integral  $i/U$  characteristic (black curve) and  $i/U$  characteristics of channel and land regions (grey curves) b) integral impedance spectra (black curve) and local spectra in the channel center (grey curves) at a cell voltage of  $U = 0.5 V$  and  $U = 0.2 V$  c) locally resolved  $i/U$  curves in channel and land areas of a repetitive unit of the 3 x 1.2 mm channel flow field, and c, e) locally resolved impedance spectra at  $U = 0.5 V$  (d) and  $U = 0.2 V$  (e).

Thereby, the spatially resolved steady state and ac impedance measurements demonstrate that the strongly increasing loop diameter of the integral impedance spectrum toward lower cell voltage and

higher current density (Figure 1b, black spectra) is not primarily indicative of a mass transport limitation in the *through the MEA* direction. It is instead a direct consequence of depletion of oxygen underneath the ribs in the direction *perpendicular to the flow channels*. This conclusion is emphasized by the weak impact of the increasing current density on the local spectrum in the channel center, when the cell voltage is decreased (Figure 1b, grey curve). Strictly speaking, only this part of the MEA can be regarded as a quasi one-dimensional cell. Consequently, use of differential cells does not generally justify a one-dimensional treatment of data by using *through the MEA* impedance models, in particular at higher cell currents where mass transport limitations underneath the ribs become important.

## Conclusions

Operation of small active area PEFCs at high gas stoichiometry (differential operation), is an efficient way to exclude inhomogeneities in the *down the channel* direction. However, care must be taken, if one-dimensional *through the MEA* PEFC impedance models are used to analyze the impedance response of these quasi two-dimensional cells. The results of submillimeter resolved EIS measurements in a differential cell with straight parallel flow channels, as presented here, clearly demonstrate that key effects, which occur as a consequence of inhomogeneous operation of PEFCs in the *down the channel* direction typically on a length scale of tens of centimeters are also significant on the millimeter scale of channels and ribs in the direction *perpendicular to the flow channels*. Inhomogeneities, which occur during operation of a PEFC in the *down the channel* direction, depend primarily on the gas stoichiometry. Phenomena, like the appearance of negative low frequency resistance values in the local spectra of the outlet region due to oxygen depletion in the *down the channel* direction [1, 4, 5] will therefore appear at low air stoichiometry, regardless of the total cell current. However, they can simply be excluded by using high gas stoichiometries. In contrast, lateral inhomogeneities in the *perpendicular to the flow channel* direction become important, primarily at higher total cell current. These inhomogeneities are a direct consequence of a mass transport limitation underneath the ribs [3, 6]. They are, therefore, system immanent and they can only be mitigated by changing the cell design or by operation of the cell on pure fully humidified gases at moderate current densities.

## References

- [1] I.A. Schneider, G.G. Scherer, in Handbook of Fuel Cells, Vol. 6, W. Vielstich, H.A. Gasteiger, H. Yokokawa, Editors, John Wiley & Sons, Chichester, UK (2009).
- [2] M.F. Mathias, D. Baker, J. Zhang, Y. Liu, W. Gu, ECS Trans. **13**(13), 129 (2008).
- [3] I.A. Schneider, M.H. Bayer, S. von Dahlen, in Polymer Electrolyte Membrane and Direct Methanol Fuel Cell Technology, C. Roth, C. Hartnig, Editors, Woodhead Publishing, Cambridge, UK, ISBN Nummer: 978-1845697747 (2010).
- [4] I.A. Schneider, M.H. Bayer, A. Wokaun, G.G. Scherer, ECS Trans. **25** (1) 937 (2009).
- [5] I.A. Schneider, D. Kramer, A. Wokaun, G.G. Scherer, J. Electrochem. Soc. **154**, B770 (2007).
- [6] I.A. Schneider, M.H. Bayer, S. von Dahlen, J. Electrochem. Soc. **158** (3) B343-B348 (2011)

# Investigation of mass transport phenomena in channel and land areas during start-up and shutdown of PEFCs

I.A. Schneider, S. von Dahlen

phone: +41 56 310 2795, e-mail: ingo.schneider@psi.ch

Our most recent work has proven that the reverse-current-phenomenon occurs in polymer electrolyte fuel cells (PEFCs) even in small regions of channels and lands on a length scale of fractions of a millimeter [1]. The results demonstrate that a high gas flow rate and a short fuel gas introduction time cannot avoid mass transport limitations underneath the ribs, which cause temporarily an inhomogeneous gas distribution over the fuel electrode and *in plane* current transients in the *perpendicular to the fuel channel* direction. A major part of these *in plane* currents is ascribed to capacitive charging currents [2, 3, 4-6]. However, the appearance of the reverse-current phenomenon is undoubtedly a prerequisite for the appearance of high electrode potentials and associated degradation phenomena. A detailed assessment of the reverse current phenomenon on the small scale of channel and land areas is therefore crucial.

In general, gas transport in the GDL underneath the ribs is primarily diffusion controlled. In this context, the effect of the flow field design, and the type of purge gas used at the fuel electrode were investigated. During the start-stop experiments, the oxidant electrode was operated on humidified air, while the fuel electrode gas feed was switched from humidified air to humidified hydrogen and vice versa by a magnetic valve. Two different types of fuel flow fields were employed in the measurements, i) 3 x 1.2 mm channel fuel flow field, and ii) 2 x 2 mm channel fuel flow field (channel:land ratio 1:1) [7]. In an investigation on the effect of the diluting inert gas  $X$  on mass transport, mixtures of  $O_2$  and  $X = He$  (4 g/mol) or  $X = SF_6$  (146 g/mol) were employed as the fuel gas ( $X$  (79 %),  $O_2$  (21 %)) instead of air ( $X = N_2$  (28 g/mol)). A high gas flow rate ensures a short residence time of the gas in the fuel flow channels. This time is well below 25 ms and the gas supply is not limiting.

## Results and Discussion

Local current transients, as observed in channel and land areas during a start-up and a shutdown process, are shown in Figure 1 for two different types of flow fields. During start-up (Figure 1a, 1c), air is replaced quasi-instantaneously by hydrogen in the fuel flow channels. Thereby, the hydrogen rich channel areas already operate as a fuel cell and drive a reverse-current through the hydrogen starved land areas. Inverse characteristics are observed during a shutdown process, where hydrogen is replaced by air in the fuel flow channels (Figure 1b, 1d).

The results shown in Figure 1 demonstrate that the local current transients for the 2 mm channel flow field last longer and exhibit higher peak values compared to the respective transients as obtained for the 1.2 mm channel flow field. This effect can, at least partially, be attributed to the increasing diffusion path length for the gases to penetrate underneath the ribs of the flow field. Since higher and longer lasting local peak currents could result in higher and longer lasting local oxidant electrode, the choice of a fuel flow field with narrow

land widths should mitigate high cathode potentials and associated corrosion phenomena.

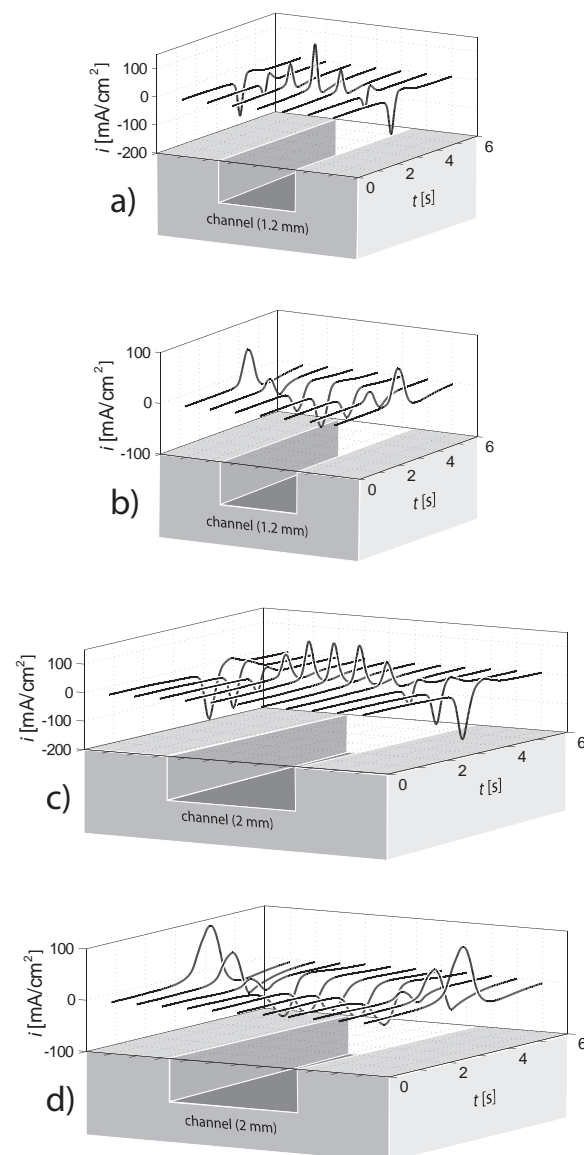


**Figure 1.** In plane current transients during (a, c) start-up and (b, d) shutdown of a  $H_2$ /air PEFC (fully humidified gases). The local current transients are shown for a (a, b) 1.2 mm channel and a (c, d) 2 mm channel fuel flow field (channel:land ratio 1:1).

Different observations have been made, whether the start-up or the shutdown process has a higher impact on carbon corrosion, but up to now this could not completely be solved [2]. In the experiments, we generally observed a faster change of the cell voltage in the start-up process of a  $H_2$ /air PEFC (Figure 2a) compared to the shutdown procedure (Figure 2b). Moreover, experimentally obtained peak currents are by a factor of two higher for the start-up process (Figure 2a, 2b).

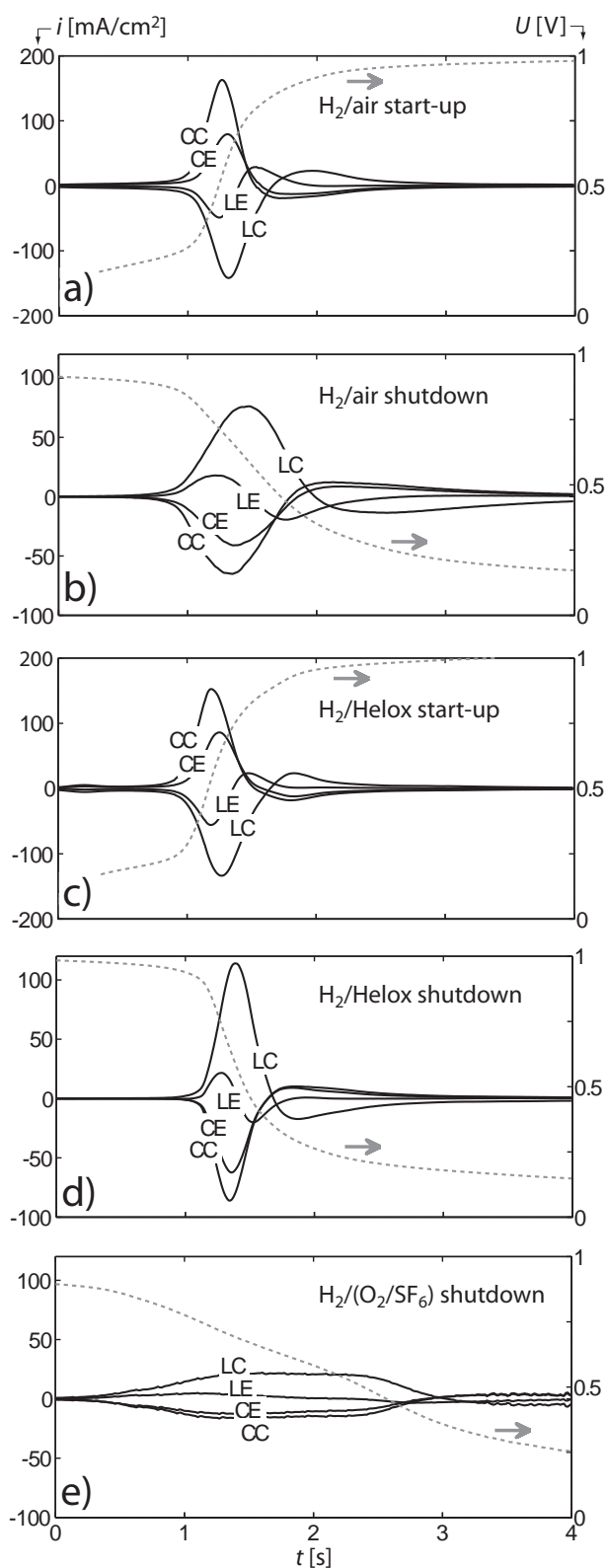


**Figure 2.** Local current transients in channel and land areas for different fuel electrode purge gases: (a, b) air, (c, d) Helox, and (e)  $\text{SF}_6$  (fully humidified gases). The transients are shown during start-up (a, c) and shutdown (b, d, e) of the PEFC in four characteristic areas of the 1.2 mm channel fuel flow field CC: channel center, CE: channel edge, LC: land center, LE: land edge.

The different characteristics of start-up and shutdown transients are much less pronounced, if Helox (21 %  $\text{O}_2$  in Helium) is used instead of air (Figure 2d, 2e). If we take into account that the characteristics of the start-up

transient is comparable for a  $\text{H}_2/\text{air}$  and a  $\text{H}_2/\text{Helox}$  cell (Figure 2a, 2c), we might conclude that gas phase mass transport limitations are less important for the transport of hydrogen (through diluted oxygen) toward the fuel electrode during start-up.

In contrast, the different characteristics of the respective shutdown transients for a  $\text{H}_2/\text{air}$  and a  $\text{H}_2/\text{Helox}$  cell (Figure 2b, 2d) indicates that the transport of molecular oxygen to the fuel electrode during shutdown is strongly dependent on the diluting inert gas. This conclusion is further corroborated if an  $\text{O}_2/\text{SF}_6$  mixture is used to purge the fuel electrode (Figure 2e).

The shutdown transients become both shorter and higher with decreasing diffusion resistance for oxygen in the order  $\text{H}_2/(\text{O}_2/\text{SF}_6) > \text{H}_2/\text{air} > \text{H}_2/\text{Helox}$  (Figure 2e, 2b, 2d). This effect, which occurs in the perpendicular to the flow channel direction, can be regarded as counterpart to the observation of higher and shorter transients in the along the channel direction toward shorter fuel gas introduction time [6].

### Conclusions

The results (Figure 2) therefore indicate that the slower voltage change and the smaller in plane current transients during shutdown of a  $\text{H}_2/\text{air}$  cell (Figure 2a, 2b) are the result of a slower change of the fuel electrode potential from hydrogen to air potential, due to a notable gas phase mass transport limitation for oxygen. This limitation is much less pronounced for hydrogen during the start-up process when the fuel electrode potential changes from the air to the hydrogen potential (Figure 2a). Note that the hydrogen concentration in the channel region is kept high during start-up by the abundant supply of hydrogen to the gas channel. In contrast, during shutdown (channel region is in 'air/air mode') only the amount of hydrogen, which is stored underneath the ribs is available as fuel for the driving voltage source (land region).

### References

- [1] I. A. Schneider, S. von Dahlen, *Electrochem. Solid State Lett.* **14** (2), B30-B33 (2011).
- [2] W. Gu, R.N. Carter, P.T. Yu, H.A. Gasteiger, *ECS Trans.* **11** (1), 963 (2007).
- [3] T.W. Patterson, R.M. Darling, *Electrochem. Solid State Lett.* **9**, A183 (2006).
- [4] Z. Siroma, N. Fujiwara, T. Ioroi, S. Yamazaki, H. Senoh, K. Yasuda, K. Tanimoto, *J. Power Sources* **172**, 155 (2007).
- [5] G. Maranzana, C. Moyne, J. Dillet, S. Didierjean, O. Lottin, *J. Power Sources* **195**, 5990 (2010).
- [6] B. Wetton, R. Bradean, K. Eggen, in *Proceedings of the 20th International Symposium on Transport Phenomena*, Victoria, BC (2009).
- [7] I.A. Schneider, S. von Dahlen, A. Wokaun, G.G. Scherer, *J. Electrochem. Soc.* **157**, B338 (2010).

# Mitigation strategies for start-stop induced degradation in channel and land areas of a PEFC

S. von Dahlen, I.A. Schneider

phone: +41 56 310 2541, e-mail: steffen.vondahlen@psi.ch

Cost reduction and durability enhancement are major technical obstacles to the commercialization of polymer electrolyte fuel cells (PEFCs). A susceptible part of PEFCs to degradation is the catalyst layer. Dissolution and migration of the platinum particles as well as the oxidation of the carbon catalyst support are critical issues. One source for carbon corrosion is the inhomogeneous anode gas composition during the start-up and shutdown process of a PEFC [1, 2], which is known as the reverse-current decay mechanism [1]. This phenomenon is illustrated in Figure 1.

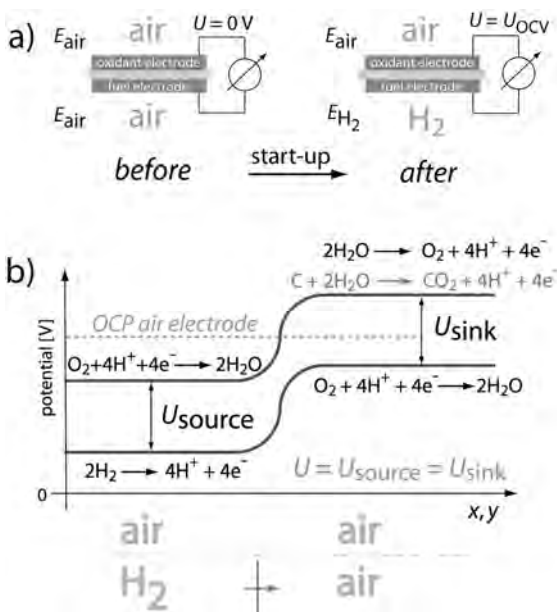


**Figure 1.** a) Schematic to illustrate the fuel and oxidant electrode potential  $E$  as well as the cell voltage  $U$  during off-state and after the start-up process, b) simplified sketch of the reverse-current phenomenon [1-4].

During a start-up process (Figure 1a), air present at the fuel electrode of a PEFC in the off-state is replaced by hydrogen. Thereby, the cell voltage  $U$  approaches open circuit voltage  $U_{\text{OCV}}$  as the potential  $E$  of the respective fuel electrode changes from the air electrode potential  $E_{\text{air}}$  to the hydrogen electrode potential  $E_{\text{H}_2}$  (Figure 1a). Similar considerations hold for the shutdown process. However, due to the finite mass transport rate in both the *along the channel* direction and the *perpendicular to the channel* direction of PEFC flow field structures, the gas is temporarily inhomogeneously distributed over the fuel electrode area (Figure 1b) during start-up and shutdown of a PEFC. As a result, significant *in plane* potential gradients exist temporarily over the electrode area (high ionic *in plane* resistivity), while the cell voltage is virtually equal in all parts of the cell (high electronic *in plane* conductivity of the bipolar plates), as illustrated in Figure 1b [2, 4]. Consequently, the inhomogeneous gas distribution over the fuel electrode leads to electronic *in plane* current transients, where hydrogen rich parts of the cell act as a voltage source

and drive a reverse-current through hydrogen starved parts, which act as a current sink (Figure 1b). Thereby, the oxidant electrode is temporarily exposed to high potentials [4] and, as a consequence, prone to carbon corrosion and Pt dissolution.

## Experimental

The experiments were conducted in the segmented microstructured flow field approach [5]. Here, the conventional flow field of the oxidant electrode is replaced by a 19-fold segmented microstructured flow field. This allows the direct measurement of the local cell current in channel and land areas with submillimeter resolution (400  $\mu\text{m}$ ). During the start-stop experiments ( $T_{\text{cell}} = 70\text{ }^\circ\text{C}$ ), the oxidant electrode was operated at humidified air, while the fuel electrode gas feed was switched from humidified air to humidified hydrogen and vice versa by a magnetic valve. Gases on both electrodes were operated on high gas flow rates of  $V_{\text{air}} = V_{\text{H}_2} = 0.2\text{ L/min}$ , so that effects in the *along the channel* direction can be neglected. The local current transients are shown in four characteristic areas of the 1.2 mm channel fuel flow field CC: channel center, CE: channel edge, LC: land center, LE: land edge (Figure 2a, inset).

## Results and Discussion

To circumvent the detrimental cell-reversal conditions emerging during the above described start-up and shutdown processes, different mitigation strategies have been developed. One mitigation strategy addresses the hydrogen introduction time [6, 7]. Here, a lower residence time of the gas front in the cell is supposed to yield a reduced carbon corrosion rate. However, this approach primarily affects phenomena in the *along the channel* direction. In the *perpendicular to the channel* direction, gas transport is primarily diffusion controlled. Here, both the flow field design and GDL properties play an important role. These properties can, however, only be improved by a change of the cell design.

It has been proposed that operation under fully humidified conditions during the start-up and shutdown processes of a PEFC has a more detrimental effect on the catalyst layer [8] than start-up under dry conditions. The local current transients during a start-up process are compared for fully humidified and subsaturated gases (40 % relative humidity, RH) in Figure 2a and b. Interestingly, the voltage transients show virtually the same characteristics in both cases, yet the local peak currents are remarkably reduced under dry conditions (Figure 2b). This significant effect might be ascribed to the higher ionic membrane resistance. The lower degradation levels, which have been reported for dry operation conditions [8] are attributed to the mitigating effect of the reduced water partial pressure on the carbon corrosion reaction [8, 9].

Another proposed strategy for mitigation of the detrimental reverse currents is a purge of the fuel gas

compartment with inert nitrogen gas during the start-up and the shutdown process [10]. With this approach, the maximum oxidation rate at the oxidant electrode is limited by the rate of oxygen crossover from the oxidant electrode to the nitrogen purged fraction of the fuel electrode [10]. Figure 2c shows the experimentally obtained local current transients and the voltage transient. Very small peak currents and a much slower voltage increase are observed. Unfortunately, this approach requires the installation of an external nitrogen supply to a fuel cell system.

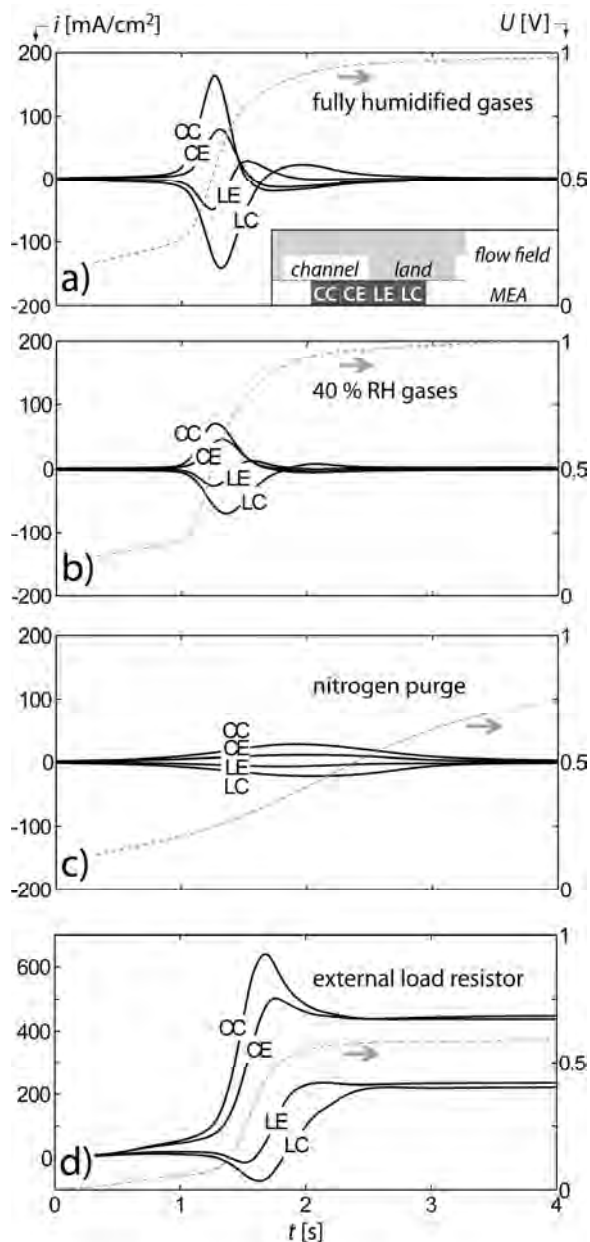


**Figure 2.** Effect of operation conditions and mitigation strategies on local current transients in channel and land areas of a hydrogen/air PEMFC during start-up: a) fully humidified gases, b) 40 % RH gases, c) effect of a nitrogen purge of the fuel gas compartment (fully humidified gases), and d) effect of an external load resistor ( $R_{load} = 1.8 \Omega cm^2$ , fully humidified gases). The transients are shown in four characteristic areas of the 1.2 mm channel fuel flow field: channel center (CC), channel edge (CE), land center (LC), land edge (LE) [3].

Another possible mitigation strategy is a potential-controlled start-up [10]. Here, an external auxiliary load is connected to the cell during start-up and shutdown to

prevent the electrode from being exposed to high potentials [10-12]. A start-up process with an external auxiliary load of  $1.8 \Omega cm^2$  is shown in Figure 2d. Here, the observed negative peak currents are smaller compared to operation without external load. This is consistent with the observed lower degradation rates [10-12]. However, this approach primarily addresses the cell voltage, which reaches a significantly lower value of approximately 0.55 V. The application of an external auxiliary load resistance substantially reduces the cathode potential during start-up and shutdown processes. High local potentials and their detrimental effect can be mitigated.

## Conclusions

Start-stop phenomena with the ascribed detrimental carbon corrosion reactions can even occur on the submillimeter scale of channels and lands. A short fuel gas introduction time during start-up and shutdown of a PEMFC cannot eliminate the reverse-current phenomenon. In general, gas transport in the GDL underneath the lands is primarily diffusion controlled. In this context, mitigation strategies must focus on the flow field design, GDL properties, and the type of purge gas used at the fuel electrode in the off-state. The flow field design and the chosen GDL properties have to be balanced with the requirements of cell operation, while mitigation strategies, which are based on the type of purge gas, the gas humidity, or the use of an external load, will affect the cell characteristics primarily during the start-up and shutdown period.

## References

- [1] C.A. Reiser, L. Bregoli, T.W. Patterson, J.S. Yi, J.D. Yang, M.L. Perry, T.D. Jarvi, *Electrochem. Solid-State Lett.*, **8**, A273 (2005).
- [2] A.P. Young, J. Stumper, E. Gyenge, *J. Electrochem. Soc.*, **156**, B913 (2009).
- [3] I.A. Schneider, S. von Dahlen, *Electrochem. Solid State Lett.* **14** (2), B30-B33 (2011).
- [4] M.V. Lauritzen, P. He, A.P. Young, S. Knights, V. Colbow, P. Beattie, *J. New Mat. Electrochem. Systems* **10**, 143 (2007).
- [5] I.A. Schneider, S. von Dahlen, A. Wokaun, G.G. Scherer, *J. Electrochem. Soc.* **157**, B338 (2010).
- [6] W. Gu, R.N. Carter, P.T. Yu, H.A. Gasteiger, *ECS Trans.* **11** (1), 963 (2007).
- [7] B. Wetton, R. Bradean, K. Eggen, in *Proceedings of the 20th International Symposium on Transport Phenomena*, Victoria, BC (2009).
- [8] J.H. Kim, E.A. Cho, J.H. Jang, H.J. Kim, T.H. Lim, I.H. Oh, J.J. Ko, S.C. Oh, *J. Electrochem. Soc.* **157**, B104 (2010).
- [9] T.J. Schmidt in *Polymer Electrolyte Fuel Cell Durability*, F.N. Buechi, M. Inaba, T.J. Schmidt, Editors, Springer, New York, 199-221 (2009).
- [10] J.P. Meyers, R.M. Darling, *J. Electrochem. Soc.* **153**, A1432 (2006).
- [11] J.H. Kim, E.A. Cho, J.H. Jang, H.J. Kim, T.H. Lim, I.H. Oh, J.J. Ko, S.C. Oh, *J. Electrochem. Soc.* **156**, B955 (2009).
- [12] J.H. Kim, E.A. Cho, J.H. Jang, H.J. Kim, T.H. Lim, I.H. Oh, J.J. Ko, I.J. Son, *J. Electrochem. Soc.* **157**, B118 (2010).

## Correlation of local water content and current density transients in channel and land areas of a PEFC

S. von Dahlen, M.H. Bayer, P. Boillat, P. Oberholzer, I.A. Schneider

phone: +41 56 310 2541, e-mail: steffen.vondahlen@psi.ch

Water management is an important issue in PEFC research. In low-temperature PEFCs, there exists a tradeoff between a sufficiently humid environment for proton conduction in the ionomer and formation of liquid water, which might impede the transport of the reactant gases to the electrodes. To investigate the effect of GDL, flooding on the local cell performance, the local water content in the GDL and the local current density in channel and land areas of a PEFC were measured simultaneously.

### Experimental

The experiment was conducted in the segmented microstructured flow field approach [1]. Here, the conventional flow field of the anode is replaced by a 19-fold segmented microstructured pin-type flow field. This allows the direct measurement of the local currents within four characteristic areas of the flow field (Figure 1, inset). At the cathode, a conventional graphite flow field (1.2 mm channel/ land width) was used along with an untreated 280  $\mu\text{m}$  thick Toray TGP-H-090 carbon paper GDL and a 200  $\mu\text{m}$  PTFE gasket. A Nafion N112 membrane was employed and the cell ( $T_{\text{cell}} = 40\text{ }^\circ\text{C}$ ) was operated on fully humidified hydrogen and air ( $V_{\text{air}} = V_{\text{H}_2} = 0.2\text{ L/min}$ ). The local water content was determined by *in plane* neutron radiography with a temporal resolution of 10 s [2, 3].

### Results and Discussion

The transient response of local water content and current density to a step from  $U = 0.96\text{ V}$  to  $U = 0.1\text{ V}$  as perturbation signal on a time scale of ten minutes is presented in Figure 1. The current density in the channel areas (CC and CE) first passes a minimum around 100 s after cell perturbation and then reaches a steady state condition of about  $i = 0.6\text{ A/cm}^2$  after 500 s (Figure 1b). In contrast, in the land areas (LE and LC), the current density drops to  $i = 0.5\text{ A/cm}^2$  during the first 100 s after the step and does not recover (Figure 1c).

A general impression of the liquid water distribution can be received by the neutron radiograms of the four distinct points in time shown in Figure 1a. Local water content is analyzed in the four characteristic areas CC, CE, LE and LC and in the two regions of the GDL, the electrode (E) and the flow field (F) side (Figure 1d, e).

Liquid water accumulates in the channel areas (Figure 1d) up to maximum values of around 15 % in the electrode side of the GDL, before reaching steady state conditions of around 10 %. This behavior might be described with water rearrangement in the GDL [4, 5] and coincides with the current density in the channel areas. However, in both electrode and flow field side of the land areas liquid water accumulation has weak influence on cell performance under limiting current conditions. This can be observed by the virtually constant current density (Figure 1c) during a significant water accumulation of up to 15 % in the land center (Figure 1e).

### Conclusions

While in the channel areas, the current density is supposed to be directly dependent on the water content, in the land areas the current density is unaffected by the significant accumulation of water in the GDL.

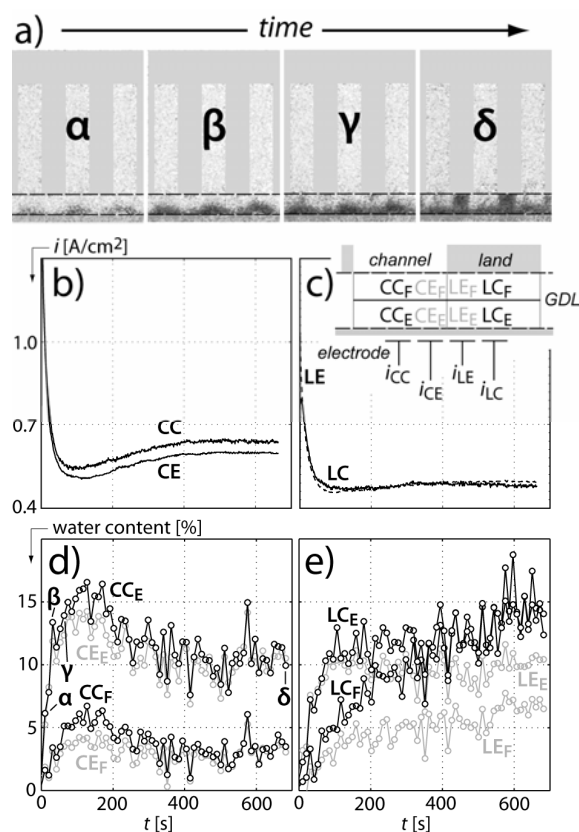


**Figure 1.** a) Voltage step experiment from  $U = 0.96\text{ V}$  to  $U = 0.1\text{ V}$  in a PEFC operated on  $\text{H}_2/\text{air}$ : a) Neutron radiograms for four distinct points in time ( $\alpha$ ,  $\beta$ ,  $\gamma$  and  $\delta$  are marked in Figure 1d), b, c) local current densities in the four characteristic areas channel center (CC), channel edge (CE), land edge (LE) and land center (LC), d, e) local water content in the four characteristic areas in the electrode (E) and the flow field (F) side of the GDL.

### References

- [1] I.A. Schneider, S. von Dahlen, A. Wokaun, G.G. Scherer, *J. Electrochem. Soc.* **157**, B338 (2010).
- [2] I.A. Schneider, S. von Dahlen, M.H. Bayer, P. Boillat, M. Hildebrandt, E.H. Lehmann, P. Oberholzer, G.G. Scherer, A. Wokaun, *J. Phys. Chem. C* **114** (27), 11998 (2010).
- [3] P. Boillat, G. Frei, E.H. Lehmann, G.G. Scherer, A. Wokaun, *Electrochem. Solid State Lett.* **13**, B25 (2010).
- [4] A.Z. Weber, R. Balliet, H.P. Gunterman, J. Newman, in *Modern Aspects of Electrochemistry* **43**, M. Schlesinger, Editor, Springer, 273 (2009).
- [5] D. Natarajan, T.V. Nguyen, *J. Electrochem. Soc.* **148**, A1324 (2001).

## TEM sectioning as a method to determine Pt losses in PEFCs

H. Schulenburg, B. Schwanitz, N. Linse

phone: +41 56 310 2125, e-mail: hendrik.schulenburg@psi.ch

During PEFC operation the Pt surface area of the cathode may shrink. Pt particle growth, platinum dissolution and re-deposition are responsible for the decrease. To compensate for these losses, catalyst layers are prepared using an excess of platinum, which is the main cost driver in PEFCs. For a systematic improvement of catalyst layers it would be helpful to quantify the different loss mechanisms. The Pt particle growth can be followed using transmission electron microscopy. Harder to access are Pt losses, due to metal dissolution and deposition in the membrane. Platinum oxidizes to  $\text{Pt}^{2+}$  or  $\text{Pt}^{4+}$ , diffuses into the membrane, and is reduced by crossover hydrogen from the anode compartment. A semiquantitative estimation of the deposited Pt is possible using energy dispersive X-ray spectroscopy (EDX) [1]. We developed a TEM section method to quantify Pt losses in the membrane.

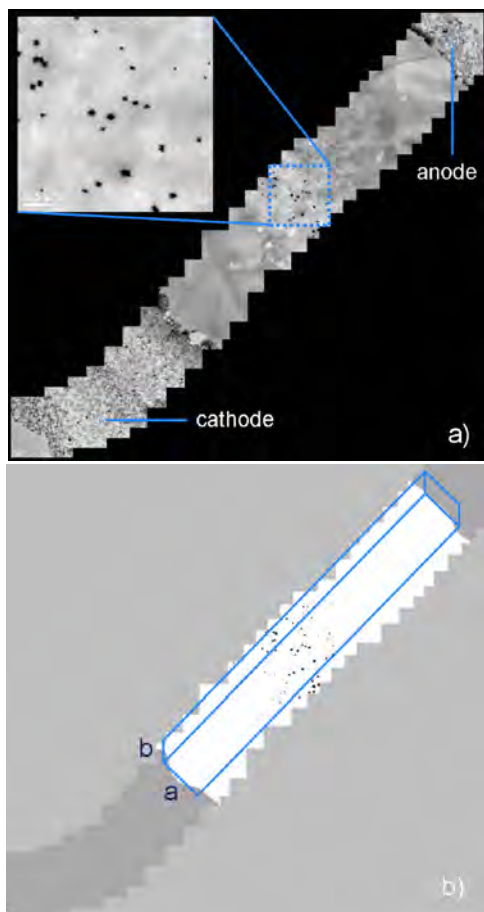


**Figure 1.** Stacked TEM images of a degraded catalyst coated membrane (a) and segmented image (b).

### Experimental

A commercial catalyst coated membrane (Gore PRIMEA, cathode loading  $0.4 \text{ mg}_{\text{Pt}}/\text{cm}^2$ ) was used. Degradation was carried out by square wave potential cycling of the cathode between open circuit potential

and 0.6 V. The potential was cycled a total of 24 000 times, at a time step of 10 s for each potential. Fully humidified  $\text{H}_2$  and  $\text{O}_2$  at a stoichiometry of 1.5/1.5 were

used at  $80^\circ\text{C}$ . The degraded CCM was embedded in an epoxy resin and cut with a Reichert-Jung Ultracut E microtome. TEM sections with a defined thickness (200 nm) were analyzed with a Phillips CM12 microscope operating at an acceleration voltage of 120 kV. TEM images of the CCMs were stitched to obtain complete cross sections (Figure 1a). Stacked images were segmented using Avizo Standard 5.1 Software (VSG, USA) (Figure 1b).

### Results

The oxidized and deposited Pt forms a band like structure in the membrane [1]. TEM images show the black Pt nanoparticles in the membrane (Figure 1a). After segmentation the Pt particles appear black and the membrane white. A cuboid in the segmented image is defined (Figure 1b) and the number and diameter of the Pt particles are counted using Avizo software. Assuming a spherical particle size of the deposited Pt particles the Pt mass in the cuboid can be calculated and related to the geometrical electrode area ( $63 \pm 12 \mu\text{g}_{\text{Pt}}/\text{cm}^2$ ). The geometric electrode area is given by the product  $a \cdot b$ , where  $a$  is obtained from the stitched TEM image and  $b$  is the thickness of the microtome section (Figure 1b).

After measuring the TEM Pt particle size before ( $2.3 \pm 0.9 \text{ nm}$ ) and after degradation ( $4.8 \pm 2.5 \text{ nm}$ ) the surface area loss mechanisms can be quantified (Figure 2). Due to dissolution and deposition of Pt in the membrane, 16% of the initial Pt surface area is lost. Particle growth is the main degradation process, which causes 44% surface area loss. At end of life 60% of the initial Pt surface area is lost.

To sum up, TEM sectioning allows the quantification of the Pt mass and surface area loss in the membrane which is a key for discrimination of different loss mechanism.

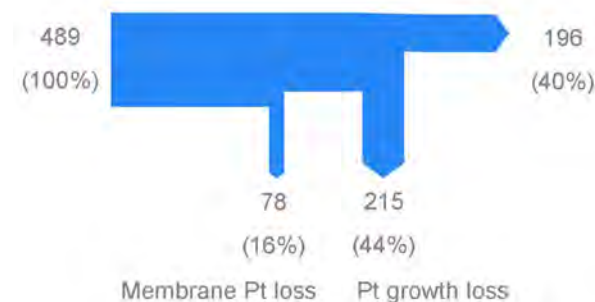


**Figure 2.** Pt surface area losses of a PEFC cathode caused by potential cycling (see experimental). TEM based surface areas given in  $\text{cm}^2_{\text{Pt}}/\text{cm}^2_{\text{geo}}$  and in percent.

### Reference

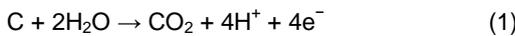
- [1] W. Bi, G.E. Gray, T.F. Fuller, *Electrochem. Solid-State Lett.* **10**, B101-B104 (2007).

# 3D imaging of catalyst support corrosion in PEFCs

H. Schulenburg, B. Schwanitz, J. Krbanjevic, N. Linse

phone: +41 56 310 2125, e-mail: hendrik.schulenburg@psi.ch

Carbon-supported Pt nanoparticles are the catalyst of choice in polymer electrolyte fuel cells (PEFCs). Especially under dynamic operating conditions, PEFC performance can deteriorate rapidly, which is one of the reasons why PEFC technology has not been introduced into the mass market, e.g., for automotive applications. Generally, two main degradation processes can be distinguished with respect to catalyst deterioration. First, sintering, dissolution, and deposition of platinum can reduce the electrochemically active Pt surface area (ECA). Second, corrosion of the carbon support (cf. Equation 1) may lead to particle detachment and porosity changes of the catalyst layer.



The pore structure of the cathode catalyst layer is critical to transport oxygen to active sites and removal of product water. Therefore, carbon corrosion can contribute to fuel cell performance loss. Both processes, loss of active Pt surface area and carbon support corrosion, are strongly promoted by elevated potentials (> 1 V) and fast potential transients. Quantification and visualization of the different degradation effects is crucial for a systematic improvement of catalyst layers. In this work, focused ion beam/scanning electron microscopy (FIB/SEM) was employed to study morphological changes in the catalyst layer. For PEFC degradation experiments, catalyst-coated membranes (CCMs) were subjected to two different degradation protocols.

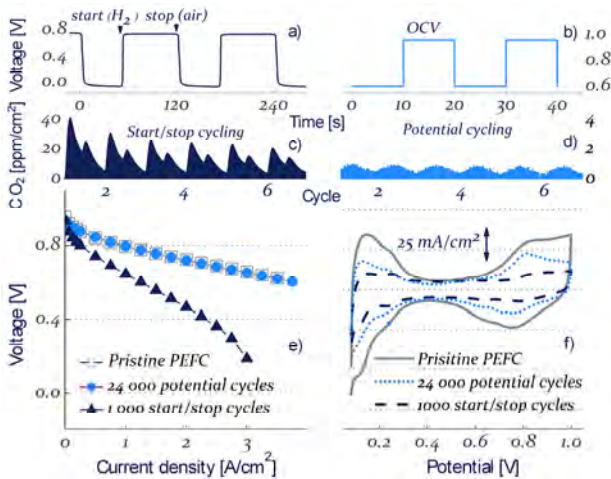


**Figure 1.** a) PEFC catalyst degradation protocols for start/stop cycling, anode alternately purged with H<sub>2</sub> and air (60s/60s), cathode purged with air, external load 3 mΩcm<sup>2</sup>, 80 °C, 70 % relative humidity (RH), 1000 cycles. b) degradation protocol for potential cycling between 0.6 V and open circuit voltage, time step 10 s, H<sub>2</sub>/O<sub>2</sub> at ambient pressure and 1.5/1.5 stoichiometry, 100% RH, 80 °C, 24 000 cycles; c) CO<sub>2</sub> concentration measured in the cathode exhaust during start/stop cycling and d) potential cycling. e) fuel cell performance at 80 °C, 100 % RH, H<sub>2</sub>/O<sub>2</sub> = 1.5/1.5 at 2.5 bar<sub>abs.</sub>; d) cyclic voltammograms measured in H<sub>2</sub>/N<sub>2</sub> mode, 80 °C, 100 mV/s, 2.5 bar<sub>abs.</sub>

## Results

Start/stop cycling of the PEFC was performed by alternating purge of the anode compartment with hydrogen and air. In a second experiment, a cell was cycled between 0.6 V and open circuit voltage (OCV) (Figure 1a, b).

	Pristine	Potential cycling <sup>a</sup>	Start/stop cycling <sup>a</sup>
Cell voltage at 1A/cm <sup>2</sup> [mV]	794	796	643
H <sub>upd</sub> surface area [m <sup>2</sup> /g <sub>Pt</sub> ]	57	14	9
Mean Pt particle size <sup>b</sup> [nm]	2.3	4.8	5.3
CO <sub>2</sub> evolution [ppm/cycle]	-	0.04	1.85
Overall porosity <sup>c</sup> [%]	40	38	5
Closed porosity <sup>c</sup> [%]	0	0	3

**Table 1.** Degradation of the PEFC cathode catalyst layer <sup>a</sup>degradation protocol cf. Figure 1, <sup>b</sup>determined by TEM, <sup>c</sup>determined by FIB/SEM.

Cell performance measured in H<sub>2</sub>/O<sub>2</sub> mode before and after the degradation experiments is displayed in Figure 1e. After 24 000 potential cycles, PEFC performance is almost unchanged. On the other hand, a distinct performance loss was observed after 1 000 start/stop cycles, especially at higher current densities.

Despite of the strongly differing performance loss rates, both degradation experiments lead to comparable Pt particle growth and loss of electrochemically active Pt area (Figure 1f and Table 1). The ECA loss alone is therefore unlikely to be responsible for performance deterioration in the case of start/stop cycling. The pronounced performance loss at high current densities indicates increased mass transport losses, caused by carbon corrosion-induced porosity changes.

Corrosion of the carbon support material can be assessed by measuring the CO<sub>2</sub> concentration in the cathode exhaust gas (cf. Equation 1). In case of potential cycling, the potential at the positive electrode never exceeds the open circuit voltage of about 960 mV and CO<sub>2</sub> evolution is very low (Figure 1d). During start/stop cycling of the cell, however, the positive electrode is exposed to potentials significantly higher than 1 V. These elevated potentials lead to a strong intensification of carbon corrosion during start-up and shut-down, which results in two CO<sub>2</sub> peaks per cycle (Figure 1c).

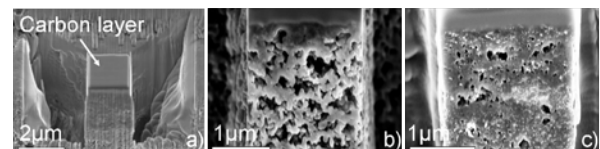


**Figure 2.** a) PEFC cathode catalyst layer before degradation; dissected columnar volume of interest b) SEM image taken during FIB/SEM serial sectioning of the pristine cathode catalyst layer, c) SEM image after start/stop degradation.

To determine porosity changes caused by corrosion of the carbon support, the pristine and degraded cathodes were investigated by FIB/SEM serial sectioning [1,2]. Repeated FIB sectioning and SEM imaging leads to a set of several hundred images. First, SEM parameters, including detector type and acceleration voltage, were optimized to obtain the highest possible resolution with a minimum depth of focus. Second, we assigned appropriate ranges of bright gray to "material" and darker gray to "pores" by visual inspection. This assignment, however, is not unambiguous in all cases. Regions possessing similar gray scale values may be located at different positions in the z-direction, where z represents the depth of the volume of interest.

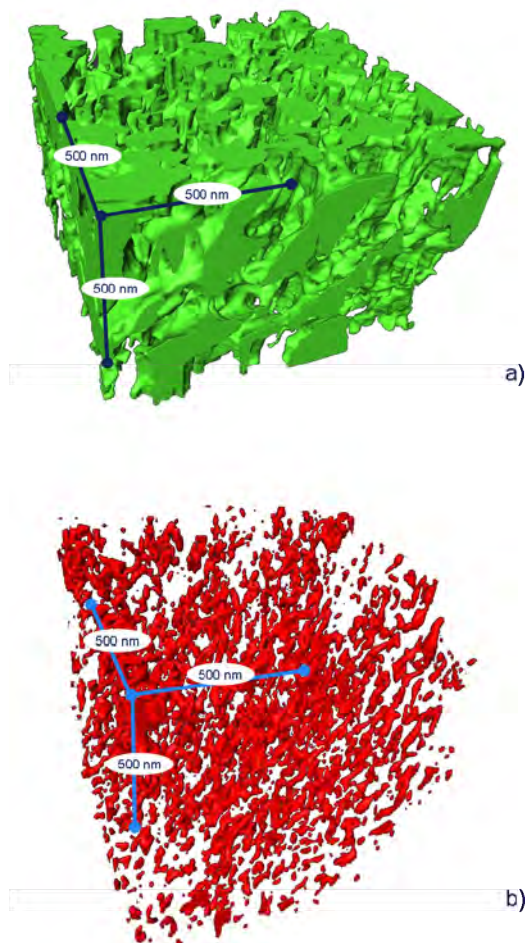


**Figure 3.** Three-dimensional pore structure of the pristine cathode catalyst layer a) and after start/stop cycling b).

To correct for this effect, successive images were analyzed to determine if the shape of the material region changes or not. If changes were detected, the respective region was assumed to be located at the machined surface and is therefore assigned as "material". If the shape of the inspected material does not change in successive images, the material is obviously not in, but below the machined surface. Therefore, those regions were assigned as "pores". The whole set of images is segmented in this way.

The three-dimensional pore structure of the cathode catalyst layer before and after start/stop cycling is shown in Figure 3. A typical voxel size in these images is  $2.5 \times 2.5 \times 10 \text{ nm}^3$  in the x, y, and z-directions. This voxel size allows for imaging of the majority of the pore volume, although micropores ( $< 2 \text{ nm}$ ) such as in carbon black primary particles, cannot be resolved.

The pore structures of the pristine and the potential cycled catalyst layers do not exhibit significant differences. In both cases, the pores form an interconnected network with a calculated porosity of around 40 % (Table 1). In contrast to potential cycling, the morphology strongly changes after start/stop induced degradation. As a result of severe carbon corrosion, the calculated porosity drops to 5 %. The average pore size strongly decreases and the previously interconnected pore network changes to a structure of predominantly isolated pores. In the pristine catalysts and after potential cycling, no isolated pores can be detected, whereas 60 % of the pore volume is not interconnected after start/stop cycling.

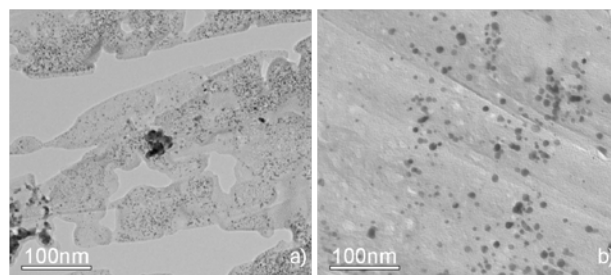


**Figure 4.** TEM micrographs of TEM lamellae, a) a pristine catalyst layer, b) after start/stop degradation

TEM lamella images of the pristine catalyst layer (Figure 4a) show the expected highly porous carbon support structure, which is also observed after potential cycling. After start/stop cycling (Figure 4b), the carbon support looks like a dense film. Platinum particles seem to be embedded in a carbon matrix. Bright round shapes with a typical diameter of  $< 50 \text{ nm}$  may be assigned to pores, which were detected in the corresponding 3D image (Figure 3b). Although start/stop induced porosity changes are drastic, carbon loss, which was calculated from the total amount of  $\text{CO}_2$  generated over the course of the experiment, is relatively low ( $\sim 8\%$ ). This finding suggests a collapse of the porous structure, caused by corrosion-induced weakening of the connections between single carbon primary particles [2].

To summarize, potential cycling and start/stop cycling leads to a comparable loss of the active Pt surface area in the cathode catalyst layers. Despite this surface area loss, the potential cycled cathode still provides enough accessible active sites for oxygen reduction. Almost no fuel cell performance loss is observed. In contrast to potential cycling, start/stop cycling causes significant corrosion of the carbon support. The resulting decrease in porosity of the corroded carbon support hinders mass transport in the cathode, leading to severe fuel cell performance loss. FIB/SEM serial sectioning and TEM lamellae prepared by FIB/SEM allow for quantifying and visualizing these porosity changes. The calculated 3D images and porosity values are a prerequisite to understand and model mass transport in catalyst layers.

## References

- [1] H. Schulenburg, B. Schwanitz, J. Krbanjevic, N. Linse, R. Mokso, M. Stampanoni, A. Wokaun, G.G. Scherer, *ECS Trans.* **33**, 1471-1481 (2010).
- [2] Z.Y. Liu, J.L. Zhang, P.T. Yu, J.X. Zhang, R. Makharia, K.L. More, E.A. Stach, *J. Electrochem. Soc.* **157**, B906-B913 (2010).

# A novel approach for a 1D-model for PEFC

M. Zaglio, A. Wokaun, J. Mantzaras, F.N. Büchi

phone: +41 56 310 5165, e-mail: maurizio.zaglio@psi.ch

The dynamic behavior of polymer electrolyte fuel cells (PEFC) is of importance for the automotive application, where rapid variation of loads must be satisfied. Models at the cell level are required to investigate the dynamic interactions of the fundamental processes, and the resultant loss mechanisms in dependence of the distribution of species and temperature.

Previously the transient behavior on the level of a differential cell has been investigated with a 1D model in the through-the-MEA direction and the most sensitive parameters have been determined with an optimization procedure based on an Evolutionary Algorithm. The 1D model predicts the transient cell potential behavior following a stepwise increase in load, at different humidity conditions, in a time range spanning from about 2s after the load change to the new steady-state. However a discrepancy between experiments and calculations is observed in the first hundreds of ms. Transport of species is considerably different in the channel and rib domains of the cell. Thus a model is developed conserving the formal 1D character, but taking into account the different properties of the two domains.

## Model

The model takes into account the channel and the rib as separate parallel domains in the through-the-MEA direction,  $z$ - in Figure 1, and will thereafter be referred to as  $1D^2$ . The gas path under the rib is longer than under the channel, and liquid phase may accumulate under the rib, with a path-length equal to that of the channel. The model incorporates multispecies, multiphase diffusion of species, transport of water through the membrane by diffusion and electro-osmotic drag, heat generation and transport in the cross section of the cell, and the electrochemical reaction in the catalyst layer. The current density distribution is calculated under the assumption of isopotential flow field plates, adjusting at each iteration the local current density to meet an equal potential in both domains. Further, the current profile is levelled to meet the total current. The new current density distribution is used at the next iteration to calculate the new sink/source terms and the new properties distribution in the different domains.

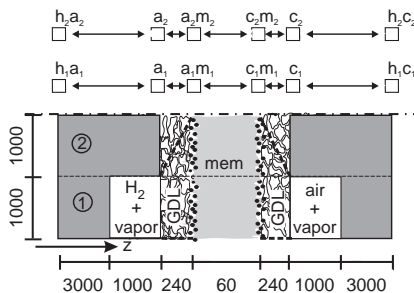


**Figure 1.** 1+1D PEFC model domains and discretization: subscript 1 refers to the domain under the channel, 2 under the rib, - - - is the symmetry axis, - - the gas path. Size in  $\mu\text{m}$ .

## Results

The experiments (from differential cell) are compared to the 1D and  $1D^2$  model calculations (see Figure 2a-b) for the operating condition summarized in Table 1. It is clear in logarithmic scale, Figure 2b, that the discrepancy in the first ms after the load change is reduced when using the  $1D^2$  model. In fact the gas transport is initially mainly responsible for the cell dynamic, and the longer path under the rib increases the concentration overpotential (see Figure 2c). At longer times, the rehydration of the membrane due to the higher water production and to the water back diffusion from anode to cathode induces a partial recovering of the potential, until the new steady state is reached after approximately 50s. Figure 2d shows the current density distribution between the two domains. Due to the water accumulating under the rib, at this operating condition the membrane is better humidified under the rib, thus the ohmic overpotential is lower and therefore the current density is higher. After the stepwise increase in load, the concentration overpotential under the rib increases. According to this, the current behavior shows an overshoot under the rib, and the new steady state is then smoothly reached in around 50s.

Temperature gas inlets	70°C
Pressure gas inlets	1.5 bar
Inlets relative humidity, an / cat	0.3 / 0.3
Current jump at $t = 0$	0.3 $\rightarrow$ 0.8 $\text{Acm}^{-2}$

**Table 1.** Operating conditions related to experiments and calculations shown in Figure 2.

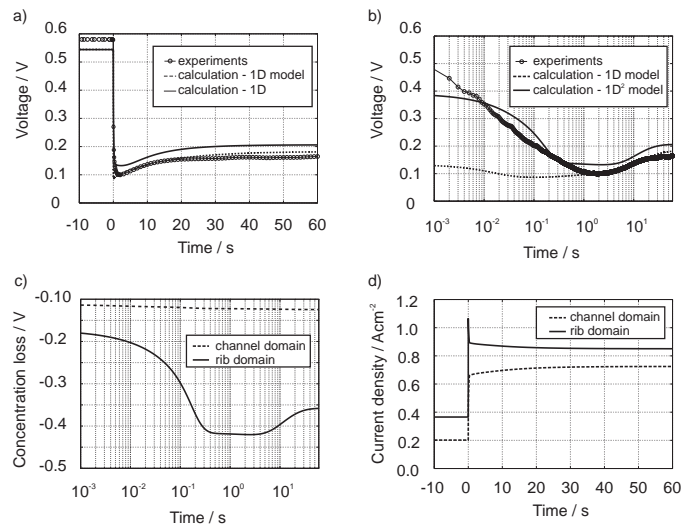


**Figure 2.** Comparison between experiments and simulations: a) cell potential response in time, linear scale; b) logarithmic scale; c) concentration overpotential calculated by the  $1D^2$  model; d) current density distribution calculated by the  $1D^2$  model.

## Development of *in situ* X-ray tomographic microscopy for PEFC

J. Eller, F. Marone, M. Stamanoni, A. Wokaun, F.N. Büchi

phone: +41 56 310 4580, e-mail: jens.eller@psi.ch

*In situ* X-ray tomographic microscopy (XTM) allows visualizing the liquid water in the gas diffusion layer (GDL) of operating polymer electrolyte fuel cells (PEFC). On the one hand experiments at the TOMCAT micro-tomography beam line of the Swiss Light Source (SLS) have been further developed by introducing single channel flow field designs, and on the other hand a process work flow allowing the separation of liquid, solid, and gas phase has been established, enabling 3D quantification of liquid water in the GDL materials.

### Experimental

Two new PEFC sample holder designs for in-situ XTM investigations were introduced in 2010. The cells can be heated by small electrical heating pads. Gas humidification at room temperature was realized by small bubblers adapted to the gas flows of 0.5 to 100 ml/min. Both XTM cells were designed such that the regions of interest completely fits into the field of view of the 4x objective ( $3.8 \times 3.8 \text{ mm}^2$ ) of the XTM microscope or reduce the material outside the field of view to a minimum. While the horizontal cell (Figure 1, left) with horizontally aligned MEA has only a short linear flow field channel of only 2.3 mm, the vertical cell (Figure 1, right) with vertically aligned MEA allowed to realize a much longer channel of 13.4 mm to achieve fluid dynamic conditions closer to technical cells. Both cells were using a single channel flow field made of graphite with 0.8 mm channel width and 0.3 mm channel depth.

All presented tomographic and post-processing results are based on XTM scans (see Figure 2) of the same vertical cell using Umicore H200 catalyst coated membrane (CCM) and Toray T060 GDLs with 20% PTFE. The wet data scan was the first in-situ XTM scan of this cell, so biasing of the measurement by the XTM itself can be excluded. Fuel cell operation conditions were:  $i=0.5 \text{ A/cm}$ ,  $T=40 \text{ C}$ ,  $\lambda_{\text{O}_2} = \lambda_{\text{H}_2} = 10.5$ , gases humidified at room temperature. Beam energy was 13.5 keV, 1001 projections, 200 ms exposure time, 3 minutes total scan time. Since the anode was almost

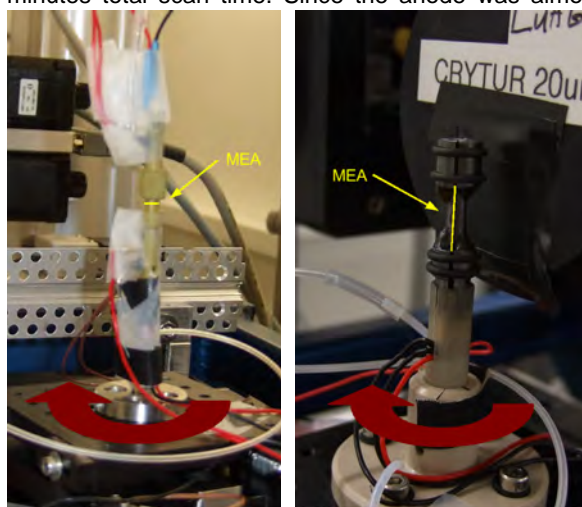


**Figure 1.** Left) XTM PEFC cell on TOMCAT sample stage with horizontally aligned MEA (left) and with vertically aligned MEA (right). The position of the MEAs is highlighted in yellow. Both images are taken from [1].

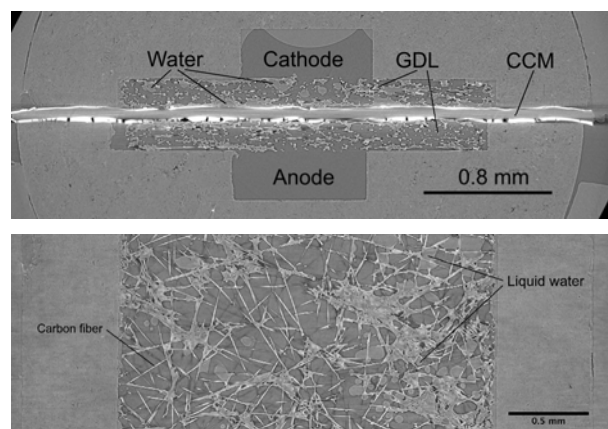


**Figure 2.** Tomographic reconstructions of in-situ XTM of the vertical cell. The GDL carbon fibers can be distinguished from the void pore space, flow field material, catalyst layer, membrane and liquid water. Top) Through-plane cut. Bottom) In-plane cut through cathode GDL.

completely dry, later only the cathode side is shown (e.g. Figure 3).

### Results

The quantification of structures and liquid water in the fine structure of the GDL in the 3D XTM data sets is a challenging task because of low contrast and overlapping in the gray scale values of the different phases. For a satisfying quantification of liquid water, a segmentation method is needed, which precisely labels the voxels representing liquid water as the liquid phase in the XTM data. Mismatched voxels would alter any further analysis and prevent accurate visual representation of the 3D data sets, which is itself a powerful tool.

A workflow based on comparison of dry and wet GDL structures was developed addressing this problem.

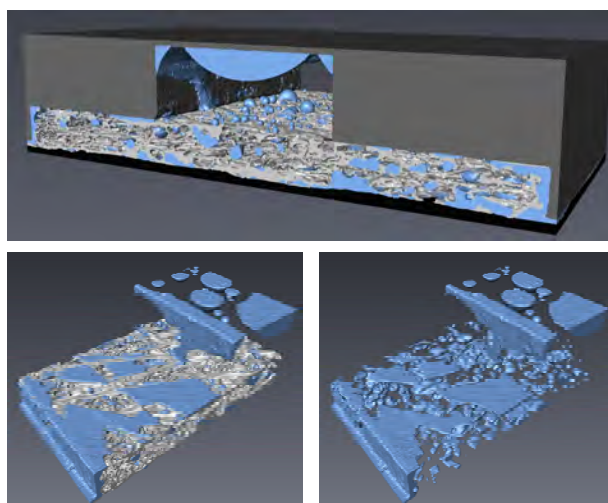


**Figure 3.** Surface rendering of the segmented XTM data of a 1.2 mm long cathode section of the vertical cell design (top). The segmentation of the different material phases allows to virtually remove the different fuel cell components: GDL and liquid water (bottom left), liquid water only (bottom right).

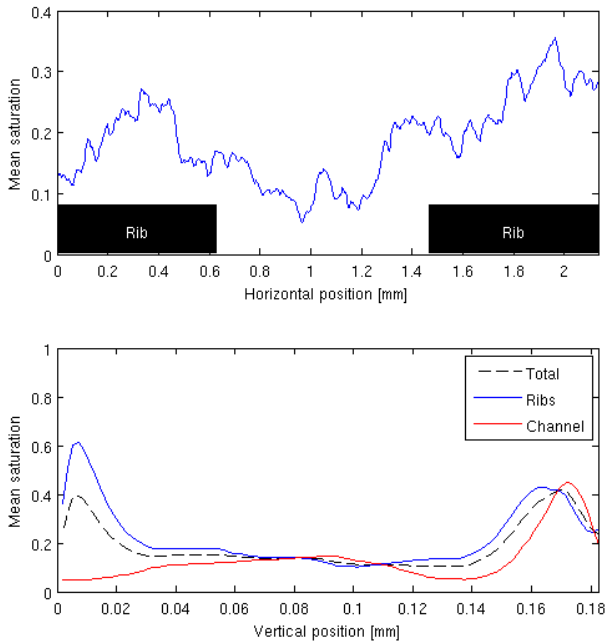


**Figure 4.** Water saturation in the GDL domain without boundary effects. Top: Mean vertical water saturation profile. Bottom: Mean horizontal water saturation profile.

After a precise alignment, subtraction of a XTM data set of a dry cell from the corresponding wet cell XTM data provides satisfying contrast to identify the liquid phase. Thereafter, the solid and the void phase can be segmented by thresholding. The result of this workflow allows the quantification and visualization of liquid water in the GDL and flow field channel, as shown in Figure 3. Nevertheless, XTM fails to provide contrast between the carbon fibers and the PTFE wet proofing layer.

Summing up the labeled water voxels along the flow field channel GDL saturations in different orientations and domains can be calculated (see Figure 4). The mean vertical saturation profiles show that, under the ribs the saturation is higher at the GDL-rib interface (0.6) than at the GDL-catalyst layer (0.4). Under the channel saturation higher than 0.2 is only reached close to the GDL-catalyst layer interface (0.4). Due to the short channel section of the data set, the mean horizontal saturation profile is noisier, but the minimum saturation can be also found under the flow field channel.

Furthermore, the size of the water clusters can be analyzed as shown in Figure 5, where different categories of water clusters are rendered in different colors or as histogram plots of water accumulated in different water cluster size categories (see Figure 6). The data in the histogram shows that droplet sizes well

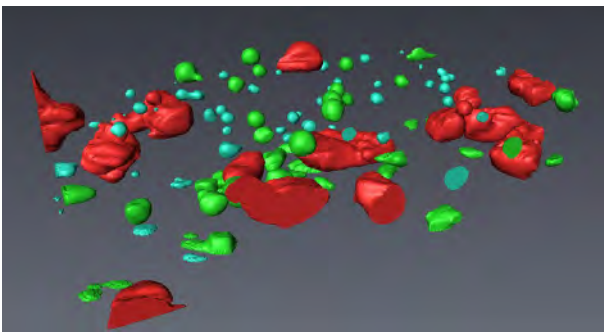


**Figure 5.** Water clusters of subsample of data set of Figure 3 colored according to different cluster size categories.

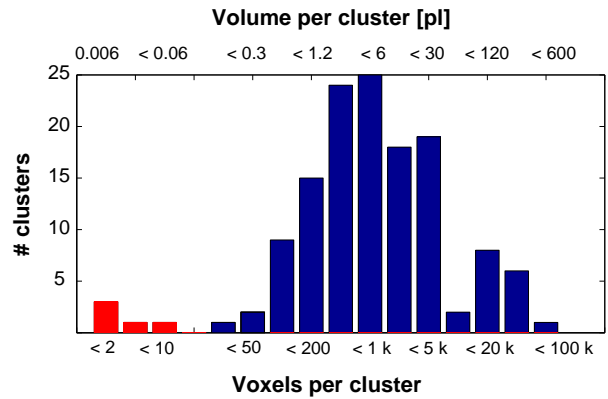


**Figure 6.** Histogram of water cluster sizes of sample shown in Figure 5.

below 1 pl can be clearly identified. The very small volumes with less than 20 voxels (red bars) are considered segmentation artifacts. The size of the maximum number of droplets (3 – 6 pl) corresponds approximately to the average pore size of the GDL.

### Radiation damage

The influence of high intensity synchrotron radiation (SR) during *in situ* PEFC synchrotron imaging experiments was so far not investigated or reported. During the in-situ XTM experiments loss in cell voltage at constant current operation was observed for both cell designs. After a beam exposure of about 80 minutes at 13.5keV or 11 keV beam energy, even holes and cracks in the membrane of the vertical design were found. During cell disassembly after such long exposure times, the membrane was found obviously damaged in the domains of SR exposure and showed brittle behavior. This change in material properties was also found for other samples with similar radiation exposure.

Besides our observations, General Motors [2] had reported about much more dramatic performance degradation during in-situ XTM scans of a similar horizontal PEFC design.

The major conclusion of all these observations is the necessity to expose the entire electrochemical active domain during the imaging experiments; otherwise cell performance degradation is compensated by non-irradiated domains and can not be detected by monitoring cell voltage and current.

The influence of the synchrotron X-ray radiation on fuel cell performance and components is subject of ongoing investigations, but still a precise maximum radiation dose, uncritical for the PEFC, is unknown.

### References

- [1] F.N. Büchi, J. Eller, F. Marone, M. Stampanoni, ECS Trans. **33**, 1397-1406 (2010).
- [2] A. Schneider, C. Wieser, J. Roth, L. Helfen, J. Power Sources, **195** (19), 6349 – 6355 (2010).

# A new fuel cell / battery hybrid concept for automotive applications

J. Bernard, M. Hofer, U. Hannesen<sup>1</sup>, A. Toth<sup>2</sup>, A. Tsukada, F.N. Büchi, P. Dietrich

phone: +41 56 310 5588, e-mail: jerome.bernard@psi.ch

In this new hybrid concept, the fuel cell is directly electrically coupled to the battery without the use of any power converter. Nevertheless it is possible to control the fuel cell power by adjusting its operating pressure, and thus the power sharing between the fuel cell and the battery stays actively controlled. This concept, referred to as passive hybrid topology, shows promising simulations results. Without the power converter, the hybrid system becomes simpler, lighter and cheaper.

## Introduction

In a fuel cell hybrid vehicle [1], the average power demand is fulfilled by a polymer electrolyte fuel cell (PEFC) system which converts hydrogen and oxygen into electrical power with only water and heat as byproducts. The transient power demand is fulfilled by a battery which is usually used in charge sustaining mode, i.e. the state of charge evolves around a prescribed value and no external charger is used. The PEFC system is traditionally coupled to the power bus with a DC/DC boost converter to match the battery voltage (Figure 1).

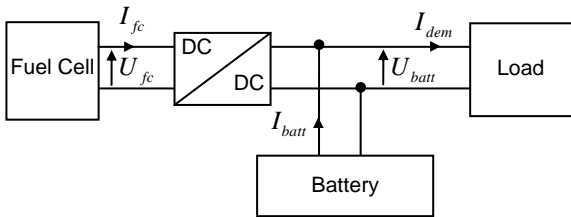


Figure 1. Active fuel cell/battery hybrid topology.

In a passive hybrid architecture (Figure 2), the fuel cell and the battery are directly connected to the bus without power converter(s). Therefore the two devices operate at the same voltage, which brings several constraints. The bus voltage and the currents regulate themselves according to the impedance of the fuel cell system and the battery, which means that the system variables (currents, voltage, powers, state of charge) are uncontrolled (no power management strategy is possible) and can therefore reach or exceed their limits, leading eventually to a system breakdown.

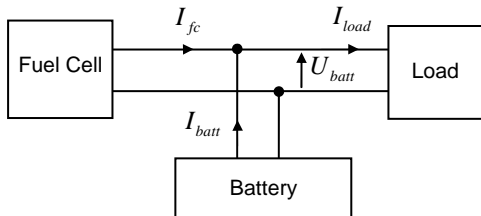


Figure 2. Passive fuel cell/battery hybrid topology.

The active hybrid architecture (Figure 1) has been established as the standard topology. However a passive hybrid topology can become a suitable solution for powertrain applications when the power sharing can be actively controlled [2]. This is achieved by controlling the gas pressure of the fuel cell, which varies its internal impedance. Since there are no DC/DC

converters, the passive hybrid is the cheaper and simpler solution, and the power losses in the electronic hardware are eliminated.

## Fuel cell system power control

The polarization curve describes the electrical characteristic of a fuel cell (Figure 3). This curve is pressure and temperature dependent. At constant temperature and voltage, the fuel cell current decreases when decreasing the gas pressures. This means that the current of a fuel cell system operating at constant voltage can be adjusted by the pressure: the minimum pressure gives the minimum current and the maximum pressure the maximum current.

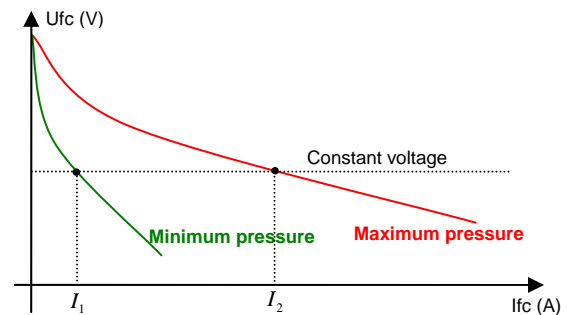


Figure 3. Example of polarization curves of a fuel cell stack at different operating pressures.

Figure 5 shows experimental results obtained with a 10kW H<sub>2</sub>/O<sub>2</sub> fuel cell stack [3-4] operated in a laboratory testbench. The load connected to the FC stack operated at a constant voltage of 50V. Until t=5s, the FC pressure (cathode and anode pressures) is nominal and the corresponding current is 85A. Then between t=5s and t=20s, the FC pressure is reduced from 100% to 30% of the nominal value, which concomitantly decreases the FC current from 85A to near 13A.

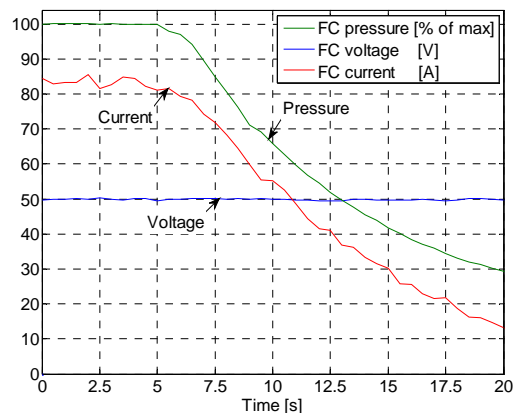


Figure 4. Current and pressure variation with a PEFC system operating at constant voltage.

This proves that the fuel cell current can be actively controlled in a passive hybrid topology where the battery operates at a nearly constant voltage.

<sup>1</sup> Belenos Clean Power Holding, Bienne

<sup>2</sup> Swatch Group, Bienne

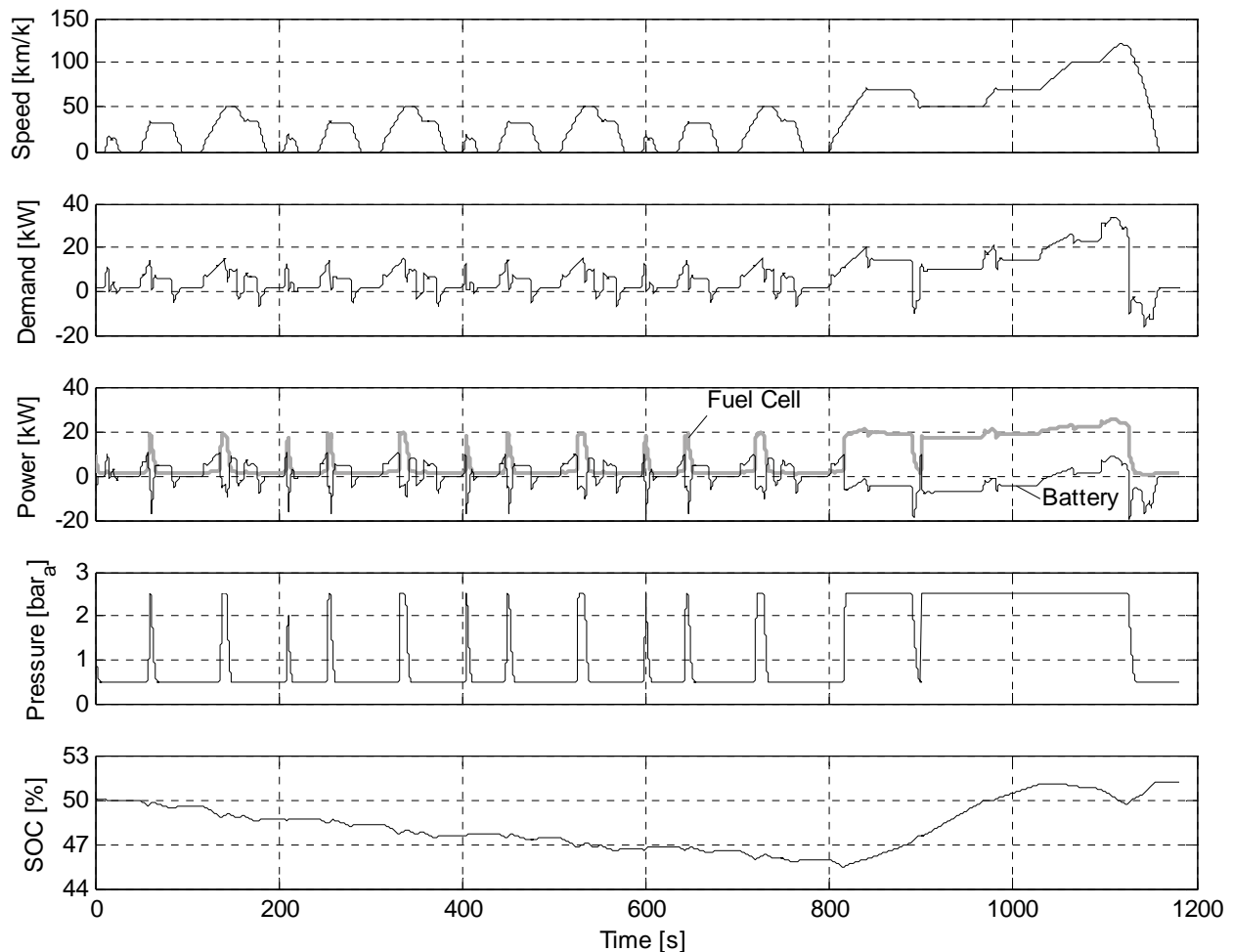


Figure 5. Simulation of the passive hybrid powertrain for the NEDCdrd driving cycle.

### Powertrain simulation

Based on the passive hybrid principle described in the previous section, a fuel cell hybrid model was built using the Matlab/Simulink software. The fuel cell sub-model is steady state fitted with real experimental data. The battery sub-model is a classical equivalent model with a voltage source in series with a resistor. The battery parameters are based on the SAFT VL 34P Li-ion cell. The power demand imposed to the hybrid source (FC+battery) is calculated with an energetic model of a car driving a defined speed cycle. The vehicle considered is a light passenger car of 1100 kg propelled by a 60kW electric motor.

A simulation result is given Figure 5 for the NEDC driving cycle. The power of the e-motor is fulfilled by the fuel cell passive hybrid power source. When the power demand becomes too important for the battery alone, or when the battery discharges fast, the FC power increases by increasing its pressure. This guarantees the sustainability of the state of charge and the fulfillment of the power demand.

### Conclusion

A fuel cell passive hybrid power source can be a practicable solution for powertrain application when the power sharing is actively controlled. Here the fuel cell power is adjusted by controlling the fuel cell pressure. Eliminating the DC/DC converters makes the system easier, lighter, smaller, and the power losses in the hardware are reduced. Because the power converter is removed, it is important to define carefully the battery

and fuel cell parameters in order that both devices operate in a matched voltage range.

Current works are devoted to experimental validations. A fuel cell and a battery of practical size for automotive application are currently under development. Laboratory experiments should provide additional evidences about the feasibility of the concept.

### Acknowledgment

The present research work has been supported by the Belenos Clean Power Holding. The authors gratefully acknowledge the support.

### References

- [1] A. Emadi, K. Rajashekara, S. Williamson, S. Lukic, IEEE Transaction on Vehicular Technology **54**, 763-770 (2005).
- [2] J. Bernard, M. Hofer, U. Hannesen, A. Toth, A. Tsukada, F. Büchi, P. Dietrich, IEEE VPPC'10, Lille (FR), 2010.
- [3] F.N. Büchi, G. Paganelli, P. Dietrich, D. Laurent, A. Tsukada, P. Varenne, A. Delfino, R. Kötz, S.A. Freunberger, P.A. Magne, D. Walser, D. Olsommer, Fuel cell **7**, 329-335 (2007).
- [4] F.N. Büchi, S.A. Freunberger, M. Reum, G. Paganelli, A. Tsukada, P. Dietrich, A. Delfino, Fuel Cells **7**, 159-164 (2007).

## Degradation of the gas separation in PEFCs characterized by local gas permeation analysis

S. Kreitmeier, A. Wokaun, F.N. Büchi

phone: +41 56 310 2127, e-mail: stefan.kreitmeier@psi.ch

In a PEFC the polymer electrolyte membrane fulfills three main functions: gas separation, electric insulation and proton conductivity. Different chemical and mechanical degradation mechanisms can cause a failure in these functions, which limit the lifetime of a fuel cell [1]. The degradation of the gas separation reduces the efficiency due to fuel leakage and is a critical safety issue, since hydrogen, permeating through the membrane, will accumulate in the air or oxygen atmosphere of the cathode. The limited lifetime arising from the degradation of the gas separation is one of the important end of life criteria in technical applications.

For studying the degradation of the gas separation the local gas transport characteristic of the membrane Nafion 211 is investigated by *in situ* gas phase analysis and morphological changes of the membrane are detected by X-ray Tomographic Microscopy. Adequate accelerated stress tests induce chemical and mechanical degradation of the gas separation and simulate fuel cell aging under dynamic operation.

### Experimental

Experiments are carried out with the gas analyzing setup, previously developed by G.A. Schuler [2]. The fuel cell has a linear flow field, an active area of 200 cm<sup>2</sup> and channel dimensions of 0.8 x 0.5 x 400 mm. Flow field plates are machined from Sigracet BMA5 (SGL Carbon) carbon plates. Electrochemical components used are Nafion NR211 membranes and Etek Elat (A6 STDSI V2.1) carbon cloth gas diffusion electrodes with a catalyst loading of 0.5 mg/cm<sup>2</sup>. For local gas analysis along the channel, 13 gas extracting ports are installed along the center channel of the linear cell. The gas is analyzed online by mass spectrometry. In order to analyze gas permeation through the membrane, helium (10 Vol. %) is added as tracer to the anode stream during operation and its permeate is analyzed in the cathode stream. By varying the pressure difference between anode and cathode it is also possible to distinguish between diffusive and convective gas transport through the membrane. Diffusive transport is characteristic for intact membranes or very small pores (<500 nm), while convective transport is found in membranes having pores >500 nm (pinholes). Hence, the convective gas transport is a measure for the presence of pinholes in the membrane. Membrane degradation is induced by 500 h accelerated stress tests, which are adopted from DoE protocols: OCV focuses on chemical membrane decomposition, rH cycling induces mechanical membrane degradation, OCV-load cycling and load cycling simulate fuel cell aging under dynamic operation.

### Results

Gas permeation is analyzed in terms of diffusive and convective gas transport. The gas diffusion through the membrane is the main gas transport initially. The diffusive gas crossover increases in Nafion 211 mainly due to mechanical degradation processes. Local humidity fluctuations cause membrane creeping and

crack formation, which results in an inhomogeneous increase in the diffusive gas transport, as shown in Figure 1A. In contrast, chemical degradation does not seem to change the diffusive gas permeation rate significantly. During the accelerated stress tests the convective gas transport increases more and more due to the formation of pinholes. It is the main gas transport after a few hundred hours. The convective gas transport, respectively, the formation of pinholes is strongly inhomogeneous in time and location, as shown in Figure 1B.

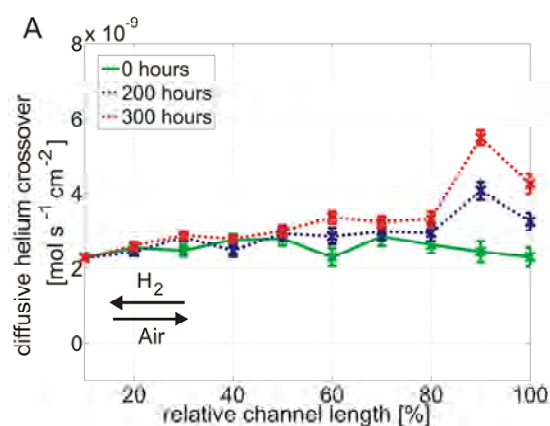


Figure 1A. The diffusive helium crossover along the center channel of the cathode at OCV-load cycling.

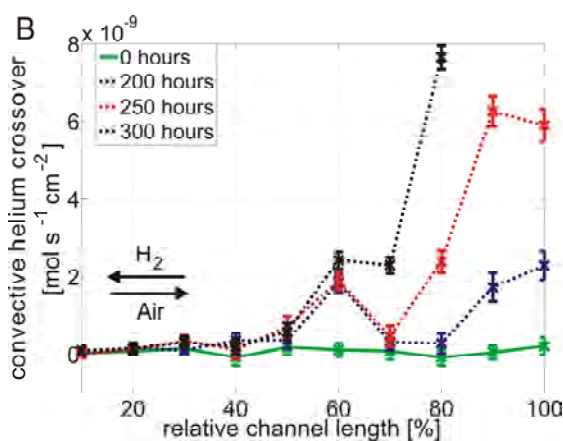
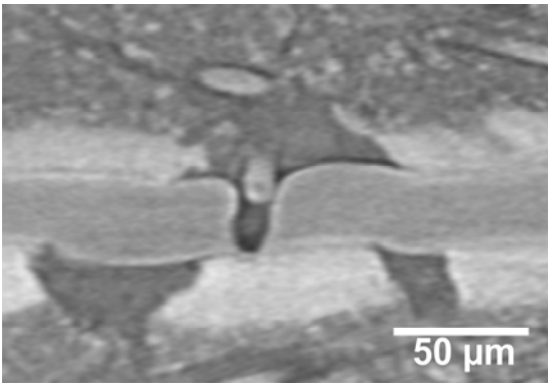
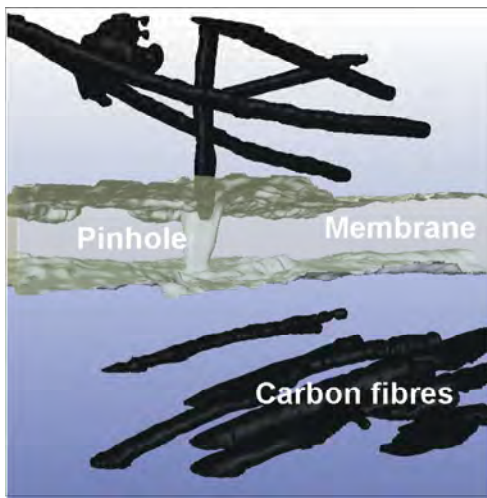


Figure 1B. The convective helium crossover along the center channel of the cathode at OCV-load cycling.

In combination with humidity fluctuations local triggers, such as sharp edges of the MPL and carbon fibers cause pinhole formation. They induce small cracks in the membrane which further evolve to pinholes with a diameter in the range of 1-10 μm. Figure 2A shows an X-ray tomogram of a pinhole found in the degraded membrane. The segmentation of this pinhole in Figure 2B visualizes the interaction between membrane and carbon fiber which may initiate pinhole formation.



**Figure 2A.** X-ray tomogram of a pinhole in the membrane found in the degraded MEA.



**Figure 2B.** 3D visualization of the pinhole. For clarity the catalyst layers of the MEA are removed.

So, mechanical degradation induced by local humidity fluctuations and the rough GDE material are the major sources for inhomogeneous pinhole formation in Nafion 211. Once pinholes have been generated, the hydrogen crossover increases which intensifies chemical membrane decomposition. Finally, both chemical and mechanical degradation processes are the reason for an exponential increase of the convective gas permeation. Therefore, for Nafion 211 the most critical degradation mechanism, causing a loss in gas separation, is pinhole formation.

#### References

- [1] A.B. La Conti, M. Hamdan, R.C. McDonald, Fuel Cell Technology and Applications, John Wiley and Sons **3**, 647-662 (2003).
- [2] G.A. Schuler, Diss. ETH, No. 18883, ETH Zürich (2010).

# BATTERIES & SUPERCAPACITORS

## MATERIALS



## Rate capability of graphite anodes in lithium-ion batteries

M. Hess, W. Märkle, P. Novák

phone: +41 56 310 2176, e-mail: michael.hess@psi.ch

Graphite is one of the most used anode materials of today's lithium-ion batteries. It has several advantages including safety, a low potential versus lithium metal, high coulombic efficiency, and a theoretical specific charge of 372 mAh/g.

For  $\text{LiFePO}_4$  cathodes, high rate capability of 400C has already been published [1]. Such fast cathodes require also fast anodes. Therefore, we investigated graphite with regard to its high rate capability. Previous results suggested that the diffusion coefficient of lithium in graphite should not limit the rates being approximately  $10^{-7}$  to  $10^{-6}$   $\text{cm}^2/\text{s}$  [2] but loading, electrode thickness, and porosity influence the possible rates significantly [3]. Therefore, we evaluated the maximum rates of these graphite electrodes for different thicknesses.

### Experimental

Thin electrodes have been prepared by a spray technique. A spray nozzle produced 1-5  $\mu\text{m}$  thick electrodes with a load of 0.07-0.09  $\text{mg}/\text{cm}^2$  of active material. For the rate tests a composition of 80:10:10 of graphite SFG6 (TIMCAL) : PVDF binder (Solvay) : Super P conductive filler (TIMCAL) was cycled in EC:DMC 1:1 with 1M  $\text{LiPF}_6$ .

For the GITT test, an electrode with 11-12  $\mu\text{m}$  thickness and 0.52  $\text{mg}/\text{cm}^2$  of active material was used. Standard electrodes have been prepared by doctor blade technique described in [3]. Figure 1 shows a SEM picture of a thin layer electrode of graphite where the copper current collector can be seen partially.



**Figure 1.** SEM picture of a typical graphite thin electrode, light gray: copper current collector, dark gray: graphite particles, SuperP has not been added for clarity

### Results

The main goal of this work was to investigate if graphite is limiting the charge/discharge process in lithium-ion batteries. Therefore, very thin electrodes of 1-5  $\mu\text{m}$  thickness have been prepared to suppress diffusion limitations within the pores of the porous electrodes. As depicted in Figure 1, the electrode consists of only one to two particle layers.

The charge and discharge curves of these thin electrodes at different rates are depicted in Figure 2. The charge rates are limited to a maximum of 5 C rate due to the increasing overpotential at higher rates which would lead to the risk of lithium plating which occurs at potentials negative to 0 V vs  $\text{Li}/\text{Li}^+$ . On the

other hand, the discharge rates with more than 80% galvanostatic capacity are possible up to 400 C rates. This would correspond to a full discharge in 9 seconds.

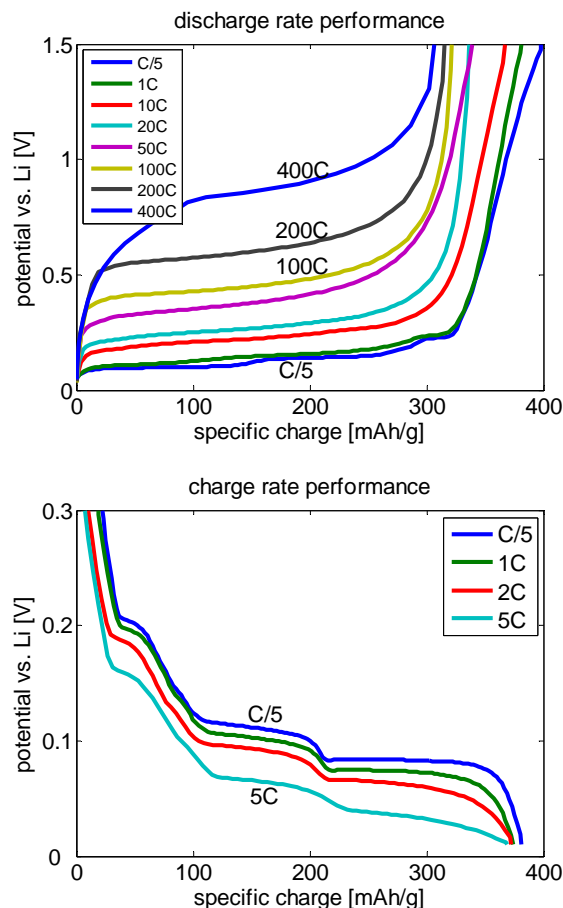


**Figure 2.** Graphite SFG6 cycled at different rates

In contrast to the thin electrodes in Figure 2, standard electrodes with thicknesses of 50  $\mu\text{m}$  can be discharged up to 20 C rates [3] and the charge process is limited to 2 C rates, respectively. This proves that graphite itself is a fast intercalation material and can be seen as the upper limit for rates in porous electrodes.

### References

- [1] B. Kang, G. Ceder, Nature Letters **458**, 190 (2009) .
- [2] K. Persson, V. A. Sethuraman, L.J. Hardwick, Y. Hinuma, Y.S. Meng, A. van der Ven, V. Srinivasan, R. Kostecki, G. Ceder, J. Phys. Chem. Lett. **1** (8), 1176 (2010).
- [3] H. Buqa, D. Goers, M. Holzapfel, M.E. Spahr, P. Novak, J. Electrochem. Soc. **152**, A474 (2005).

## Oxygen evolution from $\text{Li}_2\text{MnO}_3$ -stabilized $\text{Li}(\text{Ni}_x\text{Mn}_y\text{Co}_z)\text{O}_2$ electrode materials

H. Sommer, P. Lanz, M. Schulz-Dobrick, P. Novák

phone: +41 56 310 2457, e-mail: petr.novak@psi.ch

Electrodes for lithium-ion cells need to have stable structures over a wide potential range to maximize specific charge, energy and cycle life. Layered  $\text{LiMO}_2$  ( $M = \text{Mn}, \text{Ni}, \text{Co}$ ) structures tend to become unstable at high levels of delithiation because of the highly oxidizing nature of  $\text{Ni}^{4+}$  and  $\text{Co}^{4+}$ . Thackeray introduced high specific charge materials ( $> 200 \text{ Ah kg}^{-1}$ ) by stabilizing layered  $\text{LiMO}_2$  with  $\text{Li}_2\text{MnO}_3$ , thus forming a solid solution [1]. The small, insulating  $\text{Li}_2\text{MnO}_3$  regions stabilize the  $\text{LiMO}_2$  structure. Between 2.0 V and 4.4 V the  $\text{LiMO}_2$  component is electrochemically active; by contrast, the  $\text{Li}_2\text{MnO}_3$  component is electrochemically inactive. Electrochemical activation of  $\text{Li}_2\text{MnO}_3$  can be induced positive to 4.4 V vs.  $\text{Li}/\text{Li}^+$  and will afford an overall specific charge of about  $330 \text{ Ah kg}^{-1}$  during initial charging. In this potential range, a simultaneous extraction of lithium and oxygen ( $\text{Li}_2\text{O}$  removal) from the  $\text{Li}_2\text{MnO}_3$  component is suggested [2]. To determine the influence of the oxygen release, e.g., with regard to possible damage to the electrode surface, we applied *in situ* pressure and temperature measurements, DEMS, and combined them with electrochemical analyses.

### Experimental

Electrodes for electrochemical tests were prepared by casting a mixture of 84%  $\text{Li}_2\text{MnO}_3\text{-Li}(\text{Mn}_x\text{Ni}_y\text{Co}_z)\text{O}_2$  (BASF), 3% KS6, 6% Super P (both TIMCAL) and 7% binder (SOLEF PVDF 1015), all suspended in N-methyl-2-pyrrolidinone (Fluka), onto a Al foil. After drying, the electrodes ( $d=13 \text{ mm}^2$ ) were punched out and assembled in standard test cells, as described elsewhere [3]. The pressure measurement was performed in a cell with a diameter of 80 mm and a Honeywell sensor was used to follow the pressure in the cell during cycling. The electrodes for this experiment were prepared as described above. For the DEMS experiment the electrodes were prepared by blade-coating the oxide (mixture of 70%  $\text{Li}_2\text{MnO}_3\text{-Li}(\text{Mn}_x\text{Ni}_y\text{Co}_z)\text{O}_2$  (BASF), 10% Super P and 20% KynarFlex) and graphite (90% SFG44 (TIMCAL), 10% KynarFlex) directly onto the titanium body of the DEMS cell. The slurries were prepared in N-methyl-2-pyrrolidinone and, after casting, vacuum-dried overnight at  $120 \text{ }^\circ\text{C}$ . During the measurement, a constant stream of argon was run through the DEMS cell. The gas was transferred to the mass spectrometer via a capillary tube. The temperature measurement was carried out in a pouch cell, with a PT100 resistance thermometer assembled directly between the graphite electrode (SFG44) and the  $\text{Li}_2\text{MnO}_3\text{-Li}(\text{Mn}_x\text{Ni}_y\text{Co}_z)\text{O}_2$  electrode. For this experiment, the electrochemical cycling was conducted galvanostatically between 2.0 V and 4.7 V at a rate of C/2 and a temperature of  $36 \text{ }^\circ\text{C}$ .

### Results

First of all, the cycling stability of the  $\text{Li}_2\text{MnO}_3\text{-Li}(\text{Mn}_x\text{Ni}_y\text{Co}_z)\text{O}_2$  electrode was tested in a standard cell. Figure 1 shows the potential curve during the first, second and 50<sup>th</sup> galvanostatic cycle. Our high-performance material exhibits a reversible specific charge of about  $270 \text{ Ah kg}^{-1}$ , even after 50 cycles.

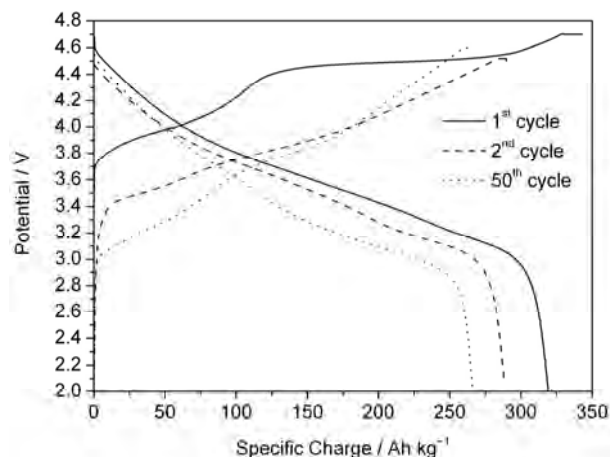


**Figure 1** Charge and discharge curves of  $\text{Li}_2\text{MnO}_3$ -stabilized  $\text{Li}(\text{Mn}_x\text{Ni}_y\text{Co}_z)\text{O}_2$  (1<sup>st</sup>, 2<sup>nd</sup> and 50<sup>th</sup> cycle).

The potential curve of the first cycle indicates a different behaviour from the subsequent ones. Therefore, the first cycles of the galvanostatic experiment were analyzed using differential plots of  $dQ/dE$  vs.  $E$  (Figure 2). At potentials around 4.5 V vs.  $\text{Li}/\text{Li}^+$ , a very intense, irreversible peak was observed, which was assigned to the suggested oxygen release [2]. In order to confirm our findings and to understand the nature of this irreversible oxidation peak, the following experimental studies were carried out.

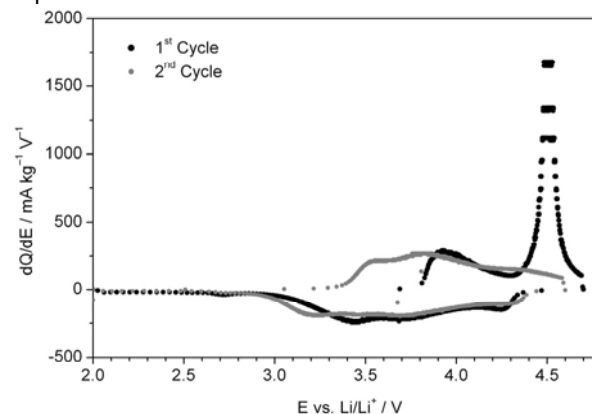


**Figure 2** Differential plot from the galvanostatic cycling experiments for  $\text{Li}_2\text{MnO}_3\text{-Li}(\text{Mn}_x\text{Ni}_y\text{Co}_z)\text{O}_2$  during the 1<sup>st</sup> and 2<sup>nd</sup> cycle.

A possible  $\text{O}_2$  evolution during the first charging process would increase the pressure in the cell. To verify this, the pressure development in a complete lithium-ion cell ( $\text{Li}_2\text{MnO}_3\text{-Li}(\text{Mn}_x\text{Ni}_y\text{Co}_z)\text{O}_2$  vs. graphite) was measured. The result of this experiment is shown in Figure 3. The pressure, which is proportional to the current output, increases during initial charging. As can be seen in Figure 3, further charging leads to an increase in pressure at 4.4 V (a), which is attributed to the oxygen release. In addition to this, labels b and c illustrate further pressure increases at higher voltage (above 4.5 V). This might be due to the release of gases caused by oxidative decomposition of electrolyte on the oxide electrode. To identify the resulting gases,

a differential electrochemical mass spectrometry (DEMS) experiment was performed.

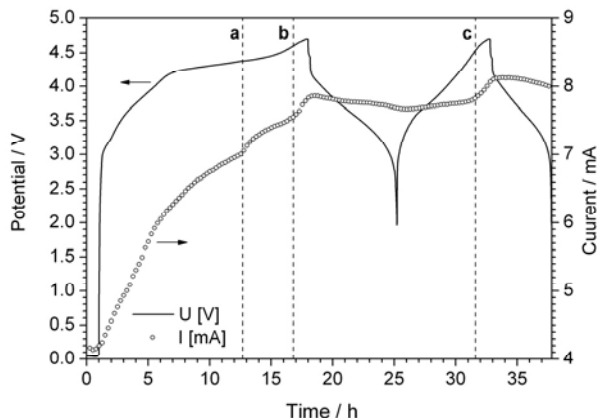


**Figure 3** Gas evolution of  $\text{Li}_2\text{MnO}_3\text{-Li}(\text{Mn}_x\text{Ni}_y\text{Co}_z)\text{O}_2$  vs. graphite (SFG44) monitored in a pressure cell in  $1\text{M LiPF}_6$  EC:DMC (1:1) electrolyte. The current of the sensor (right scale) is proportional to the pressure.

The DEMS experiment with the  $\text{Li}_2\text{MnO}_3\text{-Li}(\text{Mn}_x\text{Ni}_y\text{Co}_z)\text{O}_2$  sample was conducted under galvanostatic conditions in order to investigate the release of gases in the potential range of 2–4.7 V. Figure 4 shows the cooperative plots of the mass signal intensities as measured. At the beginning of charging, SEI (Solid Electrolyte Interphase) formation occurs at the graphite anode. The SEI formation reaction is accompanied by the release of gases from the electrolyte decomposition reaction. The involved gases are, e.g., ethylene,  $\text{CO}_2$ , and  $\text{H}_2$  (as shown in Figure 4,  $m/z=2$ ). Further charging of our sample leads to oxygen evolution, which is detected in the first cycle, while  $\text{H}_2$  and  $\text{CO}_2$  (not shown) are evolved in the high voltage region during the first and subsequent cycles. This result supports the hypothesis of an irreversible oxygen release at high potentials during the first charging process [4] and is in perfect agreement with the result of the pressure measurement (Figure 3).

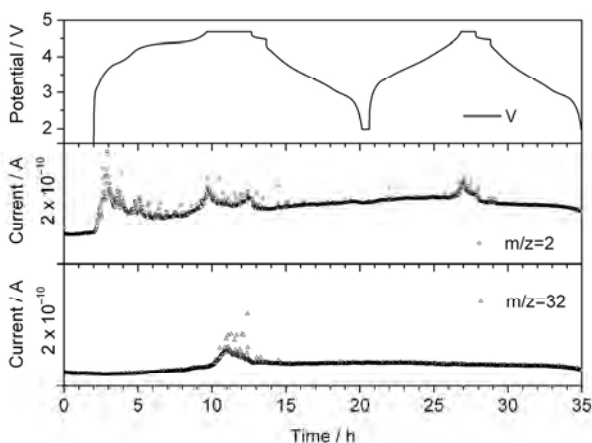


**Figure 4** Gas evolution rate expressed as a detector current in a DEMS experiment with  $\text{Li}_2\text{MnO}_3\text{-Li}(\text{Mn}_x\text{Ni}_y\text{Co}_z)\text{O}_2$  vs. SFG44 in  $1\text{M LiPF}_6$  EC:DMC (1:1) under galvanostatic conditions.

To explore the heat signature of the oxygen release, we developed an experimental setup which enabled us to monitor the thermal behaviour during charging and discharging. Figure 5 shows the initial charge and discharge profile and the concomitant temperature changes. During initial charging, the temperature is assumed to increase due to the overvoltage and SEI formation on graphite. Subsequently, the temperature decreases when the voltage is between 3.6 V and 4.1 V. As can be seen in Figure 5, further charging

leads to a release of heat. A substantial part of this heat is expected to be associated with the overvoltage, which can be determined by *Galvanostatic Intermittent Titration Technique* (GITT) experiments (Figure 6). Further contributions to the heat signature could be due to the enthalpy of reaction of structural changes [3], e.g., those occurring during the release of oxygen, which has been observed at higher potentials (4.5 V). In the *Constant Current Constant Voltage* (CCCV) process the temperature decreases to a certain value and increases again during discharge at a potential of 3.4 V vs.  $\text{Li/Li}^+$ . This process can, again, be attributed to the overpotential in this potential region.

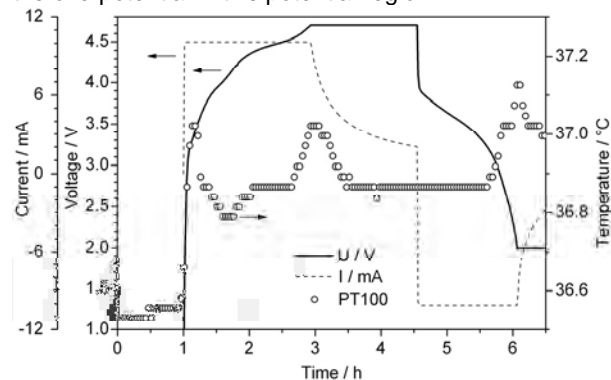


**Figure 5** Charge and discharge voltage profile of  $\text{Li}_2\text{MnO}_3\text{-Li}(\text{Mn}_x\text{Ni}_y\text{Co}_z)\text{O}_2$  electrodes vs. SFG44 graphite in pouch cells. The temperature measurement is denoted by open circles.

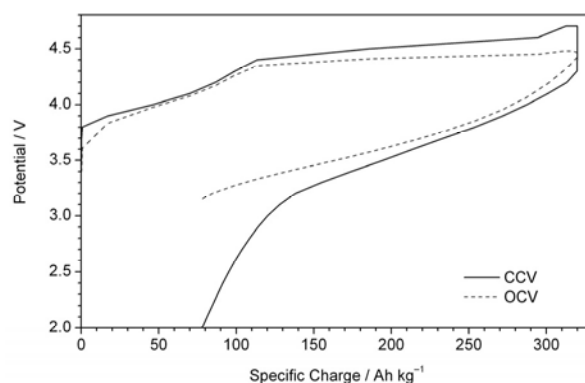


**Figure 6** GITT experiment of  $\text{Li}_2\text{MnO}_3\text{-Li}(\text{Mn}_x\text{Ni}_y\text{Co}_z)\text{O}_2$  during the first cycle in  $1\text{M LiPF}_6$  EC:DMC (1:1) electrolyte.

The agreement of all of the different, independent experimental approaches with our expectations lends sound support to the hypothesis of an irreversible oxygen release at high potentials during the first charging process.

#### Acknowledgements

The authors are very grateful for the financial support from BASF SE.

#### References

- [1] M.H. Rossouw, M.M. Thackeray, Mater. Res. Bull. **26**, 463 (1991).
- [2] D.D. MacNeil, Z. Lu, J.R. Dahn, J. Electrochem. Soc. **149**, A1332 (2002).
- [3] P Novák, W. Scheifele, F. Joho, O. Haas, J. Electrochem. Soc. **142**, 2540 (1995).
- [4] Z.H. Lu, J.R. Dahn, J. Electrochem. Soc. **149**, A815 (2002).

## Continuous flame synthesis of carbon-coated nano-LiFePO<sub>4</sub> for Li-ion batteries

O. Waser<sup>1</sup>, R. Büchel<sup>1</sup>, A. Hintennach, P. Novák, S.E. Pratsinis<sup>1</sup>

phone: +41 56 310 2457, e-mail: petr.novak@psi.ch

Olivine materials as, e. g., LiFePO<sub>4</sub> are attractive for high volume lithium-ion battery applications for hybrid or solely electric vehicles [1] because, LiFePO<sub>4</sub> is made from nontoxic and low cost raw materials [2], has a high electrochemical cycle stability, and can be charged and discharged at high rates [3]. Limitations of LiFePO<sub>4</sub> are its low electronic conductivity (ca. 10<sup>-10</sup> S cm<sup>-1</sup> [4]) and slow Li-ion diffusion along the one-dimensional channels of its olivine structure [5]. The diffusion limitation can be addressed with smaller particles (shorter diffusion paths) allowing higher charge- and discharge rates. However, for smaller particles the electrode resistance increases, due to the increased number of boundaries between nano-particles necessitating a conductive matrix, e.g., carbon black.

Carbon black containing materials typically exhibit a 10–100 times higher overall electrical conductivity compared to doped LiFePO<sub>4</sub> compounds [6]. A core-shell structure with active material as core and conductive carbon black coating as shell is assumed to be ideal for nanostructured LiFePO<sub>4</sub>. Here, a fast and single step process is presented to make such core-shell coated nano-particles.

### Experimental

LiFePO<sub>4</sub> compound as active electrode material was made by a single step, continuous flame aerosol process, capable to produce, at least, up to 700 g h<sup>-1</sup> of carbon - coated ceramic nanoparticles [7]. The LiFePO<sub>4</sub> nanoparticles were thereby, for the first time to our knowledge, *in situ* acetylene carbon black (ACB)-coated resulting in a core-shell morphology [8]. The influence of the oxygen concentration on that morphology and crystallinity of the LiFePO<sub>4</sub> particles was investigated during their *in situ* coating. A post annealing process ensured full crystallization of core LiFePO<sub>4</sub> while particle growth through sintering was retarded by their ACB-coating.

Electrodes prepared of the LiFePO<sub>4</sub> powders contained Super P carbon as an additional electrically conductive additive. Polyvinylidene fluoride (PVDF) dissolved in *N*-methylpyrrolidinone was used as binder. The mass-ratio (after drying) of LiFePO<sub>4</sub>/Super P/PVDF in the electrodes was 83/8.5/8.5. Electrochemical cycling was performed in 1 M LiPF<sub>6</sub> in ethylene carbonate/dimethyl carbonate (1:1 by mass) between 2.0 V and 4.5 V vs. Li/Li<sup>+</sup> at various discharge rates (0.5–16C, with 1C = 170 A kg<sup>-1</sup>).

### Results

Figure 1 shows two TEM images of LiFePO<sub>4</sub>/ACB nano-particles after post annealing at a) 700 and b) 800 °C for 240 min. The ACB-coating is slightly visible at the edge of the particles in both images. At higher annealing temperature, "empty" shells of the ACB-coating were detected leading to highly dispersed carbon enhancing the conductivity of post-annealed LiFePO<sub>4</sub> composites [8].

Figure 2 shows the X-Ray diffractograms of ACB-coated LiFePO<sub>4</sub> as-prepared and after annealing in Ar/H<sub>2</sub> at 700 and 800 °C for 30 and 240 min. The as-prepared particles were amorphous by XRD. After 30 min annealing at 700 °C, crystalline LiFePO<sub>4</sub> was formed. An extension of the annealing time to 60 and 240 min improved the crystallinity, as seen by the reduction of the amorphous hump at 20° < 2θ < 40°. After an annealing time of 240 min at 800 °C the amorphous part disappeared, but a new Fe<sub>2</sub>P phase was observed. This Fe<sub>2</sub>P is ascribed to the reduction of FePO<sub>4</sub> to Fe<sub>2</sub>P by carbothermal reduction with ACB. The evolution of Fe<sub>2</sub>P, however, can substantially increase the electronic conductivity of the electrode by forming a grain-boundary nano-network with carbon [9].

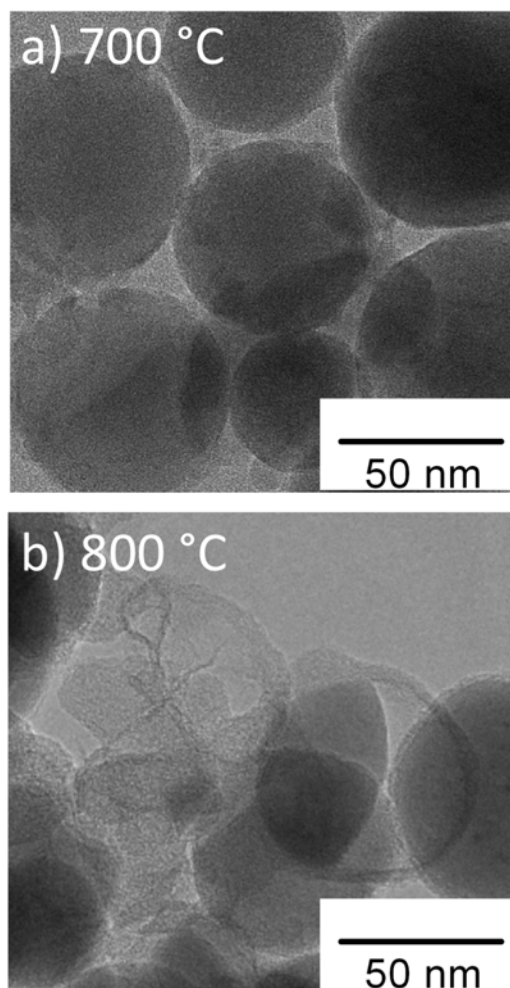


**Figure 1.** TEM images of post-annealed, *in situ* ACB-coated nano-particles of LiFePO<sub>4</sub> annealed at a) 700 and b) 800 °C.

<sup>1</sup> ETH Zürich

A comparison of different annealing temperatures for the same annealing time (240 min) on the electrochemical properties is shown in figure 3. After annealing at 800 °C the battery material exhibited a higher specific charge compared to compounds annealed at 700 °C. It was assumed that the formation of Fe<sub>2</sub>P in the compound annealed at 800 °C has enhanced the electrical conductivity of the active material increasing the useable specific charge of the LiFePO<sub>4</sub>-ACB composite. Both the core-shell LiFePO<sub>4</sub>-ACB powders annealed at 700 °C and 800 °C exhibited a good electrochemical cycling stability with an observed capacity fading of about 0.05 % per cycle and 0.01 % per cycle, respectively.

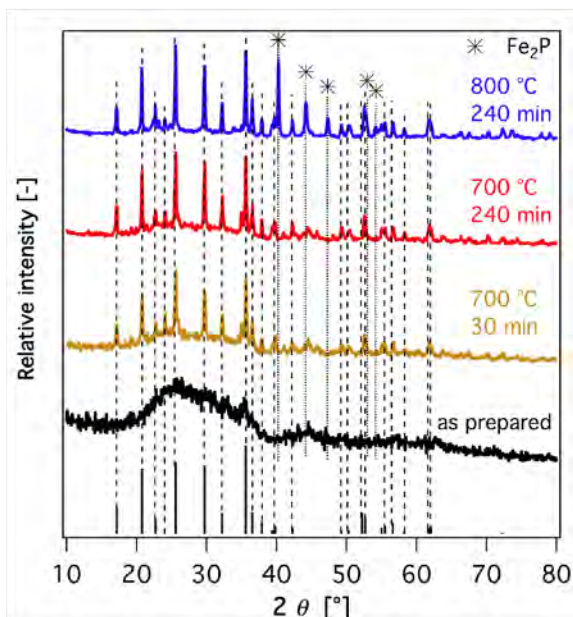


**Figure 2.** X-ray diffractograms showing as-prepared and annealed (Ar/H<sub>2</sub> atmosphere) core-shell LiFePO<sub>4</sub>-ACB. Pure LiFePO<sub>4</sub> phase was obtained at 700 °C, whereas at 800 °C 15 wt% Fe<sub>2</sub>P was formed.

At much higher discharge rates (> 4C, with 1C = 170 A kg<sup>-1</sup>) the *in situ* ACB-coated LiFePO<sub>4</sub> nanoparticles showed a very good electrochemical cycling stability (only 5–8 % loss of specific charge after 300 cycles).

The specific discharge capacity of electrodes containing post-annealed core-shell LiFePO<sub>4</sub>-ACB at various discharge rates (0.5–16C, with 1C = 170 A kg<sup>-1</sup>) is shown in figure 4. A specific charge of 163 Ah kg<sup>-1</sup> was observed for low C-rates (0.5C) corresponding to 96 % of the theoretical specific charge of LiFePO<sub>4</sub>. Higher discharge rates (> 4C) reduced the specific charge progressively. Nevertheless, the core-shell LiFePO<sub>4</sub>/ACB powders annealed at 800 °C showed significantly improved electrochemical properties compared to the powders annealed at 700 °C. This effect is ascribed to the increased conductivity in the electrode due to formation of Fe<sub>2</sub>P in interaction with highly dispersed carbon originating from empty ACB shells.

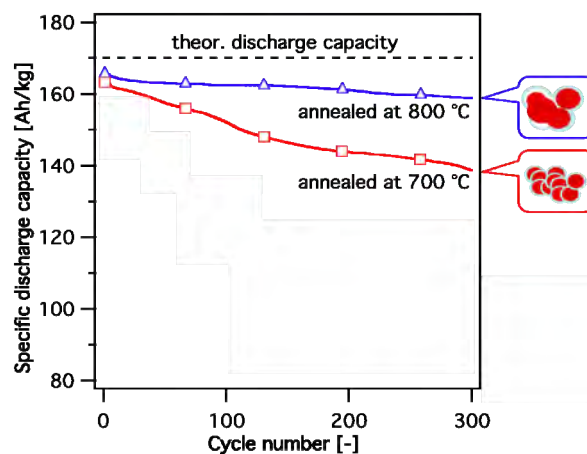


**Figure 3.** Discharge capacity per unit mass (specific charge) at a discharge rate of 2C of *in situ* ACB-coated, nano-sized LiFePO<sub>4</sub> after post-annealing at 700 and 800 °C.

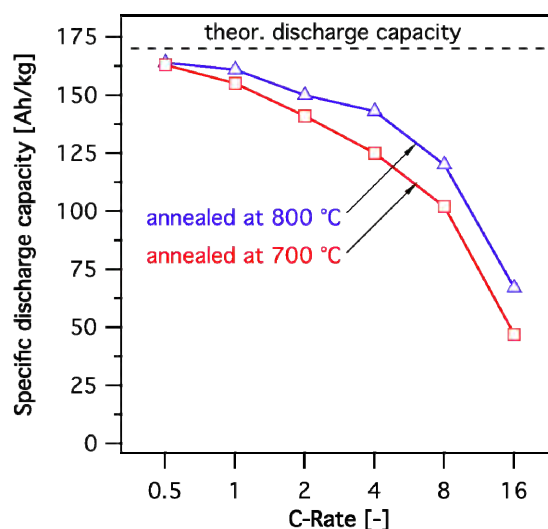


**Figure 4.** Galvanostatic discharge capacity of *in situ* ACB-coated nano-sized LiFePO<sub>4</sub> particles annealed at different temperatures. The constant current part of the total capacity at each C-Rate is shown as the average of 10 cycles after 50 cycles at a discharge rate of 2C.

## References

- [1] A.K. Padhi, K.S. Nanjundaswamy, J.B. Goodenough, *J. Electrochem. Soc.* **144**, 1188-1194 (1997).
- [2] J. Hong, C.S. Wang, X. Chen, S. Upreti, M.S. Whittingham, *Electrochem. Solid State Lett.* **12**, A33-A38 (2009).
- [3] B. Kang, G. Ceder, *Nature* **458**, 190-193 (2009).
- [4] S.Y. Chung, J.T. Bloking, Y.M. Chiang, *Nat. Mater.* **1**, 123 (2002).
- [5] D. Morgan, A. Van der Ven, G. Ceder, *Electrochem. Solid State Lett.* **7**, A30-A32 (2004).
- [6] C. Delacourt, C. Wurm, L. Laffont, J.B. Leriche, C. Masquelier, *Solid State Ionics* **177**, 333-341 (2006).
- [7] H.K. Kammler, R. Mueller, O. Senn, S.E. Pratsinis, *AIChE J.* **47**, 1533-1543 (2001).
- [8] O. Waser, R. Büchel, A. Hintennach, P. Novák, S.E. Pratsinis, *J. Aerosol Sci.* (2011), submitted.
- [9] P.S. Herle, B. Ellis, N. Coombs, L.F. Nazar, *Nat. Mater.* **3**, 147-152 (2004).

# Microwave-assisted preparation of sulphur-carbon composite materials for lithium-sulphur batteries

A. Hintennach, P. Novák

phone: +41 56 310 2457, e-mail: petr.novak@psi.ch

Today's battery systems of choice are lithium based. They can store the electricity needed for the electric engines of hybrid electric vehicles (HEVs) and full electric vehicles (EVs). Due to the need of batteries providing a very high specific energy some alternatives to lithium-ion batteries were investigated in the very close past. Compared to standard materials, sulphur offers a much higher theoretical specific charge of  $1675 \text{ Ah kg}^{-1}$ , *i. e.*, almost a magnitude more compared with the theoretical specific charge of olivine materials as  $\text{LiFePO}_4$  (ca.  $170 \text{ Ah kg}^{-1}$ ).<sup>[1]</sup> But there are a number of key issues wherefore the lithium-sulphur system was not yet implemented in HEVs: Both the tendency of lithium-sulphur to form (partly soluble) polysulphide molecules and the low electrical conductivity of elemental sulphur ( $5 \times 10^{-30} \text{ S cm}^{-1}$ ) led to the low number of applications.<sup>[1]</sup> Especially the polysulphides can diffuse to the lithium anode where they are reduced while poisoning the anode. Therefore a precise control of the behavior of the sulphide within the carbon matrix could enhance the electrochemical properties significantly.

In the present work we describe a novel microwave and sonochemical synthesis path for the preparation of sulphur-carbon compounds for lithium batteries. Model electrodes built from these as-synthesized sulphur-carbon materials showed an excellent and highly stable electrochemical performance over several hundreds of cycles with a remarkable initial specific charge of about  $1630 \text{ Ah kg}^{-1}$  and a fading of the specific charge after about 300 cycles of about 18 %.

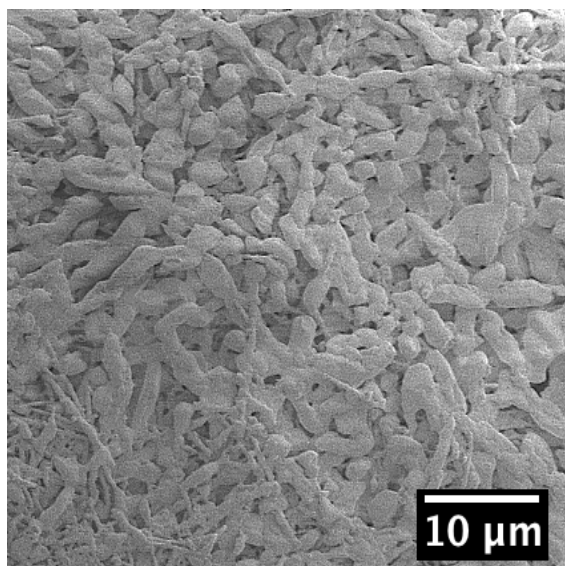


**Figure 1.** SEM image (2 kV) of the as-synthesized sulphur-carbon compound.

## Experimental

Sulphur-carbon compounds were prepared by a microwave-assisted pyrolysis which primarily based on a mixture of saccarose and potassium hydro carbonate with a second sonochemical step for the insertion of sulphur into the carbon matrix. (Details to be published.)

To prepare the suspensions for the preparation of electrodes, the as-obtained sulphur-carbon compounds were mixed with polyvinylidene fluoride (binder) dissolved in *N*-methylpyrrolidone. The proportion of the materials in the dried electrodes equalled to 90 / 10 (sulphur-carbon / binder, by mass). All electrode constituents were mixed with an ultra-sonic stirrer. LiTFS (1 M, lithium bistrifluoromethanesulfonimide; 99.95 %, Sigma Aldrich) in polyethyleneglycol-dimethylether was used as electrolyte.

## Results

A typical SEM image of the as-obtained sulphur-carbon compound is shown in figure 1. Small particles form larger agglomerations with a quite inhomogeneous particle size.

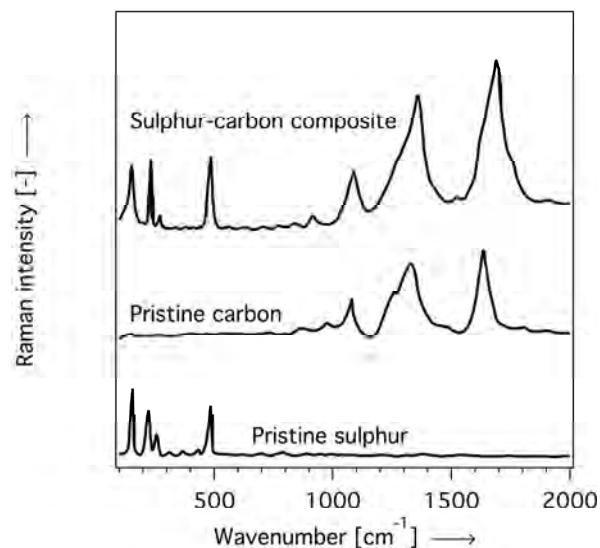


**Figure 2.** Raman spectrum of the surface of a model electrode built from the as-synthesized sulphur-carbon compounds and of its constituents.

Typical Raman spectra of pristine carbon, pristine sulphur, and a composite of these materials are shown in figure 2. While both the pristine materials carbon and sulphur, respectively, show typical bands within different regions ( $150\text{--}500 \text{ cm}^{-1}$  for the sulphur and  $1000\text{--}2000 \text{ cm}^{-1}$  for the carbon) the differentiation between the two different materials was possible in the composite. It becomes clear that structural changes of neither the sulphur nor the graphite were caused by the mixing of the materials. Please note that due to the mostly carbon-coated sulphur particles Raman spectra of sulphur within the mixture could only be recorded at

a few points where the carbon coating exhibited damages. All shown peaks could be compared with literature data for comparable compounds and materials.[2,3] Raman mappings showed a highly dispersed sulphur within the carbon composite material.

An exemplary cyclic voltammogram of the as-prepared electrodes of sulphur-carbon compounds is shown in figure 3. After the first reduction, both reductive peaks of sulphur are clearly visible during the further cycling of the sulphur-carbon composite. Compared with literature data [4–6] the first step (higher potential) can be ascribed to the transformation of sulphur to lithium polysulphides ( $\text{Li}_2\text{S}_n$ , with  $2 < n < 8$ ) while the second step (lower potential) can be explained by the change of the lithium polysulphides into lithium sulphide ( $\text{Li}_2\text{S}$ ).

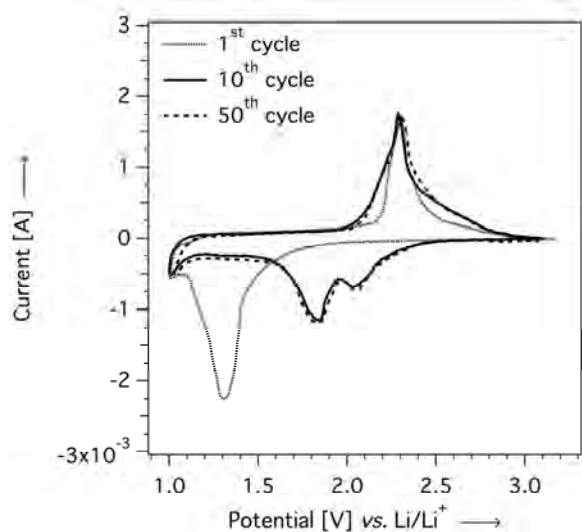


**Figure 3.** Typical cyclic voltammograms of a composite electrode containing the as-synthesized sulphur-carbon compound after different cycle numbers. Electrochemical cycling was performed in 1 M LiTFSF in PEGDME between 1.0 V and 3.0 V vs.  $\text{Li/Li}^+$  at 25 °C at a scan rate of  $0.1 \text{ mV s}^{-1}$ .

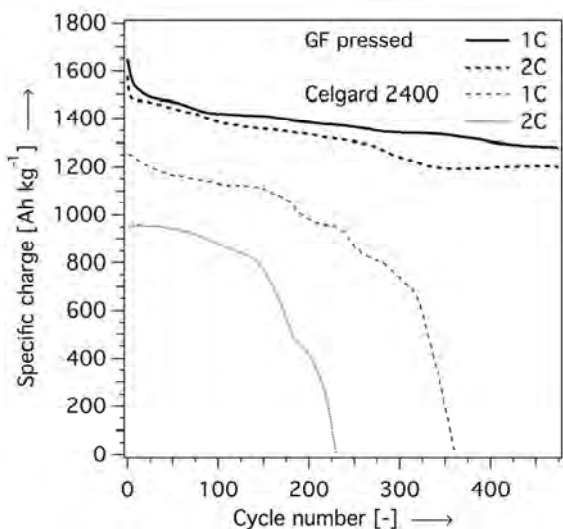


**Figure 4.** Cycling behavior at different charge/discharge rates ( $1\text{C} \approx 1675 \text{ A kg}^{-1}$ ) with different separators (Celgard 2400 vs. pressed glass fiber, GF). Electrochemical cycling was performed in 1 M LiTFSF in PEGDME between 1.0 V and 3.0 V vs.  $\text{Li/Li}^+$  at 25 °C.

Figure 4 shows the excellent discharge capacity of the material and a very good cycling behavior. A significant loss of initial specific charge during the first cycles could

be observed. This might be due to the formation of polysulphide compounds until a steady-state-like behavior. Obviously, the formed polysulphides did not show a high mobility within the electrode and these are assumed to be adsorbed at the surface of the carbon compound. This fact underlines the high quality of the as-prepared electrodes especially in comparison to published data with different approaches to immobilize the polysulphide compounds. The high cycling stability can be explained by the very fine dispersion of the sulphur powder within the very porous carbon compound, an optimal separator, and an improved preparation process.

Moreover, the discharge rate has only a moderate influence on the specific charge after 50 cycles if discharged with a discharge rate up to about 3C (*cf.* figure 5). At higher discharge rates ( $> 3\text{C}$ ) the practical specific charge during the discharge process decreases continuously.

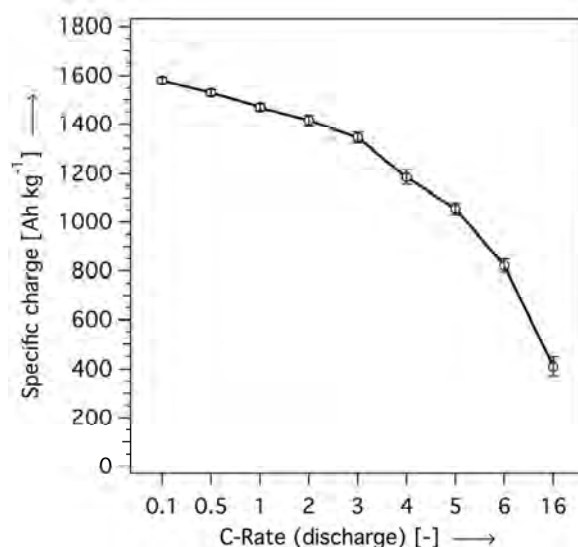


**Figure 5.** Dependence of the practical specific charge during discharge on the discharge rate (0.1–16C, with  $1\text{C} \approx 1675 \text{ A kg}^{-1}$ ) after 50 cycles. Every data point represents the average of ten cycles at the indicated discharge rate. Electrochemical cycling was performed in 1 M LiTFSF in PEGDME between 1.0 V and 3.0 V vs.  $\text{Li/Li}^+$  at 25 °C.

## References

- [1] X. Ji, K.T. Lee, L.F. Nazar, *Nat. Mat.* **8**, 500-506 (2009).
- [2] J.D. Pasteris, J.J. Freeman, S.K. Goffredi, K.R. Buck, *Chemical Geology* **180**, 3-18 (2001).
- [3] S. Ghosh, G.A. Bowmaker, R.P. Cooney, J.M. Seakins, *Synth. Met.* **95**, 63-67 (1998).
- [4] H. Yamin, A. Gorenshtein, J. Penciner, Y. Sternberg, E. Peled, *J. Electrochem. Soc.* **135**, 1045-1048 (1988).
- [5] A. Evans, M.I. Montenegro, D. Pletcher, *Electrochem. Commun.* **4**, 626-627 (2002).
- [6] A. Evans, M.I. Montenegro, D. Pletcher, *Electrochem. Commun.* **3**, 514-518 (2001).

# Synthesis of an artificial SEI on carbon by grafting and other chemical methods to decrease the irreversible charge loss

P. Verma, P. Novák

phone: +41 56 310 2161, e-mail: pallavi.verma@psi.ch

Irreversible charge loss (ICL) during the first charge is an important issue in Li-ion battery research. ICL is the charge consumed for the reduction of the electrolyte on the negative electrode during first lithiation of graphite (which is the most common active material for negative electrode). The reduction products form an inhomogeneous passive layer called the Solid Electrolyte Interphase (SEI) [1]. An ideal SEI should be electron insulating and Li-ion conducting. An efficient SEI is required for good cycling, rate capability and safe operation of the battery. In this work we attempt to prepare an artificial SEI by two main methods. The first method is grafting followed by functionality transformation. In this route we covalently immobilize an organic moiety on the carbon surface and impart it required functionality in successive steps. Various methods of grafting employed for this purpose include electrochemical grafting, *in situ* grafting (non-aqueous and aqueous), and spontaneous grafting. Another method employs alteration of the existing surface groups on the carbon into more reactive ones. Chemical reducing agents have been employed for this work.

## Experimental

I.1: Electrochemical grafting followed by functionality transformation: The scheme of modification of carbon surface (glassy carbon (GC) as well of graphite) is shown in Figure 1.

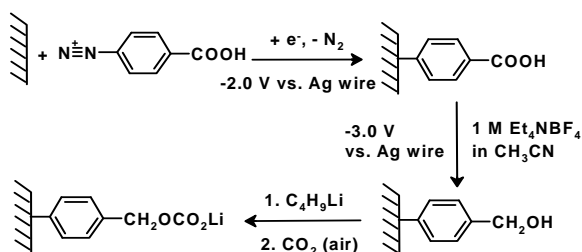


**Figure 1.** Scheme of electrochemical grafting and functionality transformation of carbon.

First, *p*-carboxybenzenediazonium tetrafluoroborate was synthesized from *p*-amino benzoic acid [2]. Then, a CV was scanned from  $-2.0\text{ V}$  to  $0.5\text{ V vs. Ag wire}$  at a rate of  $5\text{ mV/s}$ . The electrolyte for grafting was  $0.1\text{ M}$  tetraethylammonium tetrafluoroborate in  $\text{CH}_3\text{CN}$ ,  $\text{H}_2\text{O} < 50\text{ ppm}$ , containing  $5\text{ mM}$  diazonium salt. For the electrochemical reduction step, same electrolyte without diazonium salt was employed. The CV was scanned from  $-3.0\text{ V}$  to  $0.0\text{ V vs. Ag wire}$ . Electrochemical grafting as well as reduction were carried out in novel 3-electrode cell, using Pt wire as counter electrode, Ag wire as reference electrode, and SFG6 graphite (TIMCAL<sup>®</sup>, Switzerland) casted on Ti plate as working electrode. After this, the sample was treated with  $1.6\text{ M}$  *n*-butyl lithium (BuLi) in hexane,

followed by washing with anhydrous hexane. The resulting powder was then exposed to  $\text{CO}_2$  from air.

I.2: *In situ* grafting (aqueous): SFG6 graphite powder was immobilized by *p*-amino benzoic acid following the synthesis described by Martin et al. [3].

I.3: *In situ* grafting (non-aqueous):  $2.9\text{ millimoles}$  *p*-amino benzoic acid was stirred in  $50\text{ mL}$  acetonitrile. To this  $400\text{ mg}$  SFG6 graphite powder was added. Then,  $6.2\text{ millimoles}$  *tert*-butyl nitrite was added drop wise under constant and vigorous stirring. The mixture was stirred for  $2\text{ hours}$ . The powder was filtered and washed well with acetonitrile. The whole procedure was performed in the absence of  $\text{O}_2$  and moisture.

I.4: Spontaneous grafting: *p*-carboxylic benzene diazonium tetrafluoroborate was stirred in acetonitrile. To this SFG6 graphite was added. The mixture was allowed to stir for  $2\text{ hours}$ . The powder was filtered and washed well with acetonitrile. The whole procedure was performed in the absence of  $\text{O}_2$  and moisture.

II. Activation of the existing surface groups by chemical reduction: SFG6 graphite powder was treated with  $1\text{ M}$   $\text{BH}_3$  in tetrahydrofuran (THF),  $1\text{ M}$   $\text{BH}_3$  in THF followed by  $1.6\text{ M}$  BuLi in hexane,  $1.6\text{ M}$  BuLi in hexane and  $2\text{ M}$   $\text{LiAlH}_4$  in THF, individually under inert conditions. Post treatment these powders were washed with THF, hexane, hexane, and THF respectively.

For battery testing, standard cells using Li metal as counter as well as reference electrode were built. Since the surface groups on graphite after treatment were sensitive to oxidizing agents and conditions, the working electrodes were made using styrene-butadiene rubber (SBR) as binder ( $10/90$  SBR/graphite w/w) and hexane as solvent. The slurry was applied onto Ti current collector stubs and dried. The galvanostatic cycling was done at C/10 rate in  $1\text{ M}$   $\text{LiPF}_6$  in  $1:1$  ethylene carbonate: dimethyl carbonate. Same conditions were used for CV which was run at  $0.01\text{ mV/s}$ . Ultra55 scanning electron microscope (SEM) was used to visualize the surface morphology of the treated samples. Pictures were taken using In Lens detector at  $3\text{ KeV}$  accelerating voltage.

## Results

I. Grafting followed by functionality transformation: Figure 2 shows the SEM images of the samples prepared by different grafting methods. Figure 2a shows the sharp edges and smooth basal planes of pristine SFG6. SFG6 treated as per scheme in Figure 1 is shown in Figure 2b. This clearly shows a heavy and dense coating on both the prismatic as well as the basal planes. Aqueous and non-aqueous *in situ* grafted samples both show thinner and less dense coatings. Non-aqueous grafted sample shown in Figure 2c shows strands of layers across the basal and edge planes, whereas aqueous grafted sample in Figure 2d shows more homogeneous coating. Finally, the spontaneously grafted sample shown in Figure 2e shows the least thick and dense coating. Thus depending on the method of grafting, the thickness and morphology of the surface layer can be tuned.

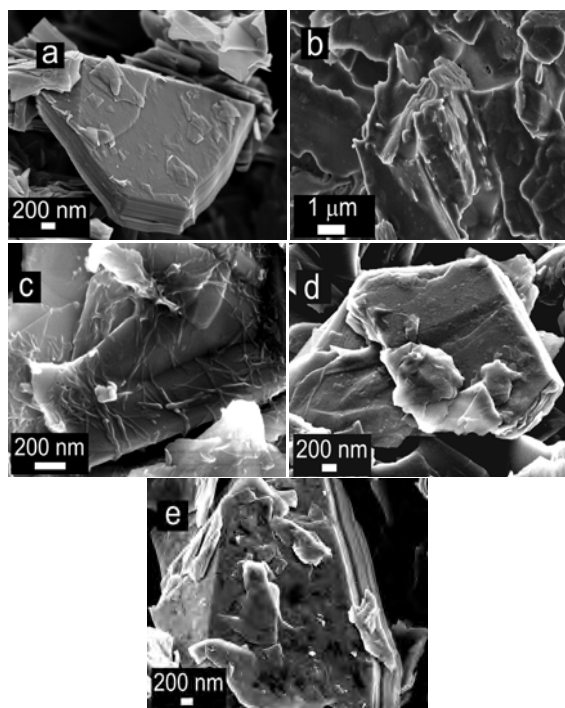


**Figure 2.** a) Pristine SFG6; b) electrochemically grafted and carbonated SFG6; c) non-aqueous in situ grafted SFG6; d) aqueous in situ grafted SFG6; e) spontaneously grafted SFG6.

Figure 3 shows the first electrochemical lithiation curves of the various grafted samples. It is evident that the course of the electrochemical lithiation is different in each case. However no significant improvement in terms of ICL was made. This is expected to be due to heavy and dense coating which insulates the particles and blocks them from undergoing charge transfer. Further study in this direction is under progress.

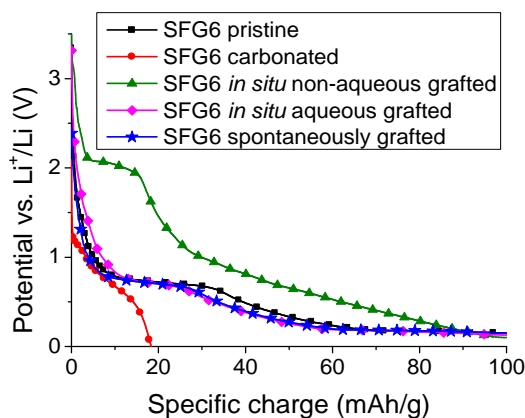


**Figure 3.** Beginning of the electrochemical lithiation profile of SFG6 samples grafted by various methods.

II. Activation of existing surface groups of graphite: Figure 4 shows a part of the CV of SFG6 samples reduced with various chemical reducing agents. This potential window is where most of the electrolyte degradation occurs, and SEI is formed. It is evident that the SEI formation step is highly diminished in the sample treated with BuLi. This is in accordance with the ICL calculated from the cycling of this sample vs. Li metal. SFG6 treated with BuLi exhibits 22% less irreversible charge consumption. However, there were concomitant issues related with this material that it exhibits lower specific charge (80% of theoretical) and

poor cyclability. The cyclability was attempted to be improved by treating the electrodes of SFG6 BuLi with various film forming additives. The best results were obtained with EC as additive; however any other significant improvements were not achieved. The SEM image of SFG6 treated with BuLi is shown in Figure 5. It clearly shows that the material is edge decorated by a ruffle of an amorphous material. The chemical nature of this ruffle is not yet fully understood but is under investigation. Since this material is exclusively edge covered, it would be interesting in terms of limiting solvent co-intercalation, which is a major issue related with propylene carbonate based electrolytes. Propylene based electrolytes are attractive for low temperature applications of Li-ion batteries.

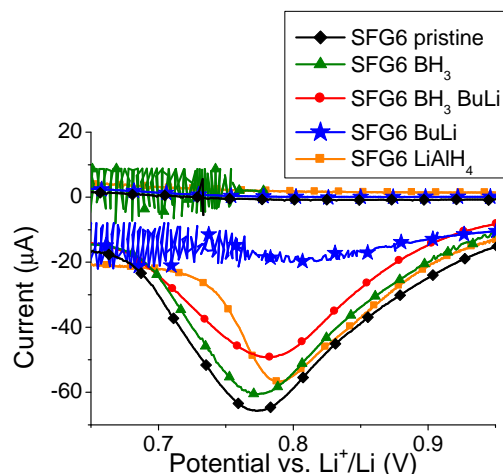


**Figure 4.** CV of SFG6 chemically reduced with different reagents.

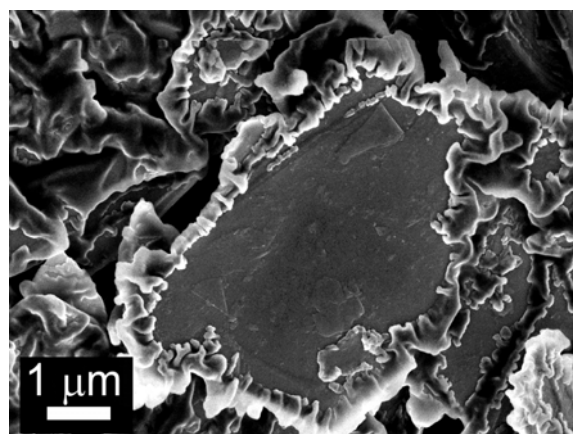


**Figure 5.** SEM image of SFG6 treated with BuLi.

## References

- [1] P. Verma, P. Maire, P. Novák, *Electrochimica Acta* **55**, 6332-6341 (2010).
- [2] M.P. Doyle, W. J. Bryker, *Journal of Organic Chemistry* **44**, 1572-1574 (1979).
- [3] C. Martin et al. *Advanced Materials* **21**, 4735-4741 (2009).

# Conductive carbon networks in positive electrodes for Li-ion batteries

W. Märkle, M.E. Spahr<sup>1</sup>, P. Novák

phone: +41 56 310 2474, e-mail: wolfgang.maerke@psi.ch

The actual trend of establishing full electric or hybrid vehicles triggered a boom in the research on new high-performance electrode materials for lithium-ion batteries, which are regarded as the most promising energy storage system for this purpose. The major focus of the research community lies in the exploration of the material and cell chemistry and in addition on the material engineering in terms of, e.g., particle size and shape, surface properties, etc. [1]. In order to compare new materials with known ones, standardized procedures with respect to electrode formulation and manufacturing are frequently used. A minor role plays the aspect of the electrode formulation and preparation as well as the choice of an appropriate electrolyte, most probably because the exploration of all the parameters which contribute to the electrode and even cell would let the number of experiments grow exponentially. Nevertheless, only an adjusted, optimized electrode structure can bring out the best of a respective “new” material as there is no general recipe valid for all cathode and anode materials. On the other hand, a potentially good material may be overlooked by using an unsuitable electrode formulation.

This study was performed in order to meet some of these described points and focused on the conductive carbon network formation in positive electrodes, which is especially important at increased current rates due to the commonly low electronic conductivity of the active materials [2]. It was intended to get insights about the correlation of the electrode structure and the electrochemical performance. Special care was taken about the preparation conditions in terms of comparable dispersion, homogenisation and coating procedures.

## Experimental

LiCoO<sub>2</sub> was used as reference material for the positive electrodes. Two different carbon blacks (CB) were applied, A: C-ENERGY™ Super C65, B: C-ENERGY™ Super C45 (both from TIMCAL Belgium). As graphite additive, KS6L (TIMCAL) was used and as binder served SOLEF PVDF 1015 (Solvay). A slurry was prepared by dispersing a respective mixture of the abovementioned components in N-methylpyrrolidone (NMP, Fluka). After homogenisation with a turbo stirrer, the slurry was casted onto an aluminum foil and dried at 80 °C in vacuum. Electrode disks (1.3 cm<sup>2</sup>) were punched out, rolled, and dried for 12 h at 120 °C in vacuum. Standard laboratory cells described elsewhere [3] were used for the experiments. As both counter and reference electrode lithium foil (Alfa Aesar) was applied. An electrolyte (500 μl ethylene carbonate/dimethyl carbonate 1:1 by weight, 1 M LiPF<sub>6</sub>, Ferro) soaked glass fiber separator was used; the electrodes and the separator were pressed against each other with a spring (pressure ~2 kg/cm<sup>2</sup>). Galvanostatic cycling was performed in the range of 3.0 – 4.2 V vs. Li/Li<sup>+</sup>. After reaching these respective limits, a potentiostatic phase was applied until the current dropped to C/5.

## Results

In Figure 1, the galvanostatic discharge capacities (excluding the potentiostatic phase) at different C-rates are shown for LiCoO<sub>2</sub> electrodes with different carbon black additives and various binder quantities. The change of the binder amount from 7% to 3% leads to either an improvement or an impairment of the electrochemical performance, depending on the CB type. Interestingly the influence of the binder amount on the galvanostatic capacity at lower current rates (50 mA/g and 1 C) is higher for CB B. It is therefore expected that the two carbon blacks form different conductive networks, which are additionally depending on the electrode preparation conditions.

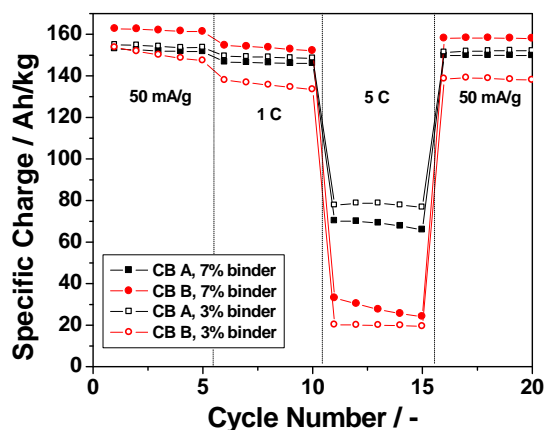


**Figure 1:** Galvanostatic discharge performance of LiCoO<sub>2</sub> electrodes with different carbon black additives (1.5 wt%) and varying amount of PVDF binder. In addition, the electrode contained 1.5 wt% KS6L graphite.

The freshly prepared, uncycled electrodes were examined with scanning electron microscopy (SEM). The pictures show clear differences in the electrode structure depending on the electrode formulation (Figure 2). The LiCoO<sub>2</sub> particles appear in bright while the carbon (CB and graphite) are dark grey. While the 7% binder containing electrodes show a homogeneous oxide/CB distribution (Figure 2a,b), the ones with reduced binder amount exhibit inhomogeneities (Figure 2c,d). With CB A, the oxide particles are more agglomerated and the surface of the CB B electrode is in this case dominated by the carbon. Despite the preparation procedure was exactly the same (amount of NMP, stirring speed and time), there is a partial demixing of the slurry with CB B and 3% binder after coating onto the current collector. Sedimentation of the LiCoO<sub>2</sub> particles and/or floating of the carbon particles, most probably occurring during the step from coating to drying lead to a non-optimal conducting network.

<sup>1</sup>TIMCAL SA, Bodio

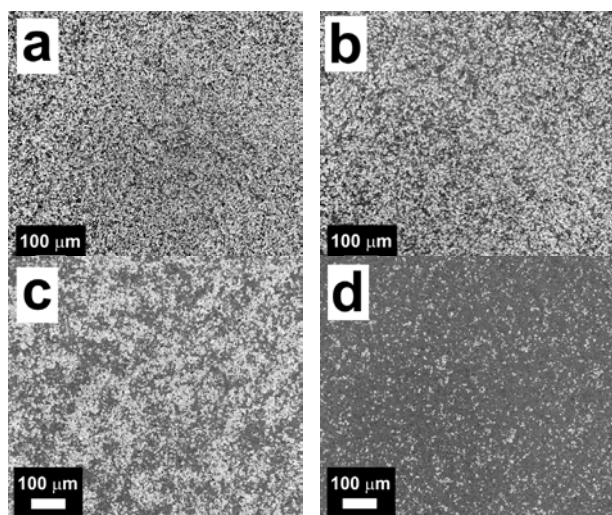


**Figure 2:** SEM pictures of freshly prepared  $\text{LiCoO}_2$  electrodes containing a) CB A, 7% binder; b) CB B, 7% binder; c) CB A, 3% binder; d) CB B, 3% binder.

In all cases the same amount of NMP was used for the slurry preparation. Qualitatively the dispersions with 7% binder were more viscous than the ones with 3%, leading to a decelerated demixing of active material and carbon additives. The stabilization of the slurry during processing, in this case by an increased viscosity through a higher binder amount, is therefore an important factor. Interestingly, in contrary to the electrode with B, the 3% binder containing CB A electrode showed better electrochemical behaviour than the 7% binder electrode. Obviously, in this case the carbon network quality is similar for both CB A electrodes and the higher amount of the electronically insulating binder is detrimental for the conductivity. It is therefore obvious that no general judging between different carbon blacks in terms of their performance as additive can be made due to the strong dependence on the preparation conditions. This has to be taken in mind for a proper choice of the suitable carbon black type.

Besides the carbon black, graphite is often used in small quantities as supplementary additive in positive electrodes. It contributes to compressibility and influences the cycling stability [2,4]. It is reasonable that the amount of the graphite has also to be balanced in order to optimize the electrode performance. In Figure 3, the electrochemical behaviour of carbon additives (CB and graphite) in different ratio is shown. The best result concerning the specific charge as well as the high rate capability was obtained for a CB A/graphite mixture of 3% each. Only graphite as additive is detrimental for the cycling as a strong fading can be observed. For 3% CB A only, the results are at higher C rates comparable with its 1.5%/1.5% and 3%/1% mixtures with graphite. Despite the 3%/3% mixture showed the best electrochemical performance among these electrodes, it has to be stated that the amount of the additives (which are passive materials) should be of course as low as possible as they decrease the energy density of the cell.

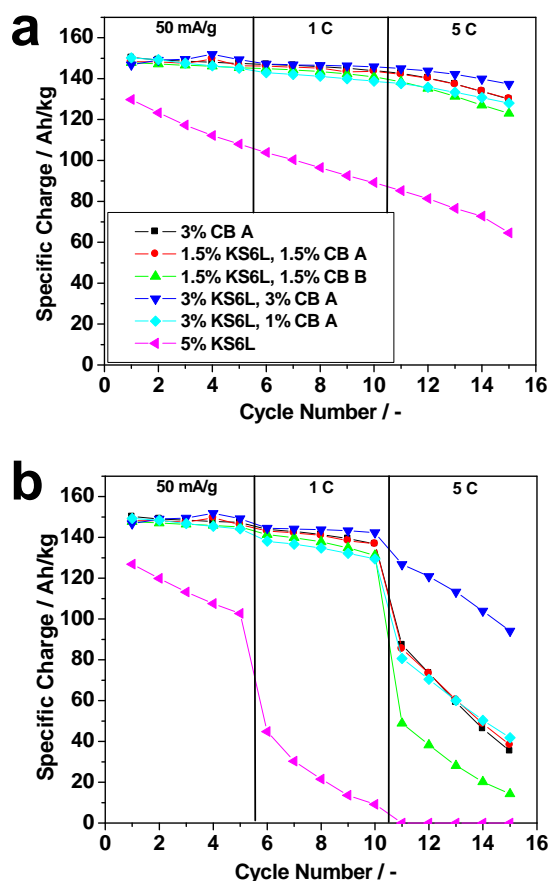


**Figure 3:** Discharge performance of  $\text{LiCoO}_2$  electrodes with different amounts of graphite and CB additives (binder amount 7 wt.%). a) Total discharge capacity, b) galvanostatic discharge capacity.

These results show that the composition and preparation of the electrodes have to be carefully balanced and the binder/CB/graphite ratio might have to be adjusted according to the active and passive materials.

All in all, the experiments indicate that many factors in the step from material to electrode have to be considered, in order to give an optimal electrochemical performance especially under high rate conditions. Further experiments with different positive electrode materials are in progress.

## References

- [1] J.F. Fergus, J. Power Sources **195**, 939-954 (2010).
- [2] M.E. Spahr, D. Goers, A. Leone, S. Stallone, E. Grivei, J. Power Sources **196**, 3404-3413(2011).
- [3] P. Novák, W. Scheifele, F. Joho, O. Haas, J. Electrochem. Soc. **142**, 2544-2540 (1995).
- [4] M.E. Spahr, P. Novák, O. Haas, R. Nesper, J. Power Sources **68**, 629-633 (1997).

# Investigation of the electrochemical activation of partially reduced graphite oxide

M.M. Hantel, T. Kaspar<sup>1</sup>, R. Nesper<sup>1</sup>, A. Wokaun, R. Kötz

phone: +41 56 310 4189, e-mail: moritz.hantel@psi.ch

Electrochemical double-layer capacitors (EDLCs) utilize the electric field of the electrochemical double-layer of their electrodes to store energy. Therefore the total capacitance scales with the available specific surface area of the electrodes. A recently discussed electrode material is graphene with a theoretical specific surface area of  $2630 \text{ m}^2\text{g}^{-1}$  [1]. This value takes into account that both sides of a graphene sheet are accessible and are able to form an electrochemical double-layer. But assembling a graphene based electrode in a perfectly ordered structure, that both layer sides are accessible for ions, is a very challenging task. An easier approach is to start with the ordered graphene structure of graphite and modify the interlayer distance  $d_{002}$ .

One possible route to increase the interlayer distance of graphite is to oxidize the bulk graphite to graphite oxide (GO) resulting in an interlayer distance of  $d_{002} = 6.1 \text{ \AA}$ . Unfortunately graphite oxide seems not to be a suitable electrode material for EDLCs due to its poor conductance. In order to improve the conductivity one can partially reduce the graphite oxide to form graphitic islands in the former completely oxidized graphene layers. This partial reduction can be done by a thermal treatment of the graphite oxide and one achieves partially reduced graphite oxide (GOpr). This material has interlayer distances up to  $4.6 \text{ \AA}$ , depending on the grade of reduction [2].

Recently we have shown that GOpr could be electrochemically activated to achieve a huge capacitance of up to  $220 \text{ Fg}^{-1}$  over a potential range above  $3 \text{ V}$  and is therefore a very suitable candidate for EDLC electrodes [3]. Since GOpr needs to be electrochemically activated to show capacitor like behaviour it is worth to take a closer look onto this process. In particular we investigated the origin of the dimensional changes occurring during activation. Such changes could be an issue for cell design and stability.

## Experimental

Partially reduced graphite oxide with an interlayer distance of  $4.4 \text{ \AA}$  (GOpr44), derived from oxidized synthetic graphite (TIMREX SFG6, TIMCAL), was assembled to a  $200 \text{ \mu m}$  PTFE-bound electrode. The used electrode composition was 80 wt.% active material (GOpr44 as received), 10 wt.% conductive agent (Super P, TIMCAL) and 10 wt.% PTFE (60 wt.% PTFE dispersion, Alfa AESER).

*In situ* expansion measurements were done with an in-house constructed dilatometer, optimized for bound electrodes, using a three electrode design for the electrochemical measurements [4]. The setup consists of an oversized counter electrode, PTFE-bound activated carbon (YP17, Kuraray Chemical Co., Japan), as well as a carbon quasi-reference from the same material. The Electrolyte for all measurements was  $1 \text{ M Et}_4\text{NBF}_4$  in acetonitrile.

Cyclic voltammetry experiments were performed separately for anode and cathode with a scan rate of  $1 \text{ mVs}^{-1}$  using an IM6e potentiostat (Zahner-Elektrik GmbH & Co. KG, Germany). For the activation process the anode was cycled between  $0.0$  and  $1.5 \text{ V}$  vs. carbon whereas the cathode was cycled between  $0.0$  and  $-2.0 \text{ V}$  vs. carbon.

X-ray diffraction measurements of the electrodes were done on a Bruker D8 system using a Bragg-Brentano diffraction mode.

## Results

In our previous study [3] we observed a significant expansion during electrochemical activation of GOpr44. In order to find out whether such a huge expansion could be avoided by pre-activation of the electrodes we performed the following set of experiments.

In the first step electrodes were either anodically or cathodically activated. Then the electrodes were disassembled from the electrochemical cell and washed with pure electrolyte solvent (acetonitrile) for  $6 \text{ h}$  and afterwards dried for  $12 \text{ h}$  at  $120^\circ \text{ C}$  under vacuum of  $10^3 \text{ Pa}$ . In the final step the electrodes were reassembled to the electrochemical cell and the activation experiment was rerun.

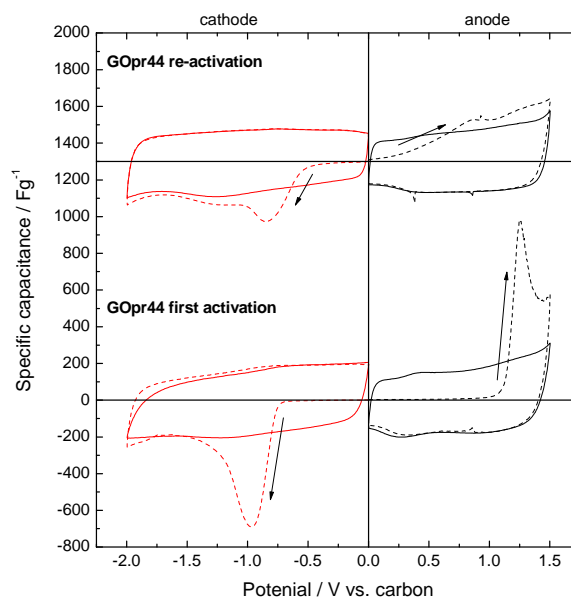


**Figure 1.** Cyclic voltammograms of GOpr44 for the first activation (bottom) as well as for a re-activation (top) by using washed pre-activated electrodes. The dashed line shows the first cycle and the continuous line the second cycle. The CVs were recorded separately for anode and cathode using  $1 \text{ M Et}_4\text{NBF}_4$  in acetonitrile with a scan rate of  $1 \text{ mVs}^{-1}$ .

The CVs of the first activation are shown in Figure 1 bottom as well as the corresponding expansion of the electrode in Figure 2 bottom. In the first sweep both

<sup>1</sup> ETH Zürich

anode and cathode show negligible capacitance until a critical potential is reached. At this potential one can observe a large current peak, which is related to the activation of the GOpr material. The potential of the half maximum of this current peak is defined as the activation potential. During the activation one can also observe a massive swelling of the electrode, reaching a maximum expansion of approximately 55 % at the vertex potential of either anode or cathode. On the back sweep both electrodes show a capacitor like behavior with an average specific capacitance of  $150 \text{ Fg}^{-1}$ . During the back sweep the electrode shrinks by approximately 35 %. For the following cycles the achieved specific capacitance stays constant and is accompanied by a reversible swelling of 35 %. Therefore one can conclude that after the electrochemical activation the properties of the material have been modified in such way that it has a capacitor like behaviour over the whole investigated potential range. This activation is accompanied by a current peak and an irreversible expansion of the electrode in the order of 20 %.

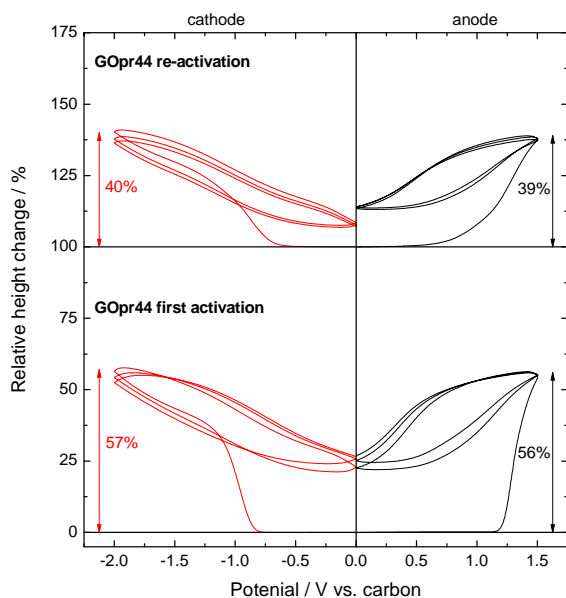


**Figure 2.** Dimensional changes of GOpr44 during the first three cycles for the first activation (bottom) and re-activation (top).

The pre activated electrodes were washed, dried and reassembled in an electrochemical cell. The resolving CVs are shown in Figure 1 top (shifted by  $1300 \text{ Fg}^{-1}$ ) and the according expansion in Figure 2 top (shifted by 100 %). One can see from the first sweep that anode and cathode have a slightly different behaviour compared to the first activation experiment. The cathode shows negligible capacitance at the beginning, followed by an activation process at a 180 mV positive shifted potential. After this re-activation the cathode shows the same behaviour as described above. The anode however shows a more or less steady increase of capacitance with increasing potential but no significant current peak which could be related to a re-activation. After reaching the vertex potential in the first cycle the anode has again a capacitor like behaviour. Beside this difference in the first sweep of the CV the anode as well as the cathode shows a significantly reduced irreversible expansion of the electrode followed by a reversible swelling of approximately 30 %, which is comparable to that during the first activation.

In addition to the electrochemical experiments X-ray diffraction was done on a washed unused electrode as well as on the washed anodically and cathodically activated electrodes. The resolving diffractograms are shown in Figure 3, each with a subtracted background and normalized to the height of the PTFE diffraction peak at  $18.2^\circ 2\theta$ . Comparing the activated electrodes with the unused baseline electrode it is obvious that the former  $d_{002}$  peak at  $20.3^\circ 2\theta$  has disappeared. In addition one could identify a new peak in the range of  $15.5$  to  $15.9^\circ 2\theta$ , which is more pronounced after the anodically activation. This signal might be a new  $d_{002}$  diffraction peak. By calculating the interlayer distance from these peak positions it seems that its value has been increased from  $4.4 \text{ \AA}$  to around  $5.6 \text{ \AA}$  during activation. This increase of approximately 27% fits nicely to the observed irreversible electrode expansion of approximately 20% during the first electrochemical activation.

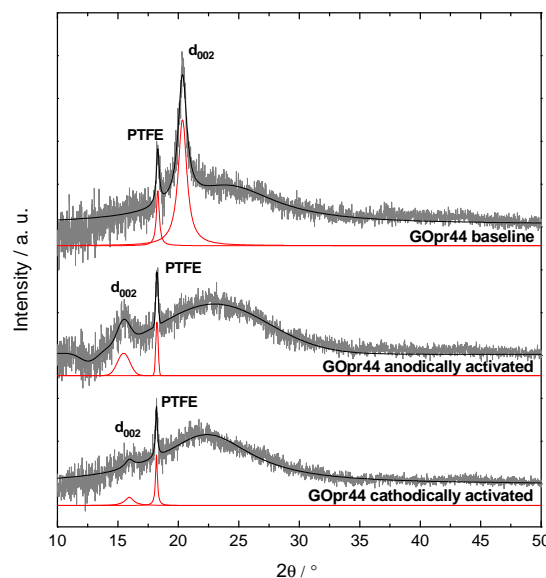


**Figure 3.** XRD diffractograms for GOpr44 electrodes showing the PTFE binder and the shifting  $d_{002}$  diffraction peak of GOpr44.

From these results one can conclude that the electrochemical activation seems to consist of an irreversible process, responsible for the peak shift of the  $d_{002}$  diffraction, as well as a reversible process, which might be due to ion and / or solvent intercalation during activation. The irreversible expansion of about 20% can be avoided by a pre-activation step, the reversible changes during charge and discharge, however, remain.

#### Acknowledgement

The authors would like to thank Swiss National Science Foundation (SNSF) for financial support (project # 200021\_126855/1).

#### References

- [1] A.K. Geim, K.S. Novoselov, Nature Materials **6** (3), 183–191 (2007).
- [2] T. Kaspar, Ph.D. thesis No. 18931, ETH Zürich (2010).
- [3] M.M. Hantel, T. Kaspar, R. Nesper, A. Wokaun, R. Kötz, Electrochem. Commun. **13** (1), 90-92 (2011).
- [4] M. Hahn, O. Barbieri, R. Gally, R. Kötz, Carbon **44** (12), 2523–2533 (2006).

# Characterization of full cell electrochemical hybrid energy storage systems

D. Cericola, P. Novák, R. Kötz, A. Wokaun

phone: +41 56 310 5172, e-mail: dario.cericola@psi.ch

The increasing importance of efficient energy storage has triggered the research of new electrochemical energy storage devices. In this context rechargeable batteries are the systems which can store the largest amount of energy per unit of mass or volume; however they are limited in power capability. In particular the rechargeable lithium-ion battery has a practical specific energy up to  $250 \text{ Whkg}^{-1}$ , and a specific power typically lower than  $1 \text{ kWkg}^{-1}$ . On the contrary the electrochemical capacitors (EC) are characterized by a very high specific power (typically higher than  $10 \text{ kWkg}^{-1}$ ) but its specific energy is typically low, around  $5 \text{ Whkg}^{-1}$ . Ideal electrochemical capacitors are charged by a purely electrostatic process which does not involve any charge transfer reaction and therefore an EC is inherently a high power device both during charge and discharge. A lithium-ion battery is charged with an electrochemical reaction which involves the diffusion of lithium ions in the bulk of the active materials. The diffusion processes in the bulk are slower than the formation of the double layer. The engineering of the lithium-ion battery allows to achieve moderately high discharge power; however, a battery is intrinsically a low power device [1,2].

The goal of having high power capability and high specific energy has been pursued by several authors with the hybridization of electrochemical capacitors and rechargeable battery in order to “combine” the high energy of the battery and the high power of the capacitor. The hybridization has been mainly carried out by combining one battery electrode with one capacitor electrode. This approach however corresponds to a serial connection of a capacitor with a battery and, thus, the specific charge will be limited by the capacitor and the specific power by the battery [3]. Another approach is to combine a capacitor with a battery in parallel. Simulations performed in our laboratory have shown that the parallel combination of commercially available devices allows for the transition from the capacitor behaviour to the battery behaviour and furthermore a significant advantage is achieved for pulsed applications [4].

There are no examples of parallel hybrids developed at the internal level (within one system) by combining battery and capacitor materials at the electrode level. Parallel hybrid systems based on bi-material electrodes have been assembled, characterized and compared with the respective serial hybrid, battery, and capacitor based on the same materials.

## Experimental

Full cell systems have been prepared using different electrode materials. The battery materials considered are a lithium titanate  $\text{Li}_4\text{Ti}_5\text{O}_{12}$  (LTO) for the negative electrode and a lithium manganese oxide  $\text{LiMn}_2\text{O}_4$  (LMO) for the positive electrode. The activated carbon (YP17) was used as capacitor material. The electrodes and bi-material electrodes were composed by 80% (w/w) of active materials, 10% (w/w) of conductive agents, and 10% of binder (PTFE). The active material loading was  $10 \pm 3 \text{ mgcm}^{-2}$ . The composition of the

different systems characterized is summarized in Table 1.

System	Positive electrode active material	Negative electrode active material	Positive Negative mass ratio
<i>Electrochemical capacitor</i>			
YP17/YP17	YP17 (100)	YP17 (100)	1.0
<i>Parallel hybrid systems using bi-material electrodes</i>			
LTO/LMOr75	LMO/YP17 (28/72)	LTO/YP17 (19/81)	1.2
LTO/LMOr50	LMO/YP17 (50/50)	LTO/YP17 (50/50)	1.3
<i>Battery</i>			
LTO/LMO	LMO (100)	LMO (100)	1.6
<i>Serial hybrid systems</i>			
LTO/YP17	YP17 (100)	LTO (100)	3.2
YP17/LMO	LMO (100)	YP17(100)	0.5

**Table 1.** Summary of the different systems characterized. Positive and negative electrode active materials and their corresponding composition (in mass ratio), positive to negative electrode mass ratio.

The electrochemical cells have been assembled in air, dried at  $120 \text{ }^\circ\text{C}$  at a pressure of 30 mbar, and then transferred, filled with the electrolyte (1 M  $\text{LiClO}_4$  in acetonitrile) and hermetically sealed in an Ar filled glove box ( $\text{H}_2\text{O}$  and  $\text{O}_2 < 1 \text{ ppm}$ ). The experimental characterization consisted in measuring constant power discharge at different power in order to draw Ragone plots for all the systems, and high current pulsed discharge cycles. A minimum cell voltage of 0.7 V and a maximum cell voltage of 3 V were applied. All the experiments have been performed with a potentiostat-galvanostat Biologic VMP3, France. The specific values reported are normalized with respect to the active material mass.

## Results

Ragone plot for the different systems reported in Table 1 are shown in Figure 1. The electrochemical capacitor (YP17/YP17 – black line) is on the material level the system with the smaller specific energy of  $30 \text{ Whkg}^{-1}$  and the higher specific power of  $50 \text{ kWkg}^{-1}$ , which is in agreement with the expectation. Similarly the battery (LTO/LMO – red line) is the device which shows the highest specific energy of  $150 \text{ Whkg}^{-1}$ . The specific power of the battery is limited to about  $3 \text{ kWkg}^{-1}$ . These values are in agreement with the expectation for a 3 V battery.

The parallel hybrid LTO/LMOr75 which has a composition close to a capacitor has an increased specific energy with respect to the capacitor (approximately doubled) while the specific power is slightly reduced (LTO/LMOr75 – blue line). When the amount of battery material is increased to 50% (w/w) in the case of the parallel hybrid LTO/LMOr50 the specific

energy increases to approximately  $90 \text{ Whkg}^{-1}$  (LTO/LMO<sub>r</sub>50 – green line), corresponding to three times the specific energy of the capacitor YP17/YP17. The specific power of the hybrid is again reduced with respect to the specific power of the capacitor to approximately  $20 \text{ kWkg}^{-1}$ .

Serial hybrid systems based on the same electrodes have been also characterized and reported in terms of Ragone plots in Figure 1. Both serial hybrids (LTO/YP17 – magenta line, and YP17/LMO – light blue line) present poor performance with respect to the other systems. The specific energy of the serial hybrids is 30 to  $50 \text{ Whkg}^{-1}$ . The specific power of the two serial hybrids is smaller than the specific power of the battery.

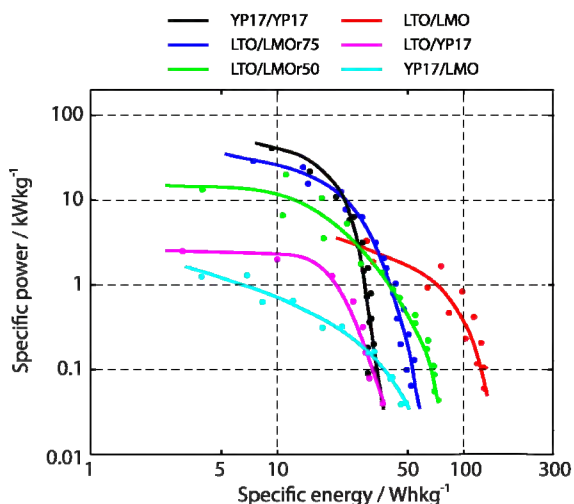


**Figure 1.** Ragone plots for the different systems summarized in Table 1.

The parallel hybrids as well as the capacitor and the battery have been discharged using a pulsed power profile. The pulse pattern is designed in order to completely discharge the system with a maximum of 250 pulses and a duty cycle of 10%. The pulse amplitude is varied between 25 and 400 C. The results are reported as specific energy available from the system during the pulse discharge against the pulse amplitude indicated as specific current in Figure 2.

It can be clearly seen that the battery (red line) is able to provide only  $55 \text{ Whkg}^{-1}$  when the pulse amplitude is  $1.5 \text{ Ag}^{-1}$  (25 C) and the energy drops to  $10 \text{ Whkg}^{-1}$  when the pulse amplitude is increased to  $3 \text{ Ag}^{-1}$  (50 C).

The capacitor (black line) is significantly less affected by the pulse amplitude and the available energy varies from 30 to  $10 \text{ Whkg}^{-1}$  by varying the pulse amplitude from 0.5 to  $8 \text{ Ag}^{-1}$  (25 to 400 C).

Both the parallel hybrid systems (blue and green line) outperform the battery and the capacitor as soon as the pulse amplitude exceeds  $2 \text{ Ag}^{-1}$ . The significant gain achieved with the parallel hybrids during pulsed application was ascribed to the recharging of the capacitor by the battery in the rest period for an external parallel hybrid [4]. The same effect was observed at the single electrode level in a model bi-material electrode [5]. It is straightforward that the recharging of the capacitor material by the battery material is also active for the bi-material electrode based on mixed active materials, on which the parallel hybrid devices are based.

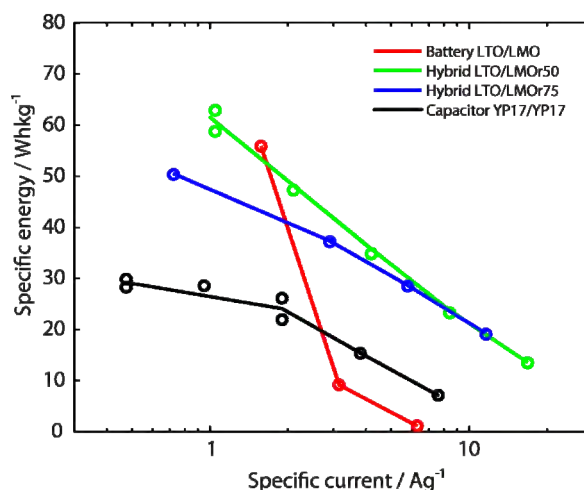


**Figure 2.** Specific energy available for a pulsed discharge against the current pulse amplitude for the parallel hybrid systems and the battery and capacitor references.

## Conclusions

The Ragone plots clearly show the benefit of the parallel hybridization with respect to the serial hybridization. The parallel hybridization is more flexible and allows to tune the specific energy and power between the capacitor and the battery according to the electrode composition. The serial hybridization is clearly not convenient since the specific energy of the hybrid is comparable to the specific energy of the capacitor while the specific power is comparable to or smaller than the specific power of the battery.

For pulsed applications the parallel hybrids clearly outperform both the battery and the capacitor. The parallel hybrids are clearly capable of delivering a remarkable high specific energy at highly demanding pulsed application exceeding the performance of both the battery and the capacitor.

## Acknowledgments

Swiss National Science Foundation is thanked for financial support (project no 200021-117607).

## References

- [1] M. Winter, R.J. Brodd, Chem. Rev. **104**, 4245-4269 (2004).
- [2] A. Burke, Electrochim. Acta **53**, 1083-1091 (2007).
- [3] M. Conte, Fuel Cell **10**, 806-818 (2010).
- [4] D. Cericola, P.W. Ruch, R. Kötz, P. Novák, A. Wokaun. J. Power Sources **195**, 2731-2736 (2010).
- [5] D. Cericola, P. Novák, A. Wokaun. R. Kötz, Electrochim. Acta **56**, 1588-1293. (2010).



# BATTERIES & SUPERCAPACITORS

## DIAGNOSTICS



# Neutron imaging of a complete lithium-ion cell with $\text{Li}_2\text{MnO}_3$ -stabilized $\text{Li}(\text{Ni}_x\text{Mn}_y\text{Co}_z)\text{O}_2$ cathode material vs. graphite

H. Sommer, A. Kaestner, E.H. Lehmann, P. Novák

phone: +41 56 310 2457, e-mail: petr.novak@psi.ch

The standard cathode material for present commercial lithium-ion batteries is layered  $\text{LiCoO}_2$ . Substitution of Co in  $\text{LiCoO}_2$  with Ni, Mn etc., compensates the high cost and high toxicity of Co.  $\text{Li}(\text{Mn}_{0.33}\text{Co}_{0.33}\text{Ni}_{0.33})\text{O}_2$  materials, called NMC, have attracted much interest because of their comparatively low cost, low toxicity, and high specific charge [1,2]. Thackeray introduced high specific charge materials ( $> 200 \text{ Ah kg}^{-1}$ ) by stabilizing layered  $\text{LiMO}_2$  with  $\text{Li}_2\text{MnO}_3$  thus forming a solid solution [1]. The electrochemical activation of  $\text{Li}_2\text{MnO}_3$  can be induced positive to 4.4 V vs.  $\text{Li/Li}^+$  and afford an overall specific charge of about  $330 \text{ Ah kg}^{-1}$  during initial charging. In this potential region a simultaneous extraction of lithium and oxygen from the  $\text{Li}_2\text{MnO}_3$  component is suggested [2]. To understand this fact, different analyses methods were applied. For example the irreversible oxidation at 4.5 V vs.  $\text{Li/Li}^+$  was further investigated with the differential electrochemical mass spectrometry (DEMS). This technique allows the qualitative analysis of the electrochemically developed gases in an electrochemical system, by using a mass spectrometer. Oxygen evolution is observed in the high voltage region but only during the first cycle while  $\text{H}_2$  and  $\text{CO}_2$  is evolved during the first and further cycles in the high voltage region. The formation of  $\text{H}_2$  and  $\text{CO}_2$  comes from the decomposition of electrolyte on both electrodes. The gaseous developments during cycling would increase the pressure in the cell. To verify this, the pressure development in a complete lithium-ion cell ( $\text{Li}_2\text{MnO}_3\text{-Li}(\text{Mn}_x\text{Ni}_y\text{Co}_z)\text{O}_2$  vs. graphite) was measured. The result of this measurement is shown in Figure 1.

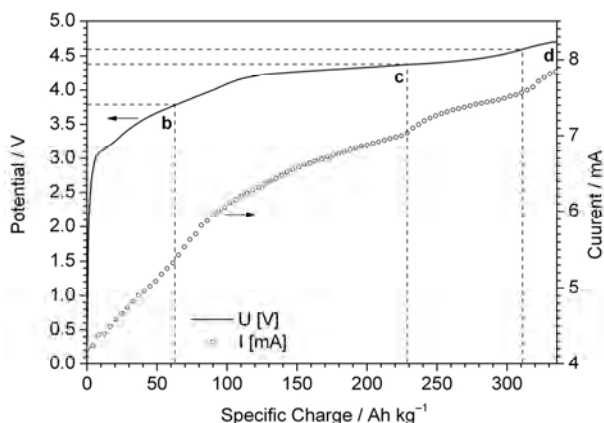


**Figure 1.** Pressure evolution in  $\text{Li}_2\text{MnO}_3\text{-Li}(\text{Mn}_x\text{Ni}_y\text{Co}_z)\text{O}_2$  vs. graphite cell with 1M  $\text{LiPF}_6$  EC:DMC (1:1) electrolyte. The current of the sensor (right scale) is proportional to the pressure.

The pressure, which is indicated by the electrical output of the sensor, increases during the initial charge. At the beginning the pressure in the cell increases due to the SEI (solid electrolyte interphase) formation. The SEI formation reaction is a decomposition reaction of the electrolyte on the graphite electrode. As can be seen, further charging leads to pressure increase at ca. 4.4 V (c), which might be the oxygen release. In addition, in the high voltage region labelled d (above 4.6 V) the pressure increases further due to the decomposition of

the electrolyte. To visualize these releases of gas, neutron imaging at the SINQ source of PSI was applied. Neutron imaging offers the ability of viewing the changes of the distribution of the liquid electrolyte inside a complete lithium-ion cell. Thus, this method allows us to observe the evolution of gas indirectly by a displacement of the electrolyte due to the gas formation.

## Experimental

The *in situ* neutron imaging experiments were performed in pouch cells. Self-standing films were used as electrodes for the electrochemical tests. For the preparation of the positive electrode a mixture of 70%  $\text{Li}_2\text{MnO}_3\text{-Li}(\text{Mn}_x\text{Ni}_y\text{Co}_z)\text{O}_2$  (BASF), 10% Super P and 20% KynarFlex all suspended in acetone was blade-coated onto a Teflon foil. The negative electrode consists of 90% SFG44 graphite (TIMCAL) and 10% binder (KynarFlex). After drying the self-standing films were pressed from both sides onto the current collector (aluminium mesh for the oxide electrode and copper mesh for the anode electrode) to produce the electrodes. The electrochemical cycling was carried out galvanostatically between 2.0 V and 4.8 V at a C/3 rate. The latest developments in neutron imaging realized at the ICON beamline [4] of the SINQ source made it possible to analyse the process during charging of a lithium-ion cell. All neutron radiograms were referenced to the radiogram of the open circuit voltage (OCV) in order to follow *in situ* the displacement of the electrolyte due to the evolution of gases.

## Results

With the applied experimental setup (through-plane imaging and pouch cells) an expected formation of oxygen for the studied electrode material is observable. In addition an evolution of gaseous products regarding to electrolyte degradation at high potentials is noticeable. The cell voltage of the pouch cell during the first cycle is shown in Figure 2.

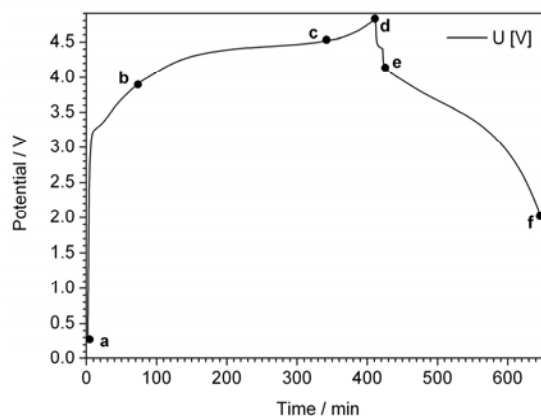


**Figure 2.** Cell voltage during the first galvanostatic cycle of a  $\text{Li}_2\text{MnO}_3\text{-Li}(\text{Mn}_x\text{Ni}_y\text{Co}_z)\text{O}_2$  electrode vs. graphite in a pouch cell with 1M  $\text{LiPF}_6$  EC:DEC:DMC (30:40:30 by wt.) electrolyte.

The labelled points correspond to the neutron images displayed in Figure 3. Image a corresponds to the initial

OCV image; however image b indicates the first gas evolution during the SEI formation. Subsequent charging to 4.5 V shows a slight increase of grey spots in the neutron image (image c) which might be the oxygen release from the electrochemical activation of  $\text{Li}_2\text{MnO}_3$ . At 4.8 V further spots appears on the images which shows a gas formation due to the electrolyte decomposition at high voltages on the oxide electrode and thus the extrusion of electrolyte in the peripheral area of the pouch cell. On the other hand, the discharge process shows only slight changes of the neutron images (images e and f).

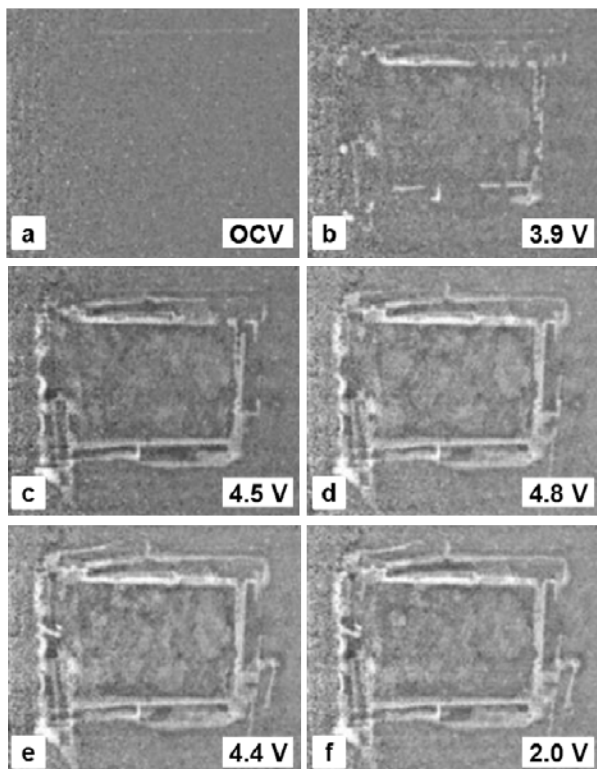


**Figure 3.** Neutron images of the initial cycle of a  $\text{Li}_2\text{MnO}_3\text{-Li}(\text{Mn}_x\text{Ni}_y\text{Co}_z)\text{O}_2$  electrode vs. graphite (SFG44, TIMCAL) in a pouch cell with 1M  $\text{LiPF}_6$  EC:DEC:DMC (30:40:30) electrolyte.

For the second cycle, only at high voltages there is an observable difference in neutron images, as illustrated in Figure 4. This is due to the electrolyte decomposition reaction at high potentials on the  $\text{Li}_2\text{MnO}_3\text{-Li}(\text{Mn}_x\text{Ni}_y\text{Co}_z)\text{O}_2$  electrode. Moreover, it can be seen that charging to high potentials has a noticeable negative influence on the lithium-ion battery.

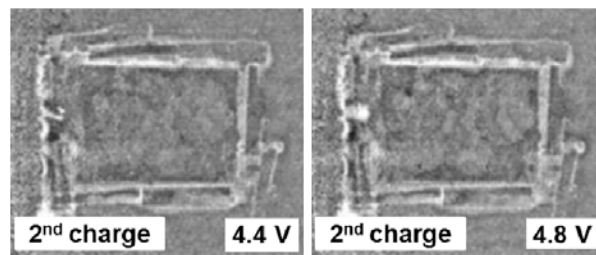


**Figure 4.** Neutron images of the 2<sup>nd</sup> charge at the potentials 4.4 V and 4.8 V vs.  $\text{Li/Li}^+$ .

The result of this experiment is in good agreement with the outcome of the DEMS investigations and the pressure measurement. The neutron imaging provides additional access to the processes in lithium-ion batteries with an imaging method. In this case, the course of gas releases during cycling is observable *in situ* and gives a sense about the aging processes in lithium-ion batteries.

### Conclusion

Neutron imaging was applied to investigate the processes in an electrochemical cell during charging. It was possible to observe the gas evolution process during the first charge and discharge. As a first test a simplified system was studied. Future experiments will be to verify the gas evolution in plane with neutron imaging.

### Acknowledgments

The authors are very grateful for the financial support from BASF SE.

### References

- [1] J. Shim, K.A. Striebel, J. Power Sources **122**, 188 (2003).
- [2] H. Cao, B. Xia, N. Xu, C. Zhang, J. Alloys and Compounds **376**, 282 (2004).
- [3] M.H. Rossouw, M.M. Thackeray, Mater. Res. Bull. **26**, 463 (1991).
- [4] G. Kuehne, G. Frei, E. Lehmann, P. Vontobel, A. Bollhalder, U. Filges, M. Schild, Swiss Neutron News **28** (2008).

## Structural investigations of $\text{Li}_2\text{MnO}_3\text{-Li}(\text{Mn}_x\text{Ni}_y\text{Co}_z)\text{O}_2$ – neutron diffraction, *in situ* X-ray diffraction and *in situ* Raman spectroscopy

C. Villevieille, H. Sommer, H. Schneider, P. Novák

phone: +41 56 310 2410, e-mail: [claire.villevieille@psi.ch](mailto:claire.villevieille@psi.ch)

The standard cathode material for present commercial lithium-ion batteries is layered  $\text{LiCoO}_2$ . So researchers worldwide are searching for high-capacity, safe, and inexpensive replacement for  $\text{LiCoO}_2$ . Nowadays, a layered transition-metal oxide  $\text{LiNi}_{1/3}\text{Mn}_{1/3}\text{Co}_{1/3}\text{O}_2$  (NMC) with hexagonal structure, first introduced by Ohzuku's group in 2001 as a candidate of cathode materials [1,2], has attracted significant interest, because the combination of nickel, manganese, and cobalt can provide many advantages compared with  $\text{LiCoO}_2$ , such as lower cost, less toxicity, milder thermal stability at charged state, better stability during cycling even at elevated temperature, and higher reversible capacity. This layered  $\text{Li}(\text{Mn}_x\text{Ni}_y\text{Co}_z)\text{O}_2$  oxide is composed of alternating slabs of  $\text{TMO}_6$  octahedra (TM = transition metal) and  $\text{LiO}_6$  octahedra. This layered oxide, NMC, is believed to be the next generation of cathode material for lithium-ion batteries. Another example of this compound class is the  $\text{Li}_2\text{MnO}_3$ -stabilized NMC material [3]. The  $\text{Li}_2\text{MnO}_3$  component fulfills an important role in the electrochemical performance of  $\text{Li}_2\text{MnO}_3$ -stabilized NMC materials: 1) the ability to activate the  $\text{Li}_2\text{MnO}_3$  component by extracting  $\text{Li}_2\text{O}$  in a controlled manner; 2) any inactivated  $\text{Li}_2\text{MnO}_3$  in the composite structure will act as a reservoir for excess lithium; 3) the  $\text{Li}_2\text{MnO}_3$  units not only serve to stabilize the capacity generating NMC regions of the electrode, but also act as solid electrolyte constituents to facilitate  $\text{Li}^+$ -ion transport through the structure [4-6].

### Experimental

The *in situ* XRD measurement were performed in a "coffee bag" cell using an automatic system, as described elsewhere [7]. The study was carried out at the Swiss Light Source (SLS) at the MS-powder beamline (X04SA) at a wavelength of 0.7085 Å with the aim to understand the structural changes of the material during cycling. The neutron diffraction was performed at the SINQ source at PSI (HRPD). The *in situ* Raman spectroscopy was performed in the cell, which allows for recording the Raman spectra from the backside of the electrode.

### Structural characterization of the starting material

In order to optimize the performance of  $\text{Li}_2\text{MnO}_3$ -stabilized  $\text{Li}(\text{Mn}_x\text{Ni}_y\text{Co}_z)\text{O}_2$  materials it is important to have the information about the structure of the material and the ratio between the  $\text{Li}(\text{Mn}_x\text{Ni}_y\text{Co}_z)\text{O}_2$  and  $\text{Li}_2\text{MnO}_3$  components. Therefore we investigated the structure of the starting material using both synchrotron X-ray diffraction and neutron diffraction, respectively (Figure 7). The synchrotron XRD pattern of  $\text{Li}_2\text{MnO}_3\text{-Li}(\text{Mn}_x\text{Ni}_y\text{Co}_z)\text{O}_2$  is depicted in Figure 7b and reveals sharp Bragg peaks, indicative of the high crystallinity of the sample. The peaks could all be indexed on the basis of a rhombohedral phase for the  $\text{Li}(\text{Mn}_x\text{Ni}_y\text{Co}_z)\text{O}_2$  cell with the following refined lattice parameters:  $a = b = 2.852(1)$  Å,  $c = 14.235(2)$  Å,  $R\text{-}3m$  space group ( $V = 100.34(2)$  Å<sup>3</sup>), and a monoclinic

phase for the  $\text{Li}_2\text{MnO}_3$  cell with the following refined lattice parameters  $a = 4.940(2)$  Å,  $b = 8.556(2)$  Å,  $c = 5.025(2)$  Å,  $\beta = 109.28^\circ$ ,  $C2/m$  space group and a cell volume of 200.5 Å<sup>3</sup>.

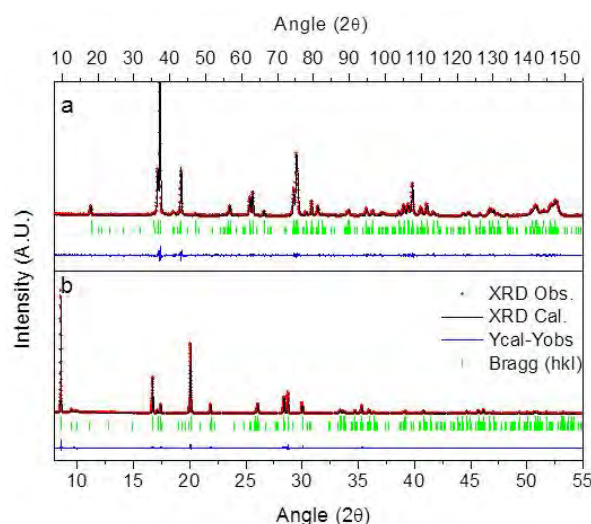


**Figure 7.** Refinement of the  $\text{Li}_2\text{MnO}_3\text{-Li}(\text{Mn}_x\text{Ni}_y\text{Co}_z)\text{O}_2$  electrode material obtained by a) neutron diffraction and b) synchrotron X-ray diffraction.

We have already tried to analyze the pattern of  $\text{Li}_2\text{MnO}_3\text{-Li}(\text{Mn}_x\text{Ni}_y\text{Co}_z)\text{O}_2$  starting material using synchrotron X-ray diffraction at the SLS, but we were not able to refine the amount of oxygen and lithium. It is a well-known challenge of X-ray diffraction that the scattering depends on the number of electrons in particular atom and decreases for lighter atoms like lithium, carbon, and also oxygen. To overcome this challenge we applied neutron diffraction at the SINQ source at PSI (Figure 7a). The refinement of the neutron pattern is in very good agreement with the data given in the literature as can be seen in table 1.

Phase	a	b	c	$\beta$	%
NMC	2.855(1)	2.855(1)	14.229(2)	120	52(1)
$\text{Li}_2\text{MnO}_3$	4.939(2)	8.554(1)	5.028(2)	109.33(2)	48(1)
Refinement parameters $\chi^2=2.48$ $R_{wp}=8.67$ , $R_{bragg}=2.15$					

**Table 1.** Refined parameters for  $\text{Li}_2\text{MnO}_3\text{-Li}(\text{Mn}_x\text{Ni}_y\text{Co}_z)\text{O}_2$ .

### *In situ* structural characterization

The charging curve of the *in situ* XRD experiment is detailed in Figure 8. The collected patterns are plotted in Figure 9.

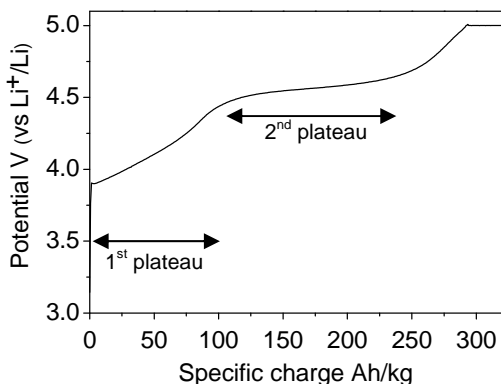


**Figure 8.** Charging curve for the  $\text{Li}_2\text{MnO}_3\cdot\text{Li}(\text{Mn}_x\text{Ni}_y\text{Co}_z)\text{O}_2$  electrode in PC/DMC 1M  $\text{LiPF}_6$  against Li counter electrode.

The changes in the sequence of patterns show some slight shift of certain peaks, especially the peaks indexed in (00l) plane. The 003 peak (2Theta angle of 8.3 to 8.7) of the  $\text{Li}_2\text{MnO}_3\cdot\text{Li}(\text{Mn}_x\text{Ni}_y\text{Co}_z)\text{O}_2$  material is plotted in Figure 9a. It can be seen that the 003 peak shifts toward lower 2Theta angle during the first plateau. This indicates the expansion of the c axis during charging. The results for the XRD measurements for the second plateau (4.5 V) are not easy to understand. In this region a simultaneous release of lithium and oxygen is suggested. The oxygen release was proven with the differential electrochemical mass spectrometry (DEMS) and should have a consequence for the structure of the sample. So far, it is not possible to detect this issue in the *in situ* XRD experiment. It should, however, be noted that the Full Width Half Maximum (FWHM) is two times higher than the values at the beginning of the XRD experiment.

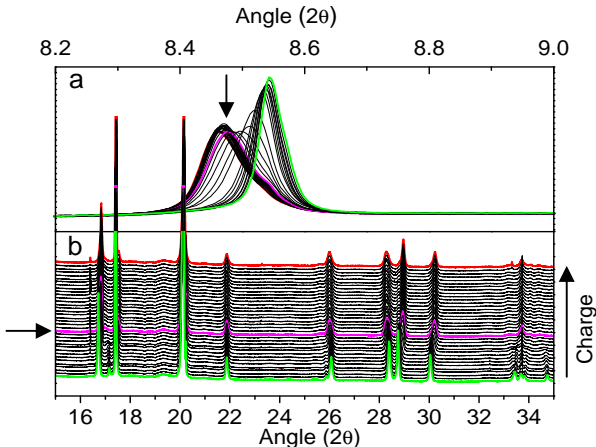


**Figure 9.** *In situ* synchrotron X-ray diffraction patterns collected during the first charge of the lithium-ion cell, a) focused on the 003 peak on the  $\text{Li}_2\text{MnO}_3\cdot\text{Li}(\text{Mn}_x\text{Ni}_y\text{Co}_z)\text{O}_2$  material, b) for the whole range of theta (wavelength 0.7085 Å).

Refinement of the patterns reveals a decrease of the a parameter and an increase of the c parameter during the first plateau. This is due to the oxidation of the transition metals which leads to a diminution of the metal-metal distance and as a consequence to a decrease of the a parameters. For the second plateau, we just observed a decrease of the intensity and an increase of the FWHM. The expected oxygen release during the second plateau is not observable in this XRD experiment. We propose two hypotheses to explain this fact:

- Oxygen vacancies are created leading to a reordering inside the electrode (oxygen diffusion from the core to the surface)

- Oxygen vacancies are just an intermediate step during cycling leading to a reordering of an oxygen structure (cations diffusion from surface to the core)

*In situ* Raman spectroscopy has proven to be a useful method to follow structural changes occurring during cycling. To prove the concept, we characterize a typical sample of the NMC family with Raman spectroscopy. The Raman spectra of the *in situ* measurement and of the reference  $\text{Li}_2\text{MnO}_3$  is illustrated in Figure 10. It can be seen that the OCV spectrum is a combination of the spectrum of  $\text{Li}_2\text{MnO}_3$  and the layered  $\text{LiMO}_2$ . In the initial charging the  $\text{Li}_2\text{MnO}_3$  peaks disappear (4.4 V) and only the  $\text{MO}_2$  are detectable. By contrast during discharging only the peaks for layered  $\text{LiMO}_2$  are observable.

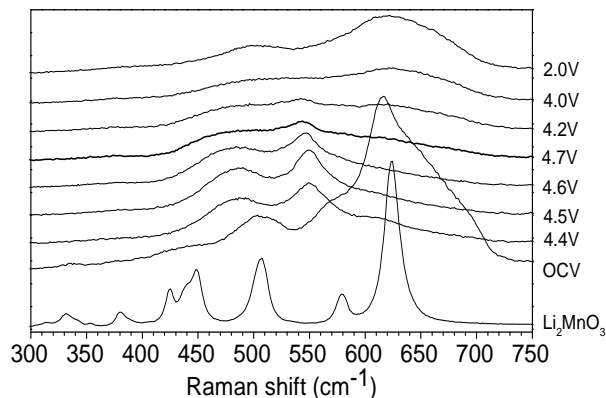


**Figure 10.** Evolution of the *in situ* Raman spectra of  $\text{Li}_2\text{MnO}_3\cdot\text{Li}(\text{Mn}_x\text{Ni}_y\text{Co}_z)\text{O}_2$  electrode.

## Conclusion

The characterization of the starting phase was successful with neutron diffraction. The presented XRD study confirms the evolution of the cell parameters but does not provide clearly the ratio of Li and oxygen during cycling. Therefore neutron diffraction is on-going to estimate this matter. However, the Raman spectroscopy documents the structural changes on the surface but does not provide data of the bulk of the material.

## Acknowledgments

The authors are very grateful for the financial support from BASF SE.

## References

- [1] T. Ohzuku, Y. Makimura, Chem. Lett. **30**, 642 (2001).
- [2] N. Yabuuchi, T. Ohzuku, J. Power Sources **119–121**, 171 (2003).
- [3] M. H. Rossouw, M. M. Thackeray, Mater. Res. Bull. **26**, 463 (1991).
- [4] N. Tran, L. Croguennec, C. Jordy, P. Biensan, C. Delmas, Solid State Ionics **176**, 1539 (2005).
- [5] Z. Lu, D. D. MacNeil, J. R. Dahn, Electrochem. Solid State Lett. **4**, A200 (2001).
- [6] D. D. MacNeil, Z. Lu, J. R. Dahn, J. Electrochem. Soc. **149**, A1332 (2002).
- [7] F. Rosciano, M. Holzappel, H. Kaiser, W. Schweifele, P. Ruch, M. Hahn, P. Novák, J. Synchron. Rad. **14**, 488 (2007).

# Combined *in situ* FTIR and Raman microscopy of electrode materials

H. Schneider, A. Hintennach, P. Maire, P. Novák

phone: +41 56 310 2115, e-mail: holger.schneider@psi.ch

*In situ* Raman microscopy has been used with great success to elucidate the processes occurring both at battery cathodes and anodes while cycling (1). In contrast to other analytical methods such as XRD measurements it is a surface sensitive method, with a typical penetration depth in the order of micrometers and does not provide data of the bulk of the materials. Raman spectroscopy proved to be very useful when the local structure was of specific interest. The structure of an electrode can be probed *in situ* with high spatial resolution in the order of  $(5\ \mu\text{m})^3$ . This has been shown, e.g., in a multipoint measurement of a disordered graphitic material, showing intercalation heterogeneities between several points examined (2).

*In situ* FTIR spectroscopy has proven to be a useful tool to follow changes occurring at the electrode materials while cycling as well. Like Raman microscopy, it is a surface sensitive method. The information which can be drawn from the FTIR spectra is complementary to the insights from Raman experiments. However, in contrast to Raman microscopy, to the best of our knowledge all *in situ* FTIR electrochemical experiments performed so far have not made use of a microscope. Therefore, they sample the changes occurring on the whole surface of the working electrode or a selected part of it but they do not deliver any spatial information.

## Experimental

We designed a new cell for combined *in situ* Raman and FTIR microscopy, which allows for both *in situ* FTIR and *in situ* Raman microscopic characterization of the same spot of the electrode. A schematic drawing of the newly designed cell is shown in Figure 1.

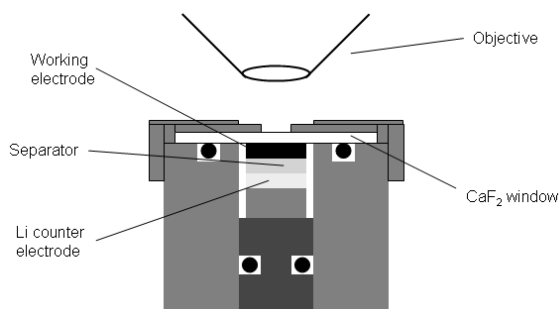


**Figure 1.** Schematic drawing of the newly designed cell for the combined *in situ* acquisition of FTIR and Raman spectra of battery electrodes.

For the FTIR experiments, we use an IR all-reflecting objective (ARO, 15 $\times$ ). The electrode material is pressed on a metal (copper or aluminum) mesh, which allows for recording the infrared spectra from the backside of the electrode. The lithium counter electrode is contacted and held in place from the bottom by a plunger which is insulated by a rubber gasket from the cell body. The  $\text{CaF}_2$  window employed is transparent for both infrared and visible light. Therefore, the new experimental setup enables us to perform both *in situ* FTIR and Raman measurements of the same sample with spatial resolution. (The resolution in the infrared

range is not as good as for the Raman microscopy, typical sample sizes are in the order of  $10\ \mu\text{m}$ – $100\ \mu\text{m}$ ).

## Results

For instance, the growth of the SEI layer on a single graphite particle can be monitored, potentially even distinguishing between basal and edge planes, while the lithium intercalation can be followed by Raman spectroscopy on the same grain. First promising tests in these directions have been performed in our laboratory, as can be seen from Figure 2, displaying infrared spectra from the surface of a graphite electrode while cycling (but without high spatial resolution in this case).

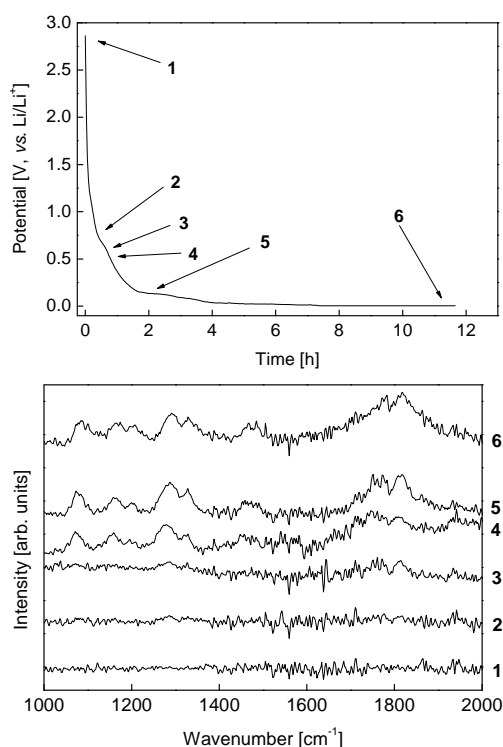


**Figure 2.** Top: Charging curve of a graphite electrode in 1M  $\text{LiPF}_6$ , EC:DMC 1:1 at 25 °C; bottom: *In situ* FTIR spectrum monitored on the surface of the same graphite electrode while charging.

## Acknowledgments

The authors are very grateful for the technical assistance from Hermann Kaiser and his help in realizing the described experimental setup.

## References

- [1] R. Baddour-Hadjean, J.-P. Pereira-Ramos, Chem. Rev. **110**, 1278 (2010).
- [2] L.J. Hardwick, H. Buqa, P. Novák, Solid State Ionics **177**, 2801 (2006).

# Study of overcharge behavior of $\text{Li}_{1+x}(\text{Ni}_{1/3}\text{Mn}_{1/3}\text{Co}_{1/3})_{1-x}\text{O}_2$ using *in situ* synchrotron diffraction

V. Godbole, J.-F. Colin, P. Novák

phone: +41 56 310 5426, e-mail: vikram.godbole@psi.ch

Previous study on NMC [ $\text{Li}_{1+x}(\text{Ni}_{1/3}\text{Mn}_{1/3}\text{Co}_{1/3})_{1-x}\text{O}_2$ ,  $x \geq 0$ ] reported that the overlithiated NMC ( $x=0.1$ ) has better cycling stability as compared to the stoichiometric ( $x=0$ ) one when cycled between 2.5-5.0 V vs.  $\text{Li}/\text{Li}^+$  [1]. Differential Electrochemical Mass Spectrometry (DEMS) measurements on these compounds during cycling revealed that there is an  $\text{O}_2$  release for the overlithiated ( $x=0.1$ ) NMC during its first charge till 5.0 V vs.  $\text{Li}/\text{Li}^+$ . This study concentrates on structural changes occurring in NMC materials ( $0 \leq x \leq 0.13$ ) when cycled till 5.0 V vs.  $\text{Li}/\text{Li}^+$ ; overcharged above the usual upper potential limit of 4.5 V vs.  $\text{Li}/\text{Li}^+$ .

## Experimental

11 different compositions of  $\text{Li}_{1+x}(\text{Ni}_{1/3}\text{Mn}_{1/3}\text{Co}_{1/3})_{1-x}\text{O}_2$  ( $0 \leq x \leq 0.10$ , varied by 0.01) were synthesized, along with the overlithiated sample with  $x=0.13$ , where almost all the Ni in the structure is oxidized from +2 to +3 oxidation state, using synthesis route described elsewhere [2]. These NMC compounds were labeled as SLS-XX, where XX denotes the percentage of overlithiation, e.g. stoichiometric NMC ( $x=0$ ) is SLS-00 and overlithiated NMC ( $x=0.10$ ) being SLS-10, and so on, and will be referred to by these abbreviations in rest of the report. The *in situ* synchrotron diffraction studies were conducted on a range of NMC compounds in a "coffee bag" cell design using an automatic sample changer [3], as described earlier [2]. For the *ex situ* measurements SLS-00 and SLS-10 samples were charged at C/100 rate with respect to their theoretical specific charges till 5.0 V vs.  $\text{Li}/\text{Li}^+$  in standard electrochemical cells. The cells were then disassembled, washed with DMC, dried and then used for *ex situ* synchrotron diffraction measurements. The synchrotron diffraction measurements were performed at the MS-powder beamline (X04SA) at SLS, PSI Villigen at a wavelength of 0.7085 Å and a spot size of 0.5 mm × 0.5 mm. The data acquisition time for the *in situ* and *ex situ* measurements was 40s and 240s respectively.

## Results

NMC crystallizes in  $R\bar{3}m$  space group (O3 phase). Figure 1 shows the cell parameters for sample with different initial lithium content ( $1+x$ ) in  $\text{Li}_{1+x}(\text{Ni}_{1/3}\text{Mn}_{1/3}\text{Co}_{1/3})_{1-x}\text{O}_2$ . As the value of  $x$  increases more and more  $\text{Ni}^{2+}$  ( $r_{\text{Ni}^{2+}} = 0.69 \text{ \AA}$ ) is oxidized into  $\text{Ni}^{3+}$  ( $r_{\text{Ni}^{3+}} = 0.56 \text{ \AA}$ ), which leads to decrease in the cell parameters. Figure 2 illustrates the *in situ* diffraction patterns recorded for SLS-13 during its 1<sup>st</sup> cycle between 2.5-5.0 V vs.  $\text{Li}/\text{Li}^+$ . New peaks are seen to appear after charging the sample positive to 4.5 V. After careful analysis these new peaks could be assigned to the O1 phase ( $P\bar{3}m1$ ). During the discharge slight shift in the cell parameter for the O1 phase was observed, however these peaks did not disappear completely, indicating that the phase transformation of the O3 phase to the O1 phase is not a completely reversible reaction.

Figure 3 shows the evolution of cell parameters for the O3 and O1 phase of SLS-00 and SLS-13 during the

first charge till 5.0 V vs.  $\text{Li}/\text{Li}^+$ . As 2-3 phases coexisted in the material, because of use of aluminium current collector with a hole [2], the cell parameter for the most advanced/delithiated O3 phase has been reported. It can be seen that SLS-00 shows similar evolution in cell parameters as reported earlier for chemically delithiated samples, wherein the  $c$  parameter increases while the  $a$  parameter drops until a certain potential, after which the cell parameter evolution is reversed [4,5]. The cell parameters for SLS-13 on the other hand reach a stable value towards the end of the first charge. The overall unit cell volume change (%) for all the samples is in agreement to those reported earlier for similar compositions [5]. However unlike the previous report [5], O1 phase was detected in our samples charged till 5.0 V vs.  $\text{Li}/\text{Li}^+$  owing to the use of synchrotron diffraction.

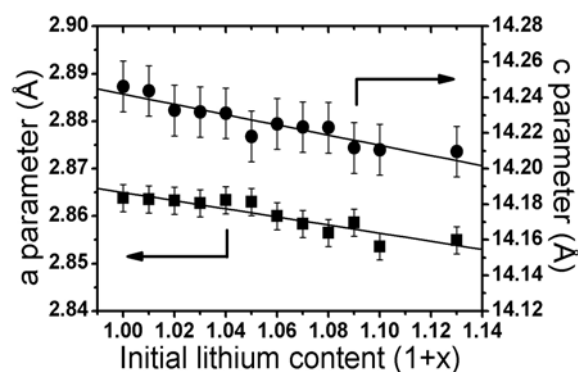


Figure 1. Cell parameters for samples with different initial lithium content ( $1+x$ ) in  $\text{Li}_{1+x}(\text{Ni}_{1/3}\text{Mn}_{1/3}\text{Co}_{1/3})_{1-x}\text{O}_2$ .

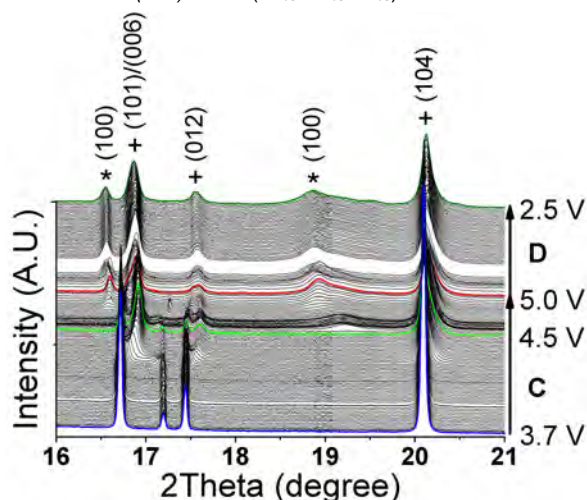
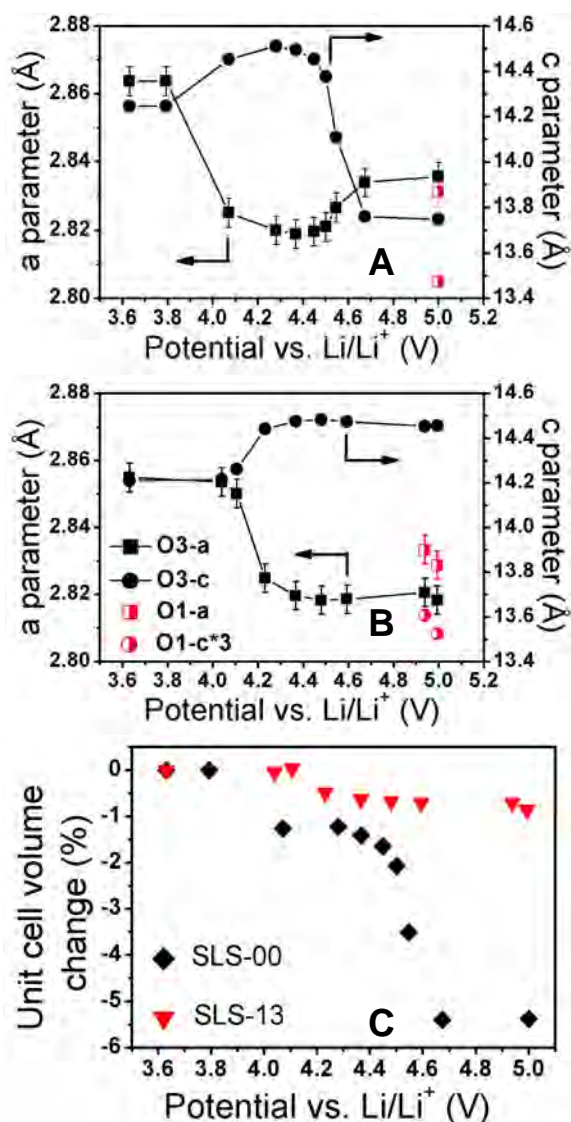


Figure 2. XRD patterns recorded *in situ* during the first cycle of SLS-13 [ $\text{Li}_{1.13}(\text{Ni}_{1/3}\text{Mn}_{1/3}\text{Co}_{1/3})_{0.87}\text{O}_2$ ] (\* marks the new O1 phase and + indicates the peaks for most delithiated O3 phase). C= 1<sup>st</sup> charge (delithiation), D= 1<sup>st</sup> discharge (lithiation).



**Figure 3.** Evolution of cell parameters for (A) SLS-00 and (B) SLS-13. *c* parameter for O1 phase has been multiplied by 3 for comparison. (C) Percentage unit cell volume change is also shown for the O3 phase in SLS-00 and SLS-13.

The O1 phase was detected in all the NMC samples including SLS-00. However as seen from Figure 4 more negative is the potential for detection of the O1 phase. This suggests that overlithiation somehow destabilizes the O3 structure so that O1 phase is formed at more negative potential.

Figure 5 reports the *ex situ* patterns recorded for SLS-00 and SLS-10 powders and electrodes after 1<sup>st</sup> charge till 5.0 V vs. Li/Li<sup>+</sup>. Peaks corresponding to the Li<sub>2</sub>MnO<sub>3</sub> ordering in the transition metal slabs of the O3 phase are clearly visible in the SLS-10 sample, while none are seen for SLS-00. The Li<sub>2</sub>MnO<sub>3</sub> ordering is usually not seen using lab diffractometer for such high Co content and low overlithiation, owing to the structural complexity in these layered compounds [6]. The *ex situ* pattern recorded at the end of 1<sup>st</sup> charge, reveals loss of Li<sub>2</sub>MnO<sub>3</sub> ordering for the SLS-10 sample. The extraction of Li from the Li<sub>2</sub>MnO<sub>3</sub> ordering is suggested to proceed via simultaneous removal of oxygen from the structure to compensate for the charge balance [7,8], which helps us explain the previously reported oxygen loss in overlithiated NMC (x=0.1) [1].

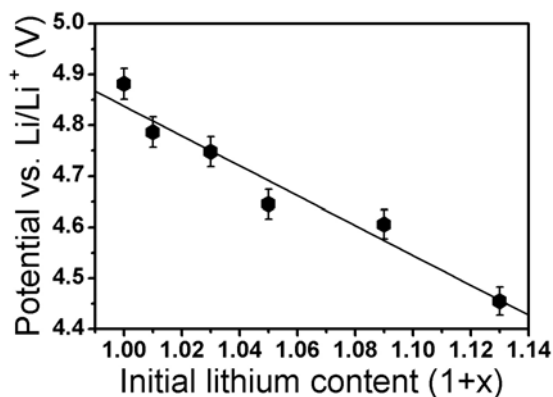


**Figure 4.** Potential for detection of O1 phase for different initial lithium content (1+x) in Li<sub>1+x</sub>(Ni<sub>1/3</sub>Mn<sub>1/3</sub>Co<sub>1/3</sub>)<sub>1-x</sub>O<sub>2</sub>.

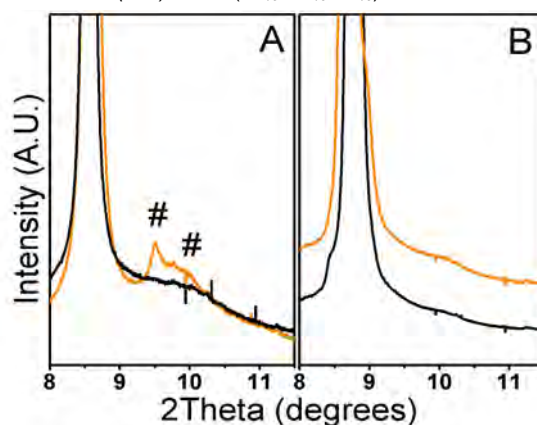


**Figure 5.** Part of the *ex situ* synchrotron patterns for (A) SLS-00 (DARK) and SLS-10 (LIGHT) powders and (B) SLS-00 and SLS-10 samples after 1<sup>st</sup> charge. # are peaks from the Li<sub>2</sub>MnO<sub>3</sub> ordering in the O3 phase.

## Conclusion

Two irreversible reactions viz. transformation of part of O3 phase to the O1 phase and loss of Li<sub>2</sub>MnO<sub>3</sub> ordering in the overlithiated sample were identified by overcharge study of the NMC samples till 5.0 V. Despite these structural changes the overlithiated NMC still delivers better charge retention as compared to the stoichiometric one, and hence is the more suitable candidate of the two for use in high voltage battery.

## References

- [1] F. La Mantia, F. Rosciano, N. Tran, P. Novák, *J. Appl. Electrochem.* **38**, 893–896 (2008).
- [2] V. Godbole, J.-F. Colin, P. Novák, *PSI Electrochemistry Laboratory Annual Report 2009*, 63-64 (2010).
- [3] F. Rosciano, M. Holzapfel, H. Kaiser, W. Scheifele, P. Ruch, M. Hahn, R. Kötz, P. Novák, *J. Synchrotron Rad.* **14**, 487-491 (2007).
- [4] S.C. Yin, Y. H. Rho, I. Swainson, L.F. Nazar, *Chem. Mater.* **18**, 1901-1910 (2006).
- [5] J.-M. Kim, N. Kumagai, Y. Kadoma, H. Yashiro, *J. Power Sources* **174**, 473-479 (2007).
- [6] M.M. Thackeray, S.H. Kang, C.S. Johnson, J.T. Vaughey, S.A. Hackney, *Electrochem. Comm.* **8**, 1531-1538 (2006).
- [7] Z. Lu, J.R. Dahn, *J. Electrochem. Soc.* **149**, A815-A822 (2002).
- [8] C.S. Johnson, N. Li, C. Lefief, M.M. Thackeray, *Electrochem. Comm.* **9**, 787-795 (2007).

## Effect of water on capacitance fading for supercapacitors using propylene carbonate as solvent

R. Kötzt, D. Cericola, D. Weingarth, A. Foelske-Schmitz, A. Wokaun

phone: +41 56 310 2057, e-mail: ruediger.koetz@psi.ch

Electrochemical double layer capacitors (EDLCs) are electrochemical energy storage devices characterized by high specific power but low specific energy when compared to batteries. In addition EDLCs provide an unsurpassed cycle stability of up to a million full charge discharge cycles with a capacitance loss of less than 20%. Such high cycle stability requires avoiding any possible side reaction originating for example from electrolyte impurities. Because the effect of electrolyte impurities on the EDLC lifetime has not been studied yet in detail, manufacturers use electrolytes as pure as possible.

The presence of water is one of the possible impurities, which will result in side reactions, most probably by the water splitting reaction or by hydrolysis of other electrolyte components such as the BF<sub>4</sub><sup>-</sup> ion. At present electrolytes containing 20-30 ppm of water are considered to be clean within a reasonable cost frame.

However, water can also be introduced into the EDLC cell from other components such as the activated carbon electrode, the separator or the housing. Therefore, the drying process of the cell components before filling with electrolyte is rather critical. The effect of the drying procedure on capacitor stability was studied by Zuckerbrod [1] and it was found that temperatures of 120°C and above are necessary for good EDLC performance.

For EDLC using graphite water contaminations in propylene carbonate (PC) based electrolyte were found by Wang and Yoshio [2] to result in significant initial capacitance loss, which was mainly attributed to the exfoliation of the graphite.

In a divided capacitor cell where the anode and cathode compartments were separated Ishimoto et al. [3] discovered that after constant voltage hold experiments the water content in the anode compartments increased to 300 ppm and decreased to 2 ppm for the negative electrode compartment. From this result it was concluded that water is consumed at the negative electrode to form H<sub>2</sub> and that water is released from the porous AC structure of the positive electrode.

In this communication we report about EDLC aging experiments in PC based electrolyte at 2.75 V cell voltage.

### Experimental

Electrochemical aging experiments were performed on activated carbon based electrochemical double layer capacitors. The active material used was the activated carbon YP17 from Kuraray chemicals – Japan. Electrodes with a diameter of 12 mm were punched out from a ~ 500 µm thick sheet of bound electrode material based on 90 wt.% of YP17 and 10 wt.% of poly tetrafluoroethylene (PTFE, Sigma-Aldrich) as binder.

The electrochemical cells were prepared by sandwiching two electrodes separated by a 30 µm thick cellulose based separator (Maxwell Technologies, Switzerland) between two spring loaded titanium

current collectors. Carbon coated aluminium foil (Gaia Akkumulatorenwerke, Germany) was placed between the titanium current collector and the carbon electrode in order to improve the contact. Experiments were performed in a three-electrode arrangement. Activated carbon was used as quasi-reference [4]. The mean active material loading was  $45 \pm 5 \text{ mgcm}^{-2}$ . Electrochemical cells were assembled in air and then dried at 120°C at a pressure of 30 mbar for 12 h. After transferring the cells into an Ar filled glove box (H<sub>2</sub>O and O<sub>2</sub> < 1 ppm), they were filled with the proper electrolyte and hermetically sealed.

The experiments were performed with dry as well as water contaminated electrolytes. The water contamination was obtained by adding high purity water (resistance > 18 MΩcm) in the proper amount to the dry electrolytes. The “dry” electrolytes had a water content of less than 30 ppm. The electrolyte used in the experiments was Et<sub>4</sub>NBF<sub>4</sub> in PC (<30 ppm H<sub>2</sub>O), and Et<sub>4</sub>NBF<sub>4</sub> in PC contaminated with 850 ppm H<sub>2</sub>O.

The aging experiments were performed as described before [5].

Nitrogen physisorption experiments were performed post mortem on the washed electrode using an Autosorb-1 (Quantachrome Instruments, USA). The recorded isotherms were evaluated according to the non-local density function theory (NLDFT) algorithm implemented in the AS1WIN software package (Quantachrome Instruments, USA) assuming the pore structure being a combination of slit and cylindrical shaped pores.

Chemical analysis of the aged and washed electrodes was performed using X-ray photoelectron spectroscopy (XPS) (ESCALAB 220iXL from Thermo Scientific, USA, formerly V.G. Scientific) by means of monochromatized Al Kα (1486.6 eV) radiation.

### Results

In order to study the effect of water contaminations on EDLC capacitance fading we investigated the aging of activated carbon (AC) based cells in PC electrolyte at a cell voltage of 2.75 V. The effect of water is evident in figures 1 and 2 and results in a significant reduction of cell and electrode capacitance during the initial 100 h of testing. Figure 1 shows that the effect of water results in a capacitance reduction by 20 % during the first 100 h of testing. A 20% capacitance loss is usually defined as the end of life criterion.

The results are in good agreement with the results published by Wang and Yoshio [2] for a similar PC based electrolyte (1.5 M TEMAPF<sub>6</sub> / PC) but during cycling tests between 0 V and 2.5 V. These authors also investigated the initial capacitance loss as a function of H<sub>2</sub>O concentration in the electrolyte. For a concentration of 850 ppm they found an initial loss of about 10% during cycling, which compares qualitatively well to the 20 % observed in our experiment for a higher constant cell voltage. In both investigations it is

clear that the effect of water is limited to the first hours of the constant voltage or cycling test, while the slope of the capacitance loss for the rest of the tests is unaffected by the water content.

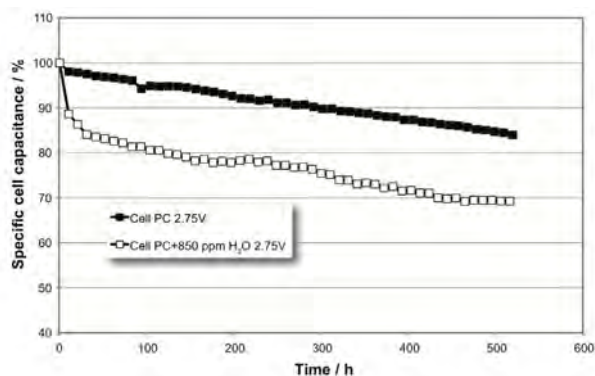


**Figure 1.** Loss of specific cell capacitance during aging at 2.75V for PC based electrolyte. Full symbols represent the dry electrolyte, open symbols the electrolyte with 850 ppm.

For the capacitance loss of the single electrodes it was found that the effect of H<sub>2</sub>O occurs on the negative electrode (see figure 2) while the positive electrode is not affected.

The observed difference between the effect of water at the positive and negative electrode is in agreement with the results obtained by Ishimoto et al. [3] who found that the water content of the electrolyte (1 M TEMABF<sub>4</sub>/PC) in a divided cell increased at the positive electrode and decreased at the negative electrode. Water is most probably consumed at the negative AC electrode, leading to the respective initial capacitance loss while water has no effect at the positive electrode.

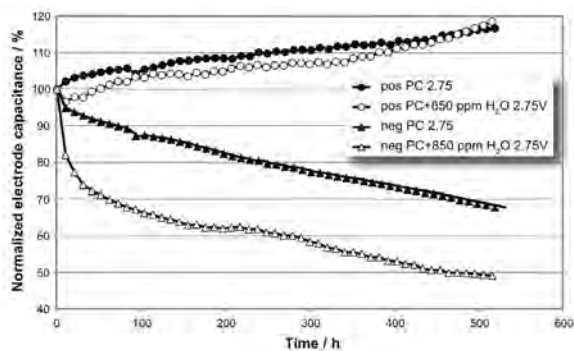


**Figure 2.** Capacitance loss of the individual electrodes during aging at 2.75 V in PC based electrolyte. Full symbols represent the “dry” electrolyte, open symbols the electrolyte with 850 ppm H<sub>2</sub>O. Circles represent positive electrodes and triangles the negative electrodes.

In order to gain more insight into the H<sub>2</sub>O induced processes occurring on the negative electrode we measured XPS spectra of the negative electrode after 100 h with and without water in the electrolyte. However, no differences could be detected in the C1s spectra of the electrodes aged in water containing electrolyte and in dry electrolyte. The spectra recorded on the negative electrodes after 100 h are almost identical to those obtained in water-free solution (see figure 3). From these results it is concluded that additional film growth in the water containing electrolytes is not the reason for the capacitance loss of the negative electrode.

Post mortem surface area measurements by N<sub>2</sub> physisorption of the electrodes indicated no significant

differences. The NLDFT surface area of the electrode aged in non aqueous PC based electrolyte was 1158 m<sup>2</sup>/g after 100h compared to 1117 m<sup>2</sup>/g in H<sub>2</sub>O containing electrolyte.

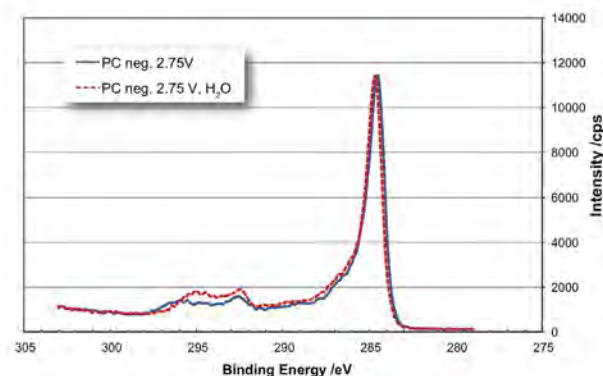


**Figure 3.** XP spectra of the C1s level of the electrodes recorded after 100 h of aging in PC based electrolyte with (dashed line) and without (full line) water contamination.

The absolute difference in surface area is not sufficient to explain the capacitance loss of 20%. A capacitance decrease by 20 % should require a surface area reduction by at least 200 m<sup>2</sup> g<sup>-1</sup> to 960 m<sup>2</sup> g<sup>-1</sup>. One possible explanation of these results could be the formation of H<sub>2</sub> gas, which partly blocks the pores and thus accessible surface area. Such H<sub>2</sub> would not show up in the XPS analysis and would also not be detected in the gas adsorption measurements. Production of H<sub>2</sub> during capacitor operation was found by Hahn et al. [6] and Ishimoto et al. [3].

## Conclusions

The effect of water contamination in electrochemical double layer capacitors on the aging behaviour was investigated for cell voltages of 2.75 V. A clear initial loss of capacitance was detected in water-contaminated electrolyte for PC based electrolyte. The capacitance fading occurs exclusively on the negative electrode. Surface analytical and surface area analysis did not indicate additional film formation or an equivalent surface area loss on the negative EDLC electrodes.

## Acknowledgments

Swiss National Science Foundation is thanked for financial support (project no 200021-117607).

## References

- [1] D. Zuckerbrod, K. Kobayashi, in: Proceedings of the 15th International Seminar on Double Layer Capacitors and Hybrid Energy Storage Devices, 101, Florida, USA, December 5-7 (2005).
- [2] Hongyu Wang, Masaki Yoshio, J. Power Sources **195**, 389 (2010).
- [3] Shuichi Ishimoto, Yuichiro Asakawa, Masanori Shinya, Katsuhiko Naoi, J. Electrochem. Society **156**, A563 (2009).
- [4] P.W. Ruch, D. Cericola, M. Hahn, R. Kötzt, A. Wokaun, J. Electroanal. Chem. **636**, 128 (2009).
- [5] P.W. Ruch, D. Cericola, A. Foelske-Schmitz, R. Kötzt, A. Wokaun, Electrochim. Acta **55**, 4412 (2010).
- [6] M. Hahn, A. Würsig, R. Gallay, P. Novák, R. Kötzt, Electrochem. Commun. **5**, 925 (2005).

# Investigation of kinetics of ion transport on supercapacitors using nanoporous starburst carbon spheres as a model electrode

Y. Sasaki, D. Cericola, N. Tatsuta<sup>1</sup>, K. Yano<sup>1</sup>, R. Kötzt,

phone: +41 56 310 2092, e-mail: yuri.sasaki@psi.ch

Electrochemical double-layer capacitors (EDLCs) are attractive energy storage devices because of high-power density, long cycle life, quick charge/discharge capability.

Activated carbon is one of the most commonly used materials for electrodes of EDLCs and generally, the specific capacitance increases with the specific surface area [1]; however, there is no general agreement on this topic. Deviations from linearity are supposed to be caused by the kinetics of ion and electron transport within the porous electrodes due to the surface chemistry or irregular porous structures [2].

To improve the performance of super-capacitors, it is important to accurately evaluate the influence of the surface interactions or regularity of the porous structures. However, activated carbons are not appropriate for this purpose due to a broad pore size distribution and irregular porous structures caused by activation processes.

Recently, monodispersed mesoporous silica spheres (hereafter abbreviated as "MMSS") was synthesized from tetramethoxysilane (TMOS) and *n*-alkyltrimethyl ammonium halide ( $C_nTMAX$ ,  $X = Cl, Br$ ) [3, 4]. Using MMSS as a template, monodispersed nanoporous carbon spheres (hereafter abbreviated as "MNCS") with a novel starburst structure was successfully fabricated via nanocasting strategy [5, 6]. Such an MNCS fabrication method enables to control the pore size and the particle diameter (i.e. pore length) accurately and independently.

At the same time, the novel low-tortuosity starburst channel of MNCS is expected to be advantageous for the effective transport of ion during charging/discharging cycles. Therefore, MNCS is an ideal material to evaluate precisely the accessibility of ion within the pore, using MNCS with the same pore size and different particle diameter as an electrode.

In this respect, the present work is aimed at investigating the effects of pore length of MNCS on ion accessibility within the pores during double-layer charging/discharging processes. It is believed that this work will be a milestone to evaluate the kinetics of ion and electron penetration within the pores of electrodes, leading to improvement of the performance of supercapacitors.

## Experimental

MMSS and MNCS were supplied from Toyota Central Research and Development Laboratories. The typical characterizations of MMSS and MNCS are shown in Figure 1 and Figure 2, respectively. Three kinds of MMSS, with the same pore size and different particle diameter, were synthesized and the corresponding MNCS were fabricated via nanocasting method. The synthesized materials are abbreviated as MMSS (or MNCS)-X ( $X = S, M, \text{ and } L$ ), where X denotes the relative length of particle diameter. MMSS with different diameters were prepared using C18TMACl as a templating agent and TMOS as a silica source, by

employing previously reported procedures [3, 4]. Furfuryl alcohol was used as a carbon source to

fabricate MNCS, utilizing MMSS as sacrificial templates [5, 6].

Inherent features of MMSS and MNCS were characterized by scanning electron micrographs (SEMs) and nitrogen adsorption measurements. SEM images were recorded using a SIGMA-V (Akashi Seisakusho). Nitrogen adsorption isotherms were measured with a Quantachrome Autosorb-1 at 77 K. The BET specific surface area was calculated from the nitrogen adsorption data. The average pore size was calculated from the BJH (MMSS) and DFT (MNCS) methods.

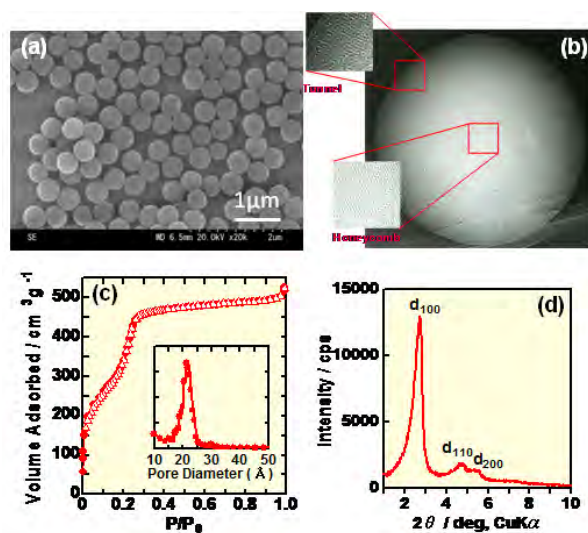


Figure 1. Characteristics of monodispersed mesoporous silica spheres (MMSS). (a) SEM, (b) TEM, (c) Nitrogen adsorption, and (d) XRD pattern of MMSS.

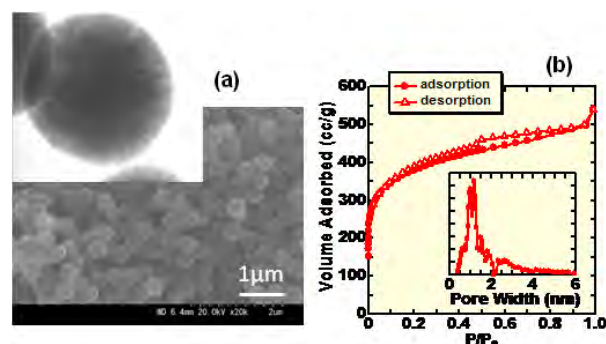


Figure 2. Characteristics of monodispersed nanoporous carbon spheres (MNCS). (a) SEM and TEM, and (b) Nitrogen adsorption of MNCS.

Electrodes were prepared by blending MNCS and poly(tetrafluoroethylene) (DuPont) in a mass ratio of 90:10 to obtain a slurry. After the evaporation of the solvent during constant stirring, the resultant material was rolled down to the thickness of 0.2 μm and dried at 120 °C in vacuo. Cyclic voltammetry (CV) was carried out with a three-electrode setup. PTFE-bound activated carbon YP17 (Kuraray Chemical Co.) was used as a quasi-reference electrode and as the counter electrode.

<sup>1</sup> Toyota Central R&D Labs., Japan

A 1M solution of TEABF<sub>4</sub> in acetonitrile (AN) was employed as the electrolyte in this study.

## Results

Physical properties of MMSS and the corresponding MNCS are listed in Table 1. To clarify the relationship between the pore length of MNCS and its capacitance, the provision of MNCS samples with the same pore diameters and different pore lengths is necessary. The results from table 1 clearly demonstrate that MNCS with different pore lengths were obtained, maintaining almost the same pore sizes and the surface areas. It is implied that MNCS materials can be ideal model electrodes to evaluate the effect of porous structure for super-capacitors. It is to be noted that the monodispersed spherical shapes are clearly observed from SEM for all the samples (data are not shown).

Sample	Code	<sup>a)</sup> Pore length / nm	Specific surface area / m <sup>2</sup> g <sup>-1</sup>	Pore size / nm
Silica	MMSS-L	1140	1110	2.50
	MMSS-M	915	1112	2.46
	MMSS-S	576	1126	2.54
Carbon	MNCS-L	939	1146	1.31
	MNCS-M	757	1112	1.31
	MNCS-S	484	1100	1.29

<sup>a)</sup> Pore length = particle diameter

**Table 1.** Physical properties of MMSS and the corresponding nanocasted MNCS.

Figure 3 shows the CV curve for MNCS-S at a scan rate of 1 mV s<sup>-1</sup>. Almost the same CV curves are recorded for MNCS-L and MNCS-M, respectively. The obtained CV curves are quasi-rectangular in shape and show the well known capacitance minimum at the potential of zero charge (pzc), indicating that all the samples have ideal capacitive behavior [7]. The specific capacitance is calculated as 73.4, 76.9 and 76.2 F/g for MNCS-S, MNCS-M, and MNCS-L respectively. With the different specific surface areas, one calculates a specific double layer capacitance of 6.7 μF/cm<sup>2</sup>, which is supposed to be reasonable for carbon electrodes in organic electrolyte [7].

The variation in the specific capacitance of the MNCS electrodes is plotted as a function of the scan rates in Figure 4. When the scan rate is increased above 20 mV s<sup>-1</sup>, the specific capacitance of MNCS-L drops rapidly; in contrast, the capacitance of MNCS-S shows a much more gradual decline. When the scan rate is 100 mV s<sup>-1</sup>, the MNCS-S maintains approximately 90 % of the initial value, whereas the MNCS-L retains only about 70 % of the capacitive ability. In the case of MNCS-M, the specific capacitance is 63.8 F/g at the scan rate of 100 mV s<sup>-1</sup>, which is approximately 76.3 % of the initial value. The obtained results clearly demonstrate the dependence on the pore length. With increasing the scan rate, the effective ion transport length is decreased, and hence the specific capacitance of the MNCS-L drops rapidly.

In classical electrochemistry theory, the ion transport time ( $\tau$ ) can be expressed by the following formula;

$$\tau = L^2/D \quad [8]$$

where L is the ion transport length and D is the ion diffusion coefficient. It is expected that the shorter the length of pores, the smaller the ion transport time, resulting in a better rate capability of the capacitor electrode material. The results obtained from Figure 4 are in good agreement with this theory. Because the fabricated MNCS samples were identical particles except for the pore length, other external causes, such

as pore size, shape, alignment, and surface chemistry, can be ignored. It is believed that MNCS will be useful as a model electrode for basic studies of ion transport within the pores for super-capacitors. Studies are underway to explore this system by changing the pore diameter of MNCS as well as the ion size in the electrolyte.

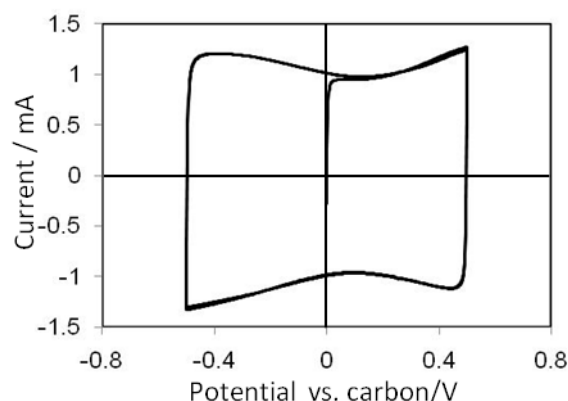


**Figure 3.** Half cell cyclic voltammogram of MNCS-S recorded at a scan rate of 1 mV s<sup>-1</sup>.

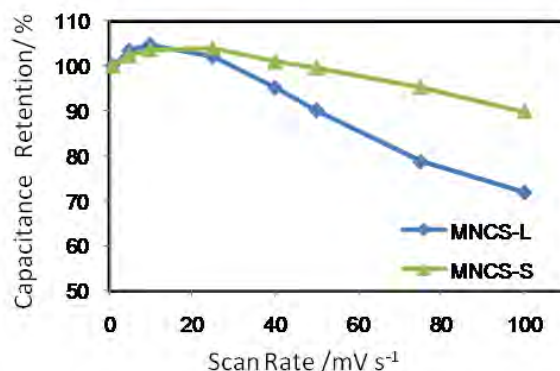


**Figure 4.** Specific capacitance of as-prepared samples at different scan rates from 1 to 100 mV s<sup>-1</sup>. Capacitance was measured at 0 V and normalized at the values of 1 mV s<sup>-1</sup>.

## Conclusions

Monodispersed nanoporous carbon spheres (MNCS) with identical porous structures, except for the pore lengths, were studied. They were found to be the promising candidates as model electrodes to investigate the basis of ion transport within the pores for super-capacitors.

## References

- [1] P. Simon, Y. Gogotsi, *Nat. Mater.* **7**, 845- 854 (2008).
- [2] G-J. Lee, S. Pyun, *Langmuir* **22**, 10659-10665 (2006).
- [3] K. Yano, Y. Fukushima, *J. Mater. Chem.* **13**, 2577-2581 (2003).
- [4] K. Yano, Y. Fukushima, *J. Mater. Chem.* **14**, 1579-1584 (2004).
- [5] T. Nakamura, Y. Yamada (Sasaki), K. Yano, *Chem. Lett.* **35**, 1436-1437 (2006).
- [6] Y. Yamada (Sasaki), T. Nakamura, K. Yano, *Langmuir* **26**, 10044-10049 (2010).
- [7] M. Hahn, M. Bärtschi, O. Barbieri, J-C. Sauter, R. Kötz, R. Gallay, *Electrochem. Solid State Lett.* **7**, A33-6 (2004).
- [8] A.J. Bard, L.R. Faulkner, *Electrochemical Methods: Fundamentals and Applications*, John Wiley & Sons, New York, (2001).



# CATALYSIS & INTERFACES



## Longevity test of sputtered anodes in PEFCs – Different recovery effects after CO-poisoning?

B. Schwanitz, H. Schulenburg, M. Horisberger, A. Wokaun, G.G. Scherer

phone: +41 56 310 5629, e-mail: bernhard.schwanitz@psi.ch

High Pt catalyst loadings and limited stability of polymer electrolyte fuel cells (PEFCs) are still strong impediments for their wider commercialization. The Pt loading for state of the art PEFCs anodes varies between 50 and 100  $\mu\text{g}/\text{cm}^2$  [1]. It is discussed that only a fraction of the catalyst particles participates in the hydrogen oxidation reaction, due to its fast kinetics [2]. Magnetron sputtered anodes with a Pt loading of 25  $\mu\text{g}/\text{cm}^2$  showed no significant performance loss in PEFCs [3]. Yet, long term stability is an issue to be considered simultaneously next to performance. A poisoning of the anode catalyst by CO seems to limit the stability [3]. Carbon monoxide is an impurity of the hydrogen feed gas. In this work we are discussing the regeneration of CO poisoned anodes.

### Experimental

PEFC anodes were obtained by DC magnetron sputtering 25  $\mu\text{g}_{\text{Pt}}/\text{cm}^2$  onto a micro porous layer of Vulcan XC72 supported on Carbon Cloth (GDL: LT1410W E-TEK), as shown else where [3]. Commercial electrode (E-TEK LT140EW; 0.5  $\text{mg}_{\text{Pt}}/\text{cm}^2$ ) functioned as a cathode. Membrane electrode assemblies (MEAs) were prepared by hot pressing without prior ionomer impregnation with Nafion 212 membranes. Long term stability of the sputtered anodes in a 30  $\text{cm}^2$  single cell was investigated at 0.5  $\text{A}/\text{cm}^2$ , 80°C, 1 bar,  $\text{H}_2/\text{O}_2 = 1.5/1.5$ , and fully humidified gases. The iE-curves were measured at the same conditions. Impedance measurements were carried out at 0.5  $\text{A}/\text{cm}^2$ . The test bench was optimised to exclude  $\text{O}_2$  on the anode side after refill of the humidifier. For regeneration, the anode was cycled three times between 0.08 - 1 V, using  $\text{N}_2$  on the anode, and  $\text{O}_2$  on the cathode side. Alternatively, a start-up/shut-down experiment was carried out, by purging the anode with 600 ml/min air and then with  $\text{H}_2$  for 8 min each.

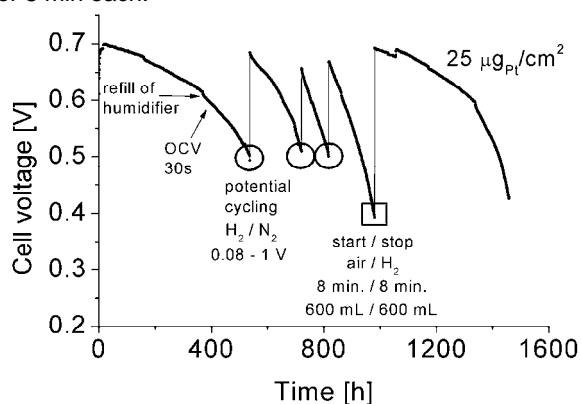


**Figure 1.** U-t-curve of a PEFC with anode loading of 25  $\mu\text{g}_{\text{Pt}}/\text{cm}^2$  running at 0.5  $\text{A}/\text{cm}^2$ , 80°C,  $\text{H}_2/\text{O}_2 = 1.5/1.5$ , 1 bar, 100% R.H. Voltage loss due to CO in  $\text{H}_2$ . Recovery effect due to either potential cycling of the anode (circle), or start/stop experiment (square). Refill of humidifier, or potential jumps to OCV showed no effect.

### Results and Discussion

In prior longevity tests at constant current (0.5  $\text{A}/\text{cm}^2$ ) with anode loadings of 25  $\mu\text{g}_{\text{Pt}}/\text{cm}^2$  the MEA showed a loss in cell voltage of ca. 20 mV after 500 h. In these experiments,  $\text{O}_2$  was introduced to the anode side after refilling the humidifier every 200 h. This was leading to an undefined recovery of the anode, obviously due to oxidation of adsorbed CO. To avoid this uncontrolled regeneration, the refilling of the humidifiers was modified, thereby no oxygen reaches the anode during refilling, and thus no changes in cell voltage occurred (Figure 1). A clear performance loss is observed before the recovery experiments. The anode was recovered several times by means of potential cycling (circle) and start-up/shut-down of the cell (square) (Figure 1). In both cases cell voltages reached similar values as at begin of life (BOL). After the start-up/shut-down experiment, the anode seems to be fully recovered (Figure 2). The iE-curve perfectly fits to the one at BOL and the impedance spectra are identical (inset Figure 2). The high frequency semicircle, which may be related to anode activation losses [3], fully recovers, in contrast to the potential cycling regeneration. Also the voltage decay after potential cycling (1.22 mV/h) is significantly higher than after BOL (0.40 mV/h) or start-up/shut-down (0.56 mV/h). Further experiments on the probably different nature of the recovery effects, due to potential cycling and start/stop, are planned.

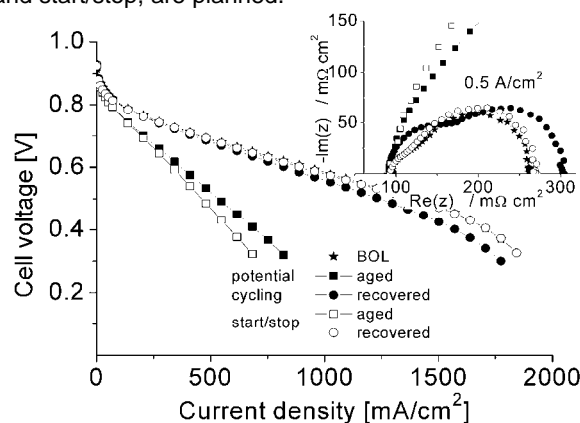


**Figure 2.** iE-curves measured for the fresh, aged, and recovered MEA as shown in Figure 1. Recovery was achieved due to potential cycling and start/stop experiment, respectively. Inset: Nyquist plots of the MEA recorded for each iE-curve at 0.5  $\text{A}/\text{cm}^2$ .

### References

- [1] H.A. Gasteiger, S.S. Kocha, B. Sompalli, F.T. Wagner, Appl. Catal. B : Environmental **56**, 9-35 (2005).
- [2] A.T. Haug, R.E. White, J.W. Weidner, W. Huang, S. Shi, T. Stoner, N. Rana, J. Electrochem. Soc **149**, A280-A287 (2002).
- [3] B. Schwanitz, H. Schulenburg, M. Horisberger, A. Wokaun, G.G. Scherer, Electrocat., doi: 10.1007/s12678-010-003z, in press.

# Platinum based cathodes for PEFCs prepared by magnetron sputtering

B. Schwanitz, H. Schulenburg, M. Horisberger, A. Wokaun, G.G. Scherer

phone: +41 56 310 5629, e-mail: bernhard.schwanitz@psi.ch

High Pt catalyst loadings and limited stability of polymer electrolyte fuel cells (PEFCs) are still strong impediments for a broader commercialization. While lowering the Pt anode loading down to  $50 \mu\text{g}/\text{cm}^2$  is straightforward [1, 2], a lowering of today's cathode loadings of ca.  $400 \mu\text{g}/\text{cm}^2$  is difficult, due to the sluggish oxygen reduction reaction (ORR) [2]. It is discussed that only a thin layer within the cathode is participating in the ORR [1]. Thus, producing thin catalyst layers by using the sputter technique can be a promising approach to enhance the Pt utilization. Furthermore, co-sputtering thin films of Pt and Co may lead to higher specific activity for the oxygen reduction and higher roughness of the electrodes.

## Experimental

PEFC cathodes were fabricated by DC magnetron sputtering of either Pt, or Pt and Co onto a micro porous layer (MPL) supported on Carbon Cloth (E-TEK LT1410W) [3]. For the  $\text{PtCo}_x$  type electrodes, alternating layers of Pt and  $\text{Co}_x$  were sputtered to formally obtain  $\text{PtCo}$  and  $\text{PtCo}_3$ , respectively.

Loading [ $\mu\text{g}_{\text{Pt}}/\text{cm}^2$ ]	OCV [mV]	$i@0.65\text{V}$ [ $\text{mA}/\text{cm}^2$ ]	$A_{\text{spec}}$ [ $\text{m}^2/\text{g}_{\text{Pt}}$ ]	$A_{\text{ESA}}$ [ $\text{cm}_{\text{Pt}}^2/\text{cm}^2$ ]
25	788	229	$9.6 \pm 1.8$	$2.4 \pm 0.5$
50	$796 \pm 7.1$	$294 \pm 33$	$9.4 \pm 0.6$	$4.7 \pm 0.3$
100	$827 \pm 9.0$	$453 \pm 45$	$4.9 \pm 0.5$	$4.9 \pm 0.5$
500	850	477	2.0	10.1
500 ETEK	$902 \pm 5.7$	$1024 \pm 96$	$21.7 \pm 3.3$	$108.7 \pm 16.4$

**Table 1.** Electrochemical active surface area ( $A_{\text{ESA}}$ ), open circuit voltage (OCV) and current density at 650 mV for different sputtered cathodes and a commercially available E-TEK electrode.

The metal loadings were controlled by the sputtering time and sputter power. For pure Pt electrodes, loadings were varied between 25 and  $500 \mu\text{g}_{\text{Pt}}/\text{cm}^2$ , whereas loadings for the  $\text{PtCo}_x$  cathodes was  $100 \mu\text{g}_{\text{Pt}}/\text{cm}^2$ . One electrode of each  $\text{PtCo}$  and  $\text{PtCo}_3$  was leached for 1 h in 1 M  $\text{HClO}_4$  (named as  $\text{PtCo}_{1\text{e}}$  and  $\text{PtCo}_{3\text{le}}$ ). Commercial electrodes (E-TEK LT140EW;  $0.5 \text{ mg}_{\text{Pt}}/\text{cm}^2$ ) were used for comparison. For all experiments, E-TEK electrodes were used as anodes. All membrane electrode assemblies (MEAs) were prepared by hot pressing the

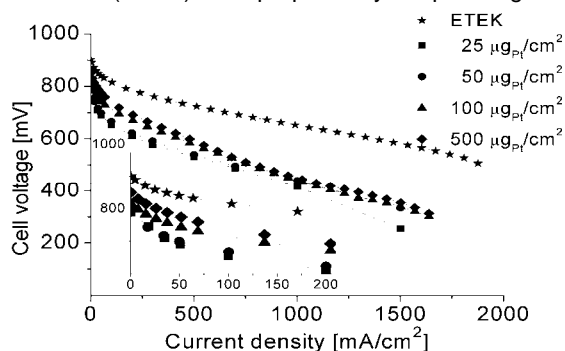


**Figure 1.**  $iE$ -curves of MEAs with sputtered (various loadings) and commercial cathodes (ETEK). ( $80^\circ\text{C}$ ,  $\text{H}_2/\text{O}_2 = 600/600 \text{ ml}/\text{min}$ , 1 bar, 100% R.H.). Inset: magnification of the  $iE$ -curve.

electrodes with Nafion 212 membranes, without prior ionomer impregnation. Performance of the sputtered cathodes was assessed in a  $30 \text{ cm}^2$  single cell ( $80^\circ\text{C}$ , 1 bar,  $\text{H}_2/\text{O}_2 = 600/600 \text{ ml}/\text{min}$ , 100% R.H.). Electrochemical active surface area ( $A_{\text{ESA}}$ ) was determined by CO-stripping voltammetry.

## Results and Discussion

For the sputtered cathodes, the electrochemical active surface area per geometric area ( $A_{\text{ESA}}$ ) was found to be 10 to 50 times smaller compared to E-TEK electrodes (Table 1). Considering that Pt is mainly deposited onto the surface of the MPL [1], an increase of Pt loading leads to less dispersed Pt particles. This means that larger particles are formed, which may agglomerate or even form films. Thus, an increase in Pt loading does not linearly increase  $A_{\text{ESA}}$ . Ink based E-TEK electrodes show a high Pt dispersion, leading to a much higher  $A_{\text{ESA}}$  and therefore to a higher fuel cell performance compared to the sputtered electrodes (Figure 1). For the latter electrodes  $A_{\text{ESA}}$  is similar, and therefore they show a similar performance. Yet, a clear order can be seen in the inset of Figure 1.

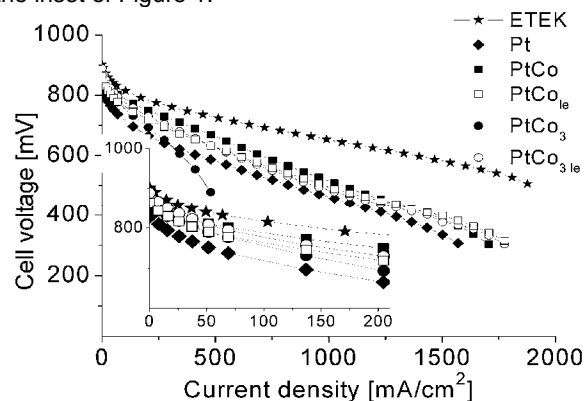


**Figure 2.**  $iE$ -curves of MEAs with sputtered  $\text{PtCo}_x$  and commercial cathodes (ETEK), before and after leaching (indicated by index  $1\text{e}$ ). The Pt content was constant ( $100 \mu\text{g}_{\text{Pt}}/\text{cm}^2$ ), while the Co content was varied. ( $80^\circ\text{C}$ ,  $\text{H}_2/\text{O}_2 = 600/600 \text{ ml}/\text{min}$ , 1 bar, 100% R.H.). Inset: magnification of the  $iE$ -curve.

An addition of Co leads to a slightly higher performance in case of  $\text{PtCo}$  (Figure 2). Yet, too much Co as in  $\text{PtCo}_3$  leads to poorer fuel cell performance, probably caused by leached  $\text{Co}^{2+}$  which blocks sulfonic acid groups in the membrane. This blocking can be avoided by *ex situ* leaching of  $\text{PtCo}_3$  electrodes.

## References

- [1] B. Schwanitz, H. Schulenburg, M. Horisberger, A. Wokaun, G.G. Scherer, *Electrocatal.*, doi: 10.1007/s12678-010-0032-z.
- [2] H.A. Gasteiger, S.S. Kocha, B. Sompalli, F.T. Wagner, *Appl. Catal. B: Environmental* **56**, 9-35 (2005).
- [3] B. Schwanitz, H. Schulenburg, M. Horisberger, A. Wokaun, G.G. Scherer, *PSI Electrochemistry Laboratory - Annual Report 2008*, 72, ISSN No. 1661-5379 (2009).

## Platinum dissolution at the anode and cathode of PEFCs caused by start/stop and load cycling

N. Linse, G.G. Scherer, A. Wokaun, L. Gubler

phone: +41 56 310 4668, e-mail: nicolas.linse@psi.ch

An important issue regarding the commercialization of polymer electrolyte fuel cells is the reduction of material costs. One approach that directly affects costs is the development of electrodes with low platinum loadings. Owing to the high exchange current density of the hydrogen oxidation reaction, the potential for a reduction of catalyst loading is particularly high at the negative electrode. Anode loadings of  $15 \mu\text{g}_{\text{Pt}}/\text{cm}^2$  without fuel cell performance loss have been recently demonstrated [1]. This high initial performance, however, can significantly deteriorate during fuel cell operation. Load cycling and particularly the exposure to elevated potentials occurring during fuel cell start-up and shut-down strongly promote catalyst degradation. In order to investigate platinum loss at the anode and cathode, fuel cells were exposed to different operation modes, including start/stop and load cycling.

### Experimental

All experiments were carried out in  $16 \text{ cm}^2$  cells with parallel flow fields and commercially available MEAs. Platinum loading at the anode and cathode was  $0.18 \text{ mg}_{\text{Pt}}/\text{cm}^2$  and  $0.4 \text{ mg}_{\text{Pt}}/\text{cm}^2$ , respectively. Start/stop cycling was performed by alternating purging of the anode compartment with hydrogen and air, while an external load of  $3 \text{ m}\Omega\text{cm}^2$  was applied to the cell. In regular intervals, electrochemically active catalyst surface area (ECA) was determined by CO stripping voltammetry. To compare start/stop induced platinum dissolution with catalyst deterioration under ordinary fuel cell operating conditions, ECA loss was additionally determined during constant load operation ( $3 \text{ m}\Omega\text{cm}^2$ ) and cycling between  $3 \text{ m}\Omega\text{cm}^2$  and open circuit voltage (OCV). All cells were operated at a humidity of 70% R.H. at  $2.5 \text{ bar}_a$  and a temperature of  $80^\circ\text{C}$ .

### Results and Discussion

Active platinum surface area loss at the fuel cell cathode is shown in Figure 1. Already in case of constant load operation, an ECA decrease of 10% can be observed after operating the cell for a time which corresponds to the duration of the cycling experiments. However, since platinum dissolution mainly takes place during the reduction of platinum oxide [2], ECA loss rate is significantly increased if the cell is exposed to periodic load changes. Cycling between open circuit voltage and  $3 \text{ m}\Omega\text{cm}^2$  causes a decrease of active platinum surface area of more than 30%. As a result of the strongly elevated potentials occurring at the positive electrode, catalyst degradation is most pronounced in case of start/stop cycling. The active platinum surface area decreases to less than 20% of the initial value after 1800 cycles. Due to the insignificant electrode polarization and the hydrogen equilibrium potential of 0 V, platinum dissolution at the fuel cell anode is usually assumed to be negligible. After cycling between OCV and  $3 \text{ m}\Omega\text{cm}^2$ , ECA loss is similar to the value obtained for constant load operation, showing that platinum dissolution at the anode is not affected by load cycling (cf. Figure 2).

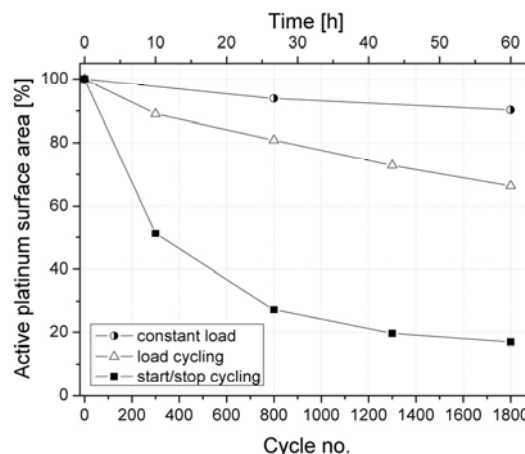


**Figure 1.** Effect of different operating modes on active platinum surface area loss at the fuel cell cathode. Duration of constant load operation was converted into a cycle number corresponding to the time interval of the cycling experiments.

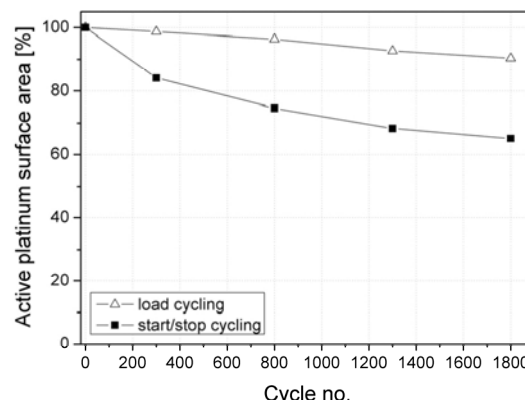


**Figure 2.** Effect of different operating modes on active platinum surface area loss at the fuel cell anode.

During start-up and shut-down of the fuel cell by purging of the anode compartment, however, the potential at the negative electrode varies between the equilibrium potentials of hydrogen ( $\sim 0 \text{ V}$ ) and oxygen ( $\sim 1 \text{ V}$ ). This exposure of the anode to alternating potentials causes substantial platinum dissolution, which results in a decrease of active platinum surface area of 35% after 1800 start/stop cycles. Especially with respect to electrodes having low catalyst loadings, fuel cell performance loss caused by start/stop induced platinum dissolution at the anode can therefore not be neglected.

### References

- [1] B. Schwanitz, H. Schulenburg, M. Horisberger, A. Wokaun, G.G. Scherer, *Electrocatal.*, doi: 10.1007/s12678-010-0032-z.
- [2] V.A.T. Dam, F.A. de Bruijn, *J. Electrochem. Soc.* **154(5)**, B494-B499 (2007).

## Investigations on the corrosion of the microporous and gas diffusion layer in PEFCs

N. Linse, G.G. Scherer, A. Wokaun, L. Gubler

phone: +41 56 310 4668, e-mail: nicolas.linse@psi.ch

Elevated potentials occurring at the positive electrode during fuel cell start-up and shut-down can cause severe corrosion of carbon [1]. As a result, the porous network of carbon nanoparticles used as support material in the catalyst layer can undergo significant structural changes, leading to a strong deterioration of fuel cell performance. In order to determine the effect of different parameters on carbon corrosion rate, the detrimental potential conditions induced by start/stop processes can be simulated by applying single potential pulses to cells operated in H<sub>2</sub>/N<sub>2</sub> mode. However, since fuel cell electrodes typically consist of several layers which all contain carbon, corrosion might not be limited to the carbon particles in the catalyst layer. Corrosion of carbon in the microporous layer (MPL) and gas diffusion layer (GDL), which is assumed not to significantly affect fuel cell performance, might lead to an undesired overestimation of the obtained corrosion rates. To assess the effect of these additional contributions, corrosion of the MPL/GDL was investigated.

### Experimental

All MEAs were fabricated by hot pressing Nafion 212 membranes with a commercially available electrode (0.4 mg<sub>Pt</sub>/cm<sup>2</sup>) and an electrode, which did not contain a catalyst layer. Afterwards, the MEAs were assembled in 16 cm<sup>2</sup> cells with parallel flow fields and operated with hydrogen at the platinum containing electrode and nitrogen at the electrode without catalyst layer. After conditioning for approximately 20 h, single triangular potential pulses (30 mV/s) with different voltage limits were applied to the cell. Starting from 1.3 V, the upper voltage limit was stepwise increased to 1.9 V. For each voltage limit, eight potential pulses were applied. After reaching the highest limit, the upper voltage limit was again decreased to 1.3 V. The lower voltage limit was 0.6 V in all cases. Carbon corrosion was monitored by measuring the CO<sub>2</sub> concentration in the exhaust gas of the positive electrode. Corrosion rates were calculated by integration of the CO<sub>2</sub> peaks developing in response to the applied potential pulses. All measurements were carried out at a temperature of 80°C with fully humidified gases.

### Results and Discussion

Carbon corrosion of the MPL/GDL was found to strongly depend on the previous exposure to high potentials. In case of freshly conditioned fuel cells, no corrosion can be detected for upper voltage limits lower than 1.6 V. At higher voltages, however, the appearance of CO<sub>2</sub> concentration peaks in the exhaust gas indicates significant MPL/GDL corrosion. If the cell was not previously exposed to elevated potentials for a longer time, CO<sub>2</sub> evolution thereby strongly increases with the number of applied potential pulses (cf. Figure 1). For an upper voltage limit of 1.7 V, maximum CO<sub>2</sub> concentration increases from 3 ppm during the first potential pulse to 12 ppm during the eighth pulse. To further investigate this continuous increase of corrosion rate, a freshly

conditioned cell was exposed to 30 consecutive potential pulses between 0.6 V and 1.7 V. The resulting carbon corrosion rates, which were calculated by integration of the developing CO<sub>2</sub> concentration peaks, are shown in Figure 2. After comparatively low CO<sub>2</sub> evolution during the first few pulses, the corrosion rate exhibits an almost linear increase and finally approaches a relatively constant level. This behaviour can be explained by gradual formation of oxide species on the carbon surface with repeating exposure to elevated potentials. These catalytic surface oxides strongly promote corrosion, hence leading to a substantial increase of carbon corrosion rate. The simultaneous formation of passive oxides and a re-reduction of catalytic species finally results in equilibrium oxide coverage, which causes the approach of corrosion rate to a constant value [2].

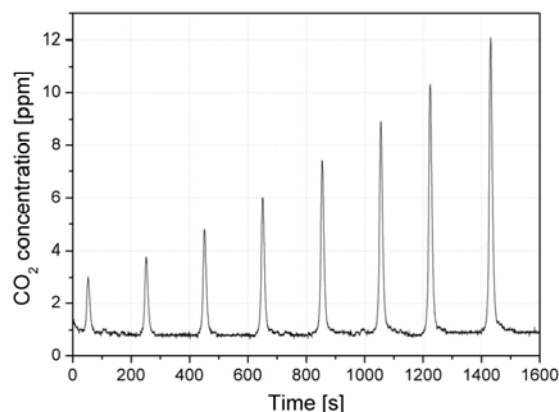


**Figure 1.** CO<sub>2</sub> evolution in response to eight subsequent potential pulses between 0.6 V and 1.7 V (30 mV/s). The cell was operated at 80°C with fully humidified hydrogen/nitrogen.

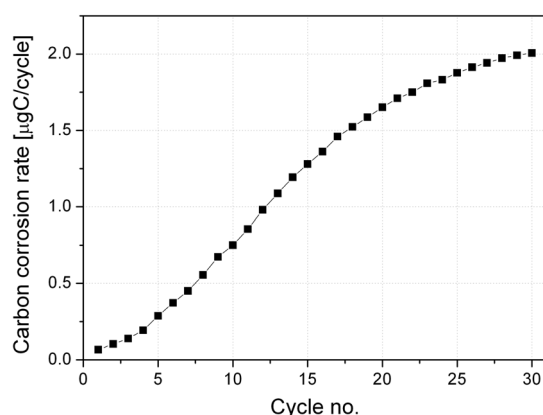


**Figure 2.** Carbon corrosion rate as function of the number of applied potential pulses between 0.6 V and 1.7 V (30 mV/s) without previous exposure to elevated potentials. Corrosion rates were calculated by integration of the CO<sub>2</sub> concentration peaks developing in response to the applied potential pulses.

After applying eight potential pulses with the highest investigated limit being 1.9 V, the upper voltage limit was again stepwise decreased. In contrast to the previous measurements with increasing upper voltage limits, CO<sub>2</sub> evolution did not depend on the number of applied potential pulses, indicating complete saturation coverage of the carbon surface with catalytic oxide species (cf. Figure 3). As a second consequence of the prior exposure to high potentials, CO<sub>2</sub> evolution can also be detected for upper voltage limits which are significantly lower than 1.6 V. This effect shows that carbon is much more prone to corrosion after the formation of catalytic surface oxide species. Compared to freshly conditioned fuel cells, the starting potential of carbon corrosion is 0.2 V lower.

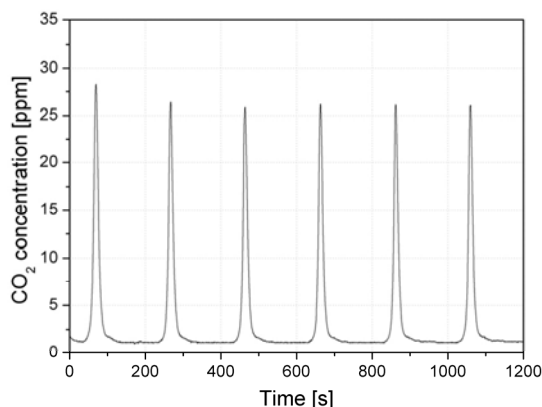


**Figure 3.** CO<sub>2</sub> evolution in response to six subsequent potential pulses between 0.6 V and 1.7 V (30 mV/s) after the cell was exposed to potentials pulses with upper limits up to 1.9 V.

The constant height of the CO<sub>2</sub> concentration peaks in case of saturated catalytic oxide coverage allows the determination of corrosion rates as function of the upper voltage limit. As shown in Figure 4, carbon corrosion rate increases exponentially from 0.02 µgC/cycle at 1.4 V to more than 10 µgC/cycle for an upper voltage limit of 1.9 V. The obtained values, however, are substantially lower than corrosion rates determined for MEAs containing a catalyst layer [3]. The comparison shows that corrosion of the MPL/GDL only accounts for less than 1% of total CO<sub>2</sub> evolution. With respect to potential pulse measurements carried out with standard fuel cell electrodes, all contributions besides the corrosion of carbon particles in the catalyst layer can consequently be neglected.

Since the formation of elevated potentials at the positive electrode is not possible without catalyst layer, MPL/GDL corrosion caused by real start/stop processes can not be directly determined. By employing reference electrodes in the membrane, maximum potentials of about 1.5 V have been measured during fuel cell start-up and shut-down by purging of the anode compartment with hydrogen and air, respectively [4]. Since corrosion in this potential range only occurs after previous exposure of the positive electrode to potentials exceeding 1.5 V, start/stop processes are not expected to cause significant MPL/GDL corrosion. Though, even without measurable carbon corrosion, changes in the surface properties of carbon can slightly affect water transport after a large number of start-up and shut-down processes [5]. Yet, the contribution of this effect to overall fuel cell performance loss is negligible compared to the strong influence of simultaneously occurring catalyst layer corrosion.

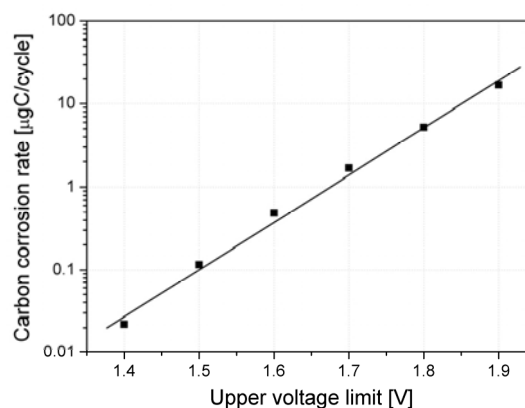


**Figure 4.** Carbon corrosion rate as function of upper voltage limit. Lower voltage limit was 0.6 V in all cases. Measurements were carried out after saturated oxidation of the carbon surface by exposure to potentials pulses with upper voltage limits of 1.9 V. Corrosion rates were calculated by integration of CO<sub>2</sub> concentration peaks developing in response to single triangular potential pulses applied to a cell operated in H<sub>2</sub>/N<sub>2</sub> mode at 80°C with fully humidified gases.

## Conclusions

To assess corrosion of the microporous and gas diffusion layer, single triangular potential pulses were applied to cells operated in H<sub>2</sub>/N<sub>2</sub> mode. Due to the initial absence of catalytic oxide species on the carbon surface, corrosion was only observed for upper voltage limits exceeding 1.5 V in case of freshly conditioned fuel cells. After reaching saturation oxide coverage by repeated exposure to elevated potentials, the starting potential for carbon corrosion was significantly decreased to 1.4 V. The results show that determination of catalyst layer corrosion by potential pulse measurements is not affected by contributions originating from oxidation of the MPL/GDL. Also elevated potentials occurring during real fuel cell start-up and shut-down by purging of the anode compartment are not expected to cause significant MPL/GDL corrosion.

## References

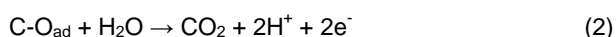
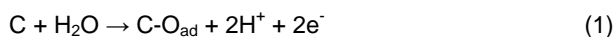
- [1] C.A. Reiser, L. Bregoli, T.W. Patterson, J.S. Yi, J.D. Yang, M.L. Perry, T.D. Jarvi, *Electrochem. Solid-State Lett.* **8(6)**, A273-A276 (2005).
- [2] K.G. Gallagher, T.F. Fuller, *Phys. Chem. Chem. Phys.* **11**, 11557-11567 (2009).
- [3] N. Linse, A. Wokaun, G.G. Scherer, L. Gubler, *PSI Electrochemistry Laboratory - Annual Report 2009*, 67, ISSN 1661-5379 (2010).
- [4] J. Kim, J. Lee, Y. Tak, *J. Power Sources* **192**, 674-678 (2009).
- [5] G. Chen, H. Zhang, H. Ma, H. Zhong, *Int. J. Hydrogen Energy* **34**, 8185-8192 (2009).

## The effect of low relative reactant gas humidity on carbon corrosion in PEFCs

N. Linse, G.G. Scherer, A. Wokaun, L. Gubler

phone: +41 56 310 4668, e-mail: nicolas.linse@psi.ch

During start-up and shut-down of a fuel cell by purging the anode compartment with hydrogen or air, respectively, certain areas of the positive electrode are exposed to potentials significantly exceeding 1 V [1]. Besides the accelerated electrochemical dissolution of the platinum catalyst, elevated potentials can cause severe corrosion of the carbon nanoparticles, which are typically used as support material for the fuel cell catalyst. The basic reaction mechanism for carbon corrosion is shown in equations 1 and 2. In a first step, surface oxide species are formed on the carbon surface, which are further oxidized to CO<sub>2</sub> in a second, rate determining step.



As a result of start/stop induced carbon corrosion, the porous network of carbon particles in the catalyst layer can undergo significant structural changes, leading to a strong deterioration of fuel cell performance [2]. Since frequent start-up and shut-down processes can not be avoided in many applications, operation strategies, which can mitigate start/stop induced degradation, have to be developed in order to improve fuel cell durability. In addition to system-based approaches, such as purging with high gas flow rates and the application of an auxiliary load during start-up and shut-down, the influence of operating parameters on carbon corrosion can be utilized to decrease degradation rates. In contrast to the time-consuming decrease of temperature, lowering of humidity is a feasible method to mitigate start/stop induced degradation in many fuel cell applications.

### Experimental

In order to determine the effect of reactant gas humidity on carbon corrosion, the elevated potentials occurring during fuel cell start-up and shut-down were simulated by applying single triangular potential pulses to cells operated in H<sub>2</sub>/N<sub>2</sub> mode. In contrast to real start/stop processes by anode purging, where the voltage, which acts as driving force for carbon corrosion, is strongly influenced by the chosen operating parameters, measurements performed in H<sub>2</sub>/N<sub>2</sub> mode ensure constant potential conditions, independent of reactant gas humidity. Carbon corrosion rates were calculated by integration of the CO<sub>2</sub> concentration peaks developing in response to the applied potential pulses (cf. Equation 2). All experiments were carried out using 16 cm<sup>2</sup> cells with parallel flow fields and MEAs fabricated by hot pressing of a Nafion 212 membrane with commercially available electrodes (0.4 mg<sub>Pt</sub>/cm<sup>2</sup>). Since corrosion rates initially show a strong decrease upon voltage cycling, all cells were exposed to 100 potential cycles between 0.6 V and 1.3 V (50 mV/s), prior to the measurements. Afterwards, eight single triangular potential pulses between 0.6 V

and 1.3 V (30 mV/s) were applied for each investigated reactant gas humidity. Due to a slight decrease of CO<sub>2</sub> evolution during the first few cycles, only the last three CO<sub>2</sub> concentration peaks were used to calculate carbon corrosion rates.

### Results and Discussion

Generally, the carbon corrosion rate shows a linear increase with increasing humidification of the reactant gases (cf. Figure 1). The direct effect of water vapour partial pressure, which is proportional to relative humidity in case of a constant temperature, originates from the requirement of one water molecule for the corrosion of one carbon atom in the rate determining reaction step (cf. Equation 2). This linear correlation, however, is not observed over the entire humidity range. If relative humidity drops below around 40%, corrosion rates significantly deviate from the theoretically expected behaviour.

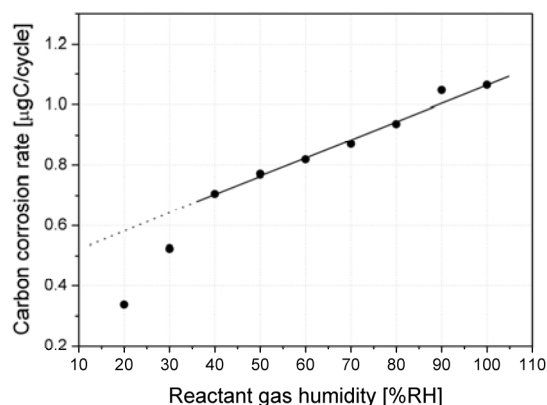


**Figure 1.** Effect of relative humidity on carbon corrosion rate. Corrosion rates were calculated by integration of CO<sub>2</sub> concentration peaks in the exhaust gas developing in response to potential pulses between 0.6 V and 1.3 V, which were applied to a cell operated in H<sub>2</sub>/N<sub>2</sub> mode at 80°C.

To be able to distinguish between the effect of relative and absolute water content, measurements with varying relative humidity were carried out at different constant water vapour partial pressures. Thereby, relative humidity was varied by increasing the temperature while keeping the absolute rate of water addition to the gas flow constant. As expected from the participation of water in the carbon oxidation reaction, corrosion rates become higher with increasing water vapour partial pressure (cf. Figure 2). Despite the increase in temperature, however, which is known to strongly promote carbon oxidation [3], corrosion rates decrease if relative humidity drops below around 35%. Since this value is independent of water vapour partial pressure, deviation from the linear behaviour at low reactant gas humidity has to be an effect of relative water content. These results show that both absolute and relative humidity strongly influence carbon corrosion behaviour.

While the effect of water vapour partial pressure can be explained by the reaction mechanism, influence of relative humidity must be based on other processes.

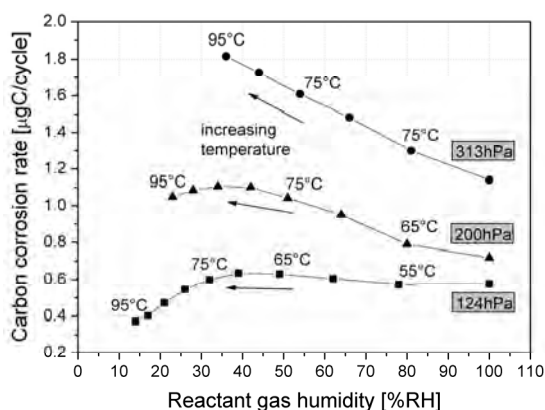


**Figure 2.** Effect of relative humidity on carbon corrosion rate at different constant water vapour partial pressures. Relative humidity was varied by increasing the temperature while keeping the rate of water injection to the gas flow constant.

One parameter that is strongly affected by relative humidity is the resistance of the proton conducting phase. In order to estimate the effect of humidity on ionomer resistance in the membrane and the catalyst layer, electrochemical impedance spectroscopy in  $H_2/N_2$  mode was performed [4]. As shown in Figure 3, a decrease of relative humidity causes an exponential increase in ionomer resistance. The resulting voltage drop in the ionomer phase can lead to a significant discrepancy between the voltage which is externally applied to the cell and the effective potential leading to carbon corrosion.

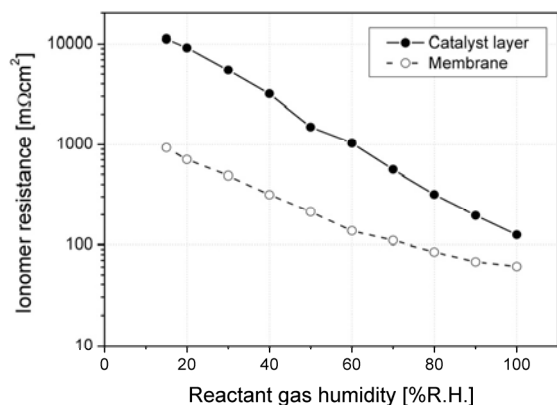


**Figure 3.** Influence of relative humidity on ionomer resistance in the membrane and catalyst layer. Resistance values were derived from impedance spectroscopy measurements carried out in  $H_2/N_2$  mode.

Figure 4 shows the potential distribution in the membrane and the catalyst layers if a voltage  $U_a$  is applied to a cell operated in  $H_2/N_2$  mode at different relative humidity. Due to the high exchange current density of the hydrogen evolution reaction and the resulting limitation of the reaction to a small region near the membrane, voltage drop at the negative electrode can be neglected. In case of fully humidified gases, maximum current densities of about  $15 \text{ mA/cm}^2$  occurring during a potential pulse between 0.6 V and 1.3 V result in a voltage drop smaller than 2 mV. The potential difference between ionomer phase and positive electrode  $\Delta\Phi_+$ , which acts as driving force for carbon

corrosion, can therefore be assumed to be equal to the applied voltage  $U_a$ .

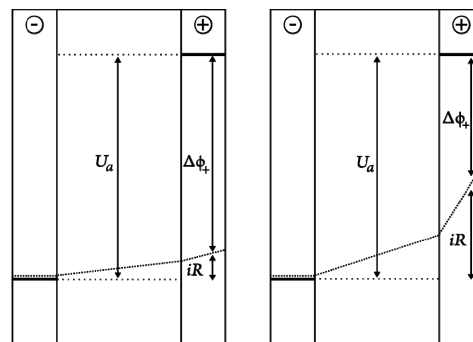


**Figure 4.** Potential distribution in the membrane (light grey) and catalyst layers (dark grey) for a potential  $U_a$  applied to a cell operated in  $H_2/N_2$  mode. In case of high relative humidity (left), voltage drop in the ionomer phase is small. At low relative humidity conditions (right), the substantially increased ionomer resistance leads to a strong decrease in potential difference between electrode and ionomer phase.

If relative humidity is significantly decreased the exponential increase of resistance causes a considerable voltage drop in the ionomer phase. Since catalyst layer resistance is approximately one order of magnitude higher compared to membrane resistance, reduction of potential at the positive electrode is mainly controlled by the voltage drop in the catalyst layer. At a relative humidity of 30%, a catalyst layer resistance of more than  $5 \text{ } \Omega\text{cm}^2$  leads to a theoretical voltage drop of about 80 mV. Due to the triangular shape of the applied potential pulse and the inhomogeneous distribution of current density within the catalyst layer, effective potential reduction is expected to be slightly lower. However, taking into account the exponential increase of corrosion rate with increasing potential [3], voltage drop in the catalyst layer is high enough to explain the strong decrease of carbon corrosion rate at low relative humidity conditions.

## Conclusions

Besides the effect of water vapour partial pressure, which can be attributed to the reaction mechanism, relative humidity can strongly influence carbon corrosion behaviour. The considerable voltage drop in the catalyst layer, caused by a strong increase of ionomer resistance at low relative humidity, substantially decreases the effective potential leading to carbon corrosion.

## References

- [1] C.A. Reiser, L. Bregoli, T.W. Patterson, J.S. Yi, J.D. Yang, M.L. Perry, T.D. Jarvi, *Electrochem. Solid-State Lett.* **8(6)**, A273-A276 (2005).
- [2] Z.Y. Liu, B.K. Brady, R.N. Carter, B. Litteer, M. Budinski, J.K. Hyun, D.A. Muller, *J. Electrochem. Soc.* **155(10)**, B979-B984 (2008).
- [3] N. Linse, A. Wokaun, G.G. Scherer, L. Gubler, *PSI Electrochemistry Laboratory - Annual Report 2009*, 67, ISSN 1661-5379 (2010).
- [4] R. Makharia, M.F. Matthias, D.R. Baker, *J. Electrochem. Soc.* **152(5)**, A970-A977 (2005).

## The effect of lower voltage limit on the assessment of catalyst layer durability in PEFCs by potential cycling

N. Linse, G.G. Scherer, A. Wokaun, L. Gubler

phone: +41 56 310 4668, e-mail: nicolas.linse@psi.ch

Catalyst layer durability under dynamic operating conditions is a key issue regarding the lifetime of polymer electrolyte fuel cells (PEFCs). A widely used approach to assess catalyst layer durability is the application of a cyclic potential to a cell operated in H<sub>2</sub>/N<sub>2</sub> mode. The resulting degradation is typically characterized by the loss of electrochemically active catalyst surface area (ECA) and changes in the porous structure of the carbon nanoparticles, which are used as support material for the fuel cell catalyst. The voltage limits, which are employed in the different studies, however, strongly vary. Lower voltage limits range from 0.1 V to 0.87 V while the upper voltage limit is usually set to values between 1.2 V and 1.4 V [1, 2]. In order to determine the effect of lower voltage limit on carbon corrosion and active catalyst surface area loss, potential cycling experiments with continuous monitoring of CO<sub>2</sub> evolution were carried out.

### Experimental

All experiments were performed using 16 cm<sup>2</sup> cells with parallel flow fields and MEAs which were fabricated by hot pressing of a Nafion 212 membrane with commercially available electrodes (0.4 mg<sub>Pt</sub>/cm<sup>2</sup>). After conditioning for approximately 20 h in H<sub>2</sub>/O<sub>2</sub> mode, the fuel cell cathode was purged with nitrogen. Afterwards, 300 triangular potential cycles (30 mV/s) with different lower voltage limits were applied to the cells. The upper voltage limit was 1.3 V in all cases. Carbon corrosion rate was continuously monitored by measuring the CO<sub>2</sub> evolution in the exhaust gas. ECA loss was determined by CO stripping voltammetry. All measurements were carried out at a temperature of 80°C with fully humidified gases.

### Results and Discussion

Dissolution of platinum mainly takes place during the reduction of platinum oxide which was previously formed at potentials exceeding around 0.8 V [3]. This dissolution mechanism implicates a strong influence of lower voltage limit on active catalyst surface area loss. Due to the missing platinum oxide reduction, dissolution is effectively hindered if potential cycling is performed with a lower voltage limit of 1.0 V. A decrease of the voltage limit below the reduction potential of platinum oxide substantially increases surface area loss rates (cf. Figure 1). Since platinum oxide is completely reduced at potentials below around 0.6 V, measurements carried out with lower voltage limits of 0.15 V and 0.6 V exhibit similar dissolution rates. The effect of lower voltage limit on carbon corrosion rate is shown in Figure 2. Due to proceeding catalyst layer degradation, corrosion rates generally decrease with increasing number of applied potential cycles. As in case of platinum dissolution, the lowest degradation rate was observed for a lower voltage limit of 1.0 V. If the lower limit is decreased to 0.6 V and 0.15 V, total carbon loss increases by a factor of 3 and 4.5, respectively. This significant reduction of corrosion rate with increasing upper voltage limit can be

explained by proceeding passivation of the carbon surface and an inhibition of the catalyzed corrosion pathway by the formation of a stable oxide layer on the platinum particles [4].

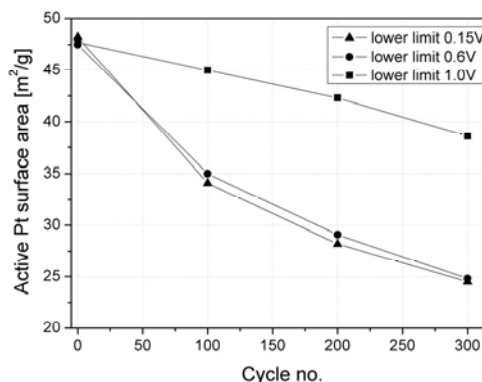


Figure 1. Effect of lower voltage limit on active platinum surface area loss. Upper voltage limit was 1.3 V in all cases.

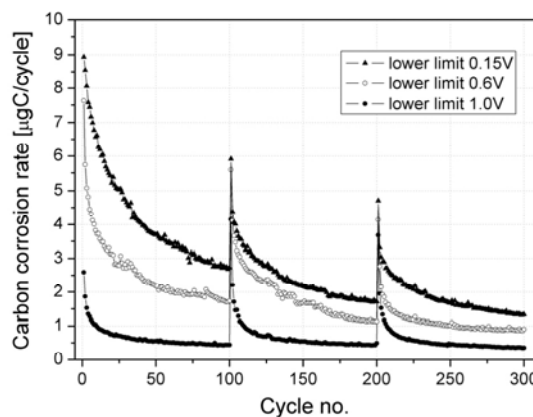


Figure 2. Effect of lower voltage limit on carbon corrosion rate. Upper voltage limit was 1.3 V in all cases. Irregularities at cycle No. 100 and 200 originate from cell characterization.

### Conclusions

Determination of catalyst layer durability by potential cycling is strongly affected by the chosen lower voltage limit. Both carbon corrosion rate and catalyst surface area loss rate increase with decreasing voltage limit.

### References

- [1] R.L. Borup, J.R. Davey, F.H. Garzon, D.L. Wood, M.A. Inbody, *J. Power Sources* **163**, 76-81 (2006).
- [2] W. Bi, Q. Sun, Y. Deng, T.F. Fuller, *Electrochim. Acta* **54**, 1826-1833 (2009).
- [3] V.A.T. Dam, F.A. de Bruijn, *J. Electrochem. Soc.* **154(5)**, B494-B499 (2007).
- [4] N. Linse, L. Gubler, G.G. Scherer, A. Wokaun, *Proceedings of the ASME 8th International Fuel Cell Science, Engineering and Technology Conference, FuelCell2010-33190* (2010).

## Acid leaching of PtCo<sub>x</sub>/C catalysts for oxygen reduction

H. Schulenburg, T. Engl, L. Klüpfel, M. Nachttegaal

phone: +41 56 310 2125, e-mail: hendrik.schulenburg@psi.ch

Several Pt-alloy catalysts, amongst Pt-Co-alloys, exhibit an enhanced activity for the oxygen reduction reaction compared to unalloyed Pt catalysts [1]. With Pt-alloy catalysts a reduction of the required Pt loading in PEFCs was demonstrated [2, 3].

PtCo<sub>x</sub> catalysts have been synthesized using a variety of Pt/Co ratios and preparation methods, including impregnation, mechanical alloying, polyol synthesis, reverse micelles, sputtering and others [4]. Both, the Pt-Co ratio and the preparation conditions have a strong impact on the catalytic activity. In general, only Pt<sub>3</sub>Co nanoparticles have been prepared with a well defined size and crystal structure using a polyol method [5], however, this method is not suitable for preparing other stoichiometries like PtCo or PtCo<sub>3</sub>. Depending on the preparation method, decreasing the Pt/Co ratio may lead to higher catalytic activity [1, 6], although the catalysts may consist of a variety of components like Pt<sub>3</sub>Co, PtCo (ordered or disordered), Co metal or oxides. In PEFCs, cobalt as a non-precious metal may dissolve from PtCo alloys. Under operation conditions (80 °C, ~ pH 0-1) leaching may be caused by electrochemical oxidation and/or the acidic PEFC environment.

In this work we are investigating the effect of acid leaching on the catalytic properties and structure of Pt<sub>3</sub>Co/C, PtCo/C and PtCo<sub>3</sub>/C catalysts. Leaching conditions were chosen, which mimic the open circuit conditions in PEFCs (80°C, pH 1). One objective of this study was to follow the changes in mass activity for oxygen reduction in the course of leaching. The leaching process may cause sintering, ripening, or detachment of PtCo<sub>x</sub> particles. Formation of completely de-alloyed particles, core-shell structures or even porous particles might be possible, too. To follow these structural changes we applied XAS, XRD, TEM and ICP-OES before and after acid leaching of PtCo<sub>3</sub>, PtCo, and Pt<sub>3</sub>Co.

### Experimental

Carbon supported PtCo<sub>x</sub> catalysts with a nominal stoichiometry of PtCo, Pt<sub>3</sub>Co and PtCo<sub>3</sub> were synthesized by milling and heating (1 h at 900 °C in Ar/ 4% H<sub>2</sub>) of dry precursors. The catalysts were cooled rapidly by sousing with liquid nitrogen. The reproducibility and activity of the resulting catalysts is comparable to impregnation preparation routes using the same educts and heat treatment protocol. As a reference catalyst, Pt/C (E-TEK) without Co(acac)<sub>2</sub> was heat-treated under the same conditions.

Leaching experiments were carried out with 200 mg catalyst powders, which were stirred for 100h at 80 °C in 20 ml 0.1 M HClO<sub>4</sub>, prepared from redistilled 70 % perchloric acid (99.999 %, Sigma) and deionized water (18.2 MΩcm<sup>-1</sup>). After leaching, the catalyst dispersions were centrifuged (3000 rpm, 5 min) and the supernatant removed. The residue was washed with water. Centrifugation and washing were repeated twice before the wet catalysts were allowed to dry in air at 60 °C.

### Results

#### Catalytic activity for oxygen reduction

The mass activity before leaching increases with increasing Co content. Acid leaching does not change the activity of PtCo<sub>3</sub>, whereas the activity of Pt<sub>3</sub>Co and PtCo increases. The leached PtCo catalyst shows the highest mass activity (0.21 A/mg<sub>Pt</sub>) for the oxygen reduction (Figure 1).

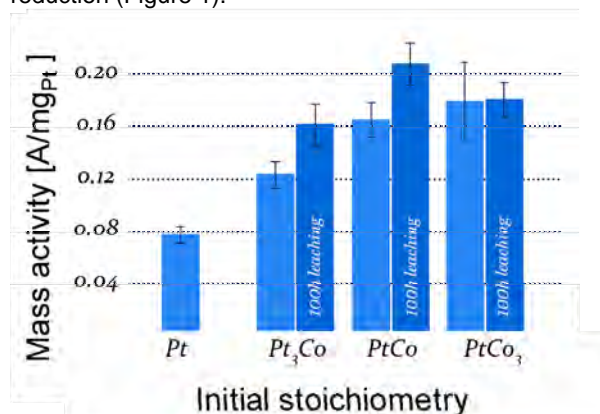


**Figure 1.** Mass activity for oxygen reduction at 0.9 V (RHE), obtained from rotating disc electrode measurements in O<sub>2</sub>-saturated 0.1M HClO<sub>4</sub>, 20 °C, 1600 rpm, anodic going sweeps from 0 to 1200 mV,  $\nu = 5\text{mV/s}$ . Activities not mass-transport corrected.

#### Inductively coupled plasma-optical emission spectroscopy (ICP-OES)

For the determination of Pt- and Co-loadings, all catalysts were decomposed by aqua regia, diluted, and analyzed by ICP-OES (Table 1). For the as-prepared catalysts the ratio of platinum to cobalt is very close to the nominal stoichiometry. For all stoichiometries, acid leaching causes substantial Co losses, namely ~ 55% of the initial value. Leaching of Pt metal is negligible.

Catalyst	Stoichiometry before leaching	Co loss [%]
Pt <sub>3</sub> Co	Pt <sub>3.0</sub> Co <sub>1.0</sub>	55.0
PtCo	Pt <sub>1.0</sub> Co <sub>1.0</sub>	55.7
PtCo <sub>3</sub>	Pt <sub>1.0</sub> Co <sub>2.9</sub>	54.6

**Table 1.** Cobalt leaching of PtCo<sub>x</sub> catalysts. Leaching conditions 100h, 0.1M HClO<sub>4</sub>, 80°C.

#### Transmission electron microscopy (TEM)

To follow changes in particle size or morphology during the leaching process, TEM images were analyzed. The average particle sizes are summed up in Table 2. Before leaching, higher cobalt contents lead to larger particles and broader particle size distributions. After leaching, the particle size decreases for catalysts with a nominal stoichiometry of PtCo<sub>3</sub> and PtCo. For Pt<sub>3</sub>Co catalysts the particle size remains almost constant. Notably, the average particle size of all catalysts after leaching is very similar, around 3.5 to 3.6 nm. A representative TEM image of a pristine catalyst is displayed in Figure 2.

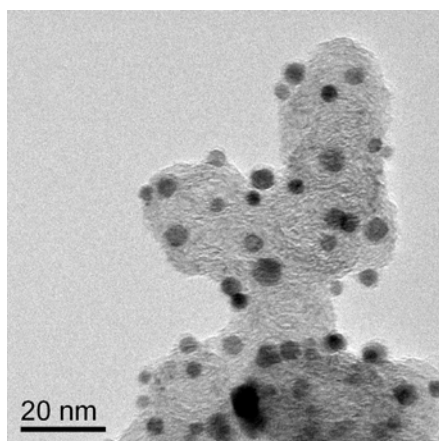


**Figure 2.** TEM image of a pristine PtCo/C catalyst prepared by heat-treatment at 900°C.

#### X-ray diffractometry (XRD)

Calculated lattice parameters of PtCo<sub>x</sub> before and after leaching are shown in Table 2. In general, all PtCo<sub>x</sub> diffraction patterns can be assigned to face centered cubic (fcc) bravais lattices. In pristine PtCo<sub>3</sub> catalysts unalloyed crystalline cobalt is observed. The corresponding reflexes disappear after acid leaching. Higher cobalt contents in PtCo<sub>x</sub> crystallites are accompanied by a shift of the reflexes to higher Bragg angles, i.e. the lattice contracts with an increasing Co/Pt ratio. The diffractograms of PtCo<sub>3</sub> show that the straightforward synthesis by heat-treatment of milled Pt/C and Co(acac)<sub>2</sub> powders allows the preparation of very cobalt rich PtCo<sub>x</sub>. For catalysts with a nominal stoichiometry of PtCo<sub>3</sub>, lattice parameters as small as 3.70 Å are accessible. Frequently, these high Co/Pt ratios lead to formation of PtCo<sub>x</sub> (x~1) and cobalt metal [6]. Leaching of PtCo<sub>3</sub> and PtCo leads to a distinct increase of the lattice constants, therefore the cobalt loss from crystalline phases is high, between 19 and 58%. The lattice parameter of Pt<sub>3</sub>Co catalysts is hardly affected by the leaching procedure. For these catalysts only 1% of the initial cobalt content is leached out of the crystalline phases.

Catalyst	Lattice parameter <sup>a</sup> [Å]	Particle size <sup>b</sup> [nm]
Pt <sub>3</sub> Co	3.87	3.4±1.1
Pt <sub>3</sub> Co leached	3.87	3.6±1.2
PtCo	3.78	3.9±1.2
PtCo leached	3.81	3.5±1.3
PtCo <sub>3</sub>	3.70	4.2±1.9
PtCo <sub>3</sub> leached	3.78	3.6±1.3

**Table 2.** XRD and TEM analysis of as prepared and acid-leached PtCo<sub>x</sub> catalysts. Prepared by heat treatment of Pt/C and Co(acac)<sub>2</sub> at 900°C.

<sup>a</sup>determined by XRD, <sup>b</sup> determined by TEM

#### Extended X-ray absorption fine structure (EXAFS)

EXAFS fit data for the Pt-edge are shown in Table 3. The Pt-Pt coordination numbers hardly change after acid leaching of Pt<sub>3</sub>Co and PtCo catalysts, while the Pt-Co coordination numbers of all catalysts are decreasing. EXAFS measurements at the Co-edge (not shown) suggest the existence of cobalt rich and cobalt oxide rich domains before leaching. After leaching these domains are less frequent.

Catalyst	Shell	Coordination number	Bond lengths [Å]
Pt <sub>3</sub> Co	Pt-Co	1.9	2.686
Pt <sub>3</sub> Co	Pt-Pt	8.5	2.729
Pt <sub>3</sub> Co leached	Pt-Co	1.5	2.687
Pt <sub>3</sub> Co leached	Pt-Pt	8.7	2.730
PtCo	Pt-Co	4.2	2.648
PtCo	Pt-Pt	5.5	2.691
PtCo leached	Pt-Co	3.7	2.652
PtCo leached	Pt-Pt	5.5	2.695
PtCo <sub>3</sub>	Pt-Co	6.6	2.608
PtCo <sub>3</sub>	Pt-Pt	3.8	2.650
PtCo <sub>3</sub> leached	Pt-Co	4.2	2.635
PtCo <sub>3</sub> leached	Pt-Pt	5.1	2.678

**Table 3.** EXAFS fit data of the Pt-edge

#### Conclusions

The heat-treated as prepared PtCo<sub>x</sub> catalysts are mainly disordered fcc-PtCo<sub>x</sub> nanoparticles (Figure 3a). Co or Co oxide rich domains are present in PtCo and PtCo<sub>3</sub> catalysts. Acid leaching leads to a substantial (~55%) decrease of the initial Co content, which is not accompanied by a decrease of catalytic activity for oxygen reduction. EXAFS measurements suggest that leaching leads to rough particle surfaces of leached Pt<sub>3</sub>Co and PtCo (Figure 3b). The PtCo<sub>3</sub> catalyst particles seem to shrink during leaching (Figure 3c). Co- and Co oxide rich domains are less frequent after leaching.

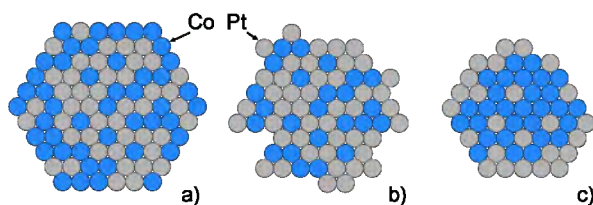


**Figure 3.** a) Proposed structure of as prepared PtCo<sub>x</sub> nanoparticles, b) acid leached PtCo, c) acid leached PtCo<sub>3</sub>.

#### References

- [1] U.A. Paulus, A. Wokaun, G.G. Scherer, T.J. Schmidt, V. Stamenkovic, V. Radmilovic, N.M. Markovic, P.N. Ross *J. Phys. Chem. B*, **106**, 4181–4191 (2002).
- [2] P. Yu, M. Pemberton, P. Plasse *J. Power Sources* **144**, 11-20 (2005).
- [3] J.-C. Lin, H.R. Kunz, J.M. Fenton in *Handbook of Fuel Cells-Fundamentals, Technology and Applications*. Ed. W. Vielstich, H.A. Gasteiger, A. Lamm, *Electrocatalysis* **2**, 457-480 (2003).
- [4] S. Mukerjee, S. Srinivasan in *Handbook of Fuel Cells-Fundamentals, Technology and Applications*. Ed. W. Vielstich, H.A. Gasteiger, A. Lamm, *Electrocatalysis* **2**, 502-519 (2003).
- [5] E. Shevchenko, D. Talapin, H. Schnabelegger, A. Kornowski, O. Festin, P. Svedlindh, M. Haase, H. Weller, *J. Am. Chem. Soc.* **125**, 9090-9101 (2003).
- [6] H. Schulenburg, E. Müller, G. Khelasvili, T. Roser, H. Bönnemann, A. Wokaun, G.G. Scherer, *J. Phys. Chem. C* **113**, 4069-4077 (2009).

## STM study of Pt/C model electrodes prepared via e-beam lithography

A. Savouchkina, A. Foelske-Schmitz, V. Guzenko, D. Weingarth, G.G. Scherer,  
A. Wokaun, R. Kötz

phone: +41 56 310 5532, e-mail: anastasia.savouchkina@psi.ch

Model electrodes consisting of platinum (Pt) nanoparticles of defined sizes and defined spatial arrangement on flat carbon supports were prepared by electron beam lithography (EBL) upon highly oriented pyrolytic graphite (HOPG) electrodes. One goal of our studies was to identify electrochemically induced processes such as carbon corrosion, Ostwald ripening or Pt dissolution using surface-sensitive techniques such as *in situ* scanning tunnelling microscopy (STM) or scanning electron microscopy (SEM) and correlate these processes to the size and arrangement of Pt nanoparticles. STM investigations of the Pt/HOPG interface are particularly challenging, as to our knowledge no successful STM imaging of Pt on the smooth, untreated HOPG has been reported in literature as yet in air or *in situ* due to the high surface mobility of Pt on a sufficiently smooth (carbon) surface such as HOPG. Gloaguen et al., for instance, investigated the Pt/oxidized HOPG system using *ex situ* STM and tapping mode AFM, as the STM tip was a too strong hindrance during *in situ* measurements [1]. Also, Atamny et al. [2] reported the limitations of STM measurements on metal/HOPG systems and described mobility of Pt particles on the smooth HOPG surface. Other recent Pt/HOPG STM studies by Brülle et al. [3] and Oh et al. [4] were either done on electrochemically oxidized HOPG or on HOPG in UHV, respectively. In this report we present the preparation of Pt/HOPG model electrodes suitable for STM studies in air as well as in sulphuric acid and show electrochemically induced Pt dissolution in sulphuric acid studied for the first time by *in situ* EC-STM.

### Experimental

HOPG was freshly cleaved and spin-coated by a double-layered poly(methyl-methacrylate) (PMMA) positive tone resist, using a photoresist layer with a smaller molecular weight of the polymer chains (PMMA 50k) as the lower and the one with the heavier chains (PMMA 950k) as the upper layer. Bake-out step at 175°C followed every spin-coating step. The rotation speed of the spin-coater was chosen as high as required to obtain the resulting thicknesses of 30 nm for each resist layer. This two-layered technique results in an undercut profile preferable for lift-off processes. Exposures of the dot arrays were performed using Vistec EBPG5000Plus electron beam lithography tool, operated at 100 keV. This e-beam writer is equipped with a pattern generator which can be operated at beam stepping frequencies up to 50 MHz, and a deflection system, capable of deflecting the beam to large angles so that a writing field as large as 512x512  $\mu\text{m}^2$  can be exposed without any stage movements. The Gaussian shaped beam was focused to approximately 10 nm in diameter at a beam current of 10 nA. Rectangular dot arrays were generated by setting the beam step size equal to the dot pitch (100 nm or 200 nm), so that the exposure of each dot was performed within a single "beam shot". The exposed

samples were developed, using isopropanol : ketone 3:1 mixture (for more details refer to [5]).

Deposition of a Pt layer (5 nm) was performed with a DC magnetron-sputtering device TIPS1 with an Ar pressure of  $10^{-3}$  mbar and a power of 30 W. The lift-off process was performed after deposition of 5 nm Pt by soaking the samples overnight in acetone and rinsing them with acetone the following day.

STM measurements were conducted using Agilent PicoLe with a 10  $\mu\text{m}$  STM scanner in constant current mode. For tip etching a gold wire with a diameter of 0.25mm (FG 999.9, Carl Schaefer AG) and hydrochloric acid (30% HCl, Baker Analyzed™ Reagent) were used. The applied DC voltage was 1.7 V. After etching, the tips were immersed into hot UHQ (ultra high quality, Millipore) water ( $> 18 \text{ M}\Omega\text{cm}^{-1}$ ) to remove all impurities. The tips were partially coated with apiezon wax to reduce faradaic currents at the tip. *In situ* STM images were recorded in 0.5 M  $\text{H}_2\text{SO}_4$  (diluted from sulfuric acid 95-97%, pa, Merck). The solution was prepared using UHQ (ultra high quality, Millipore) water ( $> 18 \text{ M}\Omega\text{cm}^{-1}$ ). During imaging, the tip potential was kept constant at 0.4 V vs. SHE and the sample potential as well as the tip bias scanned to the required potential.

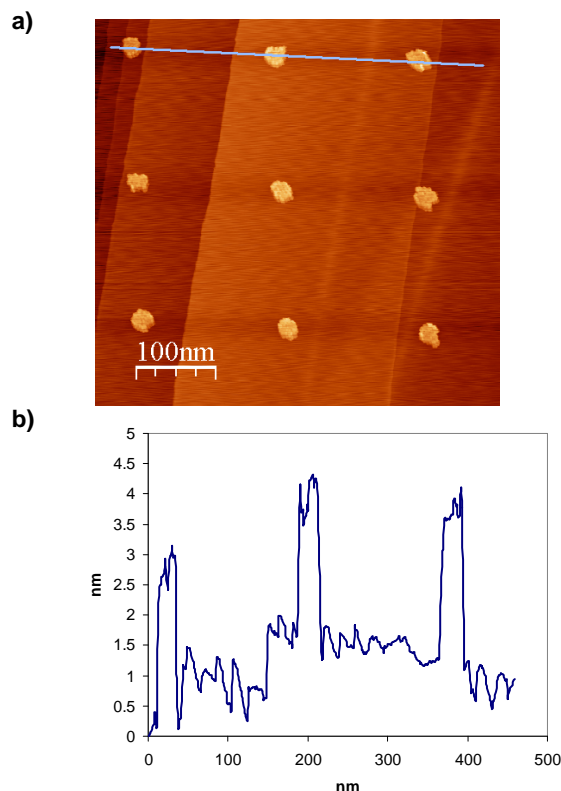


**Figure 1.** EC-STM image of EBL prepared HOPG electrode (air): a) topographic image; b) height profile

## Results

A topographic image of a sample prepared via EBL and subsequent Pt deposition is shown in Figure 1 a. The STM image displayed the arrangement of Pt dots on the HOPG surface with a distance of 200 nm between them. The diameter of the created dots is about 30 nm and the apparent height 3 nm (figure 1 b). The obtained STM image is very sharp and well-resolved; the pattern remains stable even if the same area is scanned numerous times for several hours (4-5 h). This behaviour is surprising as Pt dots of this size on untreated HOPG in air are reported to be quite mobile [2,6].

Stable STM images could also be obtained *in situ* in sulphuric acid (Figure 2 a), moreover, the dots did not move during numerous scans of the area at a constant sample potential of 0.7 V vs. SHE (indicated by arrow in Figure 2 b).

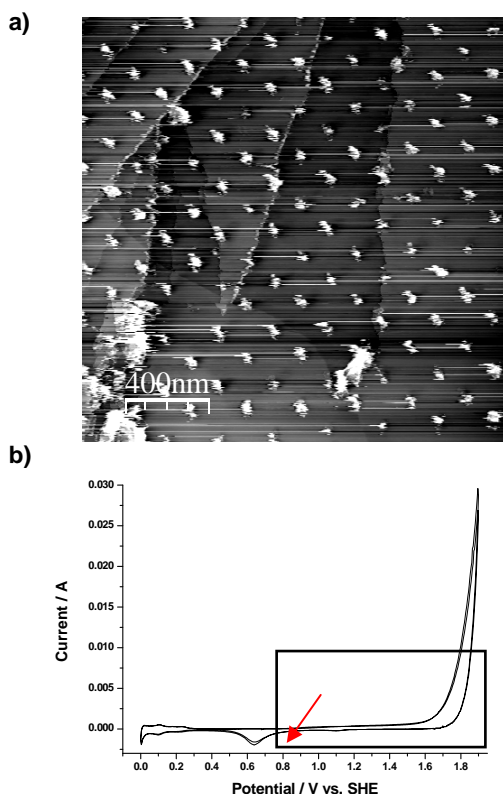


**Figure 2.** a) EC-STM image of EBL prepared Pt/HOPG model electrode (tip potential 0.4V vs. SHE, sample potential 0.7V vs. SHE, 0.5 M H<sub>2</sub>SO<sub>4</sub>) and b) Pt-wire CV recorded in 0.5 M H<sub>2</sub>SO<sub>4</sub>

The effect of oxidizing electrode potentials on Pt dots was investigated by scanning the sample potential to more anodic values starting from 0.7 to 1.9 V (see figure 2 b) and holding the potential during the image accumulation. These experiments have shown that the dots are stable up to the value of 1.3 V vs. SHE and disappear at higher potentials. At 1.9 V vs. SHE, the topographic image displayed a hole pattern corresponding to the original pattern of Pt dots (Figure 3 a). Scanning the potential back to 0.7 V and repeating the STM scan of the same area revealed that only 1 nm deep and 20 nm wide holes remained on the surface (Figure 3 b). Extending the imaged area revealed locations - next to the formerly scanned area - which also contained the above-mentioned holes, thus, Pt loss seems to be induced not solely by the STM tip.

The origin of the holes still has to be determined. They may be either a result of Pt induced carbon corrosion at

elevated potentials or defects created on HOPG surface during e-beam exposure. Formation of defects during e-beam exposure would also explain the immobilization of the dots observed during the STM measurements in air.

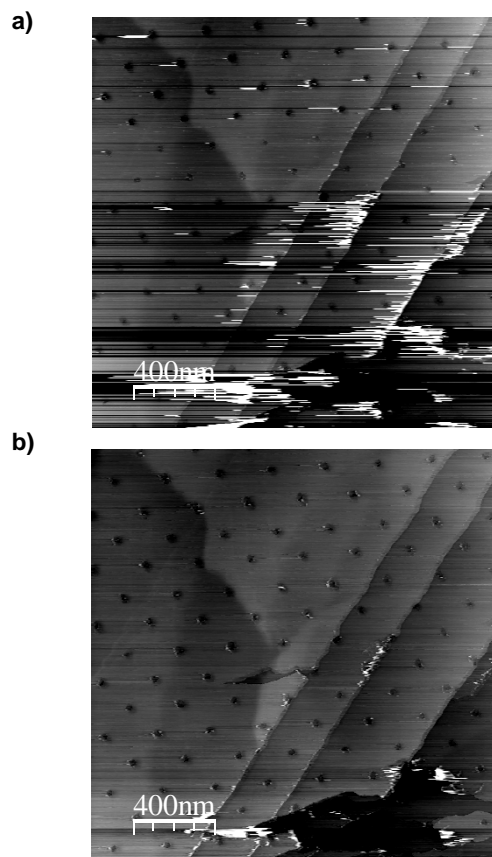


**Figure 3.** EC-STM image of EBL prepared Pt/HOPG model electrode (tip potential 0.4V vs. SHE, 0.5 M H<sub>2</sub>SO<sub>4</sub>) at sample potential a) 1.9V vs. SHE and b) 0.7V vs. SHE (after scanning back)

In conclusion, Pt/HOPG model electrodes prepared by EBL on HOPG can be successfully imaged with STM in air and *in situ* in sulphuric acid. Further studies to investigate the origin of Pt loss and formation of holes are necessary.

## Acknowledgement

The authors would like to thank Michael Horisberger (LDM, PSI) for Pt deposition and Swiss National Science Foundation (SNSF) for financing the project 200021\_121719/1.

## References

- [1] F. Gloaguen, J.M. Léger, C. Lamy, A. Marmann, U. Stimming, R. Vogel, *Electrochimica Acta* **44**, 1805-1816 (1998).
- [2] F. Atamny, A. Baiker, *Appl. Catal. A* **173**, 201-230 (1998).
- [3] T. Brülle, U. Stimming, *J. Electroanal. Chem.* **636**, 10-17 (2009).
- [4] J. Oh, T. Kondo, D. Hatake, Y. Iwasaki, Y. Honma, Y. Suda, D. Sekiba, H. Kudo, J. Nakamura, *J. Phys. Chem. Lett.* **1**, 463-466 (2010).
- [5] V.A Guzenko, J. Ziegler, A. Savouchkina, C. Padeste, C. David, doi:10.1016/j.mee.2011.02.042, *Microelectronic Engineering*.
- [6] J. Chen, K.-Y. Chan, *Mol. Simulat.* **31**, 527-533 (2005).

## Ionic liquids in vacuo: Concept and design of a newly developed *in situ* XPS cell

D. Weingarth, A. Foelske-Schmitz, R. Kötzt, A. Wokaun

phone: +41 56 310 4131, e-mail: daniel.weingarth@psi.ch

During the last decade room temperature molten salts, also known as room temperature ionic liquids (ILs), have gained considerable interest in various fields of research [1]. Consisting solely of ions and being liquid in a temperature range of  $-76^{\circ}\text{C}$  to  $416^{\circ}\text{C}$  gives them unique physical properties. Electrochemical stability windows of up to 6 V are mentioned in literature [2], making them very attractive for the use in electrochemical storage devices, such as Li-Ion batteries and electrochemical double layer capacitors (EDLC) [3]. In the latter the energy is stored by charge separation within the electrochemical double layer without any faradaic reactions. However, up to now the large potential windows of ILs could not be utilized sufficiently in EDLCs, indicating that the definition of an electrochemical stability window is vague and ill defined. A very interesting property of ILs is their very low vapour pressure. This opens the possibility for ultra high vacuum (UHV) analysis. In this context X-ray photoelectron spectroscopy (XPS) is reported to be a powerful tool for quantitative chemical analysis of ILs and for detection of impurities [4].

Recently, we reported about XPS measurements of HOPG surfaces electrochemically treated in IL, utilizing our quasi *in situ* electrochemical cell [5]. As a continuative development we designed a new XPS cell allowing for electrochemical measurements with a three electrode assembly *in situ*, while taking XP spectra. With this cell we want to investigate possible electrochemical decomposition processes of ILs and thus determine the potential limits of ILs. The design of the *in situ* XPS cell and first measurements on a platinum working electrode with the IL 1-Ethyl-3-methylimidazolium bis (trifluoromethylsulfonyl) imide [EMIM][TFSI] (Iolitec technologies) will be presented in the following.

### Experimental

The *in situ* XPS cell consists of several parts. (cf. Figure 1): The reaction vessel (PEEK) (2) is placed on a specimen holder made from stainless steel (1). The working electrode (WE) (3) is placed in a position appropriate for XPS analysis and fixed with a piece of titanium (4). Reference (RE) and counter electrode (CE) (5) are prepared of activated carbon (AC, YP17) and wetted with the IL. These electrodes are placed on the opposite side walls of the vessel and are contacted with titanium wires (all potentials are quoted against the AC reference electrode [6]). Kapton insulated wires (6) are used to independently connect working, counter and reference electrode to the respective contact. The working electrode is connected to the ground of the XPS system via the specimen holder.

Since working, reference and counter electrode have to be insulated against each other, PEEK screws (7) as well as a PEEK interlayer (9) were used.

After the assembly of the carefully cleaned parts the cell is dried for at least 4h at a temperature of  $120^{\circ}\text{C}$  at a pressure of 20 mbar and then transferred into a glove box, where it is filled with IL. The transfer to the XPS

laboratory is done in a desiccator in order to avoid air exposure.

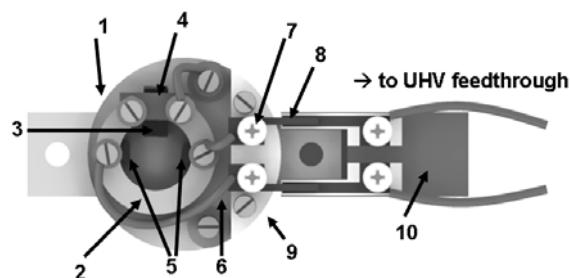


Figure 1. Scheme of the *in situ* XPS cell.

The cell is placed inside the entry lock of the UHV system and the chamber is evacuated to a pressure of  $10^{-7}$  mbar prior to transferring it into the analyzer chamber, where it is turned over to the manipulator arm (10). The manipulator arm itself serves as contact for the working electrode, whereas two sliding contacts (8) allow for contacting reference and counter electrode separately. A UHV low current feedthrough establishes the connection of a potentiostat (Versastat, PAR) to the system.

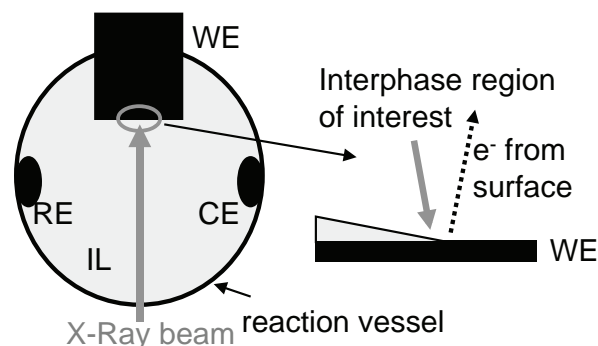


Figure 2. Desired measurement position for XP spectra indicating the interphase region.

XPS measurements are performed using a VG ESCALAB 220iXL spectrometer equipped with an Al  $K_{\alpha}$  mono-source and a magnetic lens system. The source is operated at a power of 150 Watt. A spot size of  $500\ \mu\text{m}$  diameter is chosen for excitation. The spectra are recorded in constant analyzer energy mode at a pass energy of 50 eV for survey spectra and 20 eV for high resolution acquisition of core level spectra, respectively. Figure 2 illustrates the desired measurement position for taking XP spectra (interphase region IL/WE/UHV). In this position it is possible to monitor the electrolyte as well as the electrode simultaneously, and, therefore investigate electrochemical reactions at the electrochemical interphase. Appropriate positioning of the sample in the X-ray beam is controlled by recording survey spectra. The interphase is assumed to be probed if signals of the WE, i.e. Pt occur together with signals from elements

present in the IL, i.e. N, F, S, O, C in one survey spectrum.

## Results

As a first reference measurement, a cyclic voltammogram (CV) of a Pt foil in [EMIM][TFSI] with a scan rate of  $100 \text{ mVs}^{-1}$  is shown in Figure 3, recorded with the new cell under UHV. In the potential range of -1 V to +1.5 V typical features, also observable in our standard lab cells at atmospheric pressure, are recorded (compare dashed and solid line Figure 3).

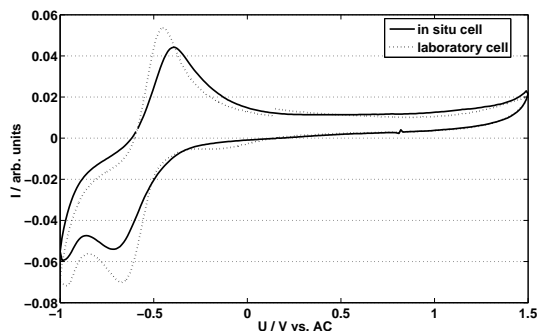


**Figure 3.** Comparison of *in situ* and lab cell cyclic voltammogram of Pt in [EMIM][TFSI].

Recording XP spectra of elements present in IL and WE at different electrode potentials revealed an interesting phenomenon. Spectra originating from the IL were shifted proportionally to the applied electrode potential, while the spectra originating from the WE were constant in binding energy.

A comparison of high resolution C1s and Pt4f spectra, recorded at 0 V and -1.5 V, illustrates the behaviour. The specific C1s peaks (Figure 4a) corresponding to CH, CN and  $\text{CF}_3$  species in the IL, shift according to the applied potential to 1.5 eV higher binding energies. The binding energy of the Pt4f signal (Figure 4 b)) originating from the Pt WE, however, stays constant, independent of the applied potential.

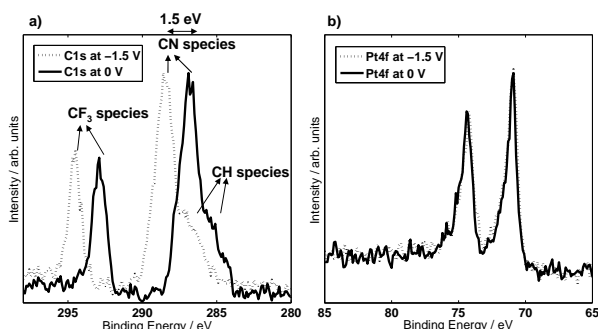


**Figure 4.** High resolution a) C1s and b) Pt4f XP spectra recorded at 0 V (solid line) and -1.5 V (dashed line).

This phenomenon can be explained by the working principle of the potentiostatically controlled three electrode arrangement, where the reference electrode determines the potential in the electrolyte. The schematic diagram in Figure 5 illustrates this behaviour with respect to the potential applied at the working electrode  $U_{WE}$ .

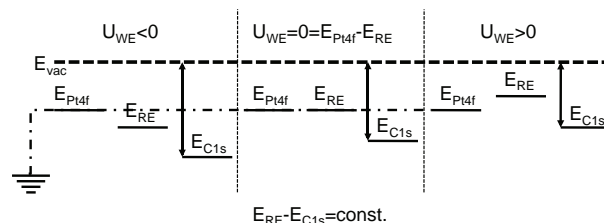


**Figure 5.** Shift of the electrolyte species with the applied potential.

The respective energy levels are shown with reference to the vacuum level. While the energetic level of the Pt WE is fixed (grounded), the potential difference between WE and RE is controlled by the potentiostat. The activated carbon RE itself has a fixed potential difference to the electrolyte level. Therefore, all electrolyte levels shift with the potential applied to the WE, which is observed by XPS.

This allows assigning certain XP spectra to the electrolyte or to the WE.

## Conclusions

With this IL based electrochemical cell it is for the first time possible to measure *in situ* XP spectra of the electrode/electrolyte interface under potential control in a three electrode arrangement. The possibility to measure the electrolyte potential *in situ* with X-ray photoelectron spectroscopy against the respective reference electrode is a completely new field. This allows for determination of exact decomposition potentials of ILs with respect to the specific working and reference electrode.

## References

- [1] T. Torimoto, T. Tsuda, K.-i. Okazaki, S. Kuwabata, *Adv. Mater.* **22**, 1196 (2010).
- [2] P. A. Z. Suarez, V. M. Selbach, J.E.L Dullius, S. Einloft, C.M.S Piatnicki, D. S. Azambuja, R. F. de Souza, J. Dupont, *Electrochim. Acta* **42**, 2533 (1997).
- [3] A. Balducci, U. Bardi, S. Caporali, M. Mastragostino, F. Soavi, *Electrochem. Commun.* **6**, 566 (2004).
- [4] K.R.J. Lovelock, I.J. Villar-Garcia, F. Maier, H.-P. Steinrueck, P. Licence, *Chem. Rev.* **110**, 5158 (2010).
- [5] A. Foelske-Schmitz, D. Weingarh, H. Kaiser, R. Kötzt, *Electrochem. Commun.* **12**, 1453 (2010).
- [6] P. Ruch, D. Cericola, M. Hahn, R. Kötzt, A. Wokaun, *J. Electroanal. Chem.* **636**, 128 (2009).

# The potential window of imidazolium based ionic liquids - A comparative XPS, DFT and electrochemical study

A. Foelske-Schmitz, I. Czekaj, D. Weingarh, R. Kötzt

phone: +41 56 310 4193, e-mail: annette.foelske@psi.ch

Ionic liquids (IL) are compounds consisting entirely of ions and exist in their liquid state at room temperature. IL are of electrochemical interest as these compounds provide large electrochemical stability windows of 4 - 6 V [1]. Furthermore, IL have almost no vapour pressure, and, therefore, can be studied using ultra high vacuum techniques such as X-ray photoelectron spectroscopy (XPS). XPS studies of IL showed that this method is perfectly suitable for quantitative chemical analysis and very sensitive to impurities [2]. Herein, we report on valence band measurements of three different 1-Ethyl-3-methylimidazolium [EMIM] based ionic liquids with varying anions. The well structured valence bands were also calculated by means of density functional theory (DFT). The calculated values of the HOMO-LUMO gaps are compared to the measured electrochemical windows.

## Experimental

XPS measurements were performed on droplets of the IL [EMIM][BF<sub>4</sub>], [EMIM][B(CN)<sub>4</sub>] and [EMIM][TFSI] using a VG ESCALAB 220iXL spectrometer equipped with a monochromatic Al K $\alpha$  X-ray source for excitation. DFT calculations were done using generalized gradient approximation (GGA, RPBE functional) implemented into cluster code StoBe (LCAO, Gaussian basis sets). Electrochemical measurements were performed on glassy carbon electrodes in an air tight cell, assembled in a glove box using freshly dried IL as electrolytes. PTFE bound activated carbon (AC) was used as reference and counter electrode.

## Results

The occupied states calculated by DFT (red lines, Figure 1) are in good agreement with the valence band spectra recorded by XPS (black lines, Figure 1).

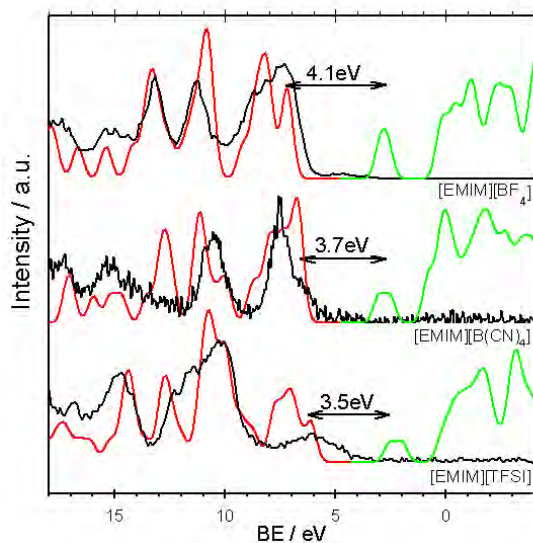


**Figure 1.** Calculated occupied (red), unoccupied (green) and measured (black) valence band spectra of [EMIM] based ionic liquids, IL and calculated HOMO-LUMO gap as indicated.

The different anions significantly influence the shape of the measured valence band spectra, which is also validated by the calculated DFT electron densities of the occupied states. Detailed DFT analysis confirms that the HOMO states are built by p- or  $\pi$ - type components of the anions. Calculation of the unoccupied states (green lines, Figure 1) reveals that the LUMO orbitals are derived from p-type components of the [EMIM] cation. The calculated HOMO-LUMO gap is highest for [EMIM][BF<sub>4</sub>] (4.1 eV) and lowest for [EMIM][TFSI] (3.5 eV).

For determination of the electrochemical stability windows, current density potential curves have been recorded (exemplarily shown for [EMIM][BF<sub>4</sub>] in Figure 2). Choosing a cut-off current of 100  $\mu$ A/cm<sup>2</sup>, the electrochemical stability windows of [EMIM][BF<sub>4</sub>] and [EMIM][TFSI] were determined to be 4.3 V and the one of [EMIM][B(CN)<sub>4</sub>] to be largest with 4.5 V.

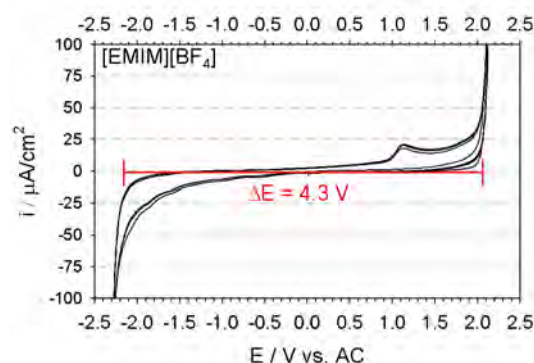


**Figure 2.** Electrochemical window of [EMIM][BF<sub>4</sub>] choosing a cut-off current of 100  $\mu$ A/cm<sup>2</sup> at a scan rate of 10 mV/s, working electrode: glassy carbon.

For [EMIM][BF<sub>4</sub>] the electrochemical data is in surprisingly good agreement with the calculated HOMO-LUMO gap. Prediction of an electrochemical stability order from the calculations, however, appears somewhat inconclusive as, for instance, for [EMIM][TFSI] a discrepancy of 20% is observed. Reasons may either refer to the calculations for which optimized structures of one ion pair in the gas phase were considered or to charge transfer reactions occurring at current densities below 100  $\mu$ A/cm<sup>2</sup>, and thus, resulting in smaller electrochemical stability windows.

Determination of exact decomposition potentials, however, is a challenging issue which is going to be processed using the newly developed *in situ* XPS cell [3].

## References

- [1] M. Galinski, A. Lewandowski, I. Stepniak, *Electrochim. Acta* **51**, 5567 (2006).
- [2] K.R.J. Lovelock, I.J. Villar-Garcia, F. Maier, H.P. Steinrück, P. Licence, *Chem. Rev.* **110**, 5158 (2010).
- [3] D. Weingarh, A. Foelske-Schmitz, R. Kötzt, A. Wokaun, this report, 89 (2011).



# THE ELECTROCHEMISTRY LABORATORY



# IMPRESSIONS



On January 6, PSI and Belenos received the Watt d'Or 2011 for the development of a fuel cell system, which has the potential to be part of a cost efficient compact car.

The fuel cell for the vehicle developed at PSI is shown below.

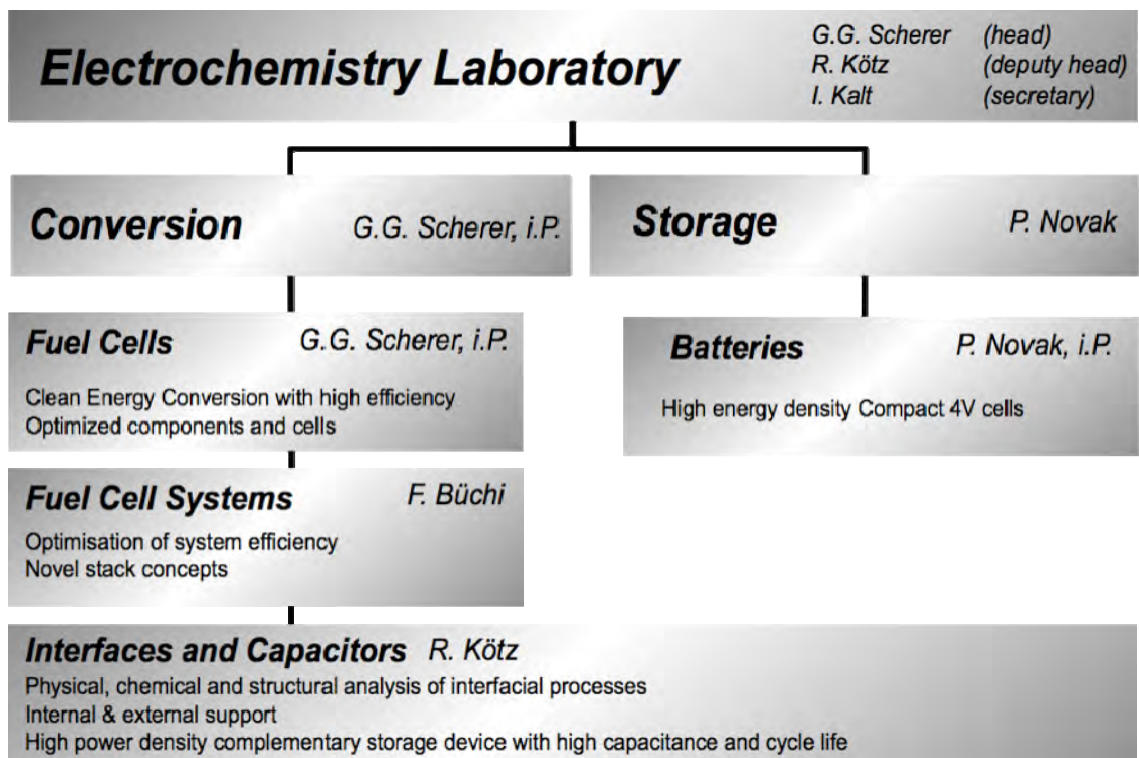


After the Kick-off Meeting of the Research Network Electrochemistry and Batteries in Ludwigshafen on August 11, 2010. PSI is represented by Prof. Petr Novák (fourth from right). (Photo: BASF)





# STRUCTURE





# ECL-PERSONNEL

## Staff

**Ben youcef Hicham, Dr. ♦ Bernard Jérôme, Dr. ♦ Boillat Pierre, Dr. ♦ Bonorand Lukas (since June) ♦ Büchi Felix, Dr.**

**Colin Jean-François, Dr. (until March)**

**Foelske Annette, Dr.**

**Gloor Thomas ♦ Gubler Lorenz, Dr.**

**Hofer Marcel**

**Junker Christoph (since March)**

**Kaiser Hermann ♦ Kalt Isabella ♦ Kötz Rüdiger, Dr.**

**Lüscher Sandro**

**Maire Pascal, Dr. (until April) ♦ Märkle Wolfgang, Dr. ♦ Marmy Christian**

**Novák Petr, Dr.**

**Perego Raffaella, Dr. (until August) ♦ Perez Sofia, Dr. (since October)**

**Roth Jörg (since October)**

**Sasaki Tsuyoshi, Dr. ♦ Sasaki Yuri, Dr. (since January) ♦ Scherer Günther G., Dr. ♦ Schneider Holger, Dr. ♦ Schneider Ingo, Dr. ♦ Schulenburg Hendrik, Dr. ♦ Siegrist Raphael ♦ Sommer Heino, Dr. (until December)**

**Thut Jürg**

**Villevieille Claire, Dr. (since April)**

## PhD Students

**Bayer Michael ♦ Bernardo Philippe ♦ Buchmüller Yves (since August)**

**Cericola Dario**

**Dockheer Sindy (until June)**

**Eller Jens**

**Godbole Vikram**

**Hantel Moritz (since January) ♦ Hess Michael ♦ Hintennach Andreas (until Oktober)**

**Jetsrisuparb Kaewta**

**Kreitmeier Stefan**

**Linse Nicolas**

**Neophytides George (since August)**

**Oberholzer Pierre**

**Savouchkina Anastasia ♦ Schuler Gabriel (until January) ♦ Schwanitz Bernhard ♦ Simmen Franziska (until May)**

**Verma Pallavi ♦ Von Dahlen Steffen**

**Wallasch Frank (until March) ♦ Weingarth Daniel (since January)**

**Zaglio Maurizio**

# THESE PHD STUDENTS FROM ECL GRADUATED IN 2010

**Dr. Gabriel Schuler**



*Untersuchung der lokalen Gasphase in Polymer-Elektrolyt-Brennstoffzellen*

Ph.D. Thesis, No. 18883, ETH Zürich, February 10, 2010

Examiners Prof. Dr. A. Wokaun, PSI/ETH Zürich  
Prof. Dr. D. Günther, ETH Zürich  
Dr. F. Büchi, PSI Villigen

**Dr. Frank Wallasch**



*Investigations on radiation grafted polymer fuel cell membranes: Preparation, characterization, application*

Ph.D. Thesis, No. 18925, ETH Zürich, March 17, 2010

Examiners Prof. Dr. A. Wokaun, PSI/ETH Zürich  
Prof. Dr. A.D. Schlüter, ETH Zürich  
Dr. G.G. Scherer, PSI Villigen  
Dr. L. Gubler, PSI Villigen

**Dr. Franziska Simmen**



*Pulsed laser deposition zur Herstellung von Modell-Phasengrenzen für elektrochemische Untersuchungen*

Ph.D. Thesis, No. 19092, ETH Zürich, June 2, 2010

Examiners Prof. Dr. A. Wokaun, PSI/ETH Zürich  
PD Dr. T. Lippert, PSI Villigen  
Prof. Dr. P. Novák, PSI/ETH Zürich  
Prof. Dr. D. Günther, ETH Zürich

**Dr. Andreas Hintennach**

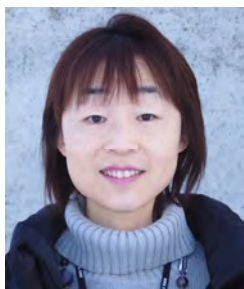


*Anwendungen der in situ Ramanmikroskopie für Lithiumionen-Batterien*

Ph.D. Thesis, No. 19090, ETH Zürich, June 2, 2010

Examiners Prof. Dr. A. Wokaun, PSI/ETH Zürich  
Prof. Dr. M. Niederberger, ETH Zürich  
Prof. Dr. P. Novák, PSI/ETH Zürich

**Dr. Yuri Yamada**



*Fabrication and investigation of the colloidal crystals from monodispersed mesoporous silica spheres*

Ph.D. Thesis, Nagoya University, Japan, December 22, 2010

Examiners Prof. Dr. T. Seki, Nagoya University  
Prof. Dr. S. Koda, Nagoya University  
Prof. Dr. N. Saito, Nagoya University  
Ass. Prof. Dr. Y. Takeoka, Nagoya University

# EXCHANGE STUDENTS, DIPLOMA THESES, SUMMER STUDENTS

<b>Thanh Long Nguyen</b>	<i>Characterization of PtCo/C catalysts for the electrochemical oxygen reduction in Polymer Electrolyte Fuel Cells</i> EPFL Lausanne, September 2009 – February 2010
<b>Adrian Waibel</b>	<i>Styrene-acrylonitrile co-grafted ETFE based membranes for fuel cells</i> ETH Zürich, November 2009 – February 2010
<b>Tiphaine Poux</b>	<i>Investigation of the electrochemical performance of lithium-sulfur batteries</i> School of Engineering, PHELMA of Grenoble, FR, February – July 2010
<b>Patrick Lanz</b>	<i>Elektrochemische Charakterisierung von <math>\text{Li}_2\text{MnO}_3</math>-stabilisiertem <math>\text{Li}(\text{Mn},\text{Ni},\text{Co})\text{O}_2</math> für Lithiumionen-Batterien</i> ETH Zürich, February – July 2010
<b>Peter Studer</b>	<i>Investigations on solvent uptake and monomer diffusion in grafted FEP-films</i> ETH Zürich, March – May 2010
<b>Adriano Tonus</b>	<i>Réalisation d'une interface homme machine pour un banc d'essai pile à combustible (Development of a Human-Machine Interface for a fuel cell testbench)</i> University of Valenciennes and Hainaut Cambrésis, FR, March – August 2010
<b>Tom Engl</b>	<i>Charakterisierung von Platin- und Platin-Kobalt-Katalysatoren zur Sauerstoffreduktion</i> Hochschule Amberg Weiden, DE, March – September 2010
<b>Tomas Rosen</b>	<i>Characterization of solid-water interactions in the micro-pore gas structure of polymer electrolyte fuel cells</i> KTH Stockholm, SE, June – August 2010

# SEMINAR, INVITED SPEAKERS

<b>Dr. Markus Schmuck,</b> MIT, Cambridge, USA	<i>Material transport in porous structure: dilute and concentrated solution theory</i> January 11, 2010
<b>Dr. Yoshinari Makimura,</b> Toyota Central R&D Labs., Inc., Aichi, JP	<i>Structural chemistry and electrochemistry of positive electrode materials for lithium-ion batteries</i> February 1, 2010.
<b>Dr. Albert Hammerschmidt,</b> Siemens AG, Erlangen, DE	<i>Wasserstoff-/Sauerstoff-Brennstoffzellen für die U-Boot-Anwendung</i> February 8, 2010.
<b>Dr. Constanze Donner,</b> Atotech, Berlin, DE	<i>Thin metal layer deposition and the role of additives</i> March 15, 2010.
<b>Prof. Bernd Speiser,</b> Universität Tübingen, DE	<i>Molekulare Elektrochemie - Redoxreaktionen an Molekülen und funktionellen Materialien</i> April 19, 2010.
<b>Dr. Whitney Colella,</b> Sandia National Laboratories, USA	<i>Optimizing the design and control of low-carbon, distributed, polygenerative fuel cell systems and energy storage devices</i> April 26, 2010.
<b>Dr. Sylvio Indris,</b> Karlsruher Institut für Technologie, DE	<i>Li ion dynamics in solids: from a single crystal to Li intercalation compounds</i> May 10, 2010.
<b>Alexey Serov,</b> Universität Bern	<i>Non-platinum catalysts for oxygen reduction in low temperature fuel cells</i> June 21, 2010.
<b>Prof. Joachim Lewerenz,</b> Helmholtz-Zentrum für Materialien und Energie, Berlin, DE	<i>Photoelectrocatalysis: from basics to advanced concepts</i> September 6, 2010.
<b>Dr. Klaus Beccu,</b> Battelle Geneva, R&D Center	<i>Vom Hydrid zum Hybrid - Entwicklung elektrochemischer Speichersysteme am Battelle F&amp;E Zentrum Genf</i> September 20, 2010.
<b>Prof. Yang Shao-Horn,</b> MIT, Cambridge, USA	<i>Overview of the battery research activities at MIT</i> October 4, 2010.
<b>Dr. Artur Braun,</b> EMPA Dübendorf	<i>X-ray and photoelectron spectroscopy on photocatalysts and materials for solar photoelectrochemical applications</i> October 25, 2010.
<b>Dr. Marlene Rodlert Bacilieri,</b> TIMCAL SA, Bodio	<i>Carbon as catalyst support in PEMFC</i> November 22, 2010.

# AWARDS

<b>A. Hintennach</b>	Swisselectric Research Award 2010 <i>Wegweisende Verbesserungen von Lithiumionen-Batterien</i> September 16, 2010
<b>H. Schneider</b>	SCS Metrohm Prize <i>Combined in situ FTIR and Raman microscopy of electrode materials – a new tool for battery scientists</i> Best oral presentation in the section Physical Chemistry Swiss Chemical Society Fall Meeting 2010, University Zürich, Zürich, September 16, 2010.
<b>L. Klüpfel, M. Nachtegaal, H. Schulenburg, T. Engl</b>	SCS 2010 Poster Award <i>XAS studies of leached PtCo catalysts for PEMFCs</i> Swiss Chemical Society, Fall Meeting 2010, University Zürich, Zürich, September 16, 2010
<b>H. Schulenburg, B. Schwantz, J. Krbanjevic, T. Engl</b>	Progress MEA 2010 Poster Award <i>3D Imaging of PEFC electrode degradation</i> Progress MEA, La Grande Motte, France, September 20-22, 2010
<b>PSI &amp; Belenos Clean Power AG</b>	Watt d'Or 2011 <i>Energieeffiziente Mobilität,</i> Bern, Januar 6, 2011

# CONFERENCES – SYMPOSIA

26<sup>th</sup> One-Day-Symposium  
May 5, 2010

*Electrochemistry in Switzerland*

Organizers: G.G. Scherer, R. Kötz and Petr Novák

Contributions from:

Patrik Schmuki, University of Erlangen, DE

Hubert Girault, EPFL, Lausanne

Alexander Wokaun, PSI, Villigen

Olivier Bucheli, HTceramix-SOFCpower, Yverdon-les-Bains

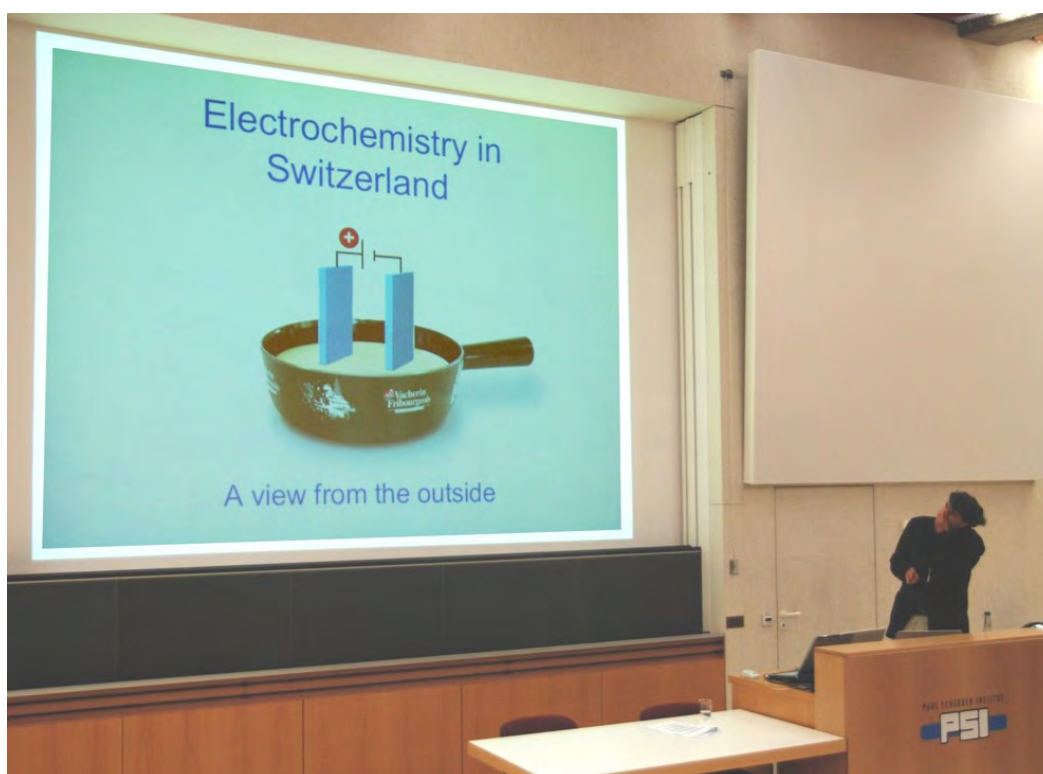
Jean-Claude Puipe, Steiger SA, Châtel-St-Denis

Laetitia Philippe, EMPA, Dübendorf

Thomas Suter, EMPA, Dübendorf

Caspar Demuth, ZHAW, Wädenswil

Louis Schlapbach, formerly Empa, Dübendorf



P. Schmuki addressing the Symposium topic in his excellent and entertaining presentation

# REVIEW ACTIVITIES OF THE LABORATORY

## Journals

ACS Nano ♦ Advanced Functional Materials ♦ Angewandte Chemie International Edition ♦ Applied Physics A

Carbon

Electrochimica Acta ♦ Electrochemistry Communications ♦ Electrochemical and Solid-State Letters♦

Ionics

Journal of the American Chemical Society ♦ Journal of Electroanalytical Chemistry ♦ Journal of the Electrochemical Society ♦ Journal of Physical Chemistry ♦ Journal of Power Sources ♦ Journal of Solid State Electrochemistry

Langmuir

Nature Materials

## Organisations

Alexander von Humboldt-Stiftung, DE ♦ ANR (Agence National de la Recherche), FR

Fudan University, Shanghai, CN

Indian Institute of Technology, New Delhi, IN

King Abdullah University of Science and Technology, Saudi Arabia, SA

SNF (Schweizerischer Nationalfond)

Technische Universität München, DE ♦ Tsinghua University, Peking, CN

Università Tor Vergate, Roma, IT ♦ Universität Ulm, DE

Wiley-VCH, Hoboken NJ, US

## Co-Referee's Report for Dissertations

I. Bilecka, ETH Zürich

A. Hintennach, PSI/ETH Zürich

Y. Mettan, ETH Zürich

G. Schuler, ETH/PSI Zürich ♦ F. Simmen, PSI/ETH Zürich

F. Wallasch, PSI/ETH Zürich

# INDUSTRIAL PARTNERS

**The Laboratory had the pleasure to collaborate with the following industrial partners during the year 2010:**

**BASF SE**, Ludwigshafen, DE ♦ **Belenos Clean Power**, Biel

**CEKA Elektrowerkzeuge AG**, Wattwil ♦ **Centro Ricerche Fiat (CRF)**, Torino, IT

**Daimler AG**, Stuttgart, DE ♦ **DANA, Reinz-Dichtungs-GmbH**, Neu-Ulm, DE

**Freudenberg Fuel Cell Component Technology KG (FFCCT)**, Weinheim, DE

**Heraeus Quarzglas GmbH & Co. KG**, Kleinostheim, DE

**MES DEA**, Stabio

**SolviCore GmbH & Co. KG**, Hanau, DE

**Umicore AG & Co. KG**, Brussels, BE

**TIMCAL SA**, Bodio

**Volkswagen**, Wolfsburg, DE

## PROJECT COLLABORATIONS WITH EXTERNAL PARTNERS

### BFE

F.N. Büchi Projektleiter	<i>Cal.PEF-CH: Modelbased investigation of PE fuel cell performance with focus on porous layer properties with ZHAW, Winterthur</i>
F.N. Büchi Projektleiter	<i>Röntgen Mikro-Tomographie an Polymerelektrolyt-Brennstoffzellen</i>
F.N. Büchi Projektleiter	<i>Gasanalysis in polymer electrolyte fuel cells</i>
L. Gubler Projektleiter	<i>Lebensdauer-Limitierungen von Brennstoffzellen-Membranen: Mechanismen, Methoden und Innovationen</i>
L. Gubler, I.A. Schneider Projektleiter	<i>go.PEF-CH: Enhancing PEFC durability and reliability under application-relevant conditions</i> Partner: Berner Fachhochschule Technik und Informatik (BFH-TI, Biel BE), CEKA Elektrowerkzeuge AG & Co. KG (Wattwil SG), MES-DEA SA. (Stabio TI)

### CCEM

F.N. Büchi Projektleiter	<i>hy.muve: Development of hydrogen powered municipal vehicle with EMPA Dübendorf and Industrial Partners</i>
-----------------------------	---

### EU

F.N. Büchi Projektleiter	<i>JTI FCH: Auto-Stack: Automotive Fuel Cell Stack Cluster Initiative for Europe</i> with Auto-Stack consortium
P. Novák Projektleiter	<i>MAHEATT (Materials for high energy accumulators in traction and tools)</i>

### Industry

W. Märkle Projektleiter	<i>Kohlenstoffe</i> Heraeus Quarzglas GmbH & Co. KG, Kleinostheim, Germany
W. Märkle Projektleiter	<i>Graphite für Lithiumionen-Batterien</i> TIMCAL SA, Bodio
P. Novák Projektleiter	<i>Projekt HE-Lion</i> BASF SE, Ludwigshafen
P. Novák Projektleiter	<i>Forschungsnetzwerk „Elektrochemie und Batterien“</i> BASF SE, Ludwigshafen, Germany
I.A. Schneider Projektleiter	<i>Diagnostics of polymer electrolyte fuel cells</i> Automotive industry

### Nationalfonds

A. Foelske-Schmitz Projektleiterin	<i>Degradation mechanisms of electro-catalysts used in polymer electrolyte fuel cells</i>
L. Gubler Projektleiter	<i>Antioxidant strategies for the stabilization of fuel cell membranes against oxidative stress</i>

R. Kötz Projektleiter	<i>Graphite oxides and graphene for electrochemical energy storage</i>
P. Novák Projektleiter	<i>Synthetic solid electrolyte interphase on carbon electrodes for lithium-ion batteries</i>
P. Novák Projektleiter	<i>New oxyphosphates as high specific charge electrode materials for lithium-ion batteries</i>
P. Novák Projektleiter	<i>Advanced materials for efficient portable energy supplies</i>

## TEACHING ACTIVITIES

### University Level Teaching

Prof. Dr. P. Novák, Prof. Dr. A. Wokaun	<i>Technische Elektrochemie</i> ETH Zürich, HS 2010
Prof. Dr. P. Novák	<i>Elektrochemie und Batterien – Von der Grundlagen zur Anwendung „HE-Lion Battery School“ der Justus-Liebig-Universität Giessen, FS 2010</i>
Prof. Dr. A. Wokaun, Dr. G.G. Scherer, Prof. Dr. K. Boulouchos	<i>Renewable Energy Technologies II</i> ETH Zürich, FS 2010

## PUBLICATIONS

### Books and Reviewed Book Chapters

H.A. Gasteiger <sup>1</sup> , H. Uchida <sup>1</sup> , V. Ramani <sup>1</sup> , A. Weber <sup>1</sup> , T.J. Schmidt <sup>1</sup> , T.F. Fuller <sup>1</sup> , P. Strasser <sup>1</sup> , P. Shirvastian <sup>1</sup> , M. Inaba <sup>1</sup> , M. Edmundson <sup>1</sup> , F.N. Büchi, D. Jones <sup>1</sup> , C. Lamy <sup>1</sup> , R. Mantz <sup>1</sup> , S.R. Narayan <sup>1</sup> , R. Darling <sup>1</sup> , T.A. Zawodzinski <sup>1</sup>	<i>Polymer electrolyte fuel cells 10</i> ISBN: 978-1-56677-820-6, ECS Transactions, <b>33</b> (2010). 218 <sup>th</sup> ECS Meeting, Las Vegas, USA, October 10–15 (2010). <sup>1</sup> external co-organizer of the 218 <sup>th</sup> ECS Meeting
I. Kalt, R. Kötz, G.G. Scherer	<i>PSI Electrochemistry Laboratory Annual Report 2009</i> ISSN 1661-5379 (2010).
P. Novák, D. Goers <sup>1</sup> , M.E. Spahr <sup>1</sup>	<i>Carbon materials in lithium-ion batteries</i> ISBN 978-1-4200-5307-4, Carbon Materials for Electrochemical Energy Storage Systems, Edited by F. Béguin, E. Frackowiak, CRC Press - Taylor and Francis Group, Boca Raton-New York, 263-328 (2010). <sup>1</sup> TIMCAL SA, Bodio

### Peer Reviewed Papers

S. Balog, U. Gasser, K. Mortensen <sup>1</sup> , L. Gubler, G.G. Scherer, H. Ben youcef	<i>Correlation between morphology, water uptake, and proton conductivity in radiation-grafted proton-exchange membranes</i> doi: 10.1002/macp.200900503, <i>Macromol. Chem. Phys.</i> <b>211</b> , 635-643 (2010). <sup>1</sup> University of Copenhagen, Frederiksberg, Denmark
H. Ben youcef, S. Alkan-Gürsel, A. Buisson <sup>1</sup> , L. Gubler, A. Wokaun, G.G. Scherer	<i>Influence of radiation-induced grafting process on mechanical properties of ETFE-based membranes for fuel cells</i> doi: 10.1002/fuce.200900200, <i>Fuel Cells</i> <b>10</b> , 401-410 (2010). <sup>1</sup> NP Grenoble, France

- J. Bernard, S. Delprat<sup>1</sup>,  
T.M. Guerra<sup>1</sup>, F.N. Büchi  
*Fuel efficient power management strategy for fuel cell hybrid powertrains*  
doi: 10.1016/j.conengprac.2009.12.009, Control Engineering Practice **18**, 408-417 (2010).  
<sup>1</sup> UVHC, LAMIH, Valenciennes, France
- P. Boillat, G. Frei,  
E.H. Lehmann,  
G.G. Scherer,  
A. Wokaun  
*Neutron imaging resolution improvements optimized for fuel cell applications*  
doi: 10.1149/1.3279636, Electrochem. Solid-State Lett. **13**, B25-B27 (2010).
- D. Cericola, P.W. Ruch,  
R. Kötz, P. Novák,  
A. Wokaun  
*Characterization of bi-material electrodes for electrochemical hybrid energy storage devices*  
doi:10.1016/j.elecom.2010.03.040, Electrochem. Commun. **12**, 812-815 (2010).
- D. Cericola, P.W. Ruch,  
R. Kötz, P. Novák,  
A. Wokaun  
*Simulation of a supercapacitor/Li-ion battery hybrid for pulsed applications*  
doi:10.1016/j.jpowsour.2009.10.104, J. Power Sources **195**, 2731-2736 (2010).
- J.-F. Colin, V. Godbole,  
P. Novák  
*In situ neutron diffraction study of Li insertion in  $Li_4Ti_5O_{12}$*   
doi.org/10.1016/j.elecom.2010.03.038, Electrochem. Commun. **12**, 804-807 (2010).
- S.M. Dockheer<sup>1</sup>, L. Gubler,  
P.L. Bounds<sup>1</sup>, A.S. Domazou<sup>1</sup>,  
G.G. Scherer, A. Wokaun,  
W.H. Koppenol<sup>1</sup>  
*Damage to fuel cell membranes. Reaction of HO with an oligomer of poly(sodium styrene sulfonate) and subsequent reaction with CO<sub>2</sub>*  
doi: 10.1039/c0cp00082e, Phys. Chem. Chem. Phys. **12**, 11609-11616 (2010).  
<sup>1</sup> ETH Zürich
- A. Foelske-Schmitz,  
D. Weingarh, H. Kaiser, R. Kötz  
*Quasi in situ XPS study of anion intercalation into HOPG from the ionic liquid [EMIM][BF<sub>4</sub>]*  
doi:10.1016/j.elecom.2010.08.007, Electrochem. Commun. **12**, 1453-1456 (2010).
- A. Foelske-Schmitz, P.W. Ruch,  
R. Kötz  
*Ion intercalation into HOPG in supercapacitor electrolyte—an X-ray photoelectron spectroscopy study*  
doi:10.1016/j.elspec.2010.07.001, J. Electron Spectrosc. Relat. Phenom. **182**, 57-62 (2010).
- L. Gubler, G.G. Scherer  
*Trends for fuel cell membrane development*  
doi:10.1016/j.desal.2009.09.101, Desalination **250**, 1034–1037 (2010).
- P. Kaspar<sup>1</sup>, Y. Jeyaram<sup>1</sup>,  
H. Jäckel<sup>1</sup>, A. Foelske, R. Kötz,  
S. Bellini<sup>1</sup>  
*Silicon nitride hardmask fabrication using a cyclic CHF<sub>3</sub>-based reactive ion etching process for vertical profile nanostructures*  
doi:10.1116/1.3501120, J. Vac. Sci. Technol. B **28**, 1179-1186 (2010).  
<sup>1</sup> ETH Zürich
- R. Kötz, P.W. Ruch, D. Cericola  
*Aging and failure mode of electrochemical double layer capacitors during accelerated constant load tests*  
doi: 10.1016/j.jpowsour.2009.08.04, J. Power Sources **195**, 923-928 (2010).
- P. Maire, H. Kaiser,  
W. Scheifele, P. Novák  
*Colorimetric determination of lithium-ion mobility in graphite composite electrodes*  
doi:10.1016/j.jelechem.2009.09.011, J. Electroanal. Chem. **644**, 127-131 (2010).
- W. Märkle, J.F. Colin, D. Goers<sup>1</sup>,  
M.E. Spahr<sup>1</sup>, P. Novák  
*In situ X-ray diffraction study of different graphites in a propylene carbonate based electrolyte at very positive potentials*  
doi:10.1016/j.electacta.2010.03.103, Electrochim. Acta **55**, 4964-4969 (2010).  
<sup>1</sup> TIMCAL SA, Bodio

- P. Nesvadba<sup>1</sup>, L. Bugnon<sup>1</sup>,  
P. Maire, P. Novák  
*Synthesis of a novel spirobisnitroxide polymer and its evaluation in organic radical battery*  
doi:10.1021/cm901374u, Chem. Mater. **22**, 783-788 (2010).  
<sup>1</sup> BASF SE, Basel
- M. Papra, F.N. Büchi, R. Kötz  
*Investigating the dynamics of a direct parallel combination of supercapacitors and polymer electrolyte fuel cells*  
doi: 10.1002/face.200900197, Fuel Cells **10**, No. 5, 873-878 (2010).
- M. Reum, A. Wokaun,  
F.N. Büchi  
*Adapted flow field structures for PEFC*  
J. Electrochem. Soc. **157**, B673-B679 (2010).
- P.W. Ruch, D. Cericola,  
A. Foelske-Schmitz, R. Kötz,  
A. Wokaun  
*Aging of electrochemical double layer capacitors with acetonitrile-based electrolyte at elevated voltages*  
doi:10.1016/j.electacta.2010.02.064, Electrochim. Acta **55**, 4412-4420 (2010).
- P.W. Ruch, M. Hahn,  
D. Cericola, A. Menzel, R. Kötz,  
A. Wokaun  
*A dilatometric and small-angle X-ray scattering study of the electrochemical activation of mesophase pitch-derived carbon in non-aqueous electrolyte solution*  
doi:10.1016/j.carbon.2010.01.032, Carbon **48**, 1880-1888 (2010).
- P.W. Ruch, D. Cericola,  
A. Foelske, R. Kötz, A. Wokaun  
*A comparison of the aging of electrochemical double layer capacitors with acetonitrile and propylene carbonate based electrolytes at elevated voltages*  
doi:10.1016/j.electacta.2009.11.098, Electrochim. Acta **55**, 2352-2357 (2010).
- I.A. Schneider, S. von Dahlen,  
A. Wokaun, G.G. Scherer  
*A segmented microstructured flow field approach for submillimeter resolved local current measurement in channel and land areas of a PEFC*  
doi: 10.1149/1.3274228, J. Electrochem. Soc. **157**, B338-B341 (2010).
- I.A. Schneider, S. von Dahlen,  
M.H. Bayer, P. Boillat,  
M. Hildebrandt, E.H. Lehmann,  
P. Oberholzer, G.G. Scherer,  
A. Wokaun  
*Local transients of flooding and current in channel and land areas of a polymer electrolyte fuel cell*  
doi: 10.1021/jp102259q, J. Phys. Chem. C **114**, 11998-12002 (2010).
- H. Schulenburg, J. Durst,  
E. Müller<sup>1</sup>, A. Wokaun,  
G.G. Scherer  
*Real surface area measurements of Pt<sub>3</sub>Co/C catalysts*  
doi:10.1016/j.jelechem.2010.02.005, J. Electroanal. Chem. **642**, 52-60 (2010).  
<sup>1</sup> ETH Zürich
- G.A. Schuler, A. Wokaun,  
F.N. Büchi  
*Local online gas analysis in PEFC using tracer gas concepts*  
J. Power Sources **195**, 1647-1656 (2010).
- B.C. Seyfang, P. Boillat,  
F. Simmen, S. Hartmann,  
G. Frei, T. Lippert,  
G.G. Scherer, A. Wokaun  
*Identification of liquid water constraints in micro polymer electrolyte fuel cells without gas diffusion layers*  
doi: 10.1016/j.electacta.2009.12.061, Electrochim. Acta **55**, 2932-2938 (2010).
- F. Simmen, A. Hintennach,  
M. Horisberger, T. Lippert,  
P. Novák, C.W. Schneider,  
A. Wokaun  
*Aspects of the surface layer formation on Li<sub>1+x</sub>Mn<sub>2</sub>O<sub>4-δ</sub> during electrochemical cycling*  
doi:10.1149/1.3464798, J. Electrochem. Soc. **157**, A1026-A1029 (2010).
- F. Simmen, T. Lippert, P. Novák,  
M. Horisberger, M. Döbeli,  
M. Mallepell, A. Wokaun  
*Influence of metal layer coated glassy carbon substrates on the properties of PLD deposited Li<sub>1+x</sub>Mn<sub>2</sub>O<sub>4-δ</sub> films*  
J. Optoelectron. Adv. Mater. **12**, 523-527 (2010).

- M.E. Spahr<sup>1</sup>, D. Goers<sup>1</sup>,  
W. Märkle, J. Dentzer<sup>2</sup>,  
A. Würsig, H. Buqa, C. Vix-  
Guterl<sup>2</sup>, P. Novák
- Overpotentials and solid electrolyte interphase formation at porous graphite electrodes in mixed ethylene carbonate-propylene carbonate electrolyte systems*  
doi:10.1016/j.electacta.2010.08.025, *Electrochim. Acta* **55**, 8928-8937 (2010).  
<sup>1</sup> TIMCAL SA, Bodio  
<sup>2</sup> Institute for Material Science of Mulhouse, France
- D. Tehlar, R. Flückiger,  
A. Wokaun, F.N. Büchi
- Investigation of channel-to-channel cross convection in serpentine flow fields*  
doi: 10.1002/face.201000034, *Fuel Cells* **10**, 1040-149 (2010).
- Y. Utaka<sup>1</sup>, Y. Tasaki<sup>2</sup>, S. Wang<sup>2</sup>,  
D. Iwasaki<sup>1</sup>, K. Waki<sup>2</sup>, N. Kubo<sup>2</sup>,  
K. Shinohara<sup>2</sup>, P. Boillat,  
G. Frei, P. Oberholzer,  
G.G. Scherer, E.H. Lehmann
- Mass transfer characteristics in porous media applying simultaneous measurement method of water visualization and oxygen diffusivity by neutron radiography*  
Trans. JSME, Series B **76**, No.771, 1964-1972 (2010).  
<sup>1</sup> Yokohama University, Japan  
<sup>2</sup> Nissan Motor Co. Ltd., Yokohama, Japan
- Y. Utaka<sup>1</sup>, Y. Tasaki<sup>2</sup>, K. Waki<sup>2</sup>,  
D. Iwasaki<sup>1</sup>, N. Kubo<sup>2</sup>,  
K. Shinohara<sup>2</sup>, P. Boillat,  
P. Oberholzer, G.G. Scherer,  
E.H. Lehmann
- Characteristics of moisture distribution and mass transfer in MPL by neutron radiography*  
Trans. JSME, Series **76**, No.772, 1995-2001 (2010).  
<sup>1</sup> Yokohama University, Japan  
<sup>2</sup> Nissan Motor Co. Ltd., Yokohama, Japan
- P. Verma, P. Maire, P. Novák
- A review of the features and analyses of the solid electrolyte interphase in Li-ion batteries*  
doi:10.1016/j.electacta.2010.05.072, *Electrochim. Acta* **55**, 6332-6341 (2010).

## Conference Proceedings / Other Papers

- S. Balog, U. Gasser,  
K. Mortensen<sup>1</sup>, L. Gubler,  
G.G. Scherer, H. Ben youcef
- Correlation between morphology, water uptake, and proton conductivity in radiation-grafted proton-exchange membranes*  
Online Proc. Polymer Materials and Membranes for Energy Devices, Volume 1269E, 1269-FF02-05, MRS Spring Meeting, San Francisco, USA, April 5-9 (2010).  
<sup>1</sup> University of Copenhagen, Frederiksberg, Denmark
- M.H. Bayer, A. Wokaun,  
G.G. Scherer, I.A. Schneider
- In situ membrane parameter determination using simultaneously locally resolved impedance spectroscopy and dynamic water partial pressure measurement in PEFCs*  
Proc. 8<sup>th</sup> Fuel Cell Science and Technology Conference ASME 2010, Fuel Cell 2010-33041, Brooklyn, New York, June 14-16 (2010).
- F.N. Büchi, J. Eller, F. Marone,  
M. Stampanoni
- Determination of local GDL saturation on the pore level by in-situ synchrotron based X-Ray tomographic microscopy*  
ECS Transactions, **33**, 1397-1406 (2010).
- N. Linse, G.G. Scherer,  
A. Wokaun, L. Gubler
- Start/stop induced carbon corrosion in polymer electrolyte fuel cells*  
Proc. 8<sup>th</sup> Fuel Cell Science and Technology Conference ASME 2010, Fuel Cell 2010-33190, Brooklyn, New York, June 14-16 (2010).
- R. Kötz, P.W. Ruch, D. Cericola,  
A. Foelske, A. Wokaun
- Aging of carbon based supercapacitors at elevated voltages*  
Extended Abstract, ICAC 2010, International Conference on Advanced Capacitors, 22-25, Kyoto, Japan, May 31 - June 2 (2010).
- I.A. Schneider, S. von Dahlen,  
M.H. Bayer, G.G. Scherer,  
A. Wokaun
- AC impedance and transient technique based PEFC diagnostics: Insights from submillimeter resolved local measurements in channel and land areas*  
ECS Transactions **33**, 1321-1334 (2010).
- H. Schulenburg, B. Schwanz,  
J. Krbanjevic, N. Linse,  
R. Mokso, M. Stampanoni,  
A. Wokaun, G.G. Scherer
- 3D Imaging of polymer electrolyte fuel cell electrodes*  
ECS Transactions **33**, 1471-1481 (2010).

M. Stampanoni, J. Reichold<sup>1</sup>,  
B. Weber<sup>2</sup>, D. Habertür<sup>3</sup>,  
J. Schittny<sup>3</sup>, J. Eller, F.N. Büchi,  
F. Marone

*Deciphering complex, functional structures with synchrotron-based  
absorption and phase contrast tomographic microscopy*  
doi: 10.1117/12.860208, Proc. SPIE 7804, 78040L (2010).

<sup>1</sup> ETH, Zürich

<sup>2</sup> University of Zürich

<sup>3</sup> University of Bern

S. von Dahlen, G.G. Scherer,  
A. Wokaun, I.A. Schneider

*Start-stop phenomena in channel and land areas of a polymer  
electrolyte fuel cell (PEFC)*

ECS Transactions **33**, 1365 (2010).

## TALKS

### Invited Talks

- P. Boillat, *New insights to fuel cell modeling from recent advances in visualization*  
8<sup>th</sup> Fuel Cell Science and Technology Conference ASME 2010, Brooklyn,  
New York, June 14-16, 2010.
- P. Boillat, *Neutron imaging study of water distribution transients in polymer  
electrolyte fuel cells (PEFCs)*  
7<sup>th</sup> Symposium on Fuel Cell Modelling and Experimental Validation  
(MODVAL7), Lausanne, March 23-24, 2010.
- F.N. Büchi, *Imaging water in PEFC using x-rays and neutrons*  
Nordic Summer School, MEA in PEFC, Utö, Sweden, June 21-22, 2010.
- D. Cericola *Electrode materials for hybrid supercapacitors*  
CIMTEC 2010 - 12<sup>th</sup> International Conference on Modern Materials and  
Technologies, Montecatini Terme, Italy, June 6-18, 2010.
- D. Cericola *Towards the reliable hybridization of electrochemical capacitors and  
rechargeable batteries*  
University of Münster, Germany, December 9, 2010.
- L. Gubler *Polymer electrolyte fuel cell activities at PSI and in CH*  
IEA Advanced Fuel Cells (Annex 25) Stationary Fuel Cells Meeting No. 2,  
Winterthur, April 27-28, 2010.
- R. Kötz *Aging of carbon based supercapacitors at elevated voltages*  
International Conference on Advanced Capacitors, Kyoto, Japan,  
May 31 - June 2, 2010.
- R. Kötz *Capacitors based on SWNTs*  
COST Action 542 HPSTM, Joint WG1/ESR's Think Tank/ Core Group  
Meeting on Nano Materials in Supercapacitor Technology, Glasgow, UK,  
March 8-9, 2010.
- R. Kötz *Supercapacitors*  
Workshop on Nanomaterials Processing for Renewable Energy, PSI  
Villigen, March 4, 2010.
- P. Maire *In situ methods for the investigation of lithium batteries*  
1<sup>st</sup> Ertl Symposium on Electrochemistry & Catalysis: From Basic  
Research to Industrial Application, Gwangju, Korea, April 13, 2010.
- P. Novák *Elektrochemische Stromspeicher – eine der grössten Herausforderungen  
der Energiezukunft*  
i-net BASEL GreentechEvent: Intelligente Netze, innovative Technologien  
und effiziente Verbraucher, Fachhochschule Nordwestschweiz, Windisch,  
October 25, 2010.
- P. Novák *Batterieforschung am Paul Scherrer Institut*  
Robert Bosch GmbH, Gerlingen-Schillerhöhe, Germany, October 22,  
2010.

- P. Novák *In situ studies of battery electrode materials*  
Joint IOP/PSI Workshop on Synchrotron/Neutron/Muon Studies on Novel Materials, Bad Zurzach, October 15, 2010.
- P. Novák *Battery research: A wedding of solid state electrochemistry with surface electrochemistry*  
Minisymposium on Inorganic and Metalorganic Chemistry, ETH Zürich, October 6, 2010.
- P. Novák *In situ look at electrodes of lithium batteries*  
61<sup>st</sup> ISE Annual Meeting, Nice, France, September 27, 2010.
- P. Novák *Effiziente Stromspeicher – Voraussetzung für die Energieversorgung von morgen*  
Key Presentation at the «Swisslectric Research Award 2010», Bern, September 16, 2010.
- P. Novák *Battery research @ PSI*  
BASF SE, Ludwigshafen, Germany, August 11, 2010.
- P. Novák *An in situ Raman look into an extreme fast reactor: One-step microwave-assisted synthesis of doped LiFePO<sub>4</sub>*  
15<sup>th</sup> Int. Meeting on Lithium Batteries, Montréal, Canada, June 29, 2010.
- P. Novák *Solid electrolyte interphase - the key to carbon electrodes in batteries*  
Keynote Presentation at the Symposium "Next Generation Battery Materials", Hanse-Wissenschaftskolleg, Delmenhorst, Germany, June 18, 2010.
- P. Novák *Advanced batteries: New concepts, old materials*  
CCMX Technology Aperitif "Materials for Energy Applications", Baden, June 8, 2010.
- P. Novák *Battery electrode materials*  
Workshop on Nanomaterials Processing for Renewable Energy, PSI Villigen, March 4, 2010.
- P. Novák *Inhomogenitäten in Elektroden: Von der Grundlagenforschung zur Entwicklung von Lithiumionen-Batterien*  
Workshop Elektrochemische Energie-Speicher und -Wandlersysteme, Hanau, Germany, February 11, 2010.
- G.G. Scherer *Development of novel proton conducting membranes for electrochemical applications prepared by radiation grafting*  
Indian Institute of Technology, New Delhi, India, January 7, 2010.
- G.G. Scherer *Solid polymer electrolytes for fuel cell applications prepared by radiation grafted*  
Università Tor Vergata, Roma, Italia, March 5, 2010.
- G.G. Scherer *Polymer electrolyte fuel cells - some aspects of electrocatalysis*  
International Symposium on Electrocatalysis, Kloster Irsee, Germany, August 23–25, 2010.
- G.G. Scherer *Proton-conducting solid polymer electrolytes for fuel cell applications status of radiation grafted membranes*  
XII International Symposium on Polymer Electrolytes, Padova, Italia, August 28 - September 3, 2010.
- G.G. Scherer *Polymer electrolyte fuel cells - humidification studies by neutron imaging*  
Neutrons for Global Energy Solutions Conference, Bonn, Germany, September 26–30, 2010.
- G.G. Scherer *Status of radiation grafted membranes for fuel cell applications*  
IRAP 2010, University of Maryland, College Park, MD, USA, October 25-29, 2010.

- G.G. Scherer *Radiation grafted polymer membranes for fuel cell applications*  
3<sup>rd</sup> Coordination Meeting International Atomic Energy Agency,  
"Development of novel absorbents and membranes by radiation-induced  
grafting for selective purposes", Budapest, Hungary, December 6-10,  
2010.
- I.A. Schneider *AC impedance and transient technique based PEFC diagnostics: Insights  
from submillimeter resolved local measurements in channel and land  
areas*  
218<sup>th</sup> Electrochem. Soc. Meeting, Las Vegas, USA, October 10-15, 2010.
- I.A. Schneider *'I don't believe my eyes are wrong – the model is wrong' transient  
techniques in PEFC diagnostics*  
Kolloquium für Physikalische Chemie, ETH Zürich, November 30, 2010.

## Other Talks

- S. Balog, U. Gasser,  
K. Mortensen<sup>1</sup>, L. Gubler,  
H. Ben youcef, G.G. Scherer *Correlation between morphology, water uptake, and proton conductivity in  
radiation grafted proton exchange membranes*  
4<sup>th</sup> Symposium Hydrogen and Energy-EMPA, Dübendorf, January 24,  
2010.  
<sup>1</sup> University of Copenhagen, Frederiksberg, Denmark
- S. Balog, U. Gasser,  
K. Mortensen<sup>1</sup>, L. Gubler,  
H. Ben youcef, G.G. Scherer *Correlation between morphology, water uptake, and proton conductivity in  
radiation grafted proton exchange membranes*  
MRS 2010 Spring Meeting, San Francisco, USA, April 6, 2010.  
<sup>1</sup> University of Copenhagen, Frederiksberg, Denmark
- S. Balog, U. Gasser,  
K. Mortensen<sup>1</sup>, L. Gubler,  
H. Ben youcef, G.G. Scherer *Morphology, water uptake, and proton conductivity in radiation grafted  
proton exchange membranes*  
American Conference on Neutron Scattering, Ottawa, Canada, June 26,  
2010.  
<sup>1</sup> University of Copenhagen, Frederiksberg, Denmark
- S. Balog, U. Gasser,  
K. Mortensen<sup>1</sup>, L. Gubler,  
H. Ben youcef, G.G. Scherer *Morphology, water uptake, and proton conductivity in radiation grafted  
proton exchange membranes*  
Swiss Soft Days, Lausanne, June 23, 2010.  
<sup>1</sup> University of Copenhagen, Frederiksberg, Denmark
- M.H. Bayer, A. Wokaun,  
G.G. Scherer, I.A. Schneider *In situ membrane parameter determination using simultaneously locally  
resolved impedance spectroscopy and dynamic water partial pressure  
measurement in PEFCs*  
8<sup>th</sup> Fuel Cell Science and Technology Conference ASME 2010, Brooklyn,  
New York, USA, June 14, 2010.
- H. Ben youcef,  
K. Jetsrisuparb, A. Waibel<sup>1</sup>,  
L. Gubler, S. Balog,  
A. Wokaun, G.G. Scherer *The role of methacrylonitrile on the performance and stability of radiation  
grafted membranes for fuel cells*  
9<sup>th</sup> International Symposium on Ionizing Radiation and Polymers,  
Maryland, USA, October 25-29, 2010.  
<sup>1</sup> ETH Zürich
- F.N. Büchi, J. Eller,  
R. Flückiger, F. Marone,  
M. Stambanoni *Development of in-situ x-ray tomographic microscopy for PEFC*  
7<sup>th</sup> Symposium on Fuel Cell Modelling and Experimental Validation  
(MODVAL 7), Morges, March 22-24, 2010.
- F.N. Büchi, J. Eller,  
F. Marone, M. Stambanoni *Developing in-situ x-ray tomographic microscopy for PEFC*  
218<sup>th</sup> Electrochem. Soc. Meeting, Las Vegas, USA, October 10-15, 2010.
- D. Cericola, R. Kötz,  
P. Novák, A. Wokaun *Bi-material electrodes for hybrid electrochemical energy storage devices*  
61<sup>st</sup> ISE Annual Meeting, Nice, France, September 26 - October 1, 2010.
- J. Eller, F.N. Büchi,  
F. Marone, M. Stambanoni,  
A. Wokaun *In-situ X-ray tomographic microscopy of liquid water in PEFC*  
Electrochemistry 2010: From Microscopic Understanding to Global  
Impact, Bochum, Germany, September 13-15, 2010.

- A. Foelske-Schmitz,  
D. Weingarh, I. Czekaj,  
R. Kötz, A. Wokaun  
*XPS and DFT study of imidazolium based ionic liquids as electrolytes for high energy electrochemical double layer capacitors*  
61<sup>st</sup> ISE Annual Meeting, Nice, France, September 26-October 1, 2010.
- A. Foelske-Schmitz,  
I. Czekaj, D. Weingarh,  
R. Kötz  
*XPS and DFT study of imidazolium based ionic liquids as electrolytes for high energy electrochemical double layer capacitors*  
GDCh Electrochemistry Meeting, Bochum, Germany, September 13-15, 2010.
- R. Francke<sup>1</sup>, D. Cericola,  
R. Kötz, S. Waldvogel<sup>2</sup>  
*Novel chelatoborates as potential conducting salts for electrochemical double layer capacitors*  
61<sup>st</sup> ISE Annual Meeting, Nice, France, September 26 - October 1, 2010.  
<sup>1</sup> Kekulé Institute for Organic Chemistry and Biochemistry, Bonn, Germany  
<sup>2</sup> University of Mainz, Germany
- S. Freunberger<sup>1</sup>,  
L.J. Hardwick<sup>1</sup>, Z. Peng<sup>1</sup>,  
V. Giordani<sup>1</sup>, Y. Chen<sup>1</sup>,  
P. Maire, P. Novák,  
J.-M. Tarascon<sup>2</sup>,  
P. G. Bruce<sup>1</sup>  
*Fundamental mechanism of the lithium-air battery*  
15<sup>th</sup> Int. Meeting on Lithium Batteries, Montréal, Canada, July 1, 2010.  
<sup>1</sup> University of St. Andrews, Scotland  
<sup>2</sup> Université de Picardie Jules Verne, Amiens, France
- L. Gubler, S.M. Dockheer<sup>1</sup>,  
G.G. Scherer, A. Wokaun,  
W.H. Koppenol<sup>1</sup>  
*Kinetics of HO<sup>•</sup> radical attack on an ionomer model compound: a pulse radiolysis study*  
Progress MEA Conference, La Grande Motte, France, September 19-22, 2010.  
<sup>1</sup> ETH Zürich
- L. Gubler, F. Wallasch,  
K. Jetsrisuparb, H. Ben  
youcef, G.G. Scherer  
*Preparation and characterization of multi-monomer pre-irradiation grafted proton conducting membranes for fuel cells*  
MRS Fall Meeting, Boston, USA, November 29 - December 3, 2010.
- V.A. Guzenko,  
A. Savouchkina, J. Ziegler,  
C. Padeste, C. David  
*Fabrication of large-scale arrays of metallic nanodots by means of high resolution E-beam lithography*  
36<sup>th</sup> International Conference on Micro- and Nanoengineering, Genoa, Italy, September 19-22, 2010.
- A. Hintennach, P. Novák  
*In situ Raman microscopy for lithium-ion batteries*  
Gordon Research Conference on Electrochemistry, Ventura, USA, January 12, 2010.
- V. Godbole, J.-F. Colin,  
P. Novák  
*In situ synchrotron diffraction study of stoichiometric and overlithiated NMC*  
12<sup>th</sup> European Powder Diffraction Conference, Darmstadt, Germany, August 29, 2010.
- N. Linse, L. Gubler,  
G.G. Scherer, A. Wokaun  
*Start/stop induced carbon corrosion in polymer electrolyte fuel cells*  
8<sup>th</sup> Fuel Cell Science and Technology Conference ASME 2010, Brooklyn, New York, USA, June 14-16, 2010.
- F. Marone, R. Mokso,  
J. Eller, D. Grolimund,  
M. Stampanoni  
*X-ray tomographic microscopy for material characterization and dynamic imaging*  
TransPore2010, Villigen PSI, August 19-20, 2010.
- W. Märkle, C.-Y. Lu,  
D. Goers<sup>1</sup>, M.E. Spahr<sup>1</sup>,  
P. Novák  
*SEI formation or exfoliation? Insights in the electrolyte decomposition kinetics on graphite for lithium-ion battery anodes*  
217<sup>th</sup> Electrochem. Soc. Meeting, Vancouver, BC, Canada, April 25-30, 2010.  
<sup>1</sup> TIMCAL SA, Bodio
- P. Oberholzer, P. Boillat,  
R. Siegrist, R. Perego,  
A. Kästner, E.H. Lehmann,  
G.G. Scherer, A. Wokaun  
*Study of transport in PEFC membranes using neutron radiography with deuterium labeling*  
7<sup>th</sup> Symposium on Fuel Cell Modelling and Experimental Validation (MODVAL7), Morges, March 23-24, 2010.

- P. Oberholzer, P. Boillat, R. Siegrist, R. Perego, A. Kästner, E.H. Lehmann, G.G. Scherer, A. Wokaun  
*Study of transport in PEFC membranes using neutron radiography with deuterium labeling*  
61<sup>st</sup> ISE Annual Meeting, Nice, France, September 26 - October 1, 2010.
- T.J. Patey, M. Nakayama<sup>1</sup>, P. Novák  
*Charge storage properties of nano-LiMn<sub>2</sub>O<sub>4</sub>*  
15<sup>th</sup> Int. Meeting on Lithium Batteries, Montréal, Canada, July 1, 2010.  
<sup>1</sup> Nagoya Institute of Technology, Nagoya, Japan
- Z. Peng<sup>1</sup>, S.A. Freunberger<sup>1</sup>, L.J. Hardwick<sup>1</sup>, Y. Cheng<sup>1</sup>, V. Giordani<sup>1</sup>, P. Novák, J.-M. Tarascon<sup>2</sup>, P.G. Bruce<sup>1</sup>  
*Oxygen electrode reactions in the non-aqueous Li-air battery*  
61<sup>st</sup> ISE Annual Meeting, Nice, France, September 26 - October 1, 2010.  
<sup>1</sup> University of St. Andrews, Scotland  
<sup>2</sup> Université de Picardie Jules Verne, Amiens, France
- N.I. Prasianakis, J. Kang, J. Mantzaras, F.N. Büchi  
*Lattice Boltzmann modeling of transport phenomena in porous media with application to polymer electrolyte fuel cell systems*  
TransPore2010, Villigen PSI, August 19-20, 2010.
- T. Sasaki, V. Godbole, H.-H. Sommer, Y. Takeuchi<sup>1</sup>, Y. Ukyo<sup>1</sup>, P. Novák  
*Structural and morphological changes of Mg-substituted Li(Ni,Co,Al)O<sub>2</sub> during overcharge reaction*  
218<sup>th</sup> Electrochem. Soc. Meeting, Las Vegas, USA, October 10-15, 2010.  
<sup>1</sup> Toyota Central R&D Labs., Inc., Nagakute, Japan
- A. Savouchkina, A. Foelske-Schmitz, R. Kötz, G.G. Scherer, A. Wokaun  
*Pt enhanced corrosion of Pt/C model electrodes*  
GDCh Electrochemistry Meeting, Bochum, Germany, September 13-15, 2010.
- I.A. Schneider, S. von Dahlen, M.H. Bayer, P. Boillat, M. Hildebrandt, E.H. Lehmann, P. Oberholzer, A. Wokaun, G.G. Scherer  
*Combined use of submillimeter resolved current density measurements and in plane neutron radiography in polymer electrolyte fuel cells*  
8<sup>th</sup> Fuel Cell Science and Technology Conference ASME 2010, Brooklyn, New York, USA, June 14-16, 2010.
- I.A. Schneider, S. von Dahlen, A. Wokaun, G.G. Scherer  
*Expanding locally resolved impedance spectroscopy toward channel and land areas of polymer electrolyte fuel cells*  
EIS 2010, Algarve, Portugal, June 7, 2010.
- H. Schneider, A. Hintennach, P. Maire, P. Novák  
*Combined in situ FTIR and Raman microscopy of electrode materials – a new tool for battery scientists*  
SCS Fall Meeting, Zürich, September 16, 2010.
- H. Schulenburg, B. Schwanitz, J. Krbanjevic, N. Linse, R. Mokso, M. Stampanoni, A. Wokaun, G.G. Scherer  
*3D Imaging of polymer electrolyte fuel cell electrodes*  
218<sup>th</sup> Electrochem. Soc. Meeting, Las Vegas, USA, October 10-15, 2010.
- H. Schulenburg, T. Engl, L. Klüpfel, M. Nachttegaal  
*Activity and stability of PtCo<sub>x</sub> catalysts for oxygen reduction in polymer electrolyte fuel cells*  
SCS Fall Meeting, Zürich, September 16, 2010.
- B. Schwanitz, H. Schulenburg, A. Wokaun, G.G. Scherer  
*Long term stability studies of ultra low Pt anodes for polymer electrolyte fuel cells*  
3<sup>rd</sup> EuChemMS Chemistry Congress, Nürnberg, Germany, August 29 - September 2, 2010.
- M. Stampanoni, C. Hintermüller, J. Reichold<sup>1</sup>, B. Weber<sup>2</sup>, J. Schittny<sup>3</sup>, D. Haberthür<sup>3</sup>, F.N. Büchi, J. Eller, F. Marone  
*Deciphering complex, functional structures with synchrotron-based absorption and phase contrast tomographic microscopy*  
SPIE Symposium Optics and Photonics, San Diego, USA, August 1-5, 2010.  
<sup>1</sup> ETH Zürich  
<sup>2</sup> University of Zürich  
<sup>3</sup> University of Bern

- S. von Dahlen,  
G.G. Scherer, A. Wokaun,  
I.A. Schneider *Start-stop phenomena in channel and land areas of a polymer electrolyte fuel cell (PEFC)*  
218<sup>th</sup> Electrochem. Soc. Meeting, Las Vegas, USA, October 10-15, 2010.
- O. Waser<sup>1</sup>, A. Hintennach,  
R. Büchel<sup>1</sup>, P. Novák,  
S.E. Pratsinis<sup>1</sup> *Carbon-coated LiFePO<sub>4</sub> nanoparticles for Li-ion batteries*  
International Aerosol Conference 2010, Helsinki, Finland, September 1, 2010.  
<sup>1</sup> ETH Zürich
- M. Zaglio, T. Colinart<sup>1</sup>,  
A. Wokaun, J. Mantzaras,  
F.N. Büchi *PEFC parameters extraction using a multiparameter optimization algorithm*  
7<sup>th</sup> Symposium on Fuel Cell Modelling and Experimental Validation (MODVAL 7), Morges, March 22-24, 2010.  
<sup>1</sup> Université de Bretagne-Sud, Lorient, France
- M. Zaglio, A. Wokaun,  
J. Mantzaras, F.N. Büchi *Model-based transient analysis of polymer electrolyte fuel cells*  
61<sup>st</sup> ISE Annual Meeting, Nice, France, September 26 - October 1, 2010.

## POSTERS

- H. Ben youcef, R. Gyr,  
L. Gubler, S. Balog,  
A. Foelske, A. Wokaun,  
G.G. Scherer *Diisopropenylbenzene as new crosslinker in radiation grafted membranes for fuel cells: Improvement of homogeneity and interfacial properties*  
9<sup>th</sup> International Symposium on Ionizing Radiation and Polymers, Maryland, USA, October 25-29, 2010.
- H. Ben youcef, R. Gyr,  
L. Gubler, S. Balog,  
A. Foelske, A. Wokaun,  
G.G. Scherer *Diisopropenylbenzene as new crosslinker in radiation grafted membranes for fuel cells*  
Progress MEA 2010, La Grande Motte, France, September 19-22, 2010.
- S.M. Dockheer, L. Gubler,  
W.H. Koppenol<sup>1</sup> *Chain scission mechanisms in a polymer electrolyte fuel cell membrane*  
26<sup>th</sup> Symposium on Electrochemistry Villigen PSI, May 5, 2010.  
<sup>1</sup> ETH Zürich
- J. Eller, F.N. Büchi,  
S. McDonald, F. Marone,  
M. Stampanoni, A. Wokaun *Visualization of in-situ liquid water distribution in polymer electrolyte fuel cells using X-ray micro tomography*  
26<sup>th</sup> Symposium on Electrochemistry, PSI Villigen, May 5, 2010.
- J. Eller, F.N. Büchi,  
F. Marone, M. Stampanoni,  
A. Wokaun *In-situ x-ray tomographic microscopy of PEFC: Development and first results*  
12<sup>th</sup> Ulm ElectroChemical Talks, Ulm, Germany, June 16-17, 2010.
- J. Eller, F. Marone,  
M. Stampanoni, A. Wokaun,  
F.N. Büchi *Development of in-situ x-ray tomographic microscopy for PEFC*  
Gordon Research Conference on Fuel Cells, Smithfield, USA, August 1-6, 2010.
- J. Eller, F.N. Büchi,  
F. Marone, M. Stampanoni,  
A. Wokaun *In-situ imaging of liquid phase in polymer electrolyte fuel cells using X-ray tomographic microscopy*  
TransPore2010, Villigen PSI, August 19-20, 2010.
- A. Foelske-Schmitz,  
I. Czekaj, R. Kötz *XPS and DFT study of imidazolium based ionic liquids*  
EUCHEM Conference on Molten Salts and Ionic Liquids 2010, Bamberg, Germany, March 14-19, 2010.
- A. Foelske-Schmitz,  
D. Weingarh, I. Czekaj,  
R. Kötz *XPS and DFT study of imidazolium based ionic liquids as electrolytes for supercapacitors*  
26<sup>th</sup> Symposium on Electrochemistry, PSI Villigen, May 5, 2010.
- M. Heß, W. Märkle, P. Novák *High rate capability of graphite anodes in lithium-ion batteries*  
SCS Fall Meeting, ETH Zürich, September 16, 2010.

- A. Hintennach, O. Waser<sup>1</sup>, S.E. Pratsinis<sup>1</sup>, P. Novák  
*Electrochemical performance of aerosol-made, in situ carbon-coated LiFePO<sub>4</sub> nanoparticles*  
15<sup>th</sup> Int. Meeting on Lithium Batteries, Montréal, Canada, June 27 - July 2, 2010.  
<sup>1</sup> ETH Zürich
- K. Jetsrisuparb, H. Ben youcef, G.G. Scherer, A. Wokaun, L. Gubler  
*Styrene / methacrylonitrile co-grafted membranes for fuel cells*  
Progress MEA Conference, La Grande Motte, France, September 19-22, 2010.
- K. Jetsrisuparb, H. Ben youcef, G.G. Scherer, A. Wokaun, L. Gubler  
*Styrene / methacrylonitrile co-grafted membranes for fuel cells*  
SCS Fall Meeting, ETH Zürich, September 16, 2010.
- E. Kirk, J. Krbanjevic, T. Vogel, A. Foelske-Schmitz, J. Gobrecht, S. Tsujino  
*All-Metal molded field emitter arrays by sputtering, evaporation and electrochemical deposition*  
Magnetron, Ion processing & Arc Technologies, European Conference 2010, Metz, France, June 15-18, 2010.
- L. Klüpfel, M. Nachtegaal, H. Schulenburg, T. Engl  
*XAS studies of leached PtCo catalysts for PEFCs*  
SCS Fall Meeting, Zürich, September 16, 2010.
- S. Kreitmeier, G.A. Schuler, A. Wokaun, F.N. Büchi  
*Pinhole formation during membrane degradation in PEFC*  
12<sup>th</sup> Ulm ElectroChemical Talks, Ulm, Germany, June 16-17, 2010.
- S. Kreitmeier, G.A. Schuler, A. Wokaun, F.N. Büchi  
*Investigation of polymer electrolyte membrane degradation based on local gas phase analysis*  
7<sup>th</sup> Symposium on Fuel Cell Modelling and Experimental Validation (MODVAL 7), Morges, March 23-24, 2010.
- S. Kreitmeier, G.A. Schuler, A. Wokaun, F.N. Büchi  
*Investigation of polymer electrolyte membrane degradation based on local gas phase analysis*  
26<sup>th</sup> Symposium on Electrochemistry, PSI Villigen, May 5, 2010.
- T. Sasaki, J.-F. Colin, V. Godbole, Y. Takeuchi<sup>1</sup>, Y. Ukyo<sup>1</sup>, P. Novák  
*Crystal structure changes during overcharge of Mg-substituted Li(Ni,Co,Al)O<sub>2</sub> by in situ synchrotron X-ray diffraction*  
15<sup>th</sup> Int. Meeting on Lithium Batteries, Montréal, Canada, June 27 - July 2, 2010.  
<sup>1</sup> Toyota Central R&D Labs., Inc., Nagakute, Japan
- T. Sasaki, A. Hintennach, Y. Ukyo<sup>1</sup>, Y. Takeuchi<sup>1</sup>, P. Novák  
*Electrochemical and morphological effects of high voltage and high temperature on Mg-substituted Li(Ni,Co,Al)O<sub>2</sub>.*  
15<sup>th</sup> Int. Meeting on Lithium Batteries, Montréal, Canada, June 27 - July 2, 2010.  
<sup>1</sup> Toyota Central R&D Labs., Inc., Nagakute, Japan
- A. Savouchkina, G.G. Scherer, A. Wokaun, R. Koetz, A. Foelske-Schmitz  
*Effect of thermal treatment of glassy carbon on corrosion of Pt/C model electrodes*  
61<sup>st</sup> ISE Annual Meeting, Nice, France, September 26 - October 1, 2010.
- Y. Yamada (Sasaki), T. Nakamura<sup>1</sup>, R. Kötzt, K. Yano<sup>1</sup>  
*Fabrication and application of hollow mesoporous silica microcapsules.*  
TransPore 2010, Villigen PSI, August 19-20, 2010.  
<sup>1</sup> Toyota Central R&D Labs., Inc., Nagakute, Japan
- H. Schneider, A. Hintennach, P. Maire, P. Novák  
*Combined in situ FTIR and Raman microscopy of electrode materials – a new tool for battery scientists*  
15<sup>th</sup> Int. Meeting on Lithium Batteries, Montréal, Canada, June 27-July 2, 2010.
- H. Schulenburg, B. Schwanzitz, J. Krbanjevic<sup>1</sup>, T. Engl  
*3D Imaging of PEFC electrode degradation*  
Progress MEA, La Grande Motte, France, September 20-22, 2010.  
<sup>1</sup> EPF, Lausanne
- H. Schulenburg, T. Engl, L. Klüpfel, M. Nachtegaal  
*Activity and stability of PtCo<sub>x</sub> Catalysts for oxygen reduction in polymer electrolyte fuel cells*  
SCS Fall Meeting, ETH Zürich, September 16, 2010.

- B. Schwanitz,  
H. Schulenburg,  
J. Krbanjevic<sup>1</sup>,  
M. Stampanoni, A. Wokaun,  
G.G. Scherer  
*Rapid aging of polymer electrolyte fuel cells electrodes - 3D morphological study by high-resolution X-ray tomography and FIB/SEM serial sectioning*  
TransPore2010, Villigen-PSI, August 19-20, 2010.  
<sup>1</sup> EPF, Lausanne
- B. Schwanitz,  
H. Schulenburg,  
M. Horisberger, A. Wokaun,  
G.G. Scherer  
*Polymer electrolyte fuel cells – Performance and longevity of ultra low Pt anodes*  
CUSO – Summer School: Nanoelectrochemistry, Villars-sur-Ollon, September 5-9, 2010.
- F. Simmen, A. Hintennach,  
M. Horisberger, T. Lippert,  
P. Novák, C.W. Schneider,  
A. Wokaun  
*Glassy carbon – a promising substrate material for pulsed laser deposition of thin  $Li_{1+x}Mn_2O_4$  electrodes*  
E-MRS Spring Meeting, Strasbourg, France, June 2010.
- P. Verma, P. Maire,  
P. Novák  
*Bridging electrografting and chemical modification to prepare carbonate modified carbon surfaces*  
61<sup>st</sup> ISE Annual Meeting, Nice, France, September 26 - October 1, 2010.
- O. Waser<sup>1</sup>, A. Hintennach,  
R. Büchel<sup>1</sup>, P. Novák,  
S.E. Pratsinis<sup>1</sup>  
*In situ carbon-coated  $LiFePO_4$  nanoparticles for Li-ion batteries*  
15<sup>th</sup> Int. Meeting on Lithium Batteries, Montréal, Canada, June 27 - July 2, 2010.  
<sup>1</sup> ETH Zürich
- O. Waser<sup>1</sup>, A. Hintennach,  
R. Büchel<sup>1</sup>, F. Krumeich<sup>1</sup>,  
P. Novák, S.E. Pratsinis<sup>1</sup>  
*In situ carbon coating of flame made  $LiFePO_4$  nanoparticles for batteries*  
The World Student Conference on Particle Technology, Delft, The Netherlands, April 26-29, 2010.  
<sup>1</sup> ETH Zürich
- D. Weingarh, A. Foelske-Schmitz, R. Kötz, A. Wokaun  
*Potential windows of the ionic liquid [EMIM][BF<sub>4</sub>] as electrolyte for electrochemical supercapacitors*  
CUSO Summer School: Nanoelectrochemistry, Villars-sur-Ollon, September 5-9, 2010.

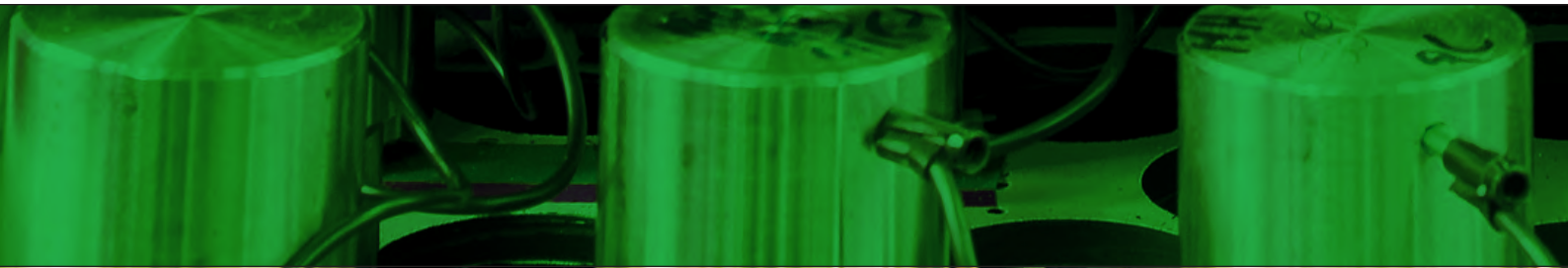
## CONFERENCES, WORKSHOPS & EXHIBITIONS

- R. Kötz  
*ESSCAP'10, 4<sup>th</sup> European Symposium on Super Capacitors & Applications*  
Bordeaux, France, October 21-22, 2010.  
Member of the International Scientific Committee
- R. Kötz  
*2010 International Conference on Advanced Capacitors*  
Kyoto, Japan, May 31 - June 2, 2010.  
Session Chair
- P. Novák  
*CIMTEC 2010 - 12<sup>th</sup> International Conference on Modern Materials and Technologies*  
Montecatini Terme, Italy, June 6-18, 2010.  
Member of the Advisory Board Symposium "Electrochemical Energy Storage Systems: the Next Evolution"
- G.G. Scherer, R. Kötz,  
P. Novák  
*Electrochemistry in Switzerland*  
26<sup>th</sup> One-Day-Symposium, PSI Villigen, May 5, 2010.  
Organizers

## MEMBERSHIPS IN EXTERNAL COMMITTEES

R. Kötz	<i>ISE Publication Committee</i> Chair
R. Kötz	<i>Electrochimica Acta</i> Member of Advisory Board
P. Novák	<i>International Society of Electrochemistry</i> Vice-President
P. Novák	<i>Materials</i> Member of the Editorial Board
P. Novák	<i>The Northeastern Center for Chemical Energy Storage (NECCES)</i> Member of the Scientific Advisory Board
G.G. Scherer	<i>Asian Polymer Association, New Delhi, India</i> Honorary Member
G.G. Scherer	<i>Editorial Board Electrocatalysis</i> Member
G.G. Scherer	<i>Kantonsschule Wohlen</i> Maturitätsprüfungsexperte Biologie/Chemie
G.G. Scherer	<i>Advisory Board European Fuel Cell Forum</i> Member





PAUL SCHERRER INSTITUT



Paul Scherrer Institut, 5232 Villigen PSI, Switzerland  
Tel. +41 (0)56 310 21 11, Fax +41 (0)56 310 21 99  
[www.psi.ch](http://www.psi.ch)